A STUDY OF MAGNETOPLASMADYNAMIC EFFECTS IN TURBULENT SUPERSONIC FLOWS WITH APPLICATION TO DETONATION AND EXPLOSION

A Thesis
Presented to
The Academic Faculty

by

Joseph C. Schulz

In Partial Fulfillment
of the Requirements for the Degree
Doctor of Philosophy in
Aerospace Engineering

School of Aerospace Engineering
Georgia Institute of Technology
August 2015

A STUDY OF MAGNETOPLASMADYNAMIC EFFECTS IN TURBULENT SUPERSONIC FLOWS WITH APPLICATION TO DETONATION AND EXPLOSION

Approved by:

Professor Suresh Menon, Advisor
School of Aerospace Engineering
Georgia Institute of Technology

Professor Wenting Sun
School of Aerospace Engineering
Georgia Institute of Technology

Professor Mitchell Walker
School of Aerospace Engineering
Georgia Institute of Technology

Professor Tim Lieuwen
School of Aerospace Engineering
Georgia Institute of Technology

Professor John Wise
School of Physics
Georgia Institute of Technology

Date Approved: May 4, 2015

ACKNOWLEDGEMENTS

I am sincerely grateful for the time I have spent in the Computational Combustion Laboratory at Georgia Tech. During this time, I have had the opportunity to work with some very wonderful and intelligent people. The experience has been tremendously rewarding. First and foremost, I would like thank my advisor, Dr. Suresh Menon, for constantly challenging me and providing me the opportunity to pursue the research presented in this thesis. Without his continual support, none of this would be possible. His advice and guidance have been instrumental in making me a more confident and able researcher. I would also like to thank my committee members, Dr. Mitchell Walker, Dr. John Wise, Dr. Wenting Sun, and Dr. Tim Lieuwen for taking the time to read this thesis and provide feedback.

While I have had the pleasure of working with many people, I would like to specifically mention a few. First, I would like to thank Dr. Kenji Miki, who was my co-worker and mentor when I first joined the CCL as an undergraduate student. I will not forget the years we spent developing our first working version of a MHD code. Nor will I forget his generous invitation to visit Japan so many years ago. Since that time, I am grateful to still count Kenji as a wonderful friend and fellow colleague. Additionally, I am happy to acknowledge many of my fellow colleagues. It has been a pleasure working with them over the years. Kalyana Gottiparthi has been a good friend and co-worker. He has taught me much about the physics of detonations and dispersed-phase flows. I would also like to thank Andy Smith, who introduced me to many new programming languages, particularly Python. The inspiration to pursue the high order finite difference methods used in this thesis is largely a result of his initiative. Additionally, I would like to thank both Matthew Clay and particularly Dr.

Reetesh Ranjan for their help, discussion, and feedback on many research projects.

Last but not least, I would like to acknowledge the Defense Threat Reduction Agency, particularly Dr. Suhithi Peiris, for providing both financial support and the computational resources on many high performance computing machines supported by the Department of Defense that made this research possible.

TABLE OF CONTENTS

LIST OF TABLES

LIST OF FIGURES

LIST OF SYMBOLS OR ABBREVIATIONS

Roman Symbols

$\mathbf{A}$, A_i, (A_x, A_y, A_z)	magnetic vector potential, $\mathrm{V{\cdot}s{\cdot}m^{-1}}$
$\mathbf{A}_{ijk}$	magnetic vector potential at $(x_{ijk}, y_{ijk}, z_{ijk})$, $\mathrm{V{\cdot}s{\cdot}m^{-1}}$
$\mathbf{B}$, B_i, (B_x, B_y, B_z)	magnetic field vector, T or $\mathrm{m{\cdot}s^{-1}}$
B_0	reference magnetic field, T or $\mathrm{m{\cdot}s^{-1}}$
$\mathbf{B}_{ijk}$	magnetic field vector at $(x_{ijk}, y_{ijk}, z_{ijk})$, T or $\mathrm{m{\cdot}s^{-1}}$
$\mathbf{b}$, b_i, (b_x, b_y, b_z)	magnetic field vector, T or $\mathrm{m{\cdot}s^{-1}}$
$\mathbf{b}_{ijk}$	magnetic field vector at $(x_{i+1/2,j,k}, y_{i,j+1/2,k}, z_{i,j,k+1/2})$, T or $\mathrm{m{\cdot}s^{-1}}$
c	speed of sound, $\mathrm{m{\cdot}s^{-1}}$
c_a	speed of the Alfven wave, $\mathrm{m{\cdot}s^{-1}}$
c_f	speed of the fast magnetosonic wave, $\mathrm{m{\cdot}s^{-1}}$
c_p	specific heat at constant pressure per unit mass, $\mathrm{J{\cdot}kg^{-1}{\cdot}K^{-1}}$
c_s	speed of the slow magnetosonic wave, $\mathrm{m{\cdot}s^{-1}}$
c_v	specific heat at constant volume per unit mass, $\mathrm{J{\cdot}kg^{-1}{\cdot}K^{-1}}$
D_k	mass diffusivity of the k^{th}species, $\mathrm{m^2{\cdot}s^{-1}}$
e	elementary charge, $1.602176565(35) \times 10^{?19}$ C
e	internal energy per unit mass, $\mathrm{J{\cdot}kg^{-1}}$
E_a	activation energy of Arrhenius reaction, $\mathrm{kJ{\cdot}mol^{-1}}$
$\mathbf{E}$, E_i, (E_x, E_y, E_z)	electric field vector, $\mathrm{V{\cdot}m^{-1}}$
$\mathbf{E}_{ijk}$	electric field vector at $(x_{ijk}, y_{ijk}, z_{ijk})$, $\mathrm{V{\cdot}m^{-1}}$
$\mathbf{f}$	flux vector in x-direction, $(\star){\cdot}\mathrm{m^{-2}{\cdot}s^{-1}}$
$\mathbf{F}$	numerical flux vector in x-direction, $(\star){\cdot}\mathrm{m^{-2}{\cdot}s^{-1}}$
$\mathbf{g}$	flux vector in y-direction, $(\star){\cdot}\mathrm{m^{-2}{\cdot}s^{-1}}$
$\mathbf{G}$	numerical flux vector in y-direction $(\star){\cdot}\mathrm{m^{-2}{\cdot}s^{-1}}$

$\mathbf{h}$	flux vector in z-direction, $(\star)\cdot\mathrm{m}^{-2}\cdot\mathrm{s}^{-1}$
$\mathbf{H}$	numerical flux vector in z-direction, $(\star)\cdot\mathrm{m}^{-2}\cdot\mathrm{s}^{-1}$
h	total enthalpy per unit mass, $\mathrm{J}\cdot\mathrm{kg}^{-1}$
J_i, (J_x, J_y, J_z)	current density vector at $(x_{ijk}, y_{ijk}, z_{ijk})$, $\mathrm{A}\cdot\mathrm{m}^{-3}]$
k_B	Boltzmann constant, $1.3806488(13) \times 10^{-23}$, $\mathrm{J}\cdot\mathrm{K}^{-1}$
l_0	reference length scale, m
Le	Lewis number
m_α	mass of particle type α, kg
Ma	Mach number
n_α	particle number density, m^{-3}
N	Stuart number or interaction parameter
N_D	number of particles inside a Debye sphere
N_s	total number of species
N_x	number of computational points in x-direction
N_y	number of computational points in y-direction
N_z	number of computational points in z-direction
p	thermodynamic pressure [Pa]
P^*	total pressure, thermodynamic plus magnetic pressure [Pa]
Pr	Prandtl number
$\mathbf{q}$	state vector of the conservative variables
$\mathbf{Q}$	state vector of the numerical conservative variables
q_α	charge of particle type α, C
q_i	heat flux vector, $\mathrm{W}\cdot\mathrm{m}^{-2}$
R	mixture averaged gas constant, $\mathrm{J}\cdot\mathrm{K}^{-1}\cdot\mathrm{mol}^{-1}$
R_α	particle gyro-radius, m
R_k	gas constant for the k^{th} species, $\mathrm{J}\cdot\mathrm{K}^{-1}\cdot\mathrm{mol}^{-1}$
Re	Reynolds number

Re_m	magnetic Reynolds number
T	equilibrium temperature, K
T_α	electron, ion, or neutral temperature, K
t	time, s
t_n	discrete time at integration step n
t_{n+1}	discrete time at integration step $n+1$
u_i, (u_x, u_y, u_z)	velocity vector at $(x_{ijk}, y_{ijk}, z_{ijk})$, m·s^{-1},
u_0,	reference velocity scale, m·s^{-1},
$V_{i,k}$	diffusion velocity of the k^{th} species, m·s^{-1}
v_a	speed of the Alfven wave, m·s^{-1}
W	mixture averaged molecular weight, mol·g^{-1}
W_k	molecular weight of the k^{th} species, mol·g^{-1}
$\mathbf{x}$, x_i, (x, y, z)	Cartesian coordinates, m
x_{ijk}	location of the computational cell in the x-dimension, m
y_{ijk}	location of the computational cell in the y-dimension, m
z_{ijk}	location of the computational cell in the z-dimension, m
X_k	mole fraction of the k^{th} species
Y_k	mass fraction of the k^{th} species

Greek Symbols

γ	ratio of specific heats
Δx	length of a computational finite-volume cell in the $x-$direction, m
Δy	length of a computational finite-volume cell in the $y-$direction, m
Δz	length of a computational finite-volume cell in the $z-$direction, m
δ_{ij}	Kronecker delta
Δh_f	enthalpy of formation per unit mass, J·kg^{-1}·mol^{-1}
ϵ_0	permittivity of free space, $8.85418781762 \times 10^{-12}$
ϵ_{ijk}	alternating tensor

γ	ratio of specific heats
ϕ	electric potential, V
η	magnetic diffusivity, $\mathrm{m}^2{\cdot}\mathrm{s}^{-1}$
η_L	width of the mixing zone, m
κ	thermal conductivity, $\mathrm{W}{\cdot}\mathrm{m}^{-1}{\cdot}\mathrm{K}^{-1}$
λ_D	Debye length, m
μ	dynamic viscosity
μ_0	magnetic permeability of free space, $4\pi \times 10^{-7}$ $\mathrm{N}{\cdot}\mathrm{A}^{-2}$
ν	kinematic viscosity
ρ	gas density, $\mathrm{kg}{\cdot}\mathrm{m}^{-3}$
ρ_c	charge density, $\mathrm{kg}{\cdot}\mathrm{m}^{-3}$
τ, τ_f	reference time scale of flow, s
τ_n	neutral particle collision time, s
τ_α	ion-ion or electron-electron collision time, s
τ_{ij}	viscous stress tensor
σ	electrical conductivity, $\mathrm{S}{\cdot}\mathrm{m}^{-1}$
σ_d	particle cross section
$\dot{\omega}$	reaction rate per unit volume, $\mathrm{kg}{\cdot}\mathrm{s}{\cdot}\mathrm{m}^{-3}$
ω	reference frequency of flow, s^{-1}
ω_{pe}	electron plasma frequency , s^{-1}
Ω_α	gyro-frequency of a particle, s^{-1}

Subscripts or Superscripts

α	particle type $(= e, i, n)$
e	electron quantity
i, j, k	Cartesian tensor indices or species indices
k	species index
n	time step index

0	reference quantity

Other Symbols

∂	partial derivative operator
∇	gradient operator
$\nabla\cdot$	divergence operator
$\sum$	summation operator
Δ	difference operator

Abbreviations

CFD	Computational Fluid Dynamics
CFL	Courant-Friedrichs-Lewy number
CT	Constrained Transport
CTU	Corner Transport Update
DNS	Direct Numerical Simulation
FD	Finite-Difference
FV	Finite-Volume
FDS	Flux Difference Splitting
FVS	Flux Vector Splitting
ISM	Interstellar Medium
LES	Large Eddy Simulation
MHD	Magnetohydrodynamics
MPI	Message Passing Interface
MUSCL	Monotone Upstream-centered Schemes for Conservation Laws
ODE	Ordinary Differential Equation
PDE	Partial Differential Equation
PDF	Probability Distribution Function
PPM	Piecewise Parabolic Method

RANS	Reynolds Averaged Navier-Stokes
RMI	Richtmyer-Meshkov Instability
RTI	Rayleigh-Taylor Instability
SSPRK	Strong Stability Preserving Runge-Kutta
WENO	Weighted Essentially Non-Oscillatory

SUMMARY

Scientists and engineers have long been interested in explosions. These ubiquitous, disruptive events occur throughout the Universe, and when controlled, they have been used by humans for both good and ill for many centuries. There are many types of explosions, but in all scenarios they involve a tremendous release of energy. Whether it is chemical, nuclear, or magnetic energy, the explosion event culminates in the outward propagation of strong pressure waves. In a stellar explosion or supernova, the blast wave propels large clouds of gas and dust through the interstellar medium (ISM) populating the Universe with the heavy matter necessary for the formation of stars and galaxies. More common, however, are chemical explosions, such as those occurring from the detonation of a high-explosive. In these events, the explosion is initiated by a detonation wave that converts chemical energy into kinetic energy providing the power to propel the blast wave. This expansion of hot gases is further supported by the combustion of the unburnt products as they mix with the surrounding air. The physical processes of both stellar and chemical explosions are similar. In general, the explosive event can be divided into two parts, one concerning the energetic conversion process, which could occur through a detonation wave, and the second concerning the mixing of the explosive products and the interaction of the blast wave with the surrounding environment.

Given the long history of using chemical explosives in engineering, the detonation and explosion of a condensed-phase material is moderately understood. Nuclear and stellar explosions, on the other hand, are far more complex and far more difficult to observe. As a result of the magnitude and scale of the event, electromagnetic

and gravitational forces, radiative heat transfer, and dispersed phase dynamics can be important. In this thesis, the effects of a magnetic field are considered. Two particular scenarios are addressed. In both cases, the effects of a magnetic field have been observed to be important, and the two scenarios align with the two sub-divisions of the explosion process previously mentioned, categorized so by the time scales in which they occur; the propagation of the detonation occurs at much shorter time scales than the blast accelerated mixing processes occurring in the aftermath of the explosion. More importantly, these scenarios highlight the two different ways in which a magnetic field can influence a plasma.

Since the ISM is known to have a persistent background magnetic field, it could influence supernova. Flow instabilities driven by the explosion can amplify the magnetic field through an inductive electromotive force, possibly to a magnitude that might alter the overall dynamics of the explosion. A similar process is often used in engineering applications of detonation and explosion, i.e., using an applied magnetic field coupled with a detonation wave to generate energy through an inductive electromotive force. From a more general perspective, the magnetic field can also affect the underlying physics governing the nature of the propagation of a detonation wave. As a result of the difficultly in extracting detailed information about how a detonation or explosion behaves in a magnetized environment, numerical simulations are often needed to further substantiate observation. A significant effort in this thesis has been the implementation of numerical methods capable of simulating detonation and explosions in such a setting, wether it be in an astrophysical environment or in the products of a high-explosive. The challenge is a result of the requirement for the magnetic field to be divergence free. This imposes a severe restriction on the extension of numerical methods developed for non-magnetized flows to magnetohydrodynamics (MHD).

Several different numerical methods for MHD have been implemented and are assessed based on their ability to simulate compressible, resistive MHD flows containing strong shocks. These methods are grouped into two categories. The first group of numerical methods are categorized by their common use of some type of divergence cleaning algorithm. The second group of numerical methods use a constrained transport algorithm, which builds the divergence free nature of the magnetic field into the numerical method itself. As a result, constrained transport methods are popular and have been commonly used in many astrophysical codes. These methods, however, are complex and difficult to extend to high orders of accuracy. Furthermore, adapting these methods for resistive MHD and ensuring they are consistent within a hybrid shock capturing scheme is not straight-forward task. In order to avoid these complications, divergence cleaning methods are often used instead. This class of numerical methods, however, suffers from the further burden of requiring proof that the cleaning algorithm is indeed adequate, particularly since the choice of the divergence cleaning algorithm can be problem dependent. Thus, it is beneficial to have a general numerical method for MHD allowing for the choice between many different options. This allows for a careful assessment of the "right" numerical method for the application such that the simulation is robust, computationally efficient, and has a high order of accuracy.

Using these numerical methods, a gaseous ionizing detonation wave is simulated in a domain allowing the detonation to freely propagate in an unconfined environment. While not all explosions necessarily produce detonation waves, most condensed-phase explosions do (it is still uncertain whether deflagration to detonation transition occurs in supernovae). In terrestrial applications, the temperature of the explosive products of a condensed-phase detonation are high enough for ionization reactions to be significant. Values of the electrical conductivity computed from numerical simulations are comparable to those measured in experiments. When a detonation wave propagates

in an applied magnetic field, numerical simulations indicate that the magnetic field affects the structure of the detonation wave, ultimately affecting the propagation of the wave. By varying the electrical conductivity through the addition of potassium and by changing the magnitude of the magnetic field, the detonation propagation is shown to be dependent on the Stuart number with the length scale based on the half-reaction distance and the time scale dependent on the velocity of the detonation wave.

Whether or not detonation occurs, the fluid mixing processes in the post-explosion flow are similar. Flow instabilities drive fluid entrainment, and as the surface area of the material interface between the different fluids increases, mixing at a molecular level becomes more significant. Eventually the mixing zone transitions from a laminar to a turbulent mixing process resulting in a final state of fully-developed turbulence. This process is altered in a magnetized plasma. In this thesis, the Richtmyer-Meshkov instability (RMI) is used to study fluid mixing. Depending on the electrical conductivity of the plasma, the magnitude of the magnetic field, and the time-scales of the RMI, the instability can be stabilized. A criteria for this is established for both ideal and resistive plasma. In a resistive plasma, the magnetic Reynolds number determines the effectiveness of the magnetic field to influence the growth rate of the RMI. If mixing is not initially inhibited by the stabilization of the RMI, the mixing process is shown to excite a dynamo process which amplifies the magnetic field until it becomes saturated. Once saturation occurs, the large-scale fluid entrainment is inhibited. Both the amplification of the magnetic field and variable density mixing in magnetized plasma has important implications in the ISM.

CHAPTER I

INTRODUCTION

With an equal sense of awe and foreboding, humans have long observed the sudden appearance and then slow fading of stars in the night sky. Perhaps the ancient observers were correct to revere such mysteries. These "guest stars" appearing in the night sky are as much symbols of life, death, and rebirth, as they actually *are* real representations of the transformative events containing the mysteries of our existence. For these bright, transient dots in the night sky are the last remains of a star. In death, this progenitor expels huge clouds of rapidly expanding gas through the Universe, populating it with the heavy matter necessary for the creation of new stars [217]. While such events are extremely rare in our galaxy, they occur with relative frequency throughout the Universe. The first recorded observation of a supernova explosion was made by Chinese astronomers in year AD 185 [39]. It was not until many years later, in the year AD 1006, that a supernova was observed by a widespread number of civilizations [75]. This supernova, occurring only 7,000 light-years away, is the brightest to have ever been recorded. One could have seen it during the day [219]. As scientific instruments have improved, more and more detailed measurements have been made, notably by Brahe in 1572, by Kepler in 1602, who observed the last supernova to have occurred in our galaxy, and recently by a number of scientists in 1987 who have obtained the most detailed data of any supernova to date [112]. From continual observation of these distant explosions and measurements of the radiation emitted in the expanding remnants, scientists are now able to classify supernovae into different types. Classification is far from understanding though, and there are still many unanswered questions.

Figure 1 is an image obtained by the Hubble Space Telescope of the remnant of the 1987 supernova (SN1987A). Generally speaking there are two types, with some sub-classifications, of supernovae explosions. They are categorically characterized based on the triggering mechanism of the explosion, either of the accretion/detonation type (Type I) or the core collapse type (Type II) [217]. SN1987A was a Type II supernova. Located in the Large Magellanic Cloud, 163,000 light-years away from Earth, it is currently the closest supernova to have occurred in the modern age. A prominent feature of SN1987A is that some 20,000 years prior, the dying star ejected a ring of dense gas about its equatorial plane. This ring is easily observable in Fig. 1 by dozens of bright spots. These distinctive "finger-like" structures were formed as a result of a hydrodynamic fluid instability occurring when any two gases of different density mix under the acceleration of gravity or through the momentum impulse of the blast wave [4, 106]. The X-ray and the synchrotron radiation emitted from the supernova remnant are still being measured today to discover more about the dynamics of supernovae remnants [205].

Yet supernovae are just one example of explosive phenomenon. The Universe is replete with such catastrophic events, from solar flares to magnetic reconnections. The difference is only in the source of energy powering the explosion [145]. In other words, the term explosion refers to any scenario in which energy (magnetic, gravitational, chemical, nuclear, etc.) is injected into a system faster than it can be smoothly equilibrated throughout the system. More exactly, an explosion occurs if the rate of energy injection is faster than the dynamic scales defined by the characteristic time (l_0/c_f), the size (l_0), and acoustic (or magneto-acoustic) velocity (c_f) of the system. The explosion results in a rapid raise in the local pressure, and if the system is unconfined, strong pressure waves or shock waves propagate outward while the hot products continue to expand and cool in time [225]. This general description is as applicable to Big Bang as it is to the explosion of a fire-cracker. Hence, a number of

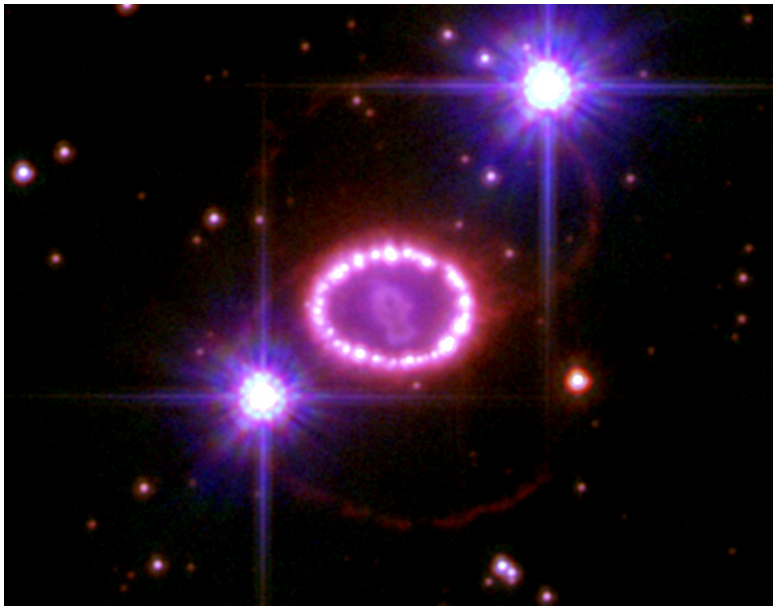

Figure 1: Image taken by the Hubble Space Telescope of SN1987A *Credit: NASA / ESA / Hubble Heritage Project.* At the time when the image was taken the estimated radius of the equatorial ring is approximately 6.23×10^12 km [150]

fundamental questions can be posed about the physics, chemistry, and dynamics of explosions, which are intimately related to both the engineering of explosives as well as to the understanding of the physical processes involved. The parallels are important. Chemical explosions in comparison to astrophysical explosions are far less complex, easier to control, and more amenable to measurement [145]. From such comparisons, scientists can more easily develop insight into the common physical processes, such as deflagration to detonation transition (DDT) [38], the role of compressible turbulence in the mixing of hot products [194], and the interaction of shock waves with surrounding matter [70], all of which are important in an explosion. Of particular interest in this thesis is the influence a background magnetic field may have on an explosion event. While such interactions are more common in astrophysical scenarios since over 90% of the baryonic matter in the Universe is in the plasma state [49, 74], potential terrestrial applications are investigated as well; however, in these applications, the additional consideration of plasma production must be addressed. Given

the differences between astrophysical and terrestrial plasma, it is important to discuss the typical characteristics of each.

In 1939, Bethe demonstrated that stars maintain their energy through the process of thermonuclear fusion [17]. As a result, it was concluded that stars consisted primarily of ionized hydrogen and helium gases. These ionized gases are visible during a solar eclipse, where the plasma near the surface of the Sun, called the coronal plasma, extends far from the surface, the shape of which is supported by the extending magnetic field lines [192]. These structures highlight the complex dynamics between a plasma and an electromagnetic field. For example, a geometrical rearrangement of the magnetic field lines along the surface can result in an explosion of magnetic energy resulting in an expulsion of plasma in the form of solar flares and coronal mass ejections. These events eventually interact with the Earth's own magnetic field creating a dynamical system referred to as space weather [95, 111, 183].

The magnetic field also plays a fundamental role in the interior of a star or planet. For instance, the sustainment of both the Sun's and Earth's magnetic field is thought to be the caused by a non-linear mechanism resulting from the interaction between turbulent velocity and magnetic field fluctuations. This interaction, referred to as turbulent dynamo, generates an electromotive force that sustains the magnetic field [110]. Such dynamo effects, whether turbulent or laminar, are also thought to be important in star formation and accretion disks despite the presence of the strong gravitational force [22]. Lastly and most applicable to this thesis, inviscid fluid instabilities in plasma are much more complex and varied [19]. For example, classical hydrodynamic instabilities, such as the Rayleigh-Taylor instability (RTI) or the Richtmyer-Meshkov instability (RMI) can behave dramatically different [33, 101]. This difference could influence the dynamics of an explosion in the presence of a background magnetic field since these fluid instabilities control the rate of mixing and the transition to turbulence in the product gases [4].

For instance, take the example of a supernova explosion. From observational data of many supernovae remnants, it is apparent that all core-collapse supernovae are non-symmetric, while Type Ia supernovae are symmetric [106, 217]. The asymmetry of Type II SN1987A is apparent in Fig. 1. While the remnants are symmetric in the equatorial plane, identifiable by the circle of bright structures, the two fainter red lines in the figure form the ends of an hour-glass shaped blast wave creating a distinct asymmetry. A possible theory is that the presence of a strong magnetic field influences the shape of the expanding blast wave. For the magnetic field to be strong enough to influence the explosion, instabilities, such as the magneto-rotational instability, are likely triggered during core collapse that result in the amplification of the background magnetic field [217]. In a similar process, as supernovae remnants expand into the interstellar space and interact with molecular clouds of warm and cold medium, fluid instabilities trigger vorticity production and the amplification of the ambient magnetic field either by large scale field line stretching or by means of a local turbulent dynamo [9, 70, 80]. These large amplifications in magnetic field, in addition to the compressional effects of shock refraction, could contribute to an increase in star formation [130]. From these few examples, it is clear that the magnetic field has an important dynamical influence of the macroscopic behavior of a plasma in an astrophysical setting.

On Earth, however, plasmas are not the norm, and given the engineering constraints on the possible ranges of gas densities and temperatures, terrestrial plasmas are typically much different in composition and are often statically confined by a strong magnetic field in comparison. For instance, the plasma in a tokamak is confined by a strong magnetic field in order to maintain steady-state fusion. Any dynamic behavior or departure from equilibrium is often disastrous. Thus, much of the early mathematical analysis of plasmas dealt with understanding how different magnetic field configurations affected plasma stability [36, 64]. Other examples of the controlled

use of a plasma by an applied magnetic field exist as well, such as in electromagnetic propulsion [97] and even in some concepts for scramjet and pulse-detonation engine systems that envision the use of electromagnetic fields for on-board power generation, additional thrust, and added flow control [21, 102]. In this thesis, the focus is in plasmas generated by a high energy explosion, and particularly the parallels that such plasma dynamics may have with that of a stellar explosion. As a result, the interest here is *not* how to maintain stability or control a plasma by a magnetic field. The interest is to study what affects the dynamics of a unconstrained, explosive plasma. Theoretical models and data suggests there is likely, but experimental data show some discrepancy in the role magnetic field has on the propagation of detonation waves [197]. Given the complexity of obtaining experimental data, numerical modeling of the ionization processes can provide a unique insight.

Magnetohydrodynamics (MHD) is the most common mathematical framework for studying the behavior of a plasma in a magnetic field. It is a macroscopic description of a plasma. Therefore, in the context of MHD, a plasma is a fluid described by the conservation laws of continuum mechanics. There is no distinction between the individual dynamics of the electrons, ions, and neutrals; the plasma behaves as a single constituent gas whose bulk motion responds to the influence of electromagnetic forces. This assumption has many important implications, which are discussed in more detail in the following chapters, but for now it is sufficient to say that while the assumptions do impose limits on the range of length and time scales where MHD is valid, the governing equations of MHD are still applicable to the wide range of physical phenomenon.

Even with these simplifying assumptions, the dynamics of MHD cover a very wide range of characteristic lengths, frequencies, and velocities [195]. This makes it difficult to develop analytical and numerical models, and to add further complexity, experimental data is limited by the practical difficulties in obtaining measurements

from a realistic system. Astrophysical measurements are often obtuse and difficult to interpret [18], and only within the last ten years has it been possible to experimentally observe turbulent dynamos in a laboratory, most notably in the von Kármán sodium experiments [143]. Moreover, electrically conducting liquids available in the laboratory are either corrosive, opaque, or very hot making them difficult to handle and control [107]. This lack of observational data of MHD flows stresses the need for accurate numerical models.

The objective of this thesis is to develop such a numerical model and use it to provide further insight into the dynamics of a plasma produced by or interacting with a flow generated by an explosion or detonation event. In the following sections, the role of plasma and its interaction with a magnetic field is discussed within the context of high energy explosions. The key questions are (1) how does a magnetic field affect the hydrodynamic behavior of either a confined or unconfined explosion or detonation, (2) what parameters govern the processes resulting in an amplification of an ambient magnetic field, and (3) how does this generated magnetic field affect shock-accelerated mixing processes. Given the broad context of these objectives, this work is divided into two parts. The first part investigates the role of a magnetic field in confined detonations. Since the energy released in a chemical detonations is much smaller than any potential astrophysical detonation, the potential for a magnetic field to have some effect on the flow must first be addressed; more specifically, are the gas products electrically conducting, are they a plasma, and what are the characteristic scales for which a MHD interaction could occur, if at all? The second part presumes the existence of plasma and addresses a more fundamental question concerning the dynamics of mixing in a magnetized medium resulting from an explosion or interacting with a strong shock. Here, the topic of MHD instabilities and the transition to turbulence is addressed for shock accelerated, variable density flows. Before the objectives of this thesis are discussed in more detail, an overview of these two topics

with a discussion of the past and current research is given below. Yet, even before that it is useful to provide some background information on MHD and plasma.

1.1 Magnetohydrodynamics

Magnetohydrodynamics (MHD) is a macroscopic model describing the fluid dynamics of plasma in a magnetic field. When plasma is tightly coupled to the dynamics of the electromagnetic field, it is often referred to as a magnetized plasma to emphasize the importance of the magnetic field. The governing equations of MHD couple the conservation equations for mass, momentum, and energy of a fluid to the dynamics of the electrodynamic fields, which are governed by Maxwell's equations. Since the plasma is treated mathematically as a fluid, the length and time scales of the plasma must satisfy the conditions for continuum fluid behavior as well as ensuring that the microscopic motions of the electrons and ions can be averaged such that the bulk motion of the plasma is an accurate representation of the plasma dynamics. The objective of this section is to provide a working definition for a plasma within the context of MHD and then discuss qualitatively the non-linear interaction of a plasma in a magnetic field. In the next chapter, a detailed derivation of the MHD equations is used to substantiate the heuristic arguments provided here.

1.1.1 Definition of Plasma

A very simple definition of a plasma is to say that it is an ionized gas. Yet, such a definition is not particularly useful. For example, the exhaust plume of a rocket is ionized, but it is unlikely to have an significant interaction with a magnetic field. Thus, it is useful to distinguish between partially ionized gases, i.e., the rocket plume, and the ionized gases one typically associates with plasma. As a first measure, the Saha equation can be used to calculate the degree of ionization of a gas in thermodynamic equilibrium. If n_i/n_n is the number density ratio of ions to neutrals, then

the Saha equation states [74]

$$\frac{n_i^2}{n_n} = \left(\frac{2\pi m_e k_B T}{h^2}\right)^{3/2} e^{-\Delta U/k_B T}, \tag{1}$$

where T is the equilibrium temperature of the gas, m_e is the mass of an electron, k_B is the Boltzmann constant, h is the Planck constant, and ΔU is the first ionization potential. For air at $T = 300$ K and with a number density of $n_n = 3 \times 10^{25}$ m^{-3}, $n_i/n_n = 2 \times 10^{-122}$. Yet, inside a tokamak, where $T = 10^8$ K, $n_i = 10^{20}$ m^{-3}, $n_i/n_n = 2.4 \times 10^{13}$ [74]. However, simply specifying an arbitrarily high threshold for n_{ion}/n_n is not ideal.

The following definition of a plasma is adopted. A plasma is a *quasi-neutral* gas of charged and neutral particles exhibiting *collective behavior* by means of long-range electromagnetic forces [36]. The consequences of this definition for a plasma are now discussed.

1. *The minimum length scale of interest, l_0, must be much larger than distance over which charge imbalance occurs.*

In other words, for the length scales of interest, the plasma is effectively charge neutral. Given a completely ionized gas, the total electron charge is $q_e n_e = -n_e e$, and the total ion charge is $n_i q_i = Z n_i e$, where n_e is the electron number density, n_i is the ion number density, Z is the atomic number of the gas, and e is the electric charge. Quasi-neutrality implies that $Z n_i \approx n_e$. This is realizable in many applications because charge imbalance only occurs at length scales where the kinetic energy of the electrons is of the same order or greater than the electric potential between the charged particles. To provide a quantitative estimate of the length scales over which charge imbalance does occur, consider a one-dimensional model for the electric potential, ϕ, in an ionized gas. The electric potential is a solution to the Poisson equation derived from Gauss's Law, which in a single dimension is [36]

$$\frac{d^2\phi}{dx^2} = \frac{e}{\epsilon}(Z n_{ion} - n_e). \tag{2}$$

Furthermore, assume that the electron number density distribution is [36]

$$n_e = n_\infty \exp\left(\frac{e\phi}{k_B T_e}\right), \tag{3}$$

where T_e is the electron temperature, and n_∞ is the number density far away from the electric potential. Using this expression and assuming that $n_i = n_\infty$, then when $|e\phi/k_B T_e| << 1$, the electric potential can be approximated as $\phi = \phi_0 \exp(-|x|/\lambda_D)$. The length scale determining magnitude of the charge imbalance is then λ_D, the Debye length [36],

$$\lambda_D = \left(\frac{k_B T_e}{4\pi n e^2}\right)^{1/2}. \tag{4}$$

This implies that if the Debye length, which is a measure of the thickness of the sheath or the distance over which charge imbalance occurs, is much smaller than the size of the system of interest, $l_0 >> \lambda_D$, then the plasma is quasi-neutral, and $Zn_i \approx n_e$.

2. *The number of particles in the plasma must be large, $N_D >>> 1$.*

This constraint is a corollary of the previous requirement of $l_0 >> \lambda_D$. As the density of the plasma increases, λ_D decreases, and the number of particles inside a sphere of radius λ_D decreases. Thus, the ability of the plasma to shield out electric potentials is more difficult in denser plasmas. The number of particles in the "Debye sphere" is computed as [36]

$$N_D = \frac{4}{3} n \pi \lambda_D^3 \approx \frac{1380 T^{3/2}}{n^{1/2}} \qquad (\text{T in } {}^o\text{K}). \tag{5}$$

Thus, in addition to $l_0 >> \lambda_D$, the number of particles inside the Debye sphere must be large, $N_D >>> 1$.

3. *The frequency of collisions between neutral and charged particles must be high enough for the gas to behave like a plasma.*

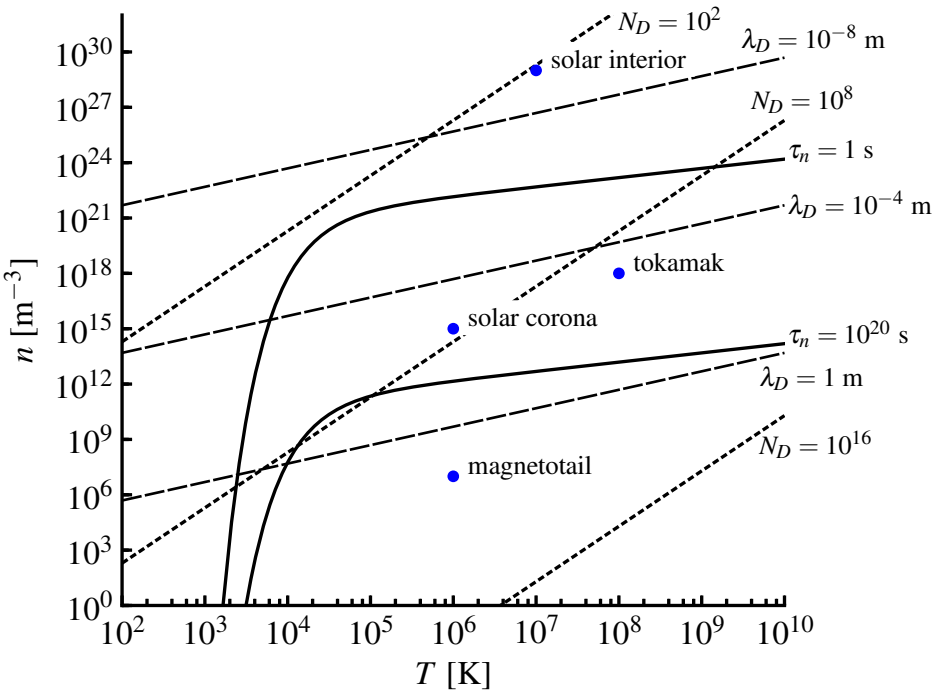

Figure 2: Conditions for collective plasma behavior as a function of the number density $n \approx n_e \approx Zn_i$ and temperature $T \approx T_e \approx T_i$ of the plasma. The criteria for τ_n, λ_D, and N_D are approximated based on the gas properties of hydrogen. The reference points for the core and coronal plasma of the sun, the magnetotail, and the tokamak as well as the scaling relationships used to compute the curves are taken from the following references [64, 74].

For a gas to be modeled as a continuum, it is assumed that the gas particles undergo a large number of collisions such that the distributions of the particle velocity are given by a Maxwell distribution, and the mean distance between the fluid particles or mean-free path, λ_f, is much smaller than l_0. This is required even for a neutral fluid. For a ionized gas, the electrons and ions must be strongly tied to the neutrals by the magnetic field. In other words, the long range Coulomb interaction between charged particles dominates over the binary collisions with neutrals and the plasma exhibits "collective behavior." If the frequency of collisions between the neutral and charged particles is ω, and if τ_n is the mean time between collisions with neutral particles, then $\omega\tau_n > 1$ is required for the gas to behave like a plasma [36].

The first two conditions ensure that the plasma the quasi-neutral. This assumptions allows for a significant simplification of the governing equations since in a quasi-neutral ionized gas, the electric field plays a secondary role. The dynamics are controlled entirely by the magnetic field. The last condition is required if the dynamics of the plasma are inherently linked to the evolution of the electromagnetic field. In addition to these considerations, the length and time scales should be large enough to average out the microscopic dynamics of the individual electron and ion particles. This condition requires more mathematical sophistication in order to demonstrate and is more quantitatively defined in the next chapter.

Figure 2 defines the conditions necessary for a plasma to exhibit collective behavior. The length and time scales are computed using the criteria discussed above, but simplified using the first order approximations [74],

$$\tau << \tau_n \equiv \frac{1}{n_n \sigma_d v_{th}} \approx \frac{10^{17}}{n_n \sqrt{T}}, \tag{6}$$

$$l_0 >> \lambda_D \equiv \sqrt{\frac{\epsilon_0 k_B T}{e^2 n}} \approx 70\sqrt{\frac{T}{n}}, \tag{7}$$

$$N_D \equiv \frac{4}{3}\pi \lambda_D^3 n \approx 1.4 \times 10^6 \sqrt{\frac{T^3}{n}} >> 1, \tag{8}$$

where σ_d is the effective collision cross section, which is approximated as 10^{-19} m^2. Using typical reference conditions, τ_n, λ_D, and N_D are computed for the plasma inside the core of the sun, the coronal plasma, the plasma in the magnetotail of the Earth, and the plasma within a tokamak [36, 64, 74]. For the range of scales that satisfy these limits, MHD is applicable. In the next section, a brief discussion of some of the important physics of a magnetized plasma is provided.

1.1.2 Dynamics of a Magnetized Plasma

The mutual interaction between the magnetic field, $\mathbf{B}$, and the velocity field, $\mathbf{u}$, is one of the most striking features of MHD. This mutual interaction occurs as a result of the laws of Faraday and Ampère, and because the Lorentz force, the electromagnetic

body force, accelerates the current carrying plasma. The non-linear interaction can best be described by arbitrarily dividing the process into three parts [49]. First, according to Faraday's law of induction, an electromotive force (emf) is created as a result of the relative movement of a plasma in a magnetic field. The emf is of order $|\mathbf{u} \times \mathbf{B}|$ and induces a current density, $\mathbf{J}$, of order $\sigma|\mathbf{u} \times \mathbf{B}|$ with σ being the electrical conductivity of the plasma. Second, Ampère's law states that a current will induce a magnetic field. The induced current caused by the emf therefore generates an induced magnetic field, which adds to the background magnetic field. The net result is that the magnetic field lines seem to be dragged along by the plasma. Lastly, the total magnetic field interacts with the induced current density resulting in a Lorentz force, $\mathbf{J} \times \mathbf{B}$. The entire process tends to reduce the relative movement of the fluid and the field. This ability for the fluid to drag a magnetic field and for a magnetic field to pull a plasma results in a "freezing together" of the plasma and the magnetic field. This effect is what causes the coronal plasma loops on the surface of the Sun [49].

The extent to which the above process can occur in a plasma is dependent upon the conductivity of the plasma, the velocity of the plasma, the strength of the imposed magnetic field, and the magnitude of the induced magnetic field, which is in turn dependent on the length scale of the flow. From these parameters as well as the density, ρ, the kinematic viscosity, ν, and the magnetic permeability of free space, μ_0, four non-dimensional parameters can be defined: the magnetic Reynolds number, Re_m, the Lundquist number, S, the interaction parameter or Stuart number, N, and the magnetic Prandtl number, Pr_m. These four non-dimensional parameters in addition to the typical non-dimensional parameters of hydrodynamic flows govern the dynamics of MHD flows. Note that the Reynolds number, Re, is directly related to Re_m and Pr_m number, so only two are independent.

The magnetic Reynolds number is a non-dimensional measure of conductivity. It can also be interpreted as the ratio between the flow time scale, $\tau = u/l_0$, and the

magnetic dissipation time scale, $\tau_m = l_0^2/\eta$, where η is the magnetic diffusivity of the flow defined as $1/\mu_0\sigma$. The currents induced by the emf convert electromagnetic energy into heat by Ohmic dissipation which results in the diffusion of the magnetic field. When $Re_m >> 1$, Ohmic dissipation is small, and the magnetic field lines act like elastic bands frozen into the conducting flow. As a consequence, the magnetic flux through any closed material loop tends to be conserved during the motion of the fluid. This is in direct analogy to Kelvin's theorem of vortex tubes and is often referred to as Alfvén's theorem [49]. The analogue between vorticity and magnetic fields provides for a qualitative understanding of the dynamics of high Reynolds number MHD flows. Dynamo action (turbulent or laminar) can be understood as the result of the stretching of magnetic flux tubes; hence, in order to conserve flux as the incremental area of the flux tube decreases, the magnetic field strength must increase. Magnetic fields are thereby intensified as a result of the stretching of vortex tubes. A second consequence of high magnetic Reynolds numbers is the importance of Alfvén waves as a mechanism for propagating energy and momentum. Alfvén waves are transverse inertial waves traveling at the velocity, $v_a = B/\sqrt{\rho\mu_0}$. At high magnetic Reynolds numbers, these waves propagate disturbances in a near elastic manner along the magnetic field lines. Colliding Alfvén wave packets have been proposed by Iroshnikov [96] and Kraichnan [109] as a mechanism for the cascade of turbulent energy in the inertial range.

At low magnetic Reynolds number, $Re_m << 1$, the magnetic field induced by fluid motion, which is of order $Re_m B_0$, is negligible by comparison with the background magnetic field, B_0. The induced electromagnetic field, however, still plays a dominant, although dissipative, role since the Lorentz force now acts to convert mechanical energy into heat on a time scale of $\tau_J = \rho/\sigma B^2$ [49]. Unlike viscous dissipation, Joule dissipation does not involve a derivative of velocity implying that the scales of motion predominately contributing to Joule dissipation are not concentrated at the

small scales [107]. The structure of turbulence can thus be drastically altered by the presence of a magnetic field. The Stuart parameter, $N = \sigma B_0^2 l_0/\rho u$, is a measure of the influence of the magnetic field. It is defined as the ratio of inertial to magnetic forces in the flow or similarly, the ratio of eddy-turnover time to the Joule dissipation time. Thus, the turbulent eddies only get stretched by the magnetic field if they survive long enough, and this only occurs if the Lorentz force is of the same order as the non-linear inertial term. When the interaction parameter is large, vorticity is still transported along the field lines by Alfvén waves, but the process is now diffusive and not oscillatory as it is in high magnetic Reynolds number limit [49]. The Lundquist number, S, is a better measure of the determining how the Alfvén waves behave in a plasma. If the Lundquist number is smaller than unity or smaller than Pr_m, Alfvén waves are suppressed by diffusion and thus disturbances propagating along the magnetic field lines are dissipated [3]. These non-dimensional parameters will be discussed later in more mathematical terms when the MHD equations are derived.

1.1.3 Limitations and Applicability of MHD

In the application of the MHD to the modeling of astrophysical and terrestrial plasmas, a number of additional assumptions are made. First, the plasma is assumed to be non-relativistic. The assumption is reasonable in many situations. However, in some astrophysical systems, highly collimated jets of plasma with velocities near the speed of light can be generated in the proximity of very massive objects, such as a black hole or neutron star. The energy supplied by the accreting material is converted into the kinetic energy used to power the jets. As a result, the effects of relativity are important in the simulation of the Active Galactic Nuclei, compact X-ray binaries, quasars, etc. [52, 134]. Additionally, relativistic jets can form in supernovae explosions, such as SN1987A, and the high energy blast shock can often relativistically accelerate particles near the shock causing gamma-ray bursts. The study of such

phenomenon is not addressed in this thesis. However, the MHD equations have been extended to include relativistic (both special and general) effects [52].

Second, radiative heat transfer is assumed to be negligible. These processes can be important both in astrophysical and terrestrial plasmas; however, they are typically only important during the initial transients. For instance, neutrinos play a critical role in the transfer of energy within the post-explosion products of a supernova [89]. Also, radiative heating is used in tokamak to sustain the temperature of the plasma [64]. The inclusion of radiation into the modeling of a plasma can be done without altering the base numerical methods developed for MHD in this thesis. They are, however, not specifically addressed here.

Lastly, as discussed in the previous section, the non-dimensional numbers can be used to justify the simplification of the MHD governing equations. For high magnetic Reynolds number flows, the dissipative effects can often be neglected. In the asymptotic limit of $Re_m \to \infty$, the ideal MHD equations can be derived. In the opposite limit, the quasi-static MHD equations can be derived. At very low magnetic Reynolds number, the dynamics of the plasma are separated from the evolution of the magnetic field, which plays a purely dissipative role. In these cases, it is not important for the criteria of a plasma to be met, since the behavior of the ionized gas is not coupled to the evolution of the magnetic field. As is discussed in the next section, this is often true of the ionized gases in a post-detonation flow.

1.2 Plasma Production by High-Energy Explosions

1.2.1 Detonation Theory

A detonation wave forms when a strong shock-wave dynamically couples to a reaction-wave in such a way that a balance occurs between the release of chemical energy and the energy expended by expansion. In the simplest of models, a detonation wave is described as a one dimensional discontinuity propagating through the mixture.

The detonation wave is presumed to propagate at the Chapman-Jouget (CJ) velocity [63], which occurs when the thermodynamic state is defined by the tangency of the Rayleigh line to the Hugoniot curve. This point also corresponds to the sonic solution and the point of minimum entropy change across the detonation. Even though the proposition of the CJ criterion is somewhat arbitrary, the theory is surprisingly well-supported. Experimental measurements are within 1-2% of the predicted CJ velocity [116].

Yet this simple theory is lacking. While the strong detonation solution can be shown to be unstable to perturbations for freely propagating detonations, thermodynamic and stability arguments cannot debunk the possibility of a weak solution [224]. The theoretical possibility of such a solution was demonstrated by von Neumann, ultimately proving the necessity of the considering the structure of the detonation in calculating the detonation speed [211]. These weak detonations or pathological detonations have been shown to occur in detonations with fast exothermic reactions followed by slower endothermic reactions, such as in H_2-Cl_2 detonations [56]. The incorporation of structure into a one dimensional model is generally credited to Zeldóvich [224], von Neumann [211], and Döoring [57] and is often referred to as the ZND model. According to this model, the reaction zone begins at the shock discontinuity or von Neumann pressure spike and is followed by an induction zone ending at a sonic surface, the CJ-plane [186]. The shock discontinuity can be described by the Rankine-Hugoniot conservation equations. As a result, both the ignition process and the acceleration of the gas backwards via expansion are accounted for properly. To determine the detonation velocity, the ZND model requires iteratively solving an eigenvalue-based problem where the CJ-plane and the shock discontinuity bound the problem [116]. There is no direct extension of ZND theory to MHD, but similar approximations have been made to study the electromagnetic effects using a simplified one dimensional detonation model.

Numerical integration of the reactive, hydrodynamic equations in one dimension confirm the ZND model. From these one dimensional simulations the stability of the detonation wave can easily be investigated. In the simplest of models, the chemical reactions are modeled by a global, one-step reactant to product Arrhenius rate mechanism, and thus the most important parameter governing stability is thus the activation energy, E_a. Increasing this value makes the detonation wave more sensitive to small changes in the temperature. Since most detonations in gas mixtures have a reasonably high activation energy ($E_a > 27$), they are only quasi-stable [116]; hence, they fluctuate in speed, and the CJ pressure correspondingly alternates, sometimes between one half to double the value. Yet on average, the detonation speed is close the predicted CJ velocity.

One dimensional models still lack the necessary physics to describe the self-sustaining mechanism of a freely propagating detonation wave. Experiments show that detonations are inherently unsteady and multi-dimensional. Internal transverse waves wrinkle the detonation front creating alternating weak incident shocks and stronger Mach stems, which are connected with the transverse wave at the triple-point. These local zones of amplified temperature and pressure cause the detonation front to pulsate in the direction of propagation forming the classical large-scale cellular structures. In the absence of weak or strong transverse waves, the detonation wave is no long self-sustaining. Experimental evidence of this has been shown by investigating the effect of detonation propagation through a channel with acoustically absorbing walls [161].

This sensitivity of detonation propagation to instabilities suggests that any mechanism interfering with cell generation and/or the chemical exothermicity of the reaction will affect the dynamics of the detonation wave. Indeed additional source terms such as frictional forces or heat loss have been shown to reduce the detonation velocity

[116]. As discussed in the next section, the electrical conductivity of gaseous detonation products are typically only a few orders of magnitude larger than the electrical conductivity of salt water. Thus, in order to increase the ionization fraction of the gaseous detonation products, the gas mixture is often seeded by low ionization particles. The inclusion of endothermic ionization reactions of the seed particles can impact on the propagation of a detonation. For condensed-phase detonations, however, this is not necessary since the electrical conductivity is much larger as a result of the significantly higher post-detonation temperatures. As discussed in Section 1.1.2, the dynamics of a plasma in a magnetic field are dependent on the Re_m, which is a non-dimensional representation of the electrical conductivity. One of the objectives of this thesis is to study the influence a magnetic field may have on a propagating detonation for terrestrial applications [102, 104, 156, 197]. The first requirement of such a study is to determine the values of Re_m in post-detonation flows. This is discussed in the next section. Following that a discussion of previously conducted experiments of a condensed-phase detonation in magnetic fields is discussed.

1.2.2 Ionization by Detonation Waves

The first measurements of the electrical conductivity in a post-detonation flow were conducted by Basu and Fay [15] for the gaseous detonation of H_2/O_2 and C_2H_2/O_2 mixtures with the inclusion of 0.667% N_2 using a D.C. probe technique. From theoretical calculation and comparison to the experimental results, the formation of NO ions was concluded to be the dominating contribution to the rise in the electrical conductivity followed by contributions from O_2 and H_2O ions. The initial pressure was varied from 0.1 to 1.0 atm. Higher initial pressures resulted in higher values of conductivity. In the case of C_2H_2/O_2 (N_2) mixtures, the theoretical calculation of conductivity included a model for the ionization of solid carbon particles. The percent concentration of C_2H_2 was varied from 30 to 80 percent. Above 50 percent

concentration C_2H_2, solid carbon particle ionization contributes most to the electrical conductivity of the plasma. Without the inclusion of this effect, the measured values of conductivity would be much larger than predicted by theory. This suggests that the finely dispersed soot particles contribute in some manner to the electrical conductivity of the gas. Following the work of Basu et al. [15], further experiments were conducted in C_2H_2/O_2 detonation showing time dependence in the conductivity measurements resulting from the differing ionization mechanism in the reaction zone as compared to those in the downstream products [32, 178]. Edwards et al. [59] have compiled a large amount of data for both H_2/O_2 and C_2H_2/O_2 mixtures. The measured conductivities are in the range of 10^{-3}-10^{-1} S·m^{-1} depending on the conditions. More recent studies of electrical conductivity in gaseous detonation have reported similar trends [129, 213].

At such low electrical conductivities, however, the dynamics of the magnetic field and the fluid are effectively decoupled, $Re_m << 1$. The electrical conductivity must be increased. In order to do this, particles with low ionization potentials, such as potassium carbonate, are injected into the flow where the formation of potassium ions increases the electrical conductivity. Basu and Fay [14] report an electrical conductivity of 270 S·m^{-1} in oxy-acetylene detonations at initial pressures of 0.1 atm when seeded with 3% potassium acetylide–a four-order of magnitude increase compared to the non-seeded electrical conductivity. More recently, similar studies using a potassium carbonate seed were done in hydrogen-oxygen detonations [129]. In this work the measured electrical conductivity was much less than expected. The researchers attribute this to poor mixing and incomplete oxidation of the potassium carbonate, however, a two-order of magnitude increase in the electrical conductivity is still observed for a 1% addition of potassium carbonate by weight. The effect of alkali metals has been studied more extensively in flames [190]. In these studies a 1% addition of potassium carbonate can result in flame extinction due to heat absorption

by the seed particle during phase transition and the increased competition for atomic oxygen in the reacting mixture. Similar affects occur in detonation waves and are explored in more detail in a later chapter.

Another method to increase the ionization fraction of the post-detonation products is to increase the release of energy in the detonation such that the post-detonation temperatures are significantly higher, i.e., 8000-10000 K in comparison to 2000-3000 K for gaseous denotations. Thus, condensed phase, heterogenous explosions produce an ionized gas with an electrical conductivity one or two orders of magnitude larger [71]. The mechanisms of ionization in such explosions are poorly understood. Theoretical predictions of the equilibrium conductivity using the Saha equation are orders of magnitude smaller than the experimentally measured values [42]. This suggests that other mechanisms are important. Arguments have been made that the plasma is highly cohesive and behaves as metal-like lattice structure. Supporting this argument are observations of long-lasting conductivities [44], density-conductivity correlations similar to metals [16], and the sudden increase in conduction when the plasma is compressed [43]. Despite this, there have been arguments against cohesion in plasma [50, 196]. The close coincidence of the shock front (i.e., the von Neumann pressure spike) and the conduction front in experimental data suggests that ionization starts long before the heat-release occurs. This supports the theory of shock-induced conduction of the unreacted explosive and the conduction by species formed early in reaction zone rather than the coalescence of condensed carbon products [196]. Measurements of electrical conductivity for a wide variety of high explosives including explosives with metal additives for enhanced conductivity have been made by many researchers [71]. The electrical conductivity for most explosives is roughly 100 S-m^{-1}, but values as high as 10^5 S-m^{-1} (liquid TNT) have been observed [71]. This suggests the potential for the plasma generated by the explosion to interact with an applied magnetic field.

1.2.3 Electromagnetic and Detonation Wave Interaction

Experimental evidence supporting the hypothesis that an externally applied magnetic field affects the structure and the propagation of a detonation is contradicting. Theoretically, an applied magnetic field can be shown to change the pressure, density, and speed of sound at the CJ point of a detonation [86, 87]. Such predictions, however, assume the post-detonation gases are infinitely conducting, which is not likely to occur at least for gaseous detonations. In the experiments of Cook et al. [42], a plasma was generated by a liquid explosive Dithekite 13 (nitrobenzene/nitric acid/water in a 63/24/13 weight ratio) and projected into a 6.4 cm diameter glass tube that then entered a 0.1 T magnetic field at a speed of 17.0 km-sec^{-1}. The plasma left the field at speed of 1.3 km-sec^{-1}. A similar experiment was conducted by Tasker et al [197] using an HMX-cast cured explosive and a 1 T magnetic field, but they did not observe any significant magnetic field effects. The conductivity of HMX is, however, much smaller than that of Dithekite 13, which could possibly explain the discrepancy. The geometrical configuration of the experiment was also different. Cook et al. [42] also report observing the plasma propagating in a helical path. As was noted by Tasker et al. [197] , this is not very likely owing to the very small Hall numbers estimated. Additional configurations using PBX-9501 were also investigated by Tasker et al. [197] to determine if any magnetic field effects could be observed. None were. There are no other known experiments nor have there been any numerical simulations of the phenomenon.

In the Dithekite 13 experiments, the Re_m is estimated to be anywhere between 1.11 and 1.78 depending on the length scale used. In the lower bound, a length scale of 0.04 m was used, an estimate of the conduction zone width recorded in experiments, and in the upper bound the diameter of the glass tube was used as the length scale. An electrical conductivity, σ, of 1300 S/m was assumed. Given this estimate, the ionized gases in the post-detonation flow could behave as a magnetized

plasma, exhibiting collective behavior. If such were the case, the magnetic field could alter the physical processes of the detonation. For gaseous detonations, $Re_m << 1$ is expected. In this case, the dynamics of the magnetic field are decoupled from the dynamics of the fluid and the plasma does not exhibit collective behavior. However, joule dissipation converts the magnetic energy of the applied magnetic field into heat. The non-linear interaction between joule dissipation and the chemical kinetics could result in an altercation of the detonation. This is investigated in a later chapter. In astrophysical applications of detonation and explosions, $Re_m >> 1$ is expected given the extremely large amounts of energy released. In the next section, the potential influence a magnetic field could have in a post-detonation flow of this type is investigated by studying the Richtmyer-Meshkov instability.

1.3 The Richtmyer-Meshkov Instability

In this section, the dynamics of fluid mixing in an explosion is discussed. As previously reviewed, the post-detonation flow is characterized by large-scale cellular structures generated by the shock-shock interaction between the transverse wave, incident shock, and Mach stem. These large-scale structures are dynamically unstable, and as a result, the burnt products and any unreacted fuel mix on a time-scale related to the vorticity production at the detonation front. In an unconfined environment, the released energy results in an outward propagating blast wave and a rarefaction wave propagating towards the center of the explosion causing implosion and a subsequent reflected shock that then propagates back through the post-detonation flow. This re-shock of the explosion products further compresses the flow and accelerates the rate of fluid mixing through the creation of a larger range of turbulent flow scales, which eventually drive the flow to a final state of fully-developed decaying turbulence [4, 29, 185]. The primary mechanism controlling the fluid dynamics and mixing in shock-accelerated, variable-density flows is the Richtmyer-Meshkov instability (RMI).

For instance, the luminous spots or "fingers" in the image of SN1987A shown in Fig. 1 are a result of the this instability. Additionally, the study of the RMI in conducting fluids not only offers insight into the behavior of MHD flows, but also has direct relevance to many engineering applications since laminar fluid instabilities are important in the transition to turbulence in real systems, and the possibility that transition could be delayed or excited using a magnetic field is relevant to many terrestrial applications, such as inertial confinement fusion [153].

1.3.1 Hydrodynamics

The Richtmyer-Meshkov instability (RMI) [135, 165] develops when a shock wave accelerates an initially perturbed interface between two fluids of different properties. During shock refraction, a misalignment between the density and pressure gradients causes vorticity generation by baroclinic torque along the interface. This unstable vortex sheet drives the amplification of the initial perturbations, which can be characterized either by a sinusoidal function of a given wavelength and amplitude (i.e., single-mode RMI) or a superposition of these perturbations (i.e., multi-mode RMI) [29]. Additional instabilities, such as the Kelvin-Helmholtz instability, result in vortex roll-up and an increase in the growth of the mixing layer. Furthermore, possible secondary shocks impacting the evolving mixing layer can substantially amplify the mixing processes [206] and quicken the transition of the layer to a fully turbulent mixing zone.

Figure 3 shows the process of shock refraction and the vorticity generation by baroclinic torque along interface. In the schematic, a single-mode interface separating the light fluid of density ρ_1 from the heavy fluid of density ρ_2 is impulsively accelerated by a shock wave initially traveling with the Mach number M_s. The configuration results in a positive density gradient across of the contact discontinuity ($\nabla\rho > 0.$) and a negative pressure gradient across the shock wave ($\nabla p < 0$). The difference in

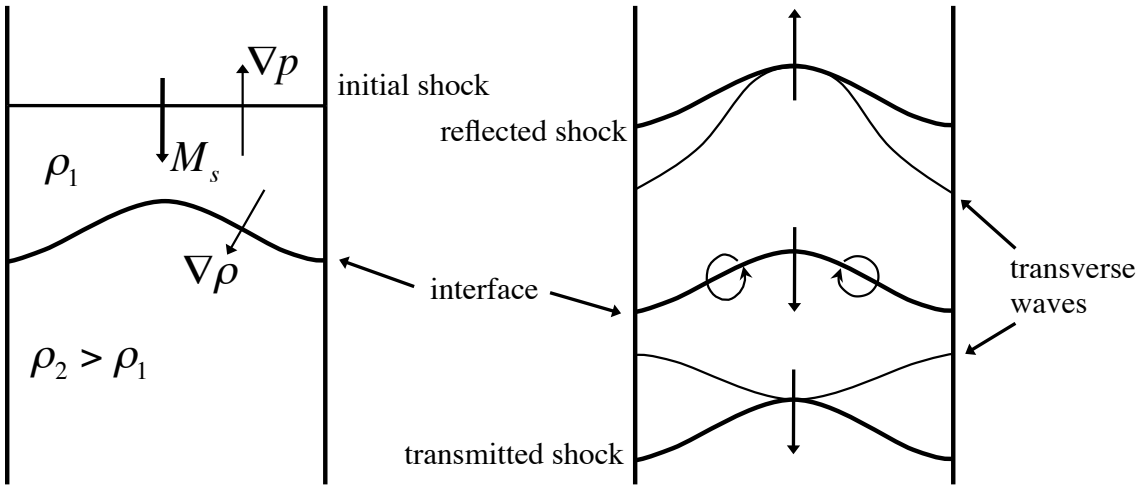

Figure 3: Schematic of the wave patterns formed during the refraction of the shock wave and the initial deposition of baroclinic torque along the interface of between a light (ρ_1) and heavy (ρ_2) gas.

the density and pressure gradient during shock refraction results in the generation of vorticity. The vorticity transport equation for a inviscid flow without body forces is

$$\frac{D\boldsymbol{\omega}}{Dt} = (\boldsymbol{\omega} \cdot \nabla) - \boldsymbol{\omega}\,(\nabla \cdot \mathbf{u}) + \frac{1}{\rho^2}\nabla\rho \times \nabla p, \tag{9}$$

where the vorticity is defined as curl of the velocity field, $\omega = \nabla \times \mathbf{u}$. The last term on the right is the baroclinic torque term. As a result of this term, a vorticity sheet is generated along the contact discontinuity making it unstable. Also shown in Fig. 3 are the resulting transmitted and reflected waves that form a shock train of transverse waves as they propagate through the gas. For a complete review of the physics of the RMI, please refer to the review articles of Zabusky [222] and Brouillette [29].

RMI is a fundamental fluid instability ubiquitous in both nature and engineering. Thus it is the topic of much experimental, analytical, and computational study [29]. The basic configuration of the RMI problem in a Cartesian geometry is shown in the Fig. 4. The first analysis of the RMI was by Richtmyer [165], who treated the RMI as the impulsive limit of the Rayleigh-Taylor instability and was able to show that the interface amplitude grows linearly in time. Experiments [34, 93, 100] show

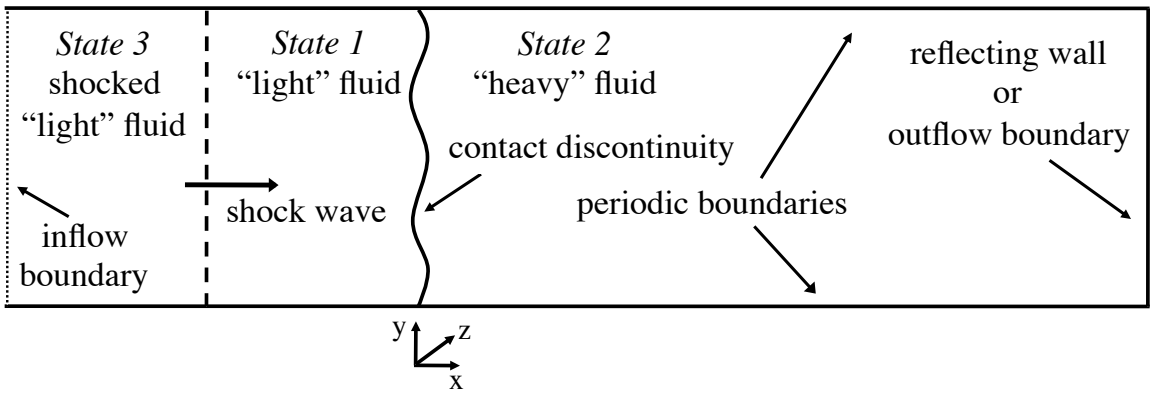

Figure 4: Schematic of a typical initial configuration of the RMI in Cartesian geometry.

good agreement with the impulsive formulation; however, as the interface amplitude increases to roughly a tenth of the perturbation wavelength [29], the RMI transitions to non-linear growth, and the linear theory is no longer valid. This phase of the instability is often described as having "bubbles" rising into the heavier fluid and "spikes" falling into the lighter fluid. Several non-linear models have been developed to predict the bubble/spike velocities and the subsequent reduction in growth of the interface width from mode saturation [85, 175, 227]. Such models show good agreement to two- and three-dimensional numerical simulations [206].

In realistic applications, however, the initial interface is more accurately quantified as a superposition of perturbations spanning a large range of amplitudes and wavelengths. In this case, the RMI quickly transitions to non-linear growth following a self-similar power-law dependence with time, $h \approx t^{\theta}$, where h is the peak-to-valley amplitude with values of θ ranging from 0.2 to 1.0. The exact value of θ is an ongoing topic of discussion [29, 30, 177]. Assuming the just-saturated mode dominates the mixing dynamics, Dimonte et al. [53] determine the overall growth of the mixing layer to have a growth exponential of $\theta \approx 0.5$. Modifications to include the effects of initial conditions, however, show that the growth from mode-coupling alone results in $\theta = 0.24$, concluding that any measured growth-rate larger than that must

be dependent on the initial conditions [199]. Recent experiments [54, 55, 158] and other analytical models [147, 162, 176] show similar discrepancies complicating the understanding of the driving factors in the RMI growth-rate. In addition, several computational studies have attempted to better understand how the RMI growth-rate depends on a number of factors including the initial multi-mode perturbations [199], the impulse strength [93, 126, 146], and the fluid composition [125].

Re-shock RMI occurs when a second shock perturbs the already evolving interface. All experiments indicate that this second impulse results in a significant increase in the mixing layer growth-rate [7, 30, 118, 210]. Yet, once again there is some discrepancy in determining functional relationship of the re-shocked RMI growth-rate. In the experiments by Leinov et al. [118] and Vetter and Sturtevant [210], the re-shock growth is observed to be linear in time ($\theta = 1$) and is proportional to the velocity jump at the re-shock interface. This is consistent with theoretical predictions [30, 35, 137], numerical parametric studies [206], and several computational studies [40, 90, 182] of the experiments by Vetter and Sturtevant[210], all of which show a linear growth-rate after re-shock. Only at very late times is there an indication of mode saturation and non-linear growth. Yet, experiments by Houas and Chemouni [94] show a growth exponential somewhere between $\theta = 2/3$ and $\theta = 1.0$, and in the gas-curtain experiments of Balakumar et al. [7] and the corresponding computational simulations of Gowardhan and Grinstein [79], the re-shock growth is much more non-linear. Thornber et al. [200] have proposed to reconcile these differences by modifying the linear model of Mikaelian [138] to depend on the molecular mixing fraction.

As summarized above, much of the focus on RMI has been on the development of the instability within the parameter space encompassing three parameters: the scales and type of initial perturbations, the impulse strength, and the fluid composition. Yet, in many applications, such as in chemical explosions with burning metal particles [6], in astrophysical dusty plasmas [189], or in the presence of a magnetic field, the growth

of the instability is altered. As discussed in the first section, gaseous detonations require seeding by low-ionization potential particles to achieve appreciable electrical conductivity. Moreover, high electrical conductivities are often achieved in condensed-phase explosions by using similar additives [71]. Thus, it could be expected that the RMI occurring in the post-detonation flow would occur in a dispersed-phase flow [185]; this, however, is not investigated here. In this thesis, the RMI is investigated with the assumption that the flow is sufficiently ionized and places no distinction of the type of plasma in question. The conclusions of this study are expected to be relevant not only to astrophysical systems, where the RMI in a magnetized plasma is most often encountered, but in terrestrial applications as well; however, in these applications the processes of ionization would introduce an additional time scale into the analysis. In the next section, the physics of the RMI in a magnetized plasma is reviewed.

1.3.2 Magnetohydrodynamics

The RMI is of fundamental importance to the study of laminar and turbulent mixing in variable density flows undergoing shock acceleration. Since for a wide variety of flows turbulent mixing is the paramount driving mechanism controlling the fluid dynamics, numerical simulations and experiments of the RMI, particularly in the condition of re-shock, are fundamental to our understanding of the mixing process. Recent advances in improving both the experimental repeatability and the diagnostic capability of the RMI have made such experiments both practical and elucidating [7]. They continue to aid and re-enforce corresponding numerical simulations. Yet given these advances, there has been very little investigation into turbulent mixing in a magnetized plasma despite its relevance to most astrophysical environments [4]. Only recently has the combined effect of scalar mixing and the turbulent MHD dynamics been investigated using simulations of forced isotropic turbulence [194].

There is direct evidence that the magnetic field influences the mixing processes in a supernova explosion. Synchrotron X-ray emission of young supernovae remnants show variations on the time scale of a year suggesting the existence of a milligauss magnetic field. Sano et al. [181] propose that the RMI, which is triggered by the passage of the supernova shock through the cold and warm interstellar medium (ISM), could be a potential mechanism for the amplification of the magnetic field, which is nominally only of the order of microgauss. Shock compression alone can not explain the increase, thus the amplification might also be the result of magnetic field line stretching induced by the vorticity generated in the RMI. Sano et al. [181] study the single-mode RMI in conditions similar to those that would occur in the ISM using two-dimensional MHD simulations. They estimate that the Mach number of the supernova shock to be 10-100 and the density ratio between the cold and warm neutral media to be 10-100. The simulations conclude that an ambient magnetic field can be easily amplified by at least a factor of 100 for Mach numbers above 50. Once the magnetic field increases beyond a certain level, it saturates as the magnetic field lines develop enough tension to suppress further growth of the RMI. In other words, both the magnetic field and velocity fields are driven to a state of equilibrium. The results of this study indicate the RMI is a promising mechanism for the explanation of the existence of strong magnetic fields in supernovae remnants.

When the ambient magnetic field is large, Samtaney et al. [179] demonstrate using two-dimensional numerical simulations that the growth of the RMI can be entirely suppressed. Note that in the simulations of Sano et al. [181], the initial background magnetic field is 5-10 orders of magnitude smaller than values used in the study of Samtaney et al. [179]. For the purposes of comparison, the magnitude of the magnetic field is often normalized by the thermodynamic pressure, $\beta^{-1} = B^2/2\mu_0 p$. Theoretically, a magnetic field perpendicular to contact discontinuity can not physically alter the production of vorticity at the interface via the baroclinic torque. Wheatley et

al. [214] explain that in magnetized plasma when there is a component of the magnetic field vector normal to the contact discontinuity, discontinuities in the transverse components of the velocity across a contact discontinuity are prohibited. Figure 5 shows the differences in the shock refraction physics for MHD. Instead of a vortex sheet forming along the interface of the two fluids and persistently driving the amplification of the interface perturbations, vorticity is instead transported away from the contact discontinuity by Alfvén waves or rotational discontinuities, which travel along the magnetic field lines. In other words, the vorticity generated by baroclinic torque during shock refraction is not given sufficient time to destabilize the interface and promote mixing.

By linearizing the ideal, incompressible magnetohydrodynamic (MHD) equations, Wheatley et al. [215, 216] show that the linearized equations predict an initial linear growth rate that reduces to zero such that the asymptotic mixing layer width is inversely proportional to the strength of the magnetic field. This inverse relationship is ultimately related to the velocity of the Alfvén wave, which Wheatley et al. [216] assume is always larger than some critical value that would be required if the RMI were to be suppressed. Such a critical value must exist, since if the magnetic field is finite, but small, it is possible for the RMI to develop unadulterated [181]. The velocity at which this transport occurs is given by the Alfvén speed, $v_a = B_0/\sqrt{\mu_0 \rho^\star}$, where $\rho^\star$ is the post-shock density. If the velocity is greater than the initial growth-rate of the RMI, then growth of the mixing layer is suppressed. In the linear regime, the growth velocity (v_{linear}) is easily estimated and a critical magnetic field strength can be defined, $B_{\text{crit}} = \sqrt{\mu_0 \rho^\star} v_{\text{linear}}$.

In the other scenario, where the magnetic field is parallel to the initial density interface, the RMI is stabilized for the same reason as the RTI in a parallel magnetic field. The movement of the flow is resisted as it moves across magnetic field lines [49]. The tensile forces causing this resistance are manifested through the Lorentz

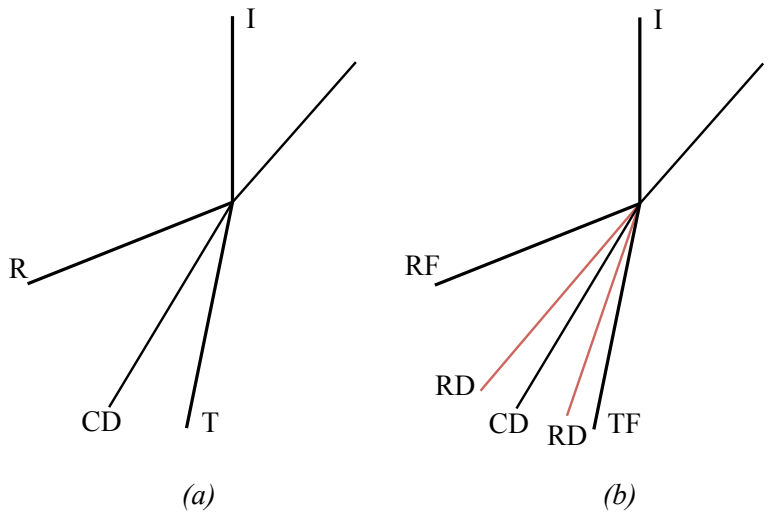

Figure 5: Wave diagram of an incident shock (I) interacting with a contact discontinuity (CD) which for (a) hydrodynamic gas generates a reflected (R) and transmitted (T) wave while for (b) magnetohydrodynamic gas generates two rotational discontinuities (RD), a fast reflected (RF) and a fast transmitted (TF) wave.

force, and in the case of the RTI and the RMI, the perturbations amplified by the deposition of vorticity during shock refraction are inhibited by this force. As a result, the instability behaves more like mass-spring-damper system where the growth-rate of the ensuing dynamics is some combination of amplification, dampening, and oscillation [49]. Analytical models derived from the linearized MHD equations seem to corroborate this explanation [31, 105, 122, 159]. In real systems, a combination of effects is likely to occur since the background magnetic field is typically randomly distributed. While such a study would be interesting, the focus in this thesis is only on the case of a magnetic field orientated normal to the contact discontinuity. A more complete understanding of this scenario is important before more general applications are studied.

While a critical magnetic field strength can be defined for the suppression of the RMI in the case two dimensional, single-mode RMI, it is worthwhile to study the

behavior in a more general set of initial parameters. As has been shown in hydrodynamic simulations of the RMI, there are observable differences in the evolution of the two dimensional and three dimensional RMI as well as for single-mode and multi-mode initializations. In three dimensional, multi-mode RMI simulations, mode coupling saturates the growth rate of the RMI faster since the full range of length scales are allowed to develop [206]. Even in the case of multi-mode, two dimensional RMI, the growth-rate is in nonlinear regime and a critical magnetic field strength is less quantifiable. Additionally, all previous numerical studies and theoretical models have assumed the plasma to be infinitely conducting ($Re_m = \infty$). In a resistive plasma, a propagating Alfvén wave is dissipated. It would be expected that for finite values of Re_m the criteria for RMI suppression in a magnetized plasma is altered. Investigating these effects is the objective of this thesis.

1.4 Computational Methods for MHD

Two key topics introduced previously are now summarized. First, the mutual interaction of a magnetic field and velocity field in a plasma is important in a variety of astrophysical and terrestrial applications and could alter the gas dynamics of an explosion. Second, this interaction, which is macroscopic in nature, is described by the governing equations of MHD, a mathematical model that treats plasma as a fluid in continuum. As a result, the governing equations of MHD, in their most simplistic form, are a set of hyperbolic partial differential equations similar to those of hydrodynamics (HD). Thus, there is significant overlap between the numerical methods used to solve the HD equations and those used to solve the MHD equations. The numerical challenges of simulating HD flows thus equally apply to MHD. The difference, and correspondingly the difficulty, in the designing numerical methods for MHD is a result of the involution condition on the magnetic field requiring zero divergence in time.

This thesis addresses two challenges in the numerical modeling of MHD flows for explosion applications. Since the governing equations of MHD are solved using methods "similar" to those used in the study of hydrodynamics, the first challenge is one typical of numerical methods applied to any high-speed flow where physical discontinuities, such as shocks, are present in an otherwise continuous, but turbulent flow. The difficulty is a result of the opposing requirements for a shock-capturing scheme, which requires numerical dissipation in order to limit numerical oscillations near discontinuities, and a low-dissipation scheme, which is needed for an accurate resolution of the turbulent flow features [117].

The second challenge is specific to MHD and stems from Gauss's law of magnetism, which states that the divergence of the magnetic field is zero, $\nabla \cdot \mathbf{B} = 0$. Here, ∇ is the divergence operator and $\mathbf{B}$ is the magnetic field vector. Mathematically, the requirement is an *involution* condition for the magnetic field [46], not technically a constraint. This means that if the magnetic field is initially divergence free, then it is so for all time. In the discrete approximation of this condition, however, the magnetic field divergence is not maintained. MHD numerical simulations therefore require some method to maintain the condition of zero magnetic divergence.

The simulation of magnetized plasma in a flows containing physical discontinuities as well as turbulence requires a numerical methodology that mets the criteria set forth by both of the aforementioned challenges. In the next section, an overview of shock-capturing schemes for both HD and MHD flows is presented, followed by a discussion of a hybrid methods, which have been used successfully in HD simulations to resolve the opposing requirements of shock-capturing and low-dissipation numerical schemes. Lastly, the algorithms traditionally used to maintain a zero magnetic divergence are discussed.

1.4.1 Shock-capturing schemes for high-speed flows

Numerical methods are typically classified based on the method of discretization of the spatial derivatives. The most straight-forward and oldest method is the finite difference (FD) method, which using the properties of Taylor expansions provides estimates of the spatial derivatives by a simple application of the theoretical definition of a derivative involving the ratio of differences across neighboring points in the discretization. Theoretically, an infinite set of difference formulas of arbitrary order can be derived [92]. As the order of approximation increases, the number of adjacent points involved in the finite difference approximation or bandwidth increases. For many high order finite difference formulas, the derivatives at different grid points are related to one another. Expressed in this way, the method becomes implicit requiring the solution to an algebraic system. Such formulations are more efficient since they limit the size of the bandwidth. They are referred to as "compact" [92, 119]. The FD method is particularly useful for a structured, uniform discretization or grid, since the actual order of the numerical approximation can be reduced if the grid is non-uniform [92]. These methods are often not amiable for applications with complex geometries.

A criteria of the FD method is that the discretized function is smooth and has continuous derivatives. In high-speed flows, this is not satisfied in the regions near flow discontinuities, and non-physical oscillations can develop since the derivatives at these points are unbounded. Thus, alternative numerical schemes are necessary. These schemes are often referred to as shock-capturing or upwind schemes since some directional biasing is necessary in order to maintain numerical stability. The first such approach highlighted the need for the numerical scheme to preserve the conservative property of the partial differential equations. In 1959, Godunov proposed a first order conservative scheme whereby the numerical fluxes were computed based on a finite volume representation of a set Riemann problems at each boundary between grid points. Most significantly, Godunov's theorem states that "linear numerical schemes

for solving partial differential equations, having the property of not generating new extrema, can be at most first-order accurate" [73].

Finite volume (FV) methods are naturally conservative since they are based on a direct discretization of the integral form of the conservation laws [92]. In contrast to FD methods, FV methods are formulated based on cell-averaged values rather than point values, thus the order of accuracy of the scheme is dependent on how these cell-averaged values are computed. Control volumes are defined by the local cell volumes of the each grid point in the mesh, and the numerical fluxes are computed at the cell faces. FV methods, first applied to the governing equations of fluid dynamics in the early 1970s [133, 131], rapidly became popular, particularly because of their adaptability in applying them to problems complex geometries. In particular, significant improvements in accuracy were made to Godunov's method.

Lax and van Leer [114, 207] formulated the foundations necessary for achieving more accurate and stable upwind schemes while still preserving the *monotonicity* of the solution, i.e., meaning the scheme produces no new local extrema in the solution. Of particular importance was the development by van Leer of the Monotone Upstream Centered Schemes for Conservation Laws (MUSCL) approach [208, 209], which is a specific type of total variation diminishing (TVD) scheme [82]. Detailed discussions of these schems can be found in many standard books on numerical methods [92, 201]. The technique uses *slope limiters* to achieve higher accuracy while restricting the interpolation order if necessary in order to ensure the scheme is monotonicity preserving. Further developments in accuracy followed in the 1980s, when Colella and Woodward introduced the Piecewise-Parabolic Method (PPM) [41]. All of these schemes are considered to be of the *Godunov-type* since they employ a Riemann solver to compute the flux at the interface of computational cell. This approach is more generally referred to as a flux difference splitting (FDS) scheme.

Beginning the late 1980s, these methods were extended to MHD [10, 28], most

notably the extension of the PPM to MHD by Dai and Woodward [47]. Since FDS methods rely on accurate solutions to the Riemann problem and since exact solutions are computationally expensive, any practical scheme must use approximate solutions to the Riemann problem, which for MHD is complicated by existence of seven characteristic waves, rather than three in HD flows. Brio and Wu [28], proposed the first approximate MHD Riemann based on a Roe-type linearized Riemann solver [167]. Since then, there have been many other approximate MHD Riemann solvers proposed [10, 223, 174]. Most significantly, a family of approximate Riemann solvers of the HLL-type, named for the developers Harten, Lax, and van Leer [83], has been adapted for MHD called the multi-state HLLD Riemann solver [142]. The majority of numerical methods in astrophysics use some type of FDS methods.

A somewhat different approach to the FDS schemes represented by MUSCL schemes [209], TVD schemes [83], and PPM schemes [41], which are usually at most second order accurate, is the class of high order essentially non-oscillatory (ENO) schemes, which are generalizations of the TVD schemes of Harten [84, 188]. Weighted essentially non-oscillatory (WENO) schemes are based on ENO schemes, but use weighting functions to select the points on the stencil over which the flow is "smooth" [187]. Since these schemes use an adaptive stencil, they are capable of sufficiently resolving both the smooth regions of the flow with high accuracy as well as resolving any discontinuity. Additionally, they are less dissipative than ENO schemes [99]. In 1994, Liu, Osher, and Chan [124] developed the first WENO scheme using a third order accurate finite volume method, and Jiang and Shu [98] later developed a general framework to achieve an arbitrary order of accuracy for finite difference WENO schemes. Their fifth order accurate finite difference WENO scheme was later extended to MHD [99]. The approach has also been adapted to provide solutions to the Hamilton-Jacobi equations for MHD [37]. A detailed discussion of WENO schemes can be found elsewhere [1]. These finite difference WENO schemes generally employ

a flux vector splitting scheme (FVS) and decompose the flux into characteristic space in order to perform directional biasing rather than requiring a Riemann problem. For flux splittings, either a Roe averaging [168] or a local or global Lax-Friedrichs averaging [201] procedure is used for the flux computation. Specific types of flux splitting methods can be necessary to avoid numerical instability [160]. While a WENO scheme can be computationally expensive in comparison to a high resolution second order method, .i.e., a MUSCL scheme, it can offer advantages if it lowers the resolution requirements [187].

Even though WENO schemes adaptively adjust to the highest possible order of accuracy based on the flow, they can still be more dissipative than a pure central differencing method [117]. Hybrid schemes have been proposed to avoid the use of a FDS or FVS upwind method in smooth regions of the flow where a low dissipation numerical scheme is necessary to directly resolve the turbulent features of the flow. switches between the numerical evaluation of the fluxes depending on the flow conditions. For stationary flows, the use of a hybrid scheme is straight-forward. Otherwise some criteria is necessary to signal the method used to evaluate the numerical flux. Hybrid schemes are often used in the study of shock / turbulence interaction. For instance, Larsson and Lele [113] use a fifth order WENO scheme with Roe flux splitting near the shock and the sixth order central difference scheme of Ducros et al. [58] elsewhere. A dynamic switch determines which scheme to use and is based on the ratio of the dilatation to the sum of the absolute value of the dilatation and the mean vorticity. Any number of combinations between shock-capturing schemes and low dissipation schemes can be developed and applied using a variety of different dynamic switches [66, 69, 163, 166]. In addition to optimizing the accuracy of the numerical flux computation, hybrid schemes also tend to be more computationally efficient than a pure WENO scheme.

1.4.2 Numerical Methods for Preserving $\nabla \cdot \mathbf{B} = 0$

The direct implementation of standard numerical methods to MHD is complicated by the criteria imposed on the magnetic field by Gauss's law of magnetism requiring that the magnetic field is divergence free. Since any numerical method, particularly a shock-capturing scheme, tends to generate non-zero values of magnetic divergence as a result of errors in the numerical discretization, some modifications to the scheme are necessary in order to avoid the accumulation of these errors in time, which if not managed can result in the unphysical transport of energy across magnetic field lines [26] as well as the potential for numerical instability [12, 37, 202]. Generally speaking, there are two approaches to numerically maintain the magnetic field divergence, divergence cleaning methods and divergence free methods.

Divergence cleaning methods can be split into two categories. The intent of the first category of divergence cleaning methods is to propagate any non-zero divergence out of the computational domain. The differences between each of the methods belonging to this category stem from how the non-zero magnetic field divergence is propagated. Powell et al. [157] introduced a method that includes source terms proportional to the magnetic field divergence, which are derived by assuming $\nabla \cdot \mathbf{B}$ is non-zero. These source terms propagate the magnetic divergence errors through the computational domain at the characteristic convection time scale of the flow. The method is often referred to as the eight wave formulation, since the degenerate characteristic related to $\nabla \cdot \mathbf{B} = 0$ is explicitly included. There are two drawbacks in this approach. The first is that the numerical formulation is non-conservative, thus there is the possibility for the shock capturing scheme to predict incorrect jump conditions near discontinuities [202]. The second is that the error propagation is dependent on the convective time scales, which could be produce errors in regions of flow recirculation.

A similar idea is developed by Dedner et al. [51], but an additional transport

equation is solved for a generalized Lagrange multiplier (GLM), which propagates errors in the magnetic field divergence out of the domain. In addition to the hyperbolic component, an optional parabolic diffusion term can be added to also dissipate the errors. The method is relatively simple to implement, conservative, and can be coupled with any numerical scheme. The primary difficulty with this method is that the transport coefficients for the GLM are arbitrarily chosen and can be problem dependent.

The second category of the divergence cleaning methods uses the properties of Hodge-Helmhotlz decomposition to split the magnetic field into solenoidal and non-solenoidal components. By solving a Poisson equation, the divergence errors in the magnetic field can be corrected. The method was first suggested by Brackbill and Barnes [26] and originally used by Zachary et al. [223], where it is now commonly referred to as the projection scheme. There are two benefits to using the projection scheme. The first benefit is that the projection scheme is easily coupled with any numerical scheme [10, 45, 174], and while solving the Poisson equation is an implicit calculation, several standard numerical implementations are available to perform this calculation efficiently [61]. Second, the Hodge-Helmholtz decomposition guarantees that the magnetic field is divergent free in the entire domain. This is not necessarily true for either the GLM method or Powell's eight-wave formulation. However, there is some criticism of the projection scheme. First, since an implicit solve of the Poisson equation is necessary, specification of the boundary conditions is more complex. The second criticism is that the successive application of the projection scheme can corrupt the magnetic field at high wave numbers in turbulence simulations [11]. Lastly, in a practical implementation of any divergence cleaning method, there is a certain degree of finesse involved in their application since these methods are not "built-in" to the numerical method.

In contrast, divergence free methods maintain the magnetic divergence by design.

In general, these methods are referred to as *constrained transport* (CT) schemes, but in their practical implementation there is a wide variation in the design. Evans and Hawley [60] first introduced the concept of CT to applications of MHD. In their original formulation, staggered electric and magnetic fields were used to design difference operators that ensure that the discrete magnetic divergence error is always of the order of mesh discretization. Since then, there have been many variations on the concept of CT [37, 67, 115, 127, 193]. Differences in these schemes result in how the magnetic field variables defined at the staggered grid points are used to compute the cell centered magnetic fields and how the magnetic field components of the numerical fluxes are computed and combined in the CT scheme to update the magnetic field. For instance, Balsara and Spicer [13], Dai and Woodward [48], Ryu et al. [174] all construct expressions using Ohm's law for the electric field as a function of the fluxes computed at each cell-face, which is then differenced to update the staggered magnetic field component within the CT approach. Gardiner et al. [67, 68] develop a spatially unsplit CT method using the corner transport update (CTU) method of Collela [41], and Londrillo et al. [127] also develop a multidimensional implementation of CT based on a third order ENO scheme. Additionally, there are several unstaggered CT methods [37, 88, 62, 103, 171], which are useful for simulations using adaptive mesh refinement. The popularity of the CT scheme is a result of its assurance that the magnetic divergence is properly maintained. The primary drawback in these methods, which is particularly true of the multidimensional implementations, is that they can be quite difficult to implement and highly sensitive to particulars of the implementation.

1.5 Objectives

The motivation of this thesis is to develop a general approach to the simulation of MHD flows. By implementing several different numerical methods, the advantages

and disadvantages of certain combinations of algorithms and models can be assessed. While a particular emphasis is placed a certain class of problems in this thesis, the approach adopted here can be applied to a wide variety of MHD astrophysical and terrestrial flows. These applications, particularly to turbulence modeling, will be discussed in the final chapter. The contribution of this thesis is demonstrated in following three objectives.

1. **Implement a numerical method for magnetohydrodynamics capable of simulating turbulence in high-speed flows for a wide variety applications.**

   In development of a numerical method for MHD in this thesis, three important criteria have been identified that need to be satisfied for a general class of turbulent high-speed flows. The first is not unique to MHD. Since high-speed flows contain discontinuities in the conservative variables, shock-capturing methods are required. By design, however, these methods are often too dissipative to adequately resolve turbulent motions in continuous regions of the flow without imposing severe restrictions on the required grid resolution. A hybrid methodology, unique to this thesis, is proposed. The second criteria is that the numerical method must satisfy the condition for a divergence free magnetic field. Several methods are implemented. This thesis proposes that there is not a single algorithm ideally suited for maintaining a divergence-free magnetic field. The last requirement relates to the assumptions about transport properties in a plasma. A general approach to implementing a numerical method for resistive MHD is again adopted. For instance at low magnetic Reynolds number flows, accurate calculations of the electrical conductivity are essential. In other instances, power-law models are adequate to the physical processes incorporated by the inclusion of the non-ideal MHD terms. Several numerical tests are used to verify the proper implementation of each numerical method.

2. **Determine the effect of an external magnetic field on the propagation of a gaseous detonation.**

   In the application of the numerical method implemented in this thesis, gaseous detonations are simulated in mixtures of hydrogen and air seeded with potassium carbonate, a low ionization potential molecule, which is used to increase the electrical conductivity of the flow. A detailed model for the ionization and computation of the electrical conductivity of the mixture in the post-detonation flow is implemented. The reduced kinetic model for the ionization process includes rates for electron impact ionization, charge exchange, and dissociative recombination. The mixture-averaged transport model for the calculation of the electrical conductivity is based on Chapman-Enskog theory. The computed electrical conductivity in gaseous hydrogen-air detonations are compared to experimental measurements. This, along with comparisons of the detonation properties to theoretical calculations, validate the numerical approach. Next, the effect of a magnetic field on the propagation of a detonation wave is investigated. The numerical method is capable of solving either the full MHD equations or the quasi-static form of the MHD equations, which are valid for low magnetic Reynolds number flows. Numerical simulations indicate that the magnetic Reynolds number of the post-detonation is small enough for the quasi-static assumption to valid. Using the quasi-static MHD numerical method, the effect of the magnetic field on the propagation of a detonation wave is found to be a function of a Stuart number based on the length scale of the half-reaction zone and a time-scale of the detonation velocity.

3. **Investigate how the Richtmyer-Meshkov instability (RMI) develops in a resistive magnetized plasma.**

   In another application of the numerical method, the RMI in a magnetized

plasma is simulated. As previously discussed, the RMI is an important mechanism for initiating mixing in the post-explosion flow. It is also particularly relevant to understanding the mixing processes in the ISM. Additionally, simulations of the RMI are used to evaluate each of the different numerical methods. The RMI is analyzed in a variety of configurations in both a strongly and weakly magnetized medium. While the RMI has been shown to be stabilized in a magnetized plasma, this thesis proposes a generalized criteria for stability that includes non-ideal MHD affects. In a strongly magnetized medium, the affects of resistivity are investigated as a function of the Lundquist number. In weakly magnetized medium, the role of the small-scale dynamo is discussed.

1.6 Thesis Layout

This thesis is organized as follows.

- Chapter 2 introduces the governing equations of a magnetized, electrically-conducting flow. These equations couple the conservation equations of mass, species, momentum, and energy with Maxwell's equations, which given some assumptions result in the governing equations of MHD. The thermodynamic and transport models are discussed as well as kinetic models for the species source term. Lastly, some fundamental non-dimensional numbers of MHD are introduced.

- Chapter 3 provides a discussion and detailed description of the numerical methods implemented in this thesis. These methods are verified using a series of numerical tests that have been historically used to evaluate MHD numerical methods.

- Chapter 4 discusses the application of the numerical methods implemented here to problems relevant to the study of MHD in astrophysical and terrestrial applications. In this chapter, the base hydrodynamic numerical method is validated and the advantages and disadvantages of each of the numerical methods is discussed.

- ◇ Chapter 5 gives a detailed analysis of ionization in gaseous detonation waves and discusses how the propagation of the detonation is affected by an applied magnetic field. This application utilizes the quasi-static form of the MHD equations and highlights the ability of the numerical method to compute the properties of a plasma in a complex, reacting flow.

- ◇ Chapter 6 details how the physics of variable density mixing in shock accelerated flows are modified in a magnetized plasma. The numerical results are compared to theoretical predictions and a criteria for the stability of the magnetic field is established for resistive plasmas.

- ◇ Chapter 7 summarizes the motivations and objectives of this thesis with respect to the results provided in the previous chapters. Lastly, tasks for future work are discussed.

CHAPTER II

GOVERNING EQUATIONS OF MHD

In an ionized gas, many new physical processes become important. For example, since electrons are less massive than ions, there is a likelihood for thermodynamic non-equilibrium to develop between the electrons and ions of the ionized gas. Also, in the presence of an electromagnetic field, the motions of the electrons and ions are altered. This adds a new range of dynamics. Thus, it is important to understand the range of physics described by the governing equations of MHD. To develop an appreciation for the assumptions of the MHD model, the governing equations are derived starting with a microscopic description of an ionized gas and ending with the macroscopic fluid model of MHD. Figure 6 illustrates this approach. The discussion below follows that of several introductory text books. The kinetic theory of ionized gases is most rigorously discussed in Braginskii [27]. Both Freidberg [64] and Sutton [195] derive and introduce the MHD equations from an engineering perspective, while Goedbloed and Poedts discuss the MHD equations from the perspective of astrophysics [74]. For more details on the derivation presented in this chapter, particularly Sec. 2.2, see the previously mentioned authors. Goedbloed and Poedts [74] is particularly useful, and their discussion is used as a primary guideline for the approach adopted here.

As a note to the reader, in Secs. 2.1 and 2.2 vector notation is used extensively. Thus, all subscripts are used for distinguishing different variables. In Sec. 2.3, tensor notation is adopted since it is more commonly used in the literature concerning the type of studies conducted in this thesis. The tensor form of the MHD equations presented here has been previously used as the basis for deriving the filtered equations for the large-eddy simulation (LES) of the MHD equations [139, 140].

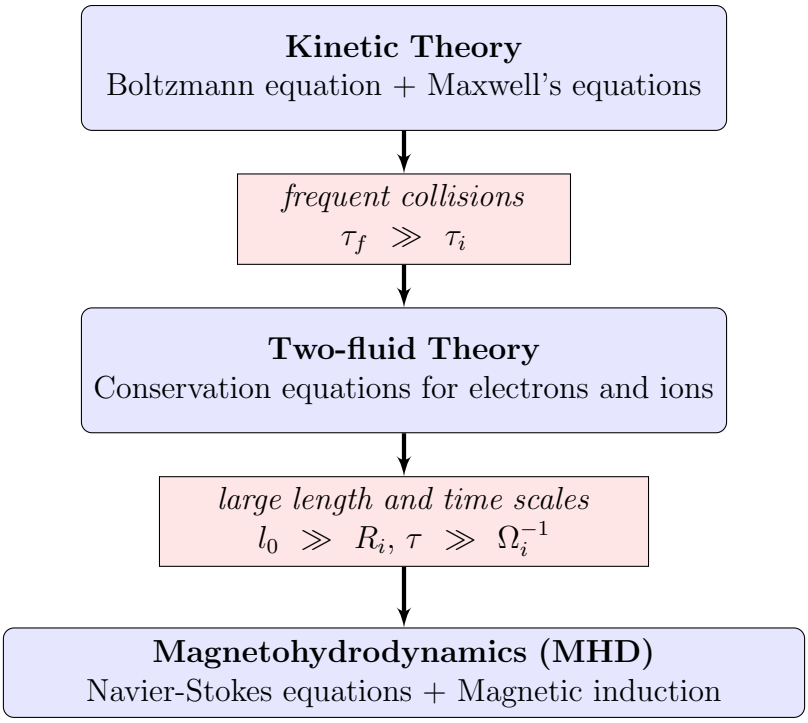

Figure 6: Theoretical descriptions of a plasma and the required criteria for each model. More details are provided within the text. τ_f is characteristic time scale of a fluid, l_0 and τ are the characteristic length and time scales of a plasma as described by MHD, τ_i is the ion-collision time scale ($> \tau_e$, the electron collision time scale), and R_i amd Ω_i are the ion gyro-radii and gyro-frequency, both of which represent the largest microscopic length and time scales of a plasma. This figure is adapted from Goedbloed and Poedts [74].

2.1 Single-particle Motion

From a fundamental perspective, Lagrangian equations for the force and heat balance of each individual particle can be used to describe the plasma dynamics. While it is probably apparent that such an approach is untenable for a large number of particles. The analysis of the equation of motion for a single particle is instructive. Consider the time-dependent motion of a non-relativistic, charged particle moving in an electric and magnetic field, given by $\mathbf{E}(\mathbf{x}, t)$ and $\mathbf{B}(\mathbf{x}, t)$, respectively, where the vector $\mathbf{x}$ in Cartesian space is defined as $\mathbf{x} = (x, y, z)$, and the variable t represents time. The

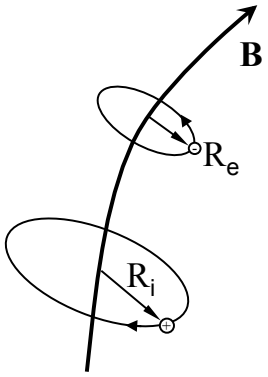

Figure 7: Schematic of the motion of a single electron and single ion in a magnetic field.

equation of motion for each particle is given by [25, 36] as

$$m_\alpha \frac{d\mathbf{v}_\alpha}{dt} = q_\alpha \left(\mathbf{E} + \mathbf{v}_\alpha \times \mathbf{B}\right), \tag{10}$$

where q_α is the charge of the particle, m_α is the mass of the particle, and $\mathbf{v}_\alpha$ is the velocity of the particle. The subscript $\alpha = (i, e)$ is used to differentiate between the negatively charged electrons and the positively charged ions. Given values for the electric and magnetic fields, it is possible to determine the particle velocity $\mathbf{v}(\mathbf{x}, t)$ in time.

As an example, consider a charged particle moving in a constant magnetic field orientated in the z-direction and defined by $\mathbf{B}(\mathbf{x}, t) = B_0\mathbf{k}$. The electric field is zero. With this simplification, an analytical solution to Eq. 10 is possible. In the direction parallel to the orientation of the magnetic field, the particle velocity is constant, $v_\parallel = v_z =$ constant. In the perpendicular plane, the particle's motion is defined by a system of two ordinary differential equations [36, 74],

$$\dot{v}_x - (q_\alpha B/m_\alpha)v_y = 0, \tag{11}$$

$$\dot{v}_y + (q_\alpha B/m_\alpha)v_x = 0. \tag{12}$$

where $\dot{v_x}$ and $\dot{v_y}$ represent the acceleration of the particle in the x and y direction. It

is now possible to define the gyro- or cyclotron frequency as

$$\Omega_\alpha \equiv \frac{|q_\alpha|B}{m_\alpha}, \tag{13}$$

and the gyro- or cyclotron radius,

$$R_\alpha \equiv \frac{v_\perp}{\Omega_\alpha}, \tag{14}$$

where $v_\perp$ is the magnitude of the particle's velocity in the plane perpendicular the magnetic field, which in this example is also a constant. The meaning of these terms is clear given the solution of the particle's motion [74],

$$x(t) = x_c + R_\alpha \cos(\Omega_\alpha t), \tag{15}$$

$$y(t) = y_c - R_\alpha \sin(\Omega_\alpha t), \tag{16}$$

$$z(t) = v_\parallel t. \tag{17}$$

Thus, a charged particle moves along the magnetic field line orbiting around a guiding center defined by the orientation of the field. In this regard, the magnetic field defines the large scale geometry of the plasma. Both R_α and Ω_α define the characteristic scales of the motion of a charged at the microscopic level. Since the difference between the mass of an electron is large, then the following scalings can be deduced [74],

$$\Omega_e \equiv \frac{eB}{m_e} \gg \Omega_i \equiv \frac{ZeB}{m_i}, \tag{18}$$

$$R_e \equiv \frac{v_{\perp,e}}{\Omega_e} \ll R_i \equiv \frac{v_{\perp,i}}{\Omega_i}. \tag{19}$$

As a result, R_i and Ω_i provide measures of the largest length and lowest frequency characteristic scales of the microscopic particle motion in an ionized gas. An important result is that for an ionized gas, the gyro-frequency is only dependent on the magnitude of the magnetic field. Thus, measurements of cyclotron radiation are an important diagnostic for determining the magnitude of the magnetic field [74, 205].

2.2 Kinetic Theory

Since an ionized gas typically consists of a many charged particles, Eq. 10 is not the most feasible representation of a plasma. Particularly since unlike neutral gases, the interaction between particles do not occur only through short-range, binary collisions. In a plasma, this interaction is long-range and collective [36]. As a result, each particle moves in the average electrostatic field created by all other particles. In order to develop a trackable mathematical framework, a statistical model for the time-dependent distribution function of each particle type is developed using kinetic theory. The result is a set of Boltzmann equations for the particle distributions, which are coupled to Maxwell equations for the electromagnetic. More details on the independent derivation of the Boltzmann equation and the Maxwell equations can be found elsewhere [20, 64].

For the purposes of this discussion, consider a fully ionized gas consisting of electrons and only one type of ion ($\alpha = (e, i)$). Thus, for a gas with atomic number Z, the positive ion charge is $q_i = Ze$, where e is the electric charge. Since the gas is fully ionized, the processes of ionization, recombination, and charge exchange reactions are in equilibrium and thus can be neglected. Kinetic theory then describes the motion of the electrons and ions by a time-dependent distribution function, $f_\alpha(\mathbf{x}, \mathbf{v}, t)$ which is a six-dimensional phase space of three position coordinates $x_i = (x, y, z)$ and three velocity coordinates $v_i = (v_x, v_y, v_z)$. The quantity $f_\alpha(\mathbf{x}, \mathbf{v}, t)d^3xd^3v$ is interpreted as the average number of particles of type α in the physical volume d^3x centered about $\mathbf{x}$ and the velocity-space d^3v centered at $\mathbf{v}$ at time t. This time-dependent behavior of $f_\alpha(\mathbf{x}, \mathbf{v}, t)$ is then described by the Boltzmann equation,

$$\frac{\partial f_\alpha}{\partial t} + \mathbf{v} \cdot \nabla f_\alpha + \frac{q_\alpha}{m_\alpha} (\mathbf{E} + \mathbf{v} \times \mathbf{B}) \cdot \frac{\partial f_\alpha}{\partial \mathbf{v}} = \left(\frac{\partial f_\alpha}{\partial t} \right)_{\text{coll}} = C_\alpha, \tag{20}$$

which depends on the electric field $\mathbf{E}$ and the magnetic field $\mathbf{B}$ given by Maxwell's

equations,

$$\nabla \times \mathbf{E} = -\frac{\partial \mathbf{B}}{\partial t}, \tag{21}$$

$$\nabla \times \mathbf{B} = \mu_0 \mathbf{J} + \frac{1}{c^2}\frac{\partial \mathbf{E}}{\partial t}, \tag{22}$$

$$\nabla \cdot \mathbf{E} = \frac{\rho_c}{\epsilon_0}, \tag{23}$$

$$\nabla \cdot \mathbf{B} = 0, \tag{24}$$

where the explicit dependence on $\mathbf{x}$ and t for each vector field has been dropped for convenience. This set of equations completes the kinetic model of a plasma. In the above equations, c is the speed of light, ρ_c is the charge density, and $\mathbf{J}$ is the current density. Both ρ_c and $\mathbf{J}$ provide the link between the electron and ion Boltzmann equations and the Maxwell equations. Averaging $f_\alpha(\mathbf{x}, \mathbf{v}, t)$ over velocity space results in the particle number density,

$$n_\alpha(\mathbf{x}, t) = \int f_\alpha(\mathbf{x}, \mathbf{v}, t) d^3v. \tag{25}$$

Likewise, the average electron or ion velocity is

$$\mathbf{u}_\alpha(\mathbf{x}, t) = \frac{1}{n_\alpha}\int \mathbf{v} f_\alpha(\mathbf{x}, \mathbf{v}, t) d^3v. \tag{26}$$

From these definitions, the charge density σ and current density $\mathbf{J}$ are defined, respectively, as

$$\rho_c(\mathbf{x}, t) = \sum q_\alpha n_\alpha, \tag{27}$$

$$\mathbf{J}(\mathbf{x}, t) = \sum q_\alpha n_\alpha \mathbf{u}_\alpha, \tag{28}$$

where the summation is taken over all particle types α. As given above, the Maxwell equations do not explicitly include the effects of polarization and magnetization, i.e. all charges and currents in the plasma are free. The permittivity and permeability are given by their vacuum values, $\epsilon_0 = 8.854 \times 10^{-12}$ F/m and $\mu_0 = 4\pi \times 10^{-7}$ N/A^2, respectively.

The term on the right-hand-side of Eq. 20, C_α, represents the effects of inter-particle collisions between particles of type α and all other particles ($C_\alpha = \sum_\beta C_{\alpha\beta}$). As a result of collisions, the particles are scattered in an out of the volume and velocity elements d^3x and d^3v. This term, however, is fundamentally different from the binary collision integral originally derived by Boltzmann. In brief, in a plasma it is necessary to distinguish the short-range, binary collisions from the long range interactions. There is a significant body of literature dedicated to this task [8, 170, 204], which is not discussed here. One simplification is to neglect this term completely. This results in the Vlasov equation [74],

$$\frac{\partial f_\alpha}{\partial t} + \mathbf{v}\cdot\nabla f_\alpha + \frac{q_\alpha}{m_\alpha}\left(\mathbf{E} + \mathbf{v}\times\mathbf{B}\right)\cdot\frac{\partial f_\alpha}{\partial \mathbf{v}} = 0 \tag{29}$$

where the long-range interactions between particles are still retained through $\mathbf{E}$ and $\mathbf{B}$, but the plasma is effectively collisionaless. Equations 20-28 represent a closed system for the microscopic dynamics of a plasma.

In order to obtain a macroscopic equations and remove the dependence on velocity space, the Boltzmann equations are expanded in a series of finite moments. However, since the expansion is truncated, a closure model is necessary to include the effects of the still unspecified higher order moments. In general, it is necessary only to consider the following moments [64, 74]:

$$\frac{\partial n_\alpha}{\partial t} + \nabla\cdot\left(n_\alpha \mathbf{u}_\alpha\right) = 0 \tag{30}$$

$$\frac{\partial}{\partial t}\Big(n_\alpha m_\alpha \mathbf{u}_\alpha\Big) + \nabla\cdot\Big(n_\alpha m_\alpha \langle\mathbf{vv}\rangle_\alpha\Big) - q_\alpha n_\alpha\left(\mathbf{E} + \mathbf{u}_\alpha\times\mathbf{B}\right) = \int C_{\alpha\beta} m_\alpha \mathbf{v} d^3v \tag{31}$$

$$\frac{\partial}{\partial t}\Big(n_\alpha \frac{1}{2} m_\alpha \langle v^2\rangle_\alpha\Big) + \nabla\cdot\Big(n_\alpha \frac{1}{2} m_\alpha \langle v^2\mathbf{v}\rangle_\alpha\Big) - q_\alpha n_\alpha \mathbf{u}_\alpha\cdot\mathbf{E} = \int C_{\alpha\beta}\frac{1}{2} m_\alpha v^2 d^3v \tag{32}$$

where $C_{\alpha\beta}$ is only nonzero for $\alpha \neq \beta$, and the quantities $\langle\mathbf{vv}\rangle_\alpha$, $\langle v^2\rangle_\alpha$, and $\langle v^2\mathbf{v}\rangle_\alpha$ are higher moments and in general defined as

$$\langle Q\rangle_\alpha(\mathbf{x},t) \equiv \frac{1}{n_\alpha}\int Q(\mathbf{x},\mathbf{v},t) f_\alpha(\mathbf{x},\mathbf{v},t) d^3v, \tag{33}$$

which cannot be evaluated unless some assumptions are made. The next step involves defining the particle velocity, $\mathbf{v}$, as the sum of the average component $\mathbf{u}_\alpha$ and a fluctuating component defined to have a zero mean. The fluctuating particle velocity is then defined as

$$\mathbf{w}_\alpha = \mathbf{v} - \mathbf{u}_\alpha. \tag{34}$$

As a result, thermal quantities, which have some physical significance, can be defined [64, 74]. These are the temperature,

$$T_\alpha \equiv \frac{m_\alpha}{3k_B}\langle w^2\rangle_\alpha, \tag{35}$$

the total pressure tensor,

$$\mathsf{P}_\alpha \equiv n_\alpha m_\alpha \langle \mathbf{ww}\rangle_\alpha, \tag{36}$$

the heat flow from random motion,

$$\mathbf{h}_\alpha \equiv \frac{1}{2} n_\alpha m_\alpha \langle w^2 \mathbf{w}\rangle_\alpha, \tag{37}$$

and the transfer of momentum and heat by collisions of unlike particles,

$$\mathbf{M}_\alpha \equiv \int C_{\alpha\beta} m_\alpha \mathbf{w}_\alpha \mathrm{d}^3 w, \tag{38}$$

$$Q_\alpha \equiv \int C_{\alpha\beta} \frac{1}{2} m_\alpha w_\alpha^2 \mathrm{d}^3 w. \tag{39}$$

Substituting these expressions in Eqs. 30-46, the equations of continuity, momentum, and energy balance are [64, 74]

$$\frac{\partial n_\alpha}{\partial t} + \nabla \cdot (n_\alpha \mathbf{u}_\alpha) = 0 \tag{40}$$

$$n_\alpha m_\alpha \left(\frac{\partial \mathbf{u}_\alpha}{\partial t} + \mathbf{u}_\alpha \cdot \nabla \mathbf{u}_\alpha \right) + \nabla \cdot \mathsf{P}_\alpha - n_\alpha q_\alpha \left(\mathbf{E} + \mathbf{u}_\alpha \times \mathbf{B} \right) = \mathbf{M}_\alpha \tag{41}$$

$$n_\alpha \left(\frac{\partial \mathcal{E}_\alpha}{\partial t} + \mathbf{u}_\alpha \cdot \nabla \mathcal{E}_\alpha \right) + \nabla \cdot (\mathbf{u}_\alpha \cdot \mathsf{P} + \mathbf{h}_\alpha) - q_\alpha n_\alpha \mathbf{u}_\alpha \cdot \mathbf{E} = Q_\alpha + \mathbf{u}_\alpha \cdot \mathbf{M}_\alpha \tag{42}$$

where $\mathcal{E}_\alpha = m_\alpha u_\alpha^2/2 + 3k_B T_\alpha/2$ is the total energy. The total pressure tensor can be decomposed into isotropic and anisotropic terms. The scalar pressure is defined as

$$p_\alpha = n_\alpha k_B T_\alpha, \tag{43}$$

and the anisotropic part is π_α. Thus, in Eq. 41,

$$\nabla \cdot \mathsf{P}_\alpha = \nabla p_\alpha + \nabla \cdot \pi_\alpha \tag{44}$$

As discussed in Freidberg [64], the energy equation is often further reduced by computing the dot product of Eq. 41 with $\mathbf{v}_\alpha$ and then subtracting the result from Eq. 42. As a result, the complete set of the two fluid equations ($\alpha = e, i$) are [64]

$$\left(\frac{\mathrm{d}n_\alpha}{\mathrm{d}t}\right)_\alpha + n_\alpha \nabla \cdot \mathbf{u}_\alpha = 0 \tag{45}$$

$$n_\alpha m_\alpha \left(\frac{\mathrm{d}\mathbf{u}_\alpha}{\mathrm{d}t}\right)_\alpha + \nabla p_\alpha - n_\alpha q_\alpha \left(\mathbf{E} + \mathbf{u}_\alpha \times \mathbf{B}\right) + \nabla \cdot \pi_\alpha = \mathbf{M}_\alpha \tag{46}$$

$$\frac{3}{2} n_\alpha k_B \left(\frac{\mathrm{d}T_\alpha}{\mathrm{d}t}\right)_\alpha + \mathsf{P}_\alpha : \nabla \mathbf{u}_\alpha + \nabla \cdot \mathbf{h}_\alpha = Q_\alpha \tag{47}$$

$$\nabla \times \mathbf{E} = -\frac{\partial \mathbf{B}}{\partial t} \tag{48}$$

$$\nabla \times \mathbf{B} = \mu_0 e \left(n_i \mathbf{u}_i - n_e \mathbf{u}_e\right) + \frac{1}{c^2}\frac{\partial \mathbf{E}}{\partial t} \tag{49}$$

$$\nabla \cdot \mathbf{E} = \frac{e}{\epsilon_0}\left(n_i - n_e\right) \tag{50}$$

$$\nabla \cdot \mathbf{B} = 0 \tag{51}$$

where

$$\left(\frac{\mathrm{d}}{\mathrm{d}t}\right)_\alpha \equiv \frac{\partial}{\partial t} + \mathbf{u}_\alpha \cdot \nabla \tag{52}$$

The above equations are still require closure since the expressions π_α, $\mathbf{h}_\alpha$, $\mathbf{M}_\alpha$, and Q_α involve higher order moments and the collision operator, $C_{\alpha\beta}$. In order to determine expressions for these terms, some assumptions are necessary [64, 74]. If the each type of particles undergo sufficient collisions, then it is possible to define a reference state based on the assumption of local thermodynamic equilibrium, which is expressed by the Maxwell distribution,

$$f_\alpha^0(\mathbf{x}, \mathbf{v}, t) = n_\alpha \left(\frac{m_\alpha}{2\pi k_B T_\alpha}\right)^{3/2} \exp\left(-\frac{m_\alpha w_\alpha^2}{2k_B T_\alpha}\right). \tag{53}$$

Based on this assumption, the temperature then defines the random thermal velocity,

$V_{T_\alpha} = (2T_\alpha/m_\alpha)^{1/2}$. For the ions, the dominant collision mechanism is from ion-ion collisions, while the electrons equilibrate both through electron-ion and electron-electron collisions [64]. For a a characteristic MHD frequency, $\omega \approx \frac{\partial}{\partial t} \approx V_{T_i}/l_0$, where l_0 is the reference MHD length scale. A quantitative criteria for this assumption is based on the collision time scales of the electrons and ions, τ_{ii} and $\tau_{ee} \approx \tau_{ei}$, which must be less than the time scales for which a hydrodynamic description of each of the particles is valid [64, 74]. This requires

$$\omega\tau_{ii} \approx V_{T_i}\tau_{ii}/l_0 << 1, \tag{54}$$

$$\omega\tau_{ee} \approx (m_e/m_i)^{1/2} V_{T_i}\tau_{ii} << 1. \tag{55}$$

In the above expression, $\tau_{ee} \approx (m_e/m_i)^{1/2}\tau_{ii}$. Additionally, the macroscopic length scale must be larger than the mean free path of the electrons and ions. This requirement is more restrictive for the electrons [64]. In conclusion, for the plasma to be collision dominated, the following criteria must be satisfied [64, 74],

$$V_{T_i}\tau_{ii}/l_0 \approx V_{T_i}\tau_{ee}/l_0 << 1 \tag{56}$$

A more detailed discussion is given elsewhere [8, 20, 27, 74]. Using transport theory along with similar scaling arguments, the following approximate expressions for the higher order moments are derived

$$\pi_{e,i} \approx \mu_{e,i}\nabla\mathbf{u}_{e,i} \tag{57}$$

$$\mathbf{h}_{e,i} \approx -\kappa_{e,i}\nabla(k_B T_{e,i}), \tag{58}$$

$$\mathbf{M}_e = -\mathbf{M}_i \approx -en_e\eta\mathbf{J}, \tag{59}$$

$$Q_e + Q_i = -(\mathbf{u}_e - \mathbf{u}_i)\cdot\mathbf{M}_e \approx \eta|\mathbf{J}|^2 \tag{60}$$

where only the leading terms are included. The transport coefficients, $\mu_{e,i}$, $\kappa_{e,i}$, and η are the electron and ion coefficients of viscosity, the electron and ion coefficients of heat conductivity, and the electrical resistivity, respectively. In general, they are

anisotropic tensors functionally dependent on the density, temperature, and magnetic field. The anisotropy of the tensor form of the transport coefficients is related to the gyro-frequencies of the electrons and ions. For instance, the electron heat conductivities, $\kappa^e_\perp/\kappa^e_\parallel \approx (\Omega_e\tau_e)^{-2} << 1$, where Ω_e is the electron gyro-frequency defined previously and τ_e is the electron collision time [74]. Obviously, electron transport can be highly anisotropic. However, theoretical estimates of the magnetic resistivity show much less anisotropy [74], $\eta = \eta_\perp = 2\eta_\parallel$.

In order to reduce the two fluid equations into the single fluid MHD equations, the macroscopic single fluid variables are defined as linear combinations of the two fluid variables [64, 74]. For instance, the definitions

$$\rho \equiv n_e m_e + n_i m_i, \tag{61}$$

$$\rho_c \equiv -e(n_e - Z n_i), \tag{62}$$

$$\mathbf{u} \equiv (n_e m_e \mathbf{u}_e - n_i m_u \mathbf{u}_i)/\rho, \tag{63}$$

$$\mathbf{J} \equiv -e(n_e \mathbf{u}_e - Z n_i \mathbf{u}_i), \tag{64}$$

$$p \equiv p_e + p_i \tag{65}$$

$$T \equiv T_e + T_i \tag{66}$$

define the gas density, the total charge density, the center of mass velocity, the current density, the pressure, and the temperature, respectively. In order to remove all the two fluid variables, the inverse relationships of Eqs. 61-66 are exploited using asymptotic arguments to neglect the high frequency, short wavelength information on the range of the length and time scales of interest [64, 74]. For instance, define the mass ratio $\mu_m = Z m_e/m_i$, then,

$$\begin{aligned} n_e &= \frac{Z\left[\rho - (m_i/Ze)\rho_c\right]}{m_i\left(1+\mu_m\right)} \approx \frac{Z}{m_i(1+\mu_m)}\rho, \\ n_i &= \frac{\rho + \mu_m(m_i/Ze)\sigma}{m_i\left(1+\mu_m\right)} \approx \frac{Z}{m_i(1+\mu_m)}\rho, \end{aligned} \tag{67}$$

where the above approximations are satisfied if $|n_e - Z n_i| << n_e$ or $m_i|\rho_c|/Ze << \rho$

[74]. Both are statements of quasi-neutrality. To demonstrate this, consider the case of a fully-ionized, cold plasma in the two fluid approximation where all thermal effects can be neglected (P_α, $\mathbf{h}_\alpha$, $\mathbf{M}_\alpha$, and Q_α are zero), but a small charge imbalance exists [74]. The electric field is given by,

$$\nabla \cdot \mathbf{E} = \frac{\rho_c}{\epsilon_0} = \frac{e}{\epsilon_0}\left(Zn_i - n_e\right). \tag{68}$$

Assuming that a small perturbation in the charge imbalance results in a faster acceleration electrons than ions as a result of the mass difference ($m_i >> m_e$), then the equation of motion for the ions simplify to $\mathbf{u}_i = 0$, and thus, $n_i \approx n_0/Z$. Linearizing the electron equations for small perturbations gives $n_e \approx n_0 + n_1(\mathbf{x}, t)$ and $\mathbf{u}_e \approx \mathbf{u}_1(\mathbf{x}, t)$. The set of equations for n_1 and $\mathbf{u}_1$ then describe the plasma oscillations resulting from a small charge imbalance [74]. This set is given by

$$\frac{\partial n_1}{\partial t} + n_0 \nabla \cdot \mathbf{u}_1 = 0, \tag{69}$$

$$m_e \frac{\partial \mathbf{u}_e}{\partial t} = -e\mathbf{E}_1, \tag{70}$$

$$\nabla \cdot \mathbf{E}_1 = -\frac{e}{\epsilon_0} n_1 \tag{71}$$

can be reduced to a single partial differential equation [74],

$$\frac{\partial^2 n_1}{\partial t^2} = -n_0 \nabla \cdot \frac{\partial \mathbf{u}_1}{\partial t} = \frac{n_0 e}{m_e} \nabla \cdot \mathbf{E}_1 = -\frac{n_0 e^2}{\epsilon m_e} n_1, \tag{72}$$

which admits solutions of the form $n_1(\mathbf{x}, t) = \hat{n}_1 \exp\left(-i\omega_{pe} t\right)$. The characteristic frequency, ω_{pe} is the electron plasma frequency, defined as

$$\omega_{pe} = \sqrt{\frac{n_0 e^2}{\epsilon m_e}} \tag{73}$$

The electron plasma frequency is a fundamental parameter of a plasma [74]. Determining the spatial variation in the amplitude of the oscillations, $\hat{n}_1(\mathbf{x})$, is more complicated, but in summary, the scale of thermal fluctuations is related to the Debye length,

$$\lambda_D \equiv \sqrt{\frac{\epsilon k_B T_e}{n_0} e^2} = \frac{V_{T,e}}{\sqrt{2}\omega_{pe}}. \tag{74}$$

The above derivation [74] demonstrates that for characteristic frequencies ($\omega = 1/\tau$) much less than the electron plasma $\omega << \omega_{pe}$ and for characteristic lengths $l_0 >> \lambda_D$, the plasma can effectively assumed to be charge neutral, $\rho_c \approx 0$. The electrons are assumed to have infinitely fast electron response time. From a similar scaling argument as in Eq. 67, the remaining two fluid variables can be removed based on the assumption of negligible electron inertia, $m_e \to 0$ or $\mu_m \to 0$. This requires that the time scales are long compared to both ω_{pe} and the electron gyro-frequency, Ω_e, and similarly that the length scales are larger than λ_D and the electron gyro-radius, R_e. More restrictively, as demonstrated more exclusively elsewhere [64, 74], this requires,

$$\omega << \Omega_i, \qquad l_0 >> R_i. \tag{75}$$

As a result of Eq. 67, $n_e = n_i \equiv n$, and thus the mass density is $\rho = m_i n$. By a similar argument, the momentum of the fluid is dominated by the movement of the ions, $\mathbf{u} = \mathbf{u_i}$, and the current density is defined as $\mathbf{J} = en\left(\mathbf{u}_i - \mathbf{u}_e\right)$. The most strenuous criteria is that of thermodynamic equilibrium between the electrons and ions [64], which implies $T_e = T_i$. This is only satisfied if there are sufficient electron-ion collisions during the MHD flow time scale. This can be stated as $\omega\tau_{eq} << 1$, where τ_{eq} is the equilibrium time scale and can be approximated as

$$\left(\frac{m_i}{m_e}\right)^{1/2} \frac{V_{T_i}\tau_{ii}}{l_0} << 1 \tag{76}$$

The time for thermodynamic equilibrium is long compared to the momentum exchange time, and thus this assumption is more restrictive than the previous assumption of requiring the plasma to be collision dominated in order to establish fluid behavior.

Through linear combinations of the two fluid equations multiplied by either mass or charge factors and use of the asymptotic results, the conservation equations for mass, momentum, and energy of a single fluid can be derived. Details can be found

elsewhere [64, 74], and only a few results are highlighted here for the purpose of demonstration. Adding the electron and ion momentum equations results in

$$\rho\left(\frac{\partial \mathbf{u}}{\partial t}+\mathbf{u}\cdot\nabla\mathbf{u}\right)-\mathbf{J}\times\mathbf{B}+\nabla p=-\nabla\cdot(\pi_i+\pi_e) \tag{77}$$

where the definition $\mathbf{M}_e=-\mathbf{M}_i$ was used [64]. The right-hand side represents the non-ideal effects of momentum transfer by random velocity fluctuations. Assuming $\pi_e\approx 0$ (π_i is larger by a factor of $(m_i/m_e)^{1/2}$) and using the first order approximation of π_i with μ as the mixture viscosity from Eq. 57 results in the Navier-Stokes equation with the addition of a MHD force term,

$$\rho\left(\frac{\partial \mathbf{u}}{\partial t}+\mathbf{u}\cdot\nabla\mathbf{u}\right)-\mathbf{J}\times\mathbf{B}+\nabla p+\nabla\cdot(\mu\nabla\mathbf{u})=0, \tag{78}$$

where the additional term for the magnetic force, $\mathbf{J}\times\mathbf{B}$, is called the Lorentz force [64]. In a similar manner, though the algebra is much more complicated, the conservation equation for the total energy can be derived were scaling arguments can be used to eliminate the electron transport terms [64, 74]. This results in an additional source term, $\mathbf{J}\cdot\mathbf{E}$, the electromagnetic power dissipation along with a work term associated with the Lorentz force.

Simplifications to Maxwell equations are now discussed. The displacement current, added by Maxwell to Ampére's law of induction, can also be shown to be negligible when the velocities of the particles constituting the plasma are assumed to be non-relativistic, $u_0 << c$. For a length scale of L and velocity scale u_0, the displacement current is shown to be $\mathcal{O}(u_0^2/c^2)$ and thereby negligible by comparison [74],

$$\begin{aligned}\frac{1}{c^2}\left|\frac{\partial \mathbf{E}}{\partial t}\right| &\approx \frac{u_0^2}{c^2}\frac{B}{l_0},\\ |\nabla\times\mathbf{B}| &\approx \frac{B}{l_0}.\end{aligned} \tag{79}$$

Thus, the current density and the magnetic field are directly related through the

pre-Maxwellian form of Ampére's law,

$$\mathbf{J} = \frac{1}{\mu_0} \nabla \times \mathbf{B} \tag{80}$$

Additionally, the assumption of quasi-neutrality can be used. To demonstrate this, it is instructive to decompose the electric field into solenoidal and non-solenoidal components, $\mathbf{E}_s$ and $\mathbf{E}_r$ respectively, where the total electric field is then given as $\mathbf{E} = \mathbf{E}_s + \mathbf{E}_i$. From Coulomb's law, the electrostatic field $\mathbf{E}_s$ is defined as irrotational, and Gauss's law states that the divergence of $\mathbf{E}_s$ is fixed by the total electric charge density, ρ_c, which on the scales of MHD is negligible. Mathematically, these two laws state

$$\nabla \cdot \mathbf{E}_s = \frac{\rho_c}{\epsilon_0} \approx 0, \tag{81}$$

$$\nabla \times \mathbf{E}_s = 0. \tag{82}$$

where the assumption of quasi-neutrality, $\sigma \approx 0$ is used. The electric field is decomposed in order to illustrate that even though a plasma is quasi-neutral, the electric field is not zero. The rotational part of the electric field $\mathbf{E}_r$ is important since it is generated by the induced electromotive force (emf) given by Faraday's law,

$$\nabla \cdot \mathbf{E}_r = 0, \tag{83}$$

$$\nabla \times \mathbf{E}_r = \frac{\partial \mathbf{B}}{\partial t}. \tag{84}$$

Therefore, the dynamics of both the electric and magnetic field are defined entirely by Faraday's law. This result has the following physical interpretation. The electrons immediately respond to any perturbation in the local charge balance, and thus, always move to establish charge neutrality. The simplified Maxwell equations are summarized

as

$$\nabla \times \mathbf{E} = -\frac{\partial \mathbf{B}}{\partial t} \qquad (\textit{Faraday's Law}), \tag{85}$$

$$\nabla \times \mathbf{B} = \mu_0 \mathbf{J} \qquad (\textit{Ampére's Law}), \tag{86}$$

$$\nabla \cdot \mathbf{J} = 0, \tag{87}$$

$$\nabla \cdot \mathbf{B} = 0, \tag{88}$$

where the subscript "r" has been dropped from the electric field. Eq. 87 is an expression of charge conservation, and Eq. 88, which has many important consequences for numerical methods of MHD, states that the magnetic field must remain solenoidal in time. In MHD, the dynamics of the electromagnetic field are entirely controlled by the magnetic field, and the electric field and the current density assume secondary roles. In order to show this, it is necessary to relate the electric field and the current density. This is achieved through Ohm's law, which can be derived by rewriting the electron momentum equation, Eq. 46 with $\alpha = e$, in terms of the single fluid variables [64, 74],

$$\mathbf{E} + \mathbf{u} \times \mathbf{B} = \frac{1}{en} \left(\mathbf{J} \times \mathbf{B} - \nabla p_e - \nabla \cdot \pi_e + \mathbf{M}_e \right) \tag{89}$$

From transport theory [64, 74], the previous result

$$\mathbf{M}_e = \eta e n \mathbf{J} \tag{90}$$

can be used to simplify Ohm's law by

$$\mathbf{E}' = \mathbf{E} + \mathbf{u} \times \mathbf{B} = \eta \mathbf{J} + \frac{\mathbf{J} \times \mathbf{B} - \nabla p_e}{en} \tag{91}$$

where the electron viscosity is neglected ($\pi_e \to 0$) and $\mathbf{E}'$ is the electric field in the frame of reference of the flow. The generalized Ohm's Law relates the electric field or current density to the velocity of the flow. This is more simply stated by

$$\mathbf{E}' = \overline{\overline{\eta}} \cdot \mathbf{J} \tag{92}$$

where $\overline{\overline{\eta}}$ is now a tensor and includes the terms $\mathbf{J} \times \mathbf{B}$ and ∇p_e, which represent the Hall effect and the electron diamagnetic drift, respectively. Both of these terms are of similar magnitude. Comparing these terms to the $\mathbf{u} \times \mathbf{B}$ results in the following [64, 74],

$$\frac{|\nabla p_e/en|}{|\mathbf{u} \times \mathbf{B}|} \approx \frac{R_i}{l_0} \tag{93}$$

where r_i is the ion gyro-radius. For $R_i/l_0 << 1$, these terms are negligible [64, 74]. As a result, in many applications, the magnetic resistivity is simply a scalar, and Ohm's law can be stated simply by

$$\mathbf{E} + \mathbf{u} \times \mathbf{B} = \eta \mathbf{J} \tag{94}$$

Combining this relationship, $\mathbf{E} = \eta\mathbf{J} - \mathbf{u} \times \mathbf{B}$ and Faraday's law results in the following,

$$\nabla \times (\eta \mathbf{J} - \mathbf{u} \times \mathbf{B}) = -\frac{\partial \mathbf{B}}{\partial t} \tag{95}$$

rearranging,

$$\frac{\partial \mathbf{B}}{\partial t} - \nabla \times (\mathbf{u} \times \mathbf{B}) + \nabla \times (\eta \mathbf{J}) = 0 \tag{96}$$

Ampere's law can then be used to remove the dependence on the current density. This gives the magnetic induction equation

$$\frac{\partial \mathbf{B}}{\partial t} - \nabla \times (\mathbf{u} \times \mathbf{B}) + \frac{1}{\mu_0} \nabla \times (\eta \nabla \times \mathbf{B}) = 0 \tag{97}$$

where the first term represents the time rate of change in the magnetic field by the electromotive force and the second term is the dissipation of the induced magnetic field by electric resistivity. This equation embodies the entirety of the electromagnetic dynamics in MHD, which illustrates the primary role of the magnetic field.

2.3 Magnetohydrodynamics

In the previous section, the key steps in the derivation of the governing equations of MHD from kinetic theory was given. The purpose of the derivation was to highlight the assumptions made in MHD theory. These assumptions are implicit within the

definition of a plasma as a quasi-neutral gas exhibiting collective behavior through long range electromagnetic forces. A plasma is quasi-neutral as long as the length scales of interest are larger the Debye length. This criteria requires that the electron plasma frequency is smaller than characteristic frequencies of the plasma. Physically, this means that the electrons respond instantaneously to any perturbations in the charge imbalance, and therefore the electron inertia can be neglected in comparison the momentum of the ions. Lastly, the result demonstrates that the conservation equations for mass, momentum, and energy in MHD can be derived through the addition of two source terms in the momentum and energy balance, the Lorentz force and the power dissipation. Most importantly, the dynamics of the electromagnetic field is reduced to a single equation for the time rate of change of the magnetic field. The following derivation begins with these assumptions and continues to develop the governing equations for a multi-species, compressible gas in thermodynamic equilibrium. Herein, tensor notation is adopted instead of the vector notation used in previous sections.

2.3.1 Conservation Equations

As shown in the previous section, the typical fluid dynamic conservation equations of mass, momentum, and energy of hydrodynamics are equally valid for plasma. For MHD, it is only necessary to the include the additional electromagnetic momentum and energy terms into the conservation balance equations and add an additional equation of the evolution of the magnetic field, whose dynamics are determined by the pre-Maxwell equations. In the following derivation, these terms are added as source terms, which are then manipulated to arrive at the conservative form of the MHD equations. The resulting set of equations still embody the assumptions highlighted in the previous section, but are derived in a more intuitive rather than formal manner. To begin, the governing equations for the mass, momentum, energy, and species

conservation of a *fluid* can be stated in the following way

$$\frac{\partial \rho}{\partial t} + \frac{\partial}{\partial x_j}\Big(\rho u_j\Big) = 0, \tag{98}$$

$$\frac{\partial \rho u_i}{\partial t} + \frac{\partial}{\partial x_j}\Big(\rho u_i u_j + p\delta_{ij} - \tau_{ij}\Big) = F_i^{\mathrm{MHD}}, \tag{99}$$

$$\frac{\partial \rho E}{\partial t} + \frac{\partial}{\partial x_i}\Big[\left(\rho E + p\right) u_i + q_i - u_j \tau_{ij}\Big] = P^{\mathrm{MHD}} + W^{\mathrm{MHD}}, \tag{100}$$

$$\frac{\partial \rho Y_k}{\partial t} + \frac{\partial}{\partial x_i}\Big[\rho Y_k \left(u_i + V_{i,k}\right)\Big] = \dot{\omega}_k \qquad \text{where} \quad k = 1, ..., N_s. \tag{101}$$

In the above equations, u_i is the velocity vector, E is the total specify energy, and Y_k is the k^{th} species mass fraction of a total N_s species. Often it is convenient to define a partial density as $\rho_k = \rho Y_k$, which makes apparent that the sum of partial densities must equal to the gas density. Hence, Eqs. 98 and 101 overdetermine the system. Either the conservation of mass, Eq. 98, is neglected in lieu of Eq. 101, or the partial densities, ρ_k, must be normalized to ensure that they sum to ρ, or identically, the species mass fractions are required to sum to one. The additional variables require further definition; the thermodynamic pressure p is computed from the equation of state defined in Sec. 2.4, the species reaction rate $\dot{\omega}_k$ is computed from a kinetic mechanism, and the shear-stress tensor τ_{ij}, the heat transfer rate q_i, and the k^{th} species diffusion flux $V_{i,k}$ are each computed from their respective transport models, which are discussed in the Sec 2.6.

From the previous section, the MHD source terms in the momentum and energy conservation equations are known to be the Lorentz force $F_i^{\mathrm{MHD}} = \epsilon_{ijk} J_j B_k$, the power disposition $P^{\mathrm{MHD}} = J_i E_i$, and the Lorentz work term $F_i^{\mathrm{MHD}} u_i$. These terms link the hydrodynamic governing equations to evolution equations for the magnetic field vector B_i, the electric field E_i, and the current density J_i. The resulting set of $10 + N_s$ independent governing equations define a set of 4 vector quantities, u_i, B_i, J_i, and E_i, and $N_s + 1$ scalar quantities, E, ρ, and Y_k. If $N_s = 1$, then there are 11 independent governing equations for 14 primitive variables. Using Ohm's law, which is discussed in the previous section, it is possible to relate J_i, and E_i through

the definition of the electrical conductivity resulting in a single expression for the magnetic field

$$\frac{\partial B_i}{\partial t} + \frac{\partial}{\partial x_j}\Big(u_j B_i - B_j u_i - \eta \frac{\partial B_i}{\partial x_j}\Big) = 0, \tag{102}$$

Thus, the system of governing equation reduces to 11 independent primitive variables determined by 11 equations. Equations 98 - 102, however, are in a non-conservative form. To write the MHD governing equations in conservative form, the Lorentz force and the electromagnetic power dissipation expressions are manipulated using some vector identities and a some algebra. As a result, the Lorentz force can be written as a stress tensor $\mathcal{M}_{ij}$, which in many ways is analogous to the kinematic stress tensor, τ_{ij} in Eq. 99. The Maxwell stress tensor is defined as

$$\frac{\partial \mathcal{M}_{ij}}{\partial x_j} = \epsilon_{ijk} J_j B_k = \frac{\partial}{\partial x_j}\left(\frac{B_i B_j}{\mu_0} - \frac{B_k B_k}{2\mu_0}\delta_{ij}\right), \tag{103}$$

where the first term is similar to a viscous stress and acts as tensile force along the magnetic field lines. The second term is defined as the magnetic pressure, $p_m = |B|^2/2\mu_0$, and since it is irrotational, it is similar to the thermodynamic pressure. Often plasmas are classified as low- or high-β plasmas where β is the ratio of thermodynamic to magnetic pressure, $\beta = p/p_m = 2\mu_0 p/|B|^2$.

There are two additional source terms in the total energy equation: a work term due to the Lorentz force, $\mathcal{M}_{ij}u_j$, and a source term resulting from the electrical power dissipation per unit volume. The later term is $J_i E_i$ and can be re-written using Faraday's law and Ampére's law in terms of B_i and E_i as

$$J_k E_k = -\left[\frac{\partial}{\partial t}\left(\frac{B_k B_k}{2\mu_0}\right) + \frac{\partial}{\partial x_k}\left(\frac{\epsilon_{kij} E'_i B_j}{\mu_0}\right)\right] \tag{104}$$

where $E'_i = E_i + \epsilon_{ijk} u_j B_k$. The first term is the rate of change of the magnetic energy density, and the second term is the Poynting flux. The Poynting flux can be re-written in terms of only the magnetic field using Ampére's law. The result is

$$\frac{\epsilon_{ijk} E'_j B_k}{\mu_0} = \frac{1}{\mu_0 \sigma}\epsilon_{ijk}\left(\epsilon_{jlm}\frac{\partial B_m}{\partial x_l}\right) B_k. \tag{105}$$

If the total energy density is redefined as the summation of the gas-dynamic energy density plus the magnetic field energy density ($E = e + u^2/2 + B^2/2\mu_0\rho$), then the total energy equation for MHD can be written in a conservative form as:

$$\frac{\partial \rho}{\partial t} + \frac{\partial}{\partial x_j}\Big(\rho u_j\Big) = 0, \tag{106}$$

$$\frac{\partial \rho u_i}{\partial t} + \frac{\partial}{\partial x_j}\Big(\rho u_i u_j + p\delta_{ij} - \tau_{ij} - \mathcal{M}_{ij}\Big) = 0, \tag{107}$$

$$\frac{\partial \rho E}{\partial t} + \frac{\partial}{\partial x_i}\Big[\,(\rho E + p)\,u_i + q_i - u_j\tau_{ij} - u_j\mathcal{M}_{ij} + \frac{1}{\mu_0\sigma}\epsilon_{ijk}\left(\epsilon_{jlm}\frac{\partial B_m}{\partial x_l}\right)B_k\Big] = 0, \tag{108}$$

$$\frac{\partial \rho Y_k}{\partial t} + \frac{\partial}{\partial x_i}\Big[\rho Y_k\,(u_i + V_{i,k})\Big] = \dot{\omega}_k \qquad \text{where} \quad k = 1, ..., N_s, \tag{109}$$

$$\frac{\partial B_i}{\partial t} + \frac{\partial}{\partial x_j}\Big(u_j B_i - B_j u_i - \eta\frac{\partial B_i}{\partial x_j}\Big) = 0, \tag{110}$$

$$\frac{\partial B_i}{\partial x_i} = 0. \tag{111}$$

In MHD, the perfect gas equation of state is still applicable, and the fluid can still be assumed to be Newtonian. This assumption is valid as long as the dipole moments of the fluid particles can be assumed negligible. Fourier's law is likewise valid. A more general form of the governing equations for an electrically conducting fluid could be obtained by not relating J_i and E_i through Ohm's law, which is valid only under the assumption that the two fields are linearly related by the electrical conductivity. Thus in a way, Ohm's law is akin to the Fourier's law or Newton's law of viscosity. More importantly, it should be remembered that the assumptions of Ohm's law are implicit in the derivation of the magnetic induction equation. All that remains for the closure of the MHD equations is a suitable definition of the electrical conductivity introduced by Ohm's law as well as the specification of the other transport properties and the definition of the equation of state.

2.3.2 Vector Form of the Governing Equations

The governing equations of MHD can be generally described as a system of time-dependent, non-linear, partial different equations (PDEs) of first order. In Cartesian geometry, such systems take the following structure

$$\frac{\partial}{\partial t}\mathbf{q}(\mathbf{x},t) + \frac{\partial}{\partial x}\Big[\mathbf{f}(\mathbf{q}(\mathbf{x},t)) + \mathbf{f}_v(\mathbf{q}(\mathbf{x},t))\Big] + \frac{\partial}{\partial y}\Big[\mathbf{g}(\mathbf{q}(\mathbf{x},t)) + \mathbf{g}_v(\mathbf{q}(\mathbf{x},t))\Big] + \frac{\partial}{\partial z}\Big[\mathbf{h}(\mathbf{q}(\mathbf{x},t)) + \mathbf{h}_v(\mathbf{q}(\mathbf{x},t))\Big] = \mathbf{s}(\mathbf{q}(\mathbf{x},t)) \tag{112}$$

where $\mathbf{x} = (x, y, z)^T \in \mathbb{R}^3$ detonates the coordinate direction in Cartesian space. The conservative variables can represented by the state vector

$$\mathbf{q}^T = [\rho, \rho u_x, \rho u_y, \rho u_z, \rho E, B_x, B_y, B_z] \tag{113}$$

A corresponding vector of primitive variables $\mathbf{w}$, which contains the variables of density, temperature, velocity, etc., can be computed from the conservative variables and through relations, such as the equation of state of the fluid. The inviscid fluxes $\mathbf{f}$, $\mathbf{g}$, $\mathbf{h}$ are given by

$$\mathbf{f} = \begin{bmatrix} \rho u_x \\ \rho u_x^2 + P^* - B_x^2 \\ \rho u_x u_y - B_x B_y \\ \rho u_x u_z - B_x B_z \\ (\rho E + P^*) u_x - B_x(\mathbf{B}\cdot\mathbf{u}) \\ 0 \\ u_x B_y - B_x u_y \\ u_x B_z - B_x u_z \end{bmatrix}, \quad \mathbf{g} = \begin{bmatrix} \rho u_y \\ \rho u_y u_x - B_y B_x \\ \rho u_y^2 + P^* - B_y^2 \\ \rho u_y u_z - B_y B_z \\ (\rho E + P^*) u_y - B_y(\mathbf{B}\cdot\mathbf{u}) \\ u_y B_x - B_y u_x \\ 0 \\ u_y B_z - B_y u_z \end{bmatrix},$$

and

$$\mathbf{h} = \begin{bmatrix} \rho u_z \\ \rho u_z u_x - B_z B_x \\ \rho u_z u_y - B_z B_y \\ \rho u_z^2 + P^* - B_z^2 \\ (\rho E + P^*) u_z - B_z(\mathbf{B} \cdot \mathbf{u}) \\ u_z B_x - B_z u_x \\ u_z B_y - B_z u_y \\ 0 \end{bmatrix},$$

and represent the inviscid, hyperbolic fluxes in the x-, y-, and z-directions, respectively. The velocity and magnetic field vectors are defined as $\mathbf{u} = (u_x, u_y, u_z)$ and $\mathbf{B} = (B_x, B_y, B_z)$, respectively. Additionally, P^* is the total pressure given by $P^* = p + B^2/2\mu_0$. The viscous fluxes $\mathbf{f}_v$, $\mathbf{g}_v$, $\mathbf{h}_v$ are given by

$$\mathbf{f}_v = \mathbf{f}_v^{HD} + \mathbf{f}_v^{MHD} = \begin{bmatrix} 0 \\ -\tau_{xx} \\ -\tau_{xy} \\ -\tau_{xz} \\ u_x\tau_{xx} + u_y\tau_{xy} + u_z\tau_{xz} - q_x \\ 0 \\ 0 \\ 0 \end{bmatrix} + \begin{bmatrix} 0 \\ 0 \\ 0 \\ 0 \\ \eta(B_y J_z - B_z J_y) \\ 0 \\ \eta J_z \\ -\eta J_y \end{bmatrix},$$

$$\mathbf{g}_v = \mathbf{g}_v^{HD} + \mathbf{g}_v^{MHD} = \begin{bmatrix} 0 \\ -\tau_{yx} \\ -\tau_{yy} \\ -\tau_{yz} \\ u_x\tau_{yx} + u_y\tau_{yy} + u_z\tau_{zz} - q_y \\ 0 \\ 0 \\ 0 \end{bmatrix} + \begin{bmatrix} 0 \\ 0 \\ 0 \\ 0 \\ \eta(B_zJ_x - B_xJ_z) \\ -\eta J_z \\ 0 \\ \eta J_x \end{bmatrix},$$

and

$$\mathbf{h}_v = \mathbf{h}_v^{\mathrm{HD}} + \mathbf{h}_v^{\mathrm{MHD}} = \begin{bmatrix} 0 \\ -\tau_{zx} \\ -\tau_{zy} \\ -\tau_{zz} \\ u_x\tau_{zx} + u_y\tau_{zy} + u_z\tau_{zz} - q_z \\ 0 \\ 0 \\ 0 \end{bmatrix} + \begin{bmatrix} 0 \\ 0 \\ 0 \\ 0 \\ \eta(B_xJ_y - B_yJ_x) \\ \eta J_y \\ -\eta J_x \\ 0 \end{bmatrix}.$$

2.4 Thermodynamic and Mixture Properties

Since the multi-component plasma mixture is assumed to be equilibrium, each of the k^{th} species in the mixture has the same temperature T and a corresponding scalar partial pressure, p_k. Furthermore, if each species is treated as an ideal gas, then the k^{th} species partial pressure is related to the partial density, ρ_k, and temperature T, by the ideal gas law

$$p_k = \rho_k \frac{\mathcal{R}}{W_k} T = \rho_k R_k T \tag{114}$$

where the R_k is the k^{th} species gas constant, which is related to $\mathcal{R}$, the universal gas constant, and W_k, the k^{th} species molecular weight. From Dalton's law of mixing,

the thermodynamic pressure is computed from the partial pressures by

$$p = \sum_{k=1}^{N_s} p_k \tag{115}$$

The equations of state of a mixture relates the thermodynamic pressure p to the gas density ρ and the gas temperature T. For the mixtures studied in this thesis, the perfect gas equation of state is valid, which is given by

$$p == \sum_{k=1}^{N_s} \rho_k R_k T = \mathcal{R} T \sum_{k=1}^{N_s} \frac{\rho_k}{W_k} = \rho \frac{\mathcal{R}}{W} T = \rho R T \tag{116}$$

where R is mixture-averaged gas constant. While the equation of state provides the relationship between the three thermodynamic state variables, it is still necessary to define the functional relationship between the internal energy and enthalpy of the gas mixture and the temperature and pressure. For a thermally perfect gas, it can be shown that the internal energy is a function of the temperature only, so that the $k-th$ species energy is

$$e_k = e_k^0 + \int_{T_0}^{T} C_{v,k}(T')dT', \tag{117}$$

where $C_{v,k}(T)$ is the specific heat at constant volume for the $k-th$ species and e_k^0 is the reference energy evaluated at a reference temperature T_0. Additionally, the $k-th$ species enthalpy h_k is defined as $h_k = e_k + p_k/\rho_k$, where enthalpy of species k is

$$h_k = h_k^0 + \int_{T_0}^{T} C_{p,k}(T')dT', \tag{118}$$

where $C_{p,k}(T)$ is the specific heat at constant pressure for the $k-th$ species and is related to $C_{v,k}(T)$ by the gas constant.

$$C_{p,k}(T) = C_{v,k}(T) + \frac{\mathcal{R}_u}{W_k} \tag{119}$$

The temperature dependent specific heats are often obtained from curve-fits of experimental measurements [132], but can also be calculated from partition functions [81], which is primarily only useful if the gas is not in thermodynamic equilibrium.

For the majority of the studies conducted in this thesis, the mixture is often assumed to be calorically perfect gas. In this model, the specific heats are independent of temperature. In such a gas, the ratio of specific heats γ for the species becomes the primary thermodynamic quantity and is defined as:

$$\gamma_k = \frac{C_{p,k}}{C_{v,k}} \tag{120}$$

The mixture averaged internal energy and enthalpy can using the weighted sum,

$$e = \sum_{k=1}^{N_s} e_k Y_k, \qquad h = \sum_{k=1}^{N_s} h_k Y_k \tag{121}$$

where Y_k is the k-th species mass fraction. The mixture averaged specific heats, C_p and C_v, can be computed similarly, and lastly the specific heat of the mixture is $\gamma = C_p/C_v$. The mass fraction is defined as the ratio of partial density to the density of the mixture,

$$Y_k \equiv \frac{\rho_i}{\rho} \tag{122}$$

Therefore, the sum of the mass fractions is one. Other similar quantities can also be defined, which are often used. The species molar concentrations per unit volume C_k, which are computed as,

$$C_k = \frac{\rho_k}{W_k} = \rho \frac{Y_k}{W_k} \tag{123}$$

The molar concentrations are often used to compute the chemical reaction rates. Additionally, the molar concentration is used to define the mole fraction, X_k as

$$X_k \equiv \frac{C_k}{\sum_{k=1} N_s C_k}. \tag{124}$$

As with the mass fractions, the mole fractions must also sum to one. The mole fractions and the mass fractions are related in the following manner,

$$X_k = Y_k \frac{W}{W_k} \tag{125}$$

2.5 Magnetohydrodynamic Waves

The system of MHD equations can be shown to have eight eigenvalues. For the moment, if the viscous and resistive fluxes $\mathbf{f}_v$, $\mathbf{g}_v$, and $\mathbf{h}_v$ are neglected, the system of equations can be simplified to a pure hyperbolic system of equation describing the ideal MHD equations, which is given by

$$\frac{\partial}{\partial t}\mathbf{q}(\mathbf{x},t) + \frac{\partial}{\partial x}\Big[\mathbf{f}(\mathbf{q}(\mathbf{x},t))\Big] + \frac{\partial}{\partial y}\Big[\mathbf{g}(\mathbf{q}(\mathbf{x},t))\Big] + \frac{\partial}{\partial z}\Big[\mathbf{h}(\mathbf{q}(\mathbf{x},t))\Big] = 0. \tag{126}$$

Without a loss of generality, consider the one-dimensional ideal MHD equation. Let $\mathbf{A} = \partial\mathbf{f}(\mathbf{q})/\partial\mathbf{q}$ be the Jacobian matrix of the flux function $\mathbf{f}(\mathbf{q})$. The system, given by Eq. 126, is consider hyperbolic if the matrix $\mathbf{A}(\mathbf{q})$ has M real eigenvalues $\lambda_1(\mathbf{q}) \leq \cdots \leq \lambda_M(\mathbf{q})$ and M linear independent right eigenvectors $\mathbf{r}_m(\mathbf{q})$ for $m = 1, \ldots, M$ defined by

$$\mathbf{A}(\mathbf{q})\mathbf{r}_m(\mathbf{q}) = \lambda_m(\mathbf{q})\mathbf{r}_m(\mathbf{q}). \tag{127}$$

For the hydrodynamic conservation equations, this condition is satisfied. Since many shock-capturing schemes rely on wave decomposition of the fluxes defined by Eq. 127, the property of hyperbolicity is extremely important. Unfortunately, the MHD conservation equations are not strictly hyperbolic since the eigenvalues become can become degenerate depending on the orientation and magnitude of the magnetic field. With the appropriate normalization, however, the eigenvectors can be defined. The dispersion relationship emits eight eigenvalues corresponding to two Alfvén waves, two fast magneto-acoustic waves, two slow magneto-acoustic waves, and one entropy wave:

$$\lambda_{2,6} = u \mp c_a, \quad \lambda_{1,7} = u \mp c_f, \quad \lambda = u \mp c_s, \quad \lambda_4 = u, \tag{128}$$

where

$$c_a = \frac{B_x}{\rho\mu_0}, \quad c_{f,s} = \left[\frac{1}{2}\left(a^2 + \widetilde{b}^2 \pm \sqrt{(c^2 + \widetilde{b}^2)^2 - 4c^2\widetilde{b}_x^2}\right)\right]^{\frac{1}{2}} \tag{129}$$

where a is the speed of sound of the mixture and $\widetilde{b}^2 = \widetilde{b}_x^2 + \widetilde{b}_y^2 + \widetilde{b}_z^2$ where $(\widetilde{b}_x, \widetilde{b}_y, \widetilde{b}_z) = (B_x, B_y, B_z)/\sqrt{\rho}$

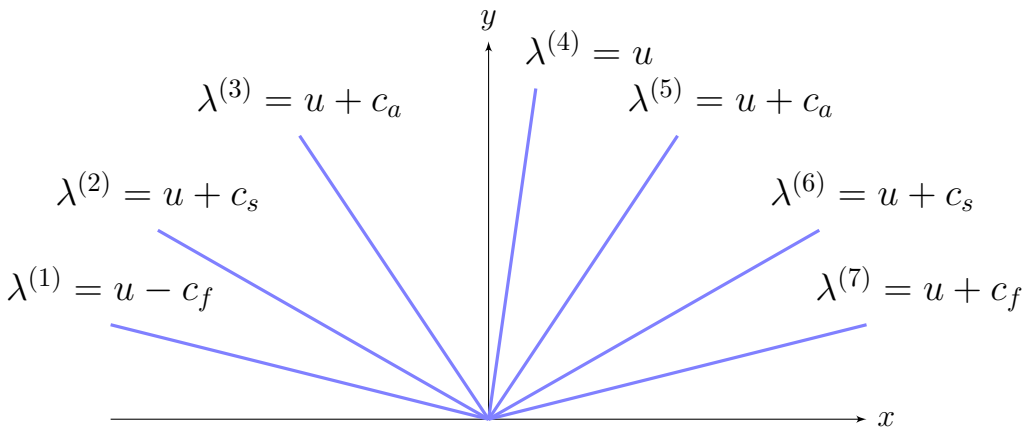

Figure 8: Schematic of the Riemann fan containing all the seven characteristics of the MHD hyperbolic system where $\lambda^{(1,7)} = u \mp c_f$,$\lambda^{(2,6)} = u \mp c_s$,$\lambda^{(3,5)} = u \mp c_a$, and $\lambda^{(4)} = u$

One of the eight eigenvalues corresponds with the divergent-free property of the magnetic field. Information is therefore only propagated along the remaining seven eigenvectors by three characteristic waves and an entropy wave [47]. Since $c_s \leq v_a \leq c_f$, degeneracy occurs when $c_s = c_f$, which happens in the limiting cases when the normal, n_i, is either parallel or perpendicular to the magnetic field, such that $B = B_n$ or $B_n = 0$. There are many references and introductory textbooks discussing the mathematical nature of the MHD equations. Relying heavily on the work of Friedrichs and Kranzer [65], a short summary is given here with emphasis on the differences between the MHD and hydrodynamic systems. More detailed information can be found in the above cited references.

Across fast or slow magnetosonic shocks, the direction and magnitude of the magnetic field is discontinuous. The tangential component of the magnetic field preserves its direction and increases its magnitude across a fast shock, while across a slow shock the tangential component retains or reverses its direction and decreases in magnitude. Also it should be noted that a discontinuity in the magnetic field necessarily creates "sheet currents" that form along the shock. The intermediate wave or Alfvén wave

is often referred to as a transverse wave since the magnetic field undergoes a rotation and the disturbances are tangential to the wave front and perpendicular to the magnetic field. The magnitude of the magnetic field remains unchanged and only the transverse components of the magnetic field and velocity change. Transverse shocks are also continuously connected with slow shocks. Contrary to hydrodynamic flows, the entropy wave or contact discontinuity does not permita discontinuity in the tangential components of velocity provided that $B_n \neq 0$. This has important consequences. A shear flow layer across which the tangential flow components vary cannot be maintained in a conducting flow. If such a disturbance exists at initial time, additional wave motions must develop to resolve it. The stabilization of the Richtmyer-Meshkov instability by a magnetic field is a direct consequence of this fact [179]. Furthermore, In a study of transition to turbulence in free-shear layers, the Orr-Sommerfield equations adapted for MHD were used in addition to DNS to show that a parallel magnetic field both enhanced and delayed transition depending upon the interaction parameter [212]. The study of laminar instability in a conducting fluid highlights the non-linear dynamics involved in MHD flows. These effects are a result of the additional characteristic modes available in a plasma.

2.6 Transport Models

If the fluid is assumed to be Newtonian such that the stresses are proportional to the local rate of strain, then the stress tensor can be mathematically defined by

$$\tau_{ij} = \mu \left(\frac{\partial u_i}{\partial x_j} + \frac{\partial u_j}{\partial x_i} \right) + \lambda \frac{\partial u_k}{\partial x_k} \delta_{ij} \tag{130}$$

where μ is the viscosity coefficient of the fluid mixture and is assumed to be a function of temperature only. The other coefficient, λ, is the bulk viscosity. From Stokes' hypothesis, the stress tensor is assumed to be traceless requiring the bulk viscosity

to be $\lambda = -2/3\,\mu$. With this assumptions, the stress terms are re-written as:

$$\tau_{ij} = 2\mu \left(S_{ij} - \frac{1}{3} S_{kk} \delta_{ij} \right) \tag{131}$$

where S_{ij} is the rate of strain tensor, given by:

$$S_{ij} = \frac{1}{2} \left(\frac{\partial u_i}{\partial x_j} + \frac{\partial u_j}{\partial x_i} \right) \tag{132}$$

There are many models for calculating the viscosity. For a single-species fluid, Sutherland's law for the viscosity is often sufficient and is given by

$$\mu = \mu_S \left(\frac{T}{T_S} \right)^{3/2} \frac{T_S + S}{T + S} \tag{133}$$

where μ_S, T_S, and S are reference values for Sutherland's model and are dependent on the species. The dependence is often given as a power-law function,

$$\mu = \mu_{T=T_0} \left(\frac{T}{T_0} \right)^n \tag{134}$$

where the exponent n depends on the gas mixture, but is usually near 0.7, and $\mu_{T=T_0}$ is the viscosity at the reference temperature T_0. If the fluid in consideration is a mixture, more advanced models are necessary, particularly if the gas mixture is ionized and consists of electrons, ions, and neutrals. These models are usually based upon the Chapman-Enskog approximations [81]. Wright and Palmer give a review of various methods for calculating the viscosity coefficient and their computational efficiency [148, 149]. In summary, the viscosity of a single species gas is given by

$$\mu_k = \frac{5}{8} \left(\frac{k_B T}{\Omega_{kk}^{(2,2)}} \right) \tag{135}$$

where $\Omega_{kk}^{(2,2)}$ is the viscosity collision integral, which has the general form,

$$\Omega_{ij}^{(l,s)}(T) = \sqrt{\frac{k_B T}{2\pi \mu_{ij}}} \int_0^\infty \exp\left(-\tau^2\right) \tau^{2s+3} Q^{(l)}(g) \mathrm{d}\tau \tag{136}$$

where $\mu_{ij} = m_i m_j / (m_i + m_j)$ is the reduced mass, $Q^{(l)}$ is the total interaction cross section computed by integrating the differential cross sections, and $\tau^2 = \mu_{ij} w^2 / 2 k_B T$,

where w^2 is the relative molecular velocity. The collision integral represents the average probability of a collision between two particles.The reduced collision integral is

$$\Omega_{ij}^{(l,s)*} = \Omega_{ij}^{(l,s)} / \left[\Omega_{ij}^{(l,s)}\right]_{\text{rigidsphere}}. \tag{137}$$

If σ_d^2 is the rigid sphere collision diameter, then

$$\Omega_{ij}^{(1,1)} \equiv \sigma_d^2 \sqrt{\frac{\pi k_B T}{2\mu_{ij}}} \left(\Omega_{ij}^{(1,1)*}\right) \tag{138}$$

$$\Omega_{ij}^{(2,2)} \equiv 2\sigma_d^2 \sqrt{\frac{\pi k_B T}{2\mu_{ij}}} \left(\Omega_{ij}^{(2,2)*}\right) \tag{139}$$

Using the reduced collision integrals, the viscosity is given by the simplified expression

$$\mu_k = 2.669 \times 10^5 \frac{\sqrt{W_k T}}{\sigma_d^2 \Omega_{kk}^{(2,2)*}} \tag{140}$$

Values for the reduced collision integrals have been tabulated in the literature [148, 149]. In a gas mixture, the species gas viscosities must be combined to produce an effective mixture-averaged viscosity. Wilke's mixing rule [218] is used here, which states

$$\mu = \sum_{k=1}^{N_s} \frac{X_k \mu_k}{\phi_k} \tag{141}$$

where

$$\phi_k = \frac{\sum_{i=1}^{N_s} \left[1 + \sqrt{\frac{n_i}{\mu_i}} \left(\frac{W_i}{W_k}\right)^{1/4}\right]^2}{\sqrt{8\left(1 + \frac{W_k}{W_i}\right)}} \tag{142}$$

While this mixing rule is the most commonly used since it is the most computationally efficient, it can be inaccurate for polar or ionized gases. In these situations, the mixing rules proposed by Gupta et al. have been shown to be more accurate [148], which is given by

$$\mu = \sum_{k=1}^{N_s} \left(\frac{X_k}{\sum_{i=1}^{N_s} \frac{X_i}{W_k} \Delta_{ki}^{(2)}} \right) \tag{143}$$

where,

$$\Delta_{ij}^{(2)} = \frac{16}{5} \sqrt{\frac{2\pi\mu_{ij}}{k_B T}} \sigma_d^2 \Omega_{ij}^{(2,2)*} \tag{144}$$

The heat flux vector has contributions from the thermal conduction and from the flux of sensible enthalpy due to species diffusion. Fourier's law is used to relate the thermal conduction to the local temperature gradient. The expression for the heat flux vector is

$$q_i = -\kappa \frac{\partial T}{\partial x_i} + \rho \sum_{1}^{N_s} Y_k h_k V_{i,k} \tag{145}$$

where the thermal conductivity κ, is also typically a function of the temperature only. For single species neutral fluid, the thermal conductivity is often calculated using the Prandtl number (Pr) to relate κ to μ. Since at low to moderate temperatures the Prandtl number can safely be assumed constant, κ is easily computed. These assumptions are more difficult to justify in flows with multiple species and in ionized gases. Just as with the viscosity, more advanced models for calculating the thermal conductivity exist. The heat conductivity consists of two parts, $k = k_{tr} + k_{int}$, a translational component and an internal component. Following Gupta et al. [81], the mixture averaged translational heat conductivity is given as

$$k_{tr} = \frac{15}{4} k_B \sum_{k=1}^{N_s} \left(\frac{X_k}{\sum_{i=1} N_s \alpha_{ki} X_k \Delta_{ki}^{(2)}} \right) \tag{146}$$

where

$$\alpha_{ij} = 1 + \frac{\left(1 - \frac{W_i}{W_j}\right)\left(0.45 - 2.54\frac{W_i}{W_j}\right)}{\left(1 + \frac{W_i}{W_j}\right)^2} \tag{147}$$

The expression for the internal component of the heat conductivity coefficient is

$$k_{int} = \sum_{k=1}^{N_s} \left(\frac{X_k C_{p,k}^{int}}{\sum_{i=1} N_s X_k \Delta_{ki}^{(1)}} \right) \tag{148}$$

where $C_{p,k}^{int}$ is the contribution to specific heat at constant pressure of all non-translational degrees of freedom, which can be computed by subtracting the constant translation component of the specific heat from the value of $C_{p,k}$ computed as a function of temperature.

The species diffusion velocities $V_{i,k}$ are modeled using a Fickian diffusion approximation, such that

$$V_{i,k} = -\frac{D_k}{Y_k}\frac{W_k}{W}\frac{\partial X_k}{\partial x_i} \tag{149}$$

where D_k is the k-th species diffusion coefficient. In a simple approximation, the species diffusion coefficients can be obtained by assuming a constant Lewis number,

$$Le = \frac{\kappa}{\rho C_p D_k} \tag{150}$$

Depending on the composition of the gas, the assumption of constant Le may not be realistic. For more complex gas mixture, the diffusion coefficients are computed to a first order approximation as averages of the binary diffusion coefficient D_{ij}, which is typically computed from a curve-fitted approximation. An effective diffusion coefficient can be computed using the averaging procedure

$$D_k = \frac{1 - X_k}{\sum_{k \neq i} X_i / D_{ki}} \tag{151}$$

There are several models available to compute the electrical conductivity of an ionized gas. Most simplistically, Lin [123] proposed that the electrical conductivity is given by $\sigma^{-1} = \sigma_{en}^{-1} + \sigma_{ei}^{-1}$, where σ_{en} is the electrical conductivity due to the electron-neutral collisions and σ_{ei} is due to the electron-ion collisions. The Saha equation can be used to determine the electron number density which then can be used to determine σ_{en} and theoretical equations exist for σ_{ei}. Other models are reviewed elsewhere [129].

In this work, a more detailed mixture-averaged electrical conductivity is computed from first-order approximations to the Champan-Enskog equations. Such calculations rely on the computation of the modified collision integral, $\Delta_{jk}^{(1)}$, between species j and species k. The electrical conductivity is then computed as:

$$\sigma = \frac{e^2}{kT}\frac{n_e}{\sum_{k \neq e} n_k \Delta_{ek}^{(1)}} \tag{152}$$

where e is the electrical charge, k is Boltzmann's constant and $\Delta_{jk}^{(1)}$ is given by:

$$\Delta_{jk}^{(1)} = \frac{8}{3}\left[\frac{2W_j W_k}{\pi \hat{R} T (W_j + W_k)}\right]^{1/2} \pi \Omega_{jk}^{(1,1)} \tag{153}$$

where $\pi\Omega_{jk}^{(1,1)}$ is the collision integral of the momentum transfer between species j and species k. The number density is defined by $n_k = \rho Y_k \hat{N}/W_k$, where $\hat{N}$ is Avogadro's number and W_k is the k^{th}-species molecular weight. Values of the collision integral between electrons and neutrals are determined either from experimental or theoretical data [220, 221]. For electron-ion collisions, theoretical expressions are used [191].

2.7 Alternate Forms of the MHD Equations

2.7.1 Non-dimensional numbers

In MHD, if the effects of temperature, chemistry and species diffusion are ignored so that the only important physics is contained within the Navier-Stokes and induction equations, the only physical properties appearing are the density, ρ, the kinematic viscosity, ν, the electrical conductivity, σ, and the magnetic permeability, μ_0. These dimensional parameters involve four fundamental units (m, kg, s, A), though they are not dimensionally independent since $(1/\mu_0\sigma)$ has the same dimension as ν. For any possible combination of length and time scales are chosen, four non-dimensional numbers can be derived.

The ratio of the kinematic and magnetic diffusivities is referred to as the magnetic Prandtl number:

$$Pr_m = \mu_0 \sigma \nu \tag{154}$$

In fundamental studies of MHD turbulence, the magnetic Prandtl number is often assumed to be unity. There are several instances where this is a poor assumption. In experimental studies of the turbulent dynamo, liquid metals are often used because of their high conductivities, however, Pr_m for these liquids are extremely small. The magnetic Prandtl number is related to two other non-dimensional parameters, the Reynolds number and the magnetic Reynolds, which are given as:

$$Re = \frac{u_0 l_0}{\nu} \tag{155}$$

$$Re_m = \mu_0 \sigma u_0 l_0 = Re Pr_m \tag{156}$$

Thus, the assumption of $Pr_m = 1$ is equivalent to assuming $Re = Re_m$. The significance of the magnetic Reynolds number as a non-dimensional measure of conductivity has already been discussed. Another non-dimensional parameter (often confused with the magnetic Reynolds number in literature) is the Lundquist number:

$$S = \sqrt{\frac{\mu_0}{\rho}}\sigma BL = \mu_0 \sigma v_a l_0 \tag{157}$$

where $v_a = B/\sqrt{\mu_0 \rho}$ is the Alfvén velocity. Thus, the Lundquist number is essentially a magnetic Reynolds number based on the Alfvén velocity. This expression is used often in research on magnetic confinement of plasma. Lastly, the interaction parameter, N, is important in MHD turbulence of low magnetic Reynolds number.

$$N = \frac{\sigma B_0^2 l_0}{\rho u_0} \tag{158}$$

Neglecting the energy equation and only considering the incompressible Navier-Stokes and magnetic induction equations, a non-dimensional set of equations can be derived based on the three dimensionless parameters, Pr_m, Re_m, and S. Using the following scales [49],

$$\begin{aligned} \hat{x}_i &\longleftrightarrow \frac{x_i}{l_0}, \qquad & \hat{u}_i &\longleftrightarrow \frac{u_i}{u_0}, \\ \hat{t} &\longleftrightarrow \frac{t u_0}{l_0}, \qquad & \hat{p} &\longleftrightarrow \frac{p}{\rho u_0^2}, \\ \hat{B}_i &\longleftrightarrow \frac{B_i}{B_0}, \qquad & \hat{J}_i &\longleftrightarrow \frac{\mu_0 l_0 J_i}{B_0}, \end{aligned} \tag{159}$$

the dimensionless governing equations are

$$\frac{\partial \hat{u}_i}{\partial \hat{t}} + \frac{\partial}{\partial \hat{x}_j}\Big(\hat{\rho}\hat{u}_i\hat{u}_j + \hat{p}\delta_{ij}\Big) = \frac{S^2}{Re_m^2}\frac{\partial \hat{\mathcal{M}}_{ij}}{\partial \hat{x}_j} + \frac{Pr_m}{Re_m}\frac{\partial \hat{\tau}_{ij}}{\partial \hat{x}_j}, \tag{160}$$

$$\frac{\partial \hat{B}_i}{\partial \hat{t}} = \frac{\partial}{\partial \hat{x}_j}\Big(\hat{u}_j\hat{B}_i - \hat{B}_j\hat{u}_i\Big) + \frac{1}{Re_m}\frac{\partial^2 \hat{B}_i}{\partial \hat{x}_j^2}. \tag{161}$$

As a side note, the magnetic field is often expressed in Alfvén units, where the magnetic field is modified, $(B_k' = B_k/\sqrt{\rho\mu_0})$, to have the same units as the velocity. The Elassässer variables, $z_i = u_i \mp B_i'$ can then be used to simplify the incompressible MHD equations. Such simplifications are not possible in compressible flows.

2.7.2 MHD Approximations

When the magnetic Reynolds number, Re_m, is much less than unity, several simplifications to the MHD equations can be made. The benefit is that the resulting set of equations are much easier to solve and computationally cheaper. These simplifications can also help facilitate fundamental understanding of MHD dynamics.

At $Re_m << 1$, the velocity field has no large influence on the magnetic field. If we assume that a steady magnetic field, $B_{ex,i}$, is applied by some external means, the magnetic field can be decomposed into two parts: the imposed field and an induced field, B_i'. The applied magnetic field, $B_{ex,i}$, is curl-free since the current responsible for this field lies outside the domain of interest, and the magnetic field B_i' is guaranteed to be small since the diffusion term dominates obviously dominates in Eq. 160 when $Re_m << 1$. If the substitution, $B_i = B_{ex,i} + B_i'$, is made in Eqs. 107 and 110, the following equations non-dimensional can then be derived,

$$\frac{\partial u_i}{\partial t} + \frac{\partial}{\partial x_j}\Big(\rho u_i u_j + p\delta_{ij}\Big) = \frac{S^2}{Re_m^2}\epsilon_{ijk}J_j' B_{ex,k} + \frac{Pr_m}{Re_m}\frac{\partial \tau_{ij}}{\partial x_j} \tag{162}$$

$$\frac{\partial B_i'}{\partial t} = \frac{\partial}{\partial x_j}\Big(u_j B_{ex,i} - B_{ex,j}u_i\Big) + \frac{1}{Re_m}\frac{\partial^2 B_i'}{\partial x_j^2} \tag{163}$$

where the second order terms were assumed negligible, and the notation, $\hat{\star}$ was dropped for convenience.This set of equations is referred to as the quasi-linear form of the MHD equations since the induction equation is linear, and the only remaining non-linear term is the inertial term in the Navier-Stokes equation. The current density J_i', is used to represent the current density to make obvious that the only current arising in the flow is entirely a result of B_i' not $B_{ex,i}$.

A more obvious form of the non-dimensional governing equations can be derived if only two dimensionless parameters (and two scales, B and L) are used. Since Re_m is small and isn't expected to play a dominant role, Pr_m and S, become the most

important. This set of dimensionless equations is given as

$$\begin{aligned}
\frac{\partial u_i}{\partial t} + \frac{\partial}{\partial x_j}\Big(\rho u_i u_j + p\delta_{ij}\Big) &= S^2 \epsilon_{ijk} J'_j B_{ex,k} + Pr_m \frac{\partial \tau_{ij}}{\partial x_j} \\
\frac{\partial B'_i}{\partial t} &= \frac{\partial}{\partial x_j}\Big(u_j B_{ex,i} - B_{ex,j} u_i\Big) + \frac{\partial^2 B'_i}{\partial x_j^2}
\end{aligned} \tag{164}$$

where the role of the Lundquist number, S, is more obvious. If it is larger than unity and larger than Pr_m, then Alfvén waves will develop. In the opposite scenario, where S is less than unity or less than Pr_m, Alfvén waves are suppressed by Ohmic or viscous dissipation. In the case that no Alfvén waves develop, $S < 1$ or $S < Pr_m$, the magnetic induction equation can be assumed steady and the time-dependent term can be dropped. Thus, the induction equation simplifies to a version of Ohm's law and the electric field can be represented as the gradient of the electric potential, ϕ_i. Still in dimensionless form, the final equations reads:

$$\begin{aligned}
\frac{\partial u_i}{\partial t} + \frac{\partial}{\partial x_j}\Big(\rho u_i u_j + p\delta_{ij}\Big) &= S^2 \epsilon_{ijk} J'_j B_{ex,k} + Pr_m \frac{\partial \tau_{ij}}{\partial x_j} \\
J'_i &= -\frac{\partial \phi_i}{\partial x_i} + \epsilon_{ijk} u_j B_{ex,k}
\end{aligned} \tag{165}$$

This set of equations is referred to as the quasi-static MHD equations, since the electromagnetic equations are no time-independent. In summary, at low magnetic Reynolds number, the Lundquist number, S, and the magnetic Prandtl number, Pr_m, are the most important. The Lundquist number, being a "Reynolds" number based on the Alfvén velocity, is representative of the ability of Alfvén waves to interact with the non-linear inertial terms.

CHAPTER III

NUMERICAL METHODS AND MODELS

3.1 Numerical Methods for Conservation Laws

In the previous chapter, the governing equations of MHD were introduced. In their ideal form, the MHD equations, just like the Euler equations, can be written as a system of hyperbolic conservation equations. Thus, given proper initial conditions and well-defined boundary conditions, the equations admit unique solutions provided they satisfy the admissibility condition of entropy inequality [72, 120]. For the purposes of discussion and without any loss of generalization, consider a two-dimensional Cartesian space defined by $\mathbf{x} = (x, y)^T$, and let $\mathbf{x}$ be represented by a computational domain discretized with a rectangular grid of $N_x \times N_y$ points separated uniformly by the widths Δx and Δy in each coordinate direction. The discrete computational points are then defined by the coordinates

$$(x_i, y_i) := (i\Delta x, j\Delta y), \quad i, j \in \mathbb{D}, \tag{166}$$

where $\mathbb{D}$ represents the integer values $i = 0, 1, \ldots, N_x - 1$ and $j = 0, 1, \ldots, N_y - 1$ in the computational domain. Additionally, it is useful to define

$$x_{i+1/2} := x_i + \frac{\Delta x}{2}, \ i \in \mathbb{D} \ \text{ and } \ y_{j+1/2} := j_i + \frac{\Delta y}{2}, \ j \in \mathbb{D}. \tag{167}$$

Furthermore, let $t_n := n\Delta t$, with $n = 1, 2, \ldots, N_t$ and time step Δt. The values at each discrete space-time point (x_i, y_j, t_n) denoted by $\mathbf{Q}^n_{i,j}$ define the piece-wise constant state vector $\mathbf{Q}(\mathbf{x}, t)$, which is an approximation of the exact solution $\mathbf{q}(\mathbf{x}, t)$. Using a suitable numerical method, initial data at $\mathbf{Q}(\mathbf{x}, t_0)$ can be integrated in time to find approximate solutions at the next time step, $\mathbf{Q}(\mathbf{x}, t + \Delta t)$. Mathematically,

these numerical methods can be analyzed with regards to their consistency, stability, convergence, and order of accuracy [72, 92, 120, 201].

The hyperbolic system of equations for MHD in two-dimensions is given as

$$\frac{\partial}{\partial t}\mathbf{q}(\mathbf{x},t) + \frac{\partial}{\partial x}\mathbf{f}(\mathbf{x},t) + \frac{\partial}{\partial x}\mathbf{g}(\mathbf{x},t) = 0, \tag{168}$$

where $\mathbf{f}$ and $\mathbf{g}$ are the exact conservative fluxes in the x- and y-directions. The viscous and resistive terms as well as the source term have been neglected for moment so that the system is purely conservative. Let the operator $\mathcal{L}$ represent the numerical approximation to system of partial differential equations (PDEs) [82], such that

$$\frac{d\mathbf{Q}(t)}{dt} = \mathcal{L}\left(\mathbf{Q}(\mathbf{x},t)\right) \tag{169}$$

In the next two sections, two different discretization operators are discussed, a finite difference method and a finite volume method. Both methods result in a numerical approximation in the conservative form. Therefore, they satisfy the discrete conservation property

$$\sum_{i,j\in\mathbb{D}} \mathbf{Q}_{i,j}^{n+1} = \sum_{i,j\in\mathbb{D}} \mathbf{Q}_{i,j}^{n}. \tag{170}$$

3.1.1 Finite Difference Methods

Finite difference methods provide a numerical solution to the differential form of the conservation equations by approximating the spatial operators in the governing equations using finite differences based on the discrete expansion of a truncated Taylor series about a point [92, 121]. If the hyperbolic system is integrated in time using a first order Euler forward stepping method [92], the numerical approximation of the conservative variables at time t_{n+1} is

$$\mathbf{Q}^{n+1}(\mathbf{x}) = \mathbf{Q}^{n}(\mathbf{x}) + \Delta t\mathcal{L}\left(\mathbf{Q}(\mathbf{x},t_n)\right), \tag{171}$$

If the spatial operator $\mathcal{L}$ represents some r-th order the central difference formula, a finite-difference approximation to the MHD hyperbolic equations is represented as

$$\mathbf{Q}_{i,j}^{n+1} = \mathbf{Q}_{i,j}^{n} - \frac{\Delta t}{\Delta x}\Big(\mathbf{F}_{i+1/2,j}\big(\mathbf{Q}(t_n)\big) - \mathbf{F}_{i-1/2,j}\big(\mathbf{Q}(t_n)\big)\Big) - \frac{\Delta t}{\Delta y}\Big(\mathbf{G}_{i,j+1/2}\big(\mathbf{Q}(t_n)\big) - \mathbf{G}_{i,j-1/2}\big(\mathbf{Q}(t_n)\big)\Big). \tag{172}$$

where $\mathbf{F}_{i\pm1/2,j}$ and $\mathbf{G}_{i,j\pm1/2}$ are defined as the *numerical fluxes* evaluated at time t_n [120]. The spatial accuracy of the scheme is determined by the method in which the numerical fluxes are computed. A family of explicit or tridiagonal compact schemes up to sixth-order can be expressed by the following system

$$\begin{aligned}\alpha_c\mathbf{F}_{i-1/2,j}^{n} + \mathbf{F}_{i+1/2,j}^{n} + \alpha_c\mathbf{F}_{i+3/2,j}^{n} = \; & a_c\Big(\mathbf{F}\big(\mathbf{Q}_{i-2,j}(t_n)\big) + \mathbf{F}\big(\mathbf{Q}_{i+3,j}(t_n)\big)\Big) + \\ & b_c\Big(\mathbf{F}\big(\mathbf{Q}_{i-1,j}(t_n)\big) + \mathbf{F}\big(\mathbf{Q}_{i+2,j}(t_n)\big)\Big) + \\ & c_c\Big(\mathbf{F}\big(\mathbf{Q}_{i,j}(t_n)\big) + \mathbf{F}\big(\mathbf{Q}_{i+1,j}(t_n)\big)\Big)\end{aligned} \tag{173}$$

where the values of the coefficients α_c, a_c, b_c, and c_c are given in Table 1, and the notation $\mathbf{F}_{i\pm1/2,j}^{n}$ is used to signify that the fluxes are evaluated at time t_n and at the cell-face in the i-direction. Similar expressions are used to determine the numerical fluxes in the other directions. For $\alpha_c = 0$, the numerical scheme is explicit, and for non-zero values of α_c, the numerical flux is dependent on the neighboring points, requiring an implicit computation of the tridiagonal system. For a numerical scheme with rth order of accuracy, the numerical stencil is defined by the required fluxes $\mathbf{F}(\mathbf{Q}_{i-r/2-1,j}^{n}, \ldots, \mathbf{Q}_{i+r/2,j}^{n})$. At inflow and outflow boundaries, the numerical stencil must be reduced by using left- and right-sided differences instead of central differences. For example, the right-sided difference

$$\begin{aligned}\mathbf{F}_{i+1/2,j}^{n} + \alpha_+\mathbf{F}_{i+3/2,j}^{n} = \; & a_+\mathbf{F}\big(\mathbf{Q}_{i,j}(t_n)\big) + b_+\mathbf{F}\big(\mathbf{Q}_{i+1,j}(t_n)\big) \\ & + c_+\mathbf{F}\big(\mathbf{Q}_{i+2,j}(t_n)\big) + d_+\mathbf{F}\big(\mathbf{Q}_{i+3,j}(t_n)\big)\end{aligned} \tag{174}$$

Since the discretization is built from finite differences, the application of high-order numerical methods is relatively easy as demonstrated. Difficulties arise when

Table 1: List of coefficients for compact and explicit central finite-difference methods.

Scheme	Central Difference				One-Sided Difference				
	α_c	a_c	b_c	c_c	$\alpha_\pm$	$a_\pm$	$b_\pm$	$c_\pm$	$d_\pm$
Explicit $\mathcal{O}(2)$	0	0	0	1/2	0	1/2	1/2	0	0
Explicit $\mathcal{O}(4)$	0	0	−1/12	7/12	0	1/4	13/12	−5/12	1/12
Explicit $\mathcal{O}(6)$	0	1/60	−2/15	37/60	–	–	–	–	–
Compact $\mathcal{O}(4)$	1/4	0	0	3/4	1	1/6	10/6	1/6	0
Compact $\mathcal{O}(6)$	1/3	0	1/36	29/36	–	–	–	–	–

$\mathbf{Q}(\mathbf{x}, t)$ is not piece-wise differentiable within the computational domain. To avoid numerical oscillations, an upwind method is required to compute the numerical fluxes in regions of the flow containing large gradients [201]. These methods are discussed in more detail in a later section.

Since Eq. 172 is a only a first order time accurate approximation, a high order time integration scheme is necessary in order to preserve the overall order of accuracy of the scheme. The time integration should be stable and total variation diminishing (TVD), meaning

$$TV(\mathbf{Q}) = \sum_i \left|\mathbf{Q}_{i+1} - \mathbf{Q}_i\right| \tag{175}$$

where the definition is provided for a single dimension, but can be extended by computing the sum of TV in each computational direction. A TVD scheme has the following property,

$$TV(\mathbf{Q}^{n+1}) \leq TV(\mathbf{Q}^n). \tag{176}$$

In general, a high order TVD and strong stability preserving (SSP) Runge-Kutta time

integration scheme can be written in the general form [78, 172, 188]

$$\begin{aligned}
\mathbf{Q}^{(0)} &= \mathbf{Q}^n \\
\mathbf{Q}^{(i)} &= \sum_{k=0}^{i-1} \left(\alpha_{ik}\mathbf{Q}^{(k)} + \Delta t \beta_{ik} \mathcal{L}\left(\mathbf{Q}^{(k)}\right)\right) \qquad i = 1, \ldots, m \\
\mathbf{Q}^{n+1} &= \mathbf{Q}^m
\end{aligned} \tag{177}$$

where the coefficients $\alpha_{i,k}$ and $\beta_{i,k}$ are non-negative and the maximum Courant-Friedrichs-Lewy (CFL) [188] is defined as

$$CFL = \max_{i,k} \frac{\alpha_{i,k}}{\beta_{i,k}} \tag{178}$$

For a two-stage, second-order SSP Runge-Kutta scheme, $\alpha_{1,1} = 1$, $\alpha_{i,2} = 1/2$, $\beta_{1,1} = 1$, and $\beta_{2,2} = 1/2$. For a three-stage, third-order SSP Runge-Kutta scheme, $\alpha_{1,1} = 1$, $\alpha_{1,2} = 3/4$, $\alpha_{1,3} = 1/3$, $\alpha_{2,2} = 1/4$, $\alpha_{3,3} = 2/3$, $\beta_{1,1} = 1$, $\beta_{2,2} = 1/4$, and $\beta_{2,2} = 2/3$. Unless specified, all other values are zero. See references for more specific information [78, 172].

3.1.2 Finite Volume Methods

In a finite-volume representation, discretization is applied to the integral form of the governing equations instead of the differential form. For a control volume $\mathcal{V}$, the differential form of the hyperbolic conservation equations, given by Eq. 168, is integrated

$$\int_{\mathcal{V}} \frac{\partial \mathbf{q}(\mathbf{x}, t)}{\partial t} \mathrm{d}\mathbf{x} + \int_{\mathcal{V}} \left(\frac{\partial \mathbf{f}(\mathbf{x}, t)}{\partial x} + \frac{\partial \mathbf{g}(\mathbf{x}, t)}{\partial y} \right) \mathrm{d}\mathbf{x} = 0, \tag{179}$$

and then using Gauss' theorem, the final integral form of the conservation laws is obtained,

$$\frac{\partial}{\partial t} \int_{\mathcal{V}} \mathbf{q}(\mathbf{x}, t) \mathrm{d}\mathbf{x} + \int_{\mathcal{S}} \left(\mathbf{f}(\mathbf{x}, t) \cdot \mathbf{n}_x + \mathbf{g}(\mathbf{x}, t) \cdot \mathbf{n}_y \right) \mathrm{d}\mathcal{S} = 0, \tag{180}$$

where $\mathbf{n}_x$ and $\mathbf{n}_y$ are the unit normal outward vectors for the control surface $\mathcal{S}$. Additionally, the conservation equations are integrated in time over the discrete interval

$[t_n, t_{n+1}]$,

$$\int_{\mathcal{V}} \mathbf{q}(\mathbf{x}, t_{n+1})\mathrm{d}\mathbf{x} - \int_{\mathcal{V}} \mathbf{q}(\mathbf{x}, t_n)\mathrm{d}\mathbf{x} + \int_{t_n}^{t_{n+1}} \int_{\mathcal{S}} \Big(\mathbf{f}(\mathbf{x}, t) \cdot \mathbf{n}_x + \mathbf{g}(\mathbf{x}, t) \cdot \mathbf{n}_y \Big) \mathrm{d}\mathcal{S}\mathrm{d}t = 0 \tag{181}$$

For a Cartesian domain, the control volume $\mathcal{V}_{i,j}$ is defined as the rectangular region around each computational point $\mathbf{x}_{i,j} = (x_i, y_j)^T$ such that its domain is

$$\mathcal{V}_{i,j} = \big[x_{i-1/2,j}, x_{i+1/2,j}\big] \times \big[y_{i,j-1/2}, y_{i,j+1/2}\big] \tag{182}$$

where Δx and Δy for each computational cell are defined as $x_{i+1/2,j} - x_{i-1/2,j}$ and $y_{i,j+1/2} - y_{i,j-1/2}$, respectively. Within each computational cell, $\mathbf{Q}_{i,j}(t)$ is then defined as the numerical approximation to the cell-averaged value at time t,

$$\mathbf{Q}_{i,j}(t) \approx \frac{1}{\mathcal{V}_{i,j}} \int_{\mathcal{V}_{i,j}} \mathbf{q}(\mathbf{x}, t)\mathrm{d}\mathbf{x}, \tag{183}$$

Additionally, the numerical fluxes are defined as averages over the cell faces

$$\mathbf{F}_{i+1/2,j}\big(\mathbf{Q}(t)\big) \approx \frac{1}{\Delta y} \int_{y_{i,j-1/2}}^{y_{i,j+1/2}} \Big(\mathbf{f}(x_{i+1/2,j}, y_{ij}, t) \Big) \mathrm{d}y, \tag{184}$$

$$\mathbf{G}_{i,j+1/2}\big(\mathbf{Q}(t)\big) \approx \frac{1}{\Delta x} \int_{y_{i-1/2,j}}^{y_{i+1/2,j}} \Big(\mathbf{f}(x_{ij}, y_{ij+1/2}, t) \Big) \mathrm{d}x. \tag{185}$$

Using these expressions and substituting them into Eq. 181,

$$\mathbf{Q}_{i,j}^{n+1} = \mathbf{Q}_{ij}^{n} - \frac{1}{\Delta x} \int_{t_n}^{t_{n+1}} \Big(\mathbf{F}_{i+1/2,j}\big(\mathbf{Q}(t)\big) - \mathbf{F}_{i-1/2,j}\big(\mathbf{Q}(t)\big) \Big) \mathrm{d}t - \frac{1}{\Delta y} \int_{t_n}^{t_{n+1}} \Big(\mathbf{G}_{i,j+1/2}\big(\mathbf{Q}(t)\big) - \mathbf{G}_{i,j-1/2}\big(\mathbf{Q}(t)\big) \Big) \mathrm{d}t \tag{186}$$

where $\mathbf{Q}_{i,j}^{n} = \mathbf{Q}_{i,j}(t_n)$ and $\mathbf{Q}_{i,j}^{n+1} = \mathbf{Q}_{i,j}(t_{n+1})$. The last step is to define a suitable approximation to time integration of the numerical fluxes in the above equation. If the numerical fluxes are be approximated at the half time step $n + 1/2$, then the following definitions apply

$$\mathbf{F}_{i+1/2,j}^{n+1/2}(\mathbf{Q}) \approx \frac{1}{\Delta y \Delta t} \int_{t_n}^{t_{n+1}} \int_{y_{i,j-1/2}}^{y_{i,j+1/2}} \Big(\mathbf{f}(x_{i+1/2,j}, y_{i,j}, t) \Big) \mathrm{d}t\mathrm{d}y, \tag{187}$$

$$\mathbf{G}_{i,j+1/2}^{n+1/2}(\mathbf{Q}) \approx \frac{1}{\Delta x \Delta t} \int_{t_n}^{t_{n+1}} \int_{y_{i-1/2,j}}^{y_{i+1/2,j}} \Big(\mathbf{f}(x_{i,j}, y_{i,j+1/2}, t) \Big) \mathrm{d}t\mathrm{d}x. \tag{188}$$

where $\mathbf{F}^{n+1/2}_{i+1/2,j}$ and $\mathbf{G}^{n+1/2}_{i,j+1/2}$ are numerical fluxes in the i- and j-directions. The evaluation of the numerical fluxes at the half time step is similar to a predictor step and is done in such a way that flux necessarily includes components from both the $x-$ and $y-$directions. Thus, the fluxes are multi-dimensional. The final form of the finite-volume representation of the hyperbolic MHD conservation equations is

$$\mathbf{Q}^{n+1}_{i,j} = \mathbf{Q}^{n}_{i,j} - \frac{\Delta t}{\Delta x}\left(\mathbf{F}^{n+1/2}_{i+1/2,j}(\mathbf{Q}) - \mathbf{F}^{n+1/2}_{i-1/2,j}(\mathbf{Q})\right) - \frac{\Delta t}{\Delta y}\left(\mathbf{G}^{n+1/2}_{i,j+1/2}(\mathbf{Q}) - \mathbf{G}^{n+1/2}_{i,j-1/2}(\mathbf{Q})\right). \tag{189}$$

The accuracy of the finite volume scheme is dependent on the integration algorithm used to compute the cell averaged quantities in Eq. 181. Extending the formal order of accuracy of finite volume schemes to orders higher than two is not as trivial as it is in a finite difference representation, since a high order approximation of the integrands involves integrating over multiple quadrature points. Instead, the numerical errors of the scheme are simply reduced by using a high order interpolation procedure to approximate $\mathbf{Q}^{n}_{i,j}$ at the cell-faces. The interpolated conservative or primitive variables are then used to compute the numerical fluxes [69]. This is an important difference between the finite volume and finite difference methods developed in this thesis. Yet, it is important to note that Eqs. 186 and 189 are in the same general form as the finite-difference representation, Eq. 172. In the next sections, the details of a finite difference and finite volume methods are discussed in application to MHD, however, in order to do that several numerical algorithms used to preserve the magnetic divergence are first introduced.

3.2 $\nabla \cdot \mathbf{B} = 0$ Perserving Methods

The divergence free condition on the magnetic field makes the direct extension of any numerical method developed for the hydrodynamic conservation equations difficult,

since when such numerical schemes are extended to MHD without modification, numerical errors accumulate and create unphysical values in the pressure and density fields. The different types of methods were reviewed in Sec. 1.4.2. Two approaches are used to limit the non-zero errors in the magnetic divergence, the projection scheme, a divergence cleaning method, and the constrained transport scheme, a divergence free method. These methods are are used for the both the finite-difference and finite-volume methods.

It is useful to think of the MHD system of equations as composed of two coupled subsystems, one evolving the conservative variables of mass, momentum, and energy, and another evolving the magnetic field. The first system is similar to the Euler form of the conservative equation. For this system, the numerical methods used to solve the Euler gas dynamic equations are directly applicable. This is referred to as the base scheme. The second evolution equation is for the magnetic field. If the base scheme is used for the numerical integration of the magnetic induction equation, then a divergence cleaning algorithm is necessary. Otherwise, the magnetic induction equation must be integrated in the particular manner, such as the method adopted by the constrained transport (CT) scheme.

3.2.1 Projection Scheme

The projection scheme provides a correction to the magnetic field after it has been incremented in time using a finite difference or finite volume numerical scheme. Let $\mathbf{B}^n$ be the magnetic field at time t^n, and let $\widehat{\mathbf{B}}$ be the magnetic field at the next time increment, $t + \Delta t$, which is not necessarily divergence free. The objective of the projection scheme is to "project" the magnetic field updated from the base scheme to a divergence free $\mathbf{B}^{n+1}$. Since any vector field can be decomposed into the sum of a curl and a gradient, then the magnetic field can be written as

$$\widehat{\mathbf{B}} = \nabla \times \mathbf{A} + \nabla\phi, \tag{190}$$

where $\mathbf{A}$ is the vector potential, and ϕ is a scalar potential representing the unphysical, divergent part of the magnetic filed. Taking the divergence of both sides yields a Poisson equation for ϕ,

$$\nabla^2 \phi = \nabla \cdot \widehat{\mathbf{B}}. \tag{191}$$

Solving the Poisson equation for the scalar function ϕ, the magnetic field can be corrected by

$$\mathbf{B}^{n+1} = \widehat{\mathbf{B}} - \nabla \phi \tag{192}$$

The numerical divergence of $\mathbf{B}^{n+1}$ should be exactly zero or within machine precision. For a uniform Cartesian grid, it can be demonstrated that the projection scheme minimizes the correction necessary to remove the divergence of the magnetic field generated by the base scheme [202].

The projection scheme does not introduce any errors in the total energy or in the conservation of the magnetic flux since these variables are independently computed by the numerical scheme. Likewise, the kinetic energy does not change due to projection, since the momentum and density are unaffected. However, the magnetic energy can change, and as a result so can the internal energy or temperature, but small changes in the temperature should not significantly affect accuracy. The main concern is the use of the projection scheme for discontinuous solutions, particularly since the numerical error associated with the magnetic divergence is larger near a discontinuity. While the projection scheme could lower the accuracy of the base scheme by spreading the error globally since it is implicit, numerous numerical tests indicate that this does not happen. See Toth [202] for a comparison of between methods for many numerical tests. In fact, even for discontinuous solutions, the projection scheme can be proved to be consistent and as accurate as the base scheme [202].

The projection scheme requires one to solve a Poisson equation for ϕ. For uniform Cartesian grid geometries with periodic boundary conditions, Poisson solvers are usually extremely efficient, only requiring 20 to 30 % if the total CPU time [173,

174, 202]. For more complex geometries, the computational cost may be larger. In practice, it is not necessary to perform the projection operation at every iteration nor is it necessary to reduce the $\nabla \cdot \widehat{\mathbf{B}}$ errors to the precision of round off error, just to some small value relative to the initial error.

There are two primary benefits to using the projection scheme. The first is that the projection scheme is ideally used to ensure that the initial magnetic field is divergence free when discretized on the computational mesh. This is of particular importance in turbulence simulations where the initial magnetic field does is not prescribed analytically. The second benefit of the projection scheme is that it can be easily combined with any numerical scheme, even high order methods. As is discussed in the next section, constrained transport methods can be extremely complex, particularly when in the extension to a high order method. This makes the projection scheme ideal for the high order finite difference schemes discussed in the previous sections.

3.2.2 Constrained Transport Methods

For simplicity, the CT method is presented here only for a two dimensional uniform Cartesian grid. Extensions to three-dimensional geometry is simple. Note that in a two-dimensional implementation, the B_z component of the magnetic field can be updated directly by the base scheme since it does not contribute any error to $\nabla \cdot \mathbf{B}$. Typically, the CT method employs a staggered representation of the magnetic field vectors, as illustrated in Figs. 9 and 10. In the ensuing notation, the uppercase $\mathbf{B}$ is used to represent cell-centered values while the lower case $\mathbf{b}$ is used to represent the staggered components. In the CT scheme, only $\nabla \cdot \mathbf{b} = 0$ is guaranteed. Let $\mathcal{E} = -\mathbf{u} \times \mathbf{B} + \eta \mathbf{J}$ be defined at the cell corners $x_{i+1/2,j}, y_{i,j+1/2}$. Integrating over the cell surfaces using Stoke's theorem results in the discrete form of the induction

equation given by

$$b^{x,n+1}_{i+1/2,j} = b^{x,n}_{i+1/2,j} - \frac{\Delta t}{\Delta y}\left(\mathcal{E}_{z,i+1/2,j+1/2} - \mathcal{E}_{z,i+1/2,j-1/2}\right) \tag{193}$$

$$b^{y,n+1}_{i,j+1/2} = b^{y,n}_{i,j+1/2} + \frac{\Delta t}{\Delta x}\left(\mathcal{E}_{z,i+1/2,j+1/2} - \mathcal{E}_{z,i-1/2,j+1/2}\right) \tag{194}$$

If the magnetic field is initially divergence free, then $\nabla \cdot \mathbf{b}^n$, which is numerically defined as

$$(\nabla \cdot \mathbf{b})_{i,j} = \frac{b^x_{i+1/2,j} - b^x_{i-1/2,j}}{\Delta x} + \frac{b^y_{i,j+1/2} - b^y_{i,j-1/2}}{\Delta y}, \tag{195}$$

then substituting the expressions for $b^{x,n+1}_{i+1/2,j}$ and $b^{y,n+1}_{i,j+1/2}$ in Eqs. 193 and 194 it is easy to show that $\nabla \cdot \mathbf{b}^{n+1}$ is zero by definition. Most CT schemes follow this formulation. Differences between CT implementations arise in how the cell corner electric fields, i.e., $\mathcal{E}_{z,i+1/2,j+1/2}$, are computed. Typically, this requires some interpolation procedure to translate the numerical fluxes computed at the cell faces, which is more natural, to the cell corner. However, given values for the cell corner electric field, the magnetic field is easily integrated in time. The updated values of the cell centered magnetic field values are then computed as straight averages,

$$B^{x,n+1}_{i,j} = \frac{b^{x,n+1}_{i+1/2,j} + b^{x,n+1}_{i-1/2,j}}{2} \tag{196}$$

$$B^{y,n+1}_{i,j} = \frac{b^{y,n+1}_{i,j+1/2} + b^{y,n+1}_{i,j-1/2}}{2} \tag{197}$$

These values are used in the next time step. Since the conservative variables are integrated using the base scheme, the total energy density at the new time step E^{n+1}, which contains the a magnetic energy term, needs to be reconciled. Thus, E^{n+1} must be corrected either to conserve the total energy or to keep the pressure the same before and after the time update. The later option tends to improve the numerical stability in some problems where it is necessary to maintain the positivity of the pressure.

Two methods to determine $\mathcal{E}_{z,i+1/2,j+1/2}$ are presented. The first approach, which is most commonly used, is to define $\mathcal{E}_{z,i+1/2,j+1/2}$ as a simple arithmetic average,

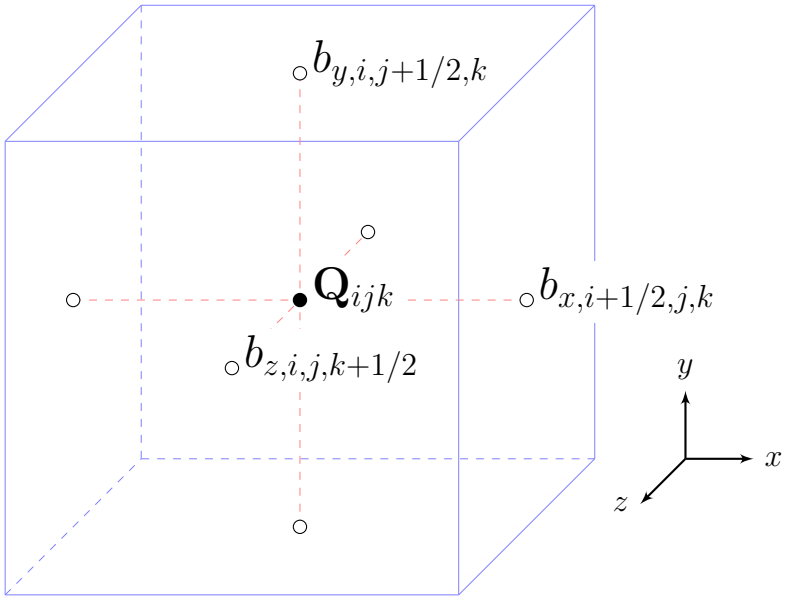

Figure 9: Illustration of the staggered stencil for the constrained transport scheme where the conservative variables are computed at the cell-center and the magnetic field is computed cell-faces.

$\overline{\mathcal{E}}_{z,i+1/2,j+1/2}$, which can be computed as

$$\overline{\mathcal{E}}_{z,i+1/2,j+1/2} = \frac{1}{4}\left(\mathcal{E}_{z,i+1/2,j} + \mathcal{E}_{z,i,j+1/2} + \mathcal{E}_{z,i+1,j+1/2} + \mathcal{E}_{z,i+1/2,j}\right) \tag{198}$$

Exploiting the fact that the electric field values at the cell faces, i.e., $\mathcal{E}_{z,i+1/2,j}$, are actually evaluated as fluxes in the base scheme, this averaging procedure can be written as,

$$\overline{\mathcal{E}}_{z,i+1/2,j+1/2} = \frac{1}{4}\left(-F^{\mathcal{E}_z}_{i+1/2,j} - F^{\mathcal{E}_z}_{i+1/2,j+1} + G^{\mathcal{E}_z}_{i,j+1/2} + G^{\mathcal{E}_z}_{i+1,j+1/2}\right) \tag{199}$$

where $F^{\mathcal{E}_z}_{i+1/2,j}$ and $G^{\mathcal{E}_z}_{i,j+1/2}$ are the corresponding transverse magnetic field components in the $\mathbf{F}_{i+1/2,j}$ and $\mathbf{G}_{i,j+1/2}$ numerical flux vectors. In this manner, any numerical scheme can be easily coupled with a CT algorithm. It is important to mention, however, that the averaging procedure here is at most second-order accurate, thus using this particular CT algorithm could reduce the order of a high order base scheme.

A more accurate approach is to compute an average value of $\mathcal{E}_z$ at the cell corner using a spatial integration procedure. For instance, using a first order expansion, the

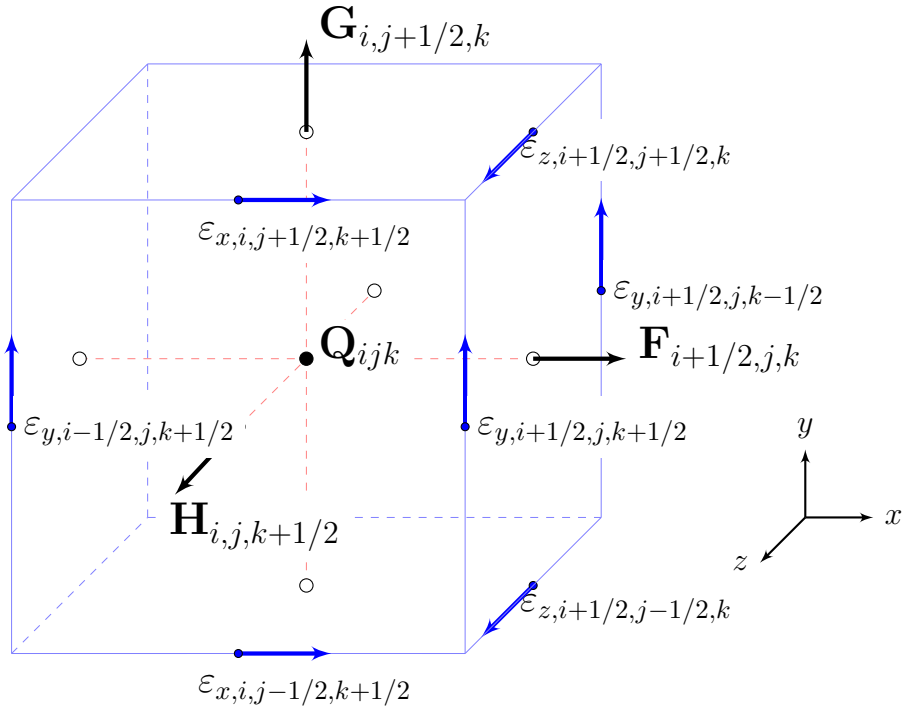

Figure 10: Illustration of the location of the numerical fluxes for the flux constrained transport scheme in three-dimensions.

result is

$$\mathcal{E}_{z,i+1/2,j+1/2} = \mathcal{E}_{z,i+1/2,j} + \frac{\Delta y}{2}\left(\frac{\partial \mathcal{E}_z}{\partial y}\right)_{i+1/2,j+1/4}. \tag{200}$$

Following the same procedure in each direction results in the following expression,

$$\begin{aligned}\mathcal{E}_{z,i+1/2,j+1/2} =& \frac{1}{4}\left(\mathcal{E}_{z,i+1/2,j} + \mathcal{E}_{z,i,j+1/2} + \mathcal{E}_{z,i+1,j+1/2} + \mathcal{E}_{z,i+1/2,j}\right) \\ &+ \frac{\Delta y}{8}\left(\left(\frac{\partial \mathcal{E}_z}{\partial y}\right)_{i+1/2,j+1/4} - \left(\frac{\partial \mathcal{E}_z}{\partial y}\right)_{i+1/2,j+3/4}\right) \\ &+ \frac{\Delta x}{8}\left(\left(\frac{\partial \mathcal{E}_z}{\partial x}\right)_{i+1/4,j+1/2} - \left(\frac{\partial \mathcal{E}_z}{\partial x}\right)_{i+3/4,j+1/4}\right).\end{aligned} \tag{201}$$

To complete the formulation it is necessary to approximate to the derivatives of $\mathcal{E}_z$. This can be done by finding an approximate solution for the evolution equations of

$(\partial B_x/\partial x)$ and $(\partial B_y/\partial y)$. Using a Lax-Friedrichs estimate with the maximum wave-speed α gives the following approximations,

$$\left(\frac{\partial \mathcal{E}_z}{\partial x}\right)_{i+1/4,j+1/2} = \frac{1}{\Delta x}\left(\mathcal{E}_{z,i+1/2,j} - \mathcal{E}_{z,i,j} + \mathcal{E}_{z,i+1/2,j+1} - \mathcal{E}_{z,i,j+1}\right) + \frac{\alpha}{\Delta x}\left(b^x_{i+1/2,j} - b^x_{i,j} + b^x_{i+1/2,j+1} - b^x_{i,j+1}\right), \tag{202}$$

and similarly in the y-direction,

$$\left(\frac{\partial \mathcal{E}_z}{\partial y}\right)_{i+1/2,j+1/4} = \frac{1}{\Delta y}\left(\mathcal{E}_{z,i,j+1/2} - \mathcal{E}_{z,i,j} + \mathcal{E}_{z,i+1,j+1/2} - \mathcal{E}_{z,i+1,j}\right) + \frac{\alpha}{\Delta y}\left(b^y_{i,j+1/2} - b^y_{i,j} + b^y_{i+1,j+1/2} - b^x_{i+1,j}\right). \tag{203}$$

For a values of $\alpha = 0$, this procedure relaxes to the arithmetic averaging method discussed previously. Other methods are addressed and compared elsewhere [68]. The advantage of these methods is that they are consistent with the integration algorithm. Many CT methods are not and produce errors for plane-parallel, grid-aligned flows since they lack directional bias in the averaging formula [67].

3.3 A Finite Difference Flux Vector Splitting Scheme

While the particulars of the FD scheme presented here is not new, the method of combining this FVS scheme with a central explicit or implicit FD scheme is a new approach to the numerical simulation of MHD. In Sec. 3.1.1, a family of high order FD schemes were introduced. In this section, a FVS scheme using WENO flux reconstruction is discussed. In a later section, the details of the hybrid switching function is discussed. This method is combined with both the projection scheme as well as integrated into the CT method. The details of the WENO reconstruction procedure are now discussed.

For simplicity of notation, consider a one-dimensional, hyperbolic conservation equation,

$$\frac{\partial Q}{\partial t} + \frac{\partial F}{\partial x} = 0, \tag{204}$$

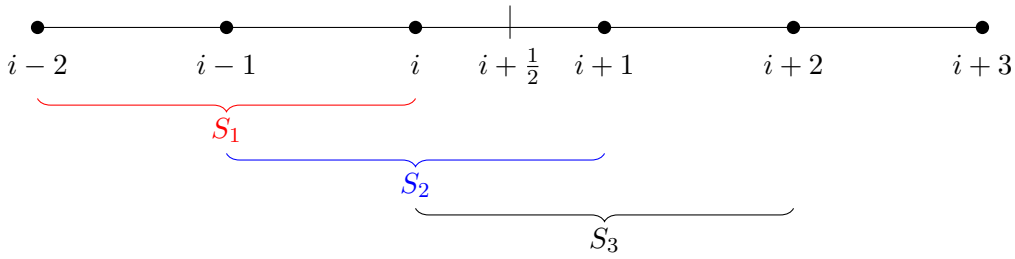

Figure 11: Three sub-stencils for WENO $\mathcal{O}(5)$ used in computing the left flux at $i+1/2$

where Q and F now represent single, corresponding elements in the vectors $\mathbf{Q}$ and $\mathbf{F}$. Likewise, the semi-discrete form in a single dimension is written as,

$$\frac{dq_i(t)}{dt} = -\frac{1}{\Delta x}\left(F_{i+1/2} - F_{i-1/2}\right), \tag{205}$$

Then, following a classical fifth-order WENO scheme of Jiang and Shu [99], the numerical flux, $F_{i+1/2}$, in the x-direction, is defined through the convex, weighted combination of interpolated values of three $(k = 0, 1, 2)$ third-order sub-stencils, $S_k = (x_{i+k-2}, x_{i+k-1}, x_{i+k})$. These sub-stencils are illustrated in Fig. 11. Mathematically,

$$F_{i+1/2} = \sum_{k=0}^{2} \omega_k F_{i+1/2}^k \tag{206}$$

where

$$F_{i+1/2}^k = F^k(x_{i+1/2}) = \sum_{j=0}^{2} c_{kj} F_{i-k+j} \tag{207}$$

The weights ω_k are defined as

$$\omega_k = \frac{\alpha_k}{\sum_{l=0}^{2} \alpha_l}, \qquad \alpha_k = \frac{d_k}{(\beta_k + \epsilon)^p} \tag{208}$$

The smoothness indicators $\beta_k (k = 0, 1, 2)$ are given by

$$\begin{aligned}
\beta_0 &= \frac{13}{12}\left(F_{i-2} - 2F_{i-1} + F_i\right)^2 + \frac{1}{4}\left(F_{i-1} - 4F_{i-1} + 3F_i\right)^2 \\
\beta_1 &= \frac{13}{12}\left(F_{i-1} - 2F_i + F_{i+1}\right)^2 + \frac{1}{4}\left(F_{i-1} - F_{i+1}\right)^2 \\
\beta_1 &= \frac{13}{12}\left(F_i - 2F_{i+1} + F_{i+2}\right)^2 + \frac{1}{4}\left(3F_i - 4F_{i+1} + F_{i+2}\right)^2
\end{aligned} \tag{209}$$

The process described above is applied to each flux in the vector $\mathbf{F}$. Likewise, the same procedure is repeated in each direction in order to compute the y- and z-directional fluxes as well. In summary, the following general steps are used to compute the numerical fluxes for a FVS using WENO reconstruction are as follows:

1. In the i-direction, evaluate all the conservative variables at each cell-face location $(x_{i+1/2,j,k}, y_{i+1/2,j,k}, z_{i+1/2,j,k})$. A simple arithmetic average is used,

$$\mathbf{Q}_{i+1/2,j,k} = \frac{1}{2}\left(\mathbf{Q}_{i,j,k} + \mathbf{Q}_{i+1,j,k}\right) \tag{210}$$

2. Using $\mathbf{Q}_{i+1/2,j,k}$ compute the primitive variables $\mathbf{W}_{i+1/2,j,k}$, which are needed to compute the left eigenvectors $\mathbf{L}_{i+1/2,j,k}$, the right eigenvectors $\mathbf{R}_{i+1/2,j,k}$, and the eigenvalues $\lambda_{i+1/2,j,k}$ at the averaged state.

3. Project the fluxes of the conservative variables at the average state into characteristic space using the left eigenvectors,

$$f^{(s)}_{m,j,k} = \mathbf{L}^{(s)}_{i+1/2,j,k} \cdot \mathbf{F}_{m,j,k}, \quad m \in [i-2, i+3] \tag{211}$$

   where s represents the individual characteristic waves. For the MHD system of equations, there are seven independent characteristics. The stencil size m spans $i-2$ to $i+3$ for a fifth-order WENO reconstruction. For higher orders, m is larger.

4. For either Roe or local Lax Friedrichs flux splitting, the sign of each eigenvalue is checked at both sides of the interface. If $\lambda_i \lambda_{i+1} > 0$, then Roe flux splitting is used. If $\lambda^{(s)}_{i+1/2,j,k} > 0$, then

$$\begin{aligned} f^{(s),+}_{m,j,k} &= f^{(s)}_{m,j,k}, \\ f^{(s),-}_{m,j,k} &= 0, \end{aligned} \tag{212}$$

otherwise

$$f^{(s),+}_{m,j,k} = 0,$$
$$f^{(s),-}_{m,j,k} = f^{(s)}_{m,j,k}. \tag{213}$$

If $\lambda_{i,j,k}\lambda_{i+1,j,k} < 0$, the left and right characteristic fluxes are computed using LLF flux splitting. The conservative variables are projected into characteristic space similar to Eq. 211,

$$\varphi^{(s)}_{m,j,k} = \mathbf{L}^{(s)}_{i+1/2,j,k}\mathbf{Q}_{m,j,k}, \quad m \in [i-2, i+3] \tag{214}$$

The left and right flux functions at the grid points in the WENO-Z stencils are then computed using the LLF technique,

$$\begin{aligned} f^{(s),+}_{m,j,k} &= \frac{1}{2}\left(f^{(s)}_{m,j,k} + \max_{l\in[i-2,i+3]}\left|\lambda^{(s)}_{l}\right|\varphi^{(s)}_{m,j,k}\right), \\ f^{(s),-}_{m,j,k} &= \frac{1}{2}\left(f^{(s)}_{m,j,k} - \max_{l\in[i-2,i+3]}\left|\lambda^{(s)}_{l}\right|\varphi^{(s)}_{m,j,k}\right) \end{aligned} \tag{215}$$

5. The numerical fluxes at the $x_{i+1/2,j,k}$ interface can then be computing using WENO-Z reconstruction,

$$f^{(s),\pm}_{i+1/2,j,k} = \begin{cases} f^{(s),\pm Roe}_{i+1/2,j,k} & \text{if } \lambda_{i,j,k}\lambda_{i+1,j,k} > 0 \\ f^{(s),\pm LLF}_{i+1/2,j,k} & \text{if } \lambda_{i,j,k}\lambda_{i+1,j,k} < 0 \end{cases} \tag{216}$$

6. Lastly, the characteristic fluxes are then projected back to physical space using the right eigenvectors,

$$\mathbf{F}_{i+1/2,j,k} = \mathbf{R}_{i+1/2,j,k}\left(\mathbf{f}^{+}_{i+1/2,j,k} + \mathbf{f}^{-}_{i+1/2,j,k}\right) \tag{217}$$

Once the x-directional flux is computed, the other two numerical fluxes, $\mathbf{F}_{i,j+1/2,k}$ and $\mathbf{H}_{i,j,k+1/2}$, are computed in a similar manner. The left and right eigenvectors used here were derived for a multi-species mixture. Note that since the conservative fluxes are characteristically projected, the left and right eigenvectors are based on the

Jacobian of the conservative variables. When coupled with a CT scheme, these fluxes are used in the computing the cell-corner electric field, which is then in turn used to update the magnetic field. If a projection scheme is used, then no additional changes need to be made to the time-integration procedure.

3.4 A Finite Volume Unsplit Flux Difference Splitting Scheme

A multi-dimensional unsplit FDS method is used to numerical solve the finite-volume representation of the governing equations. For a typical finite-volume, shock-capturing scheme, a reconstruction step is first used to compute the primitive state variables at the points where the flux derivatives are required $(i+1/2, j+1/2)$, and then a Riemann solver is used to evaluate the numerical fluxes, $\mathbf{F}^{n+1/2}_{i,j+1/2}$ and $\mathbf{G}^{n+1/2}_{i,j+1/2}$ at the half time step. The method developed here is only two-dimensional. Identifying the Riemann solver as some function $\mathcal{R}(\mathbf{W})$, then

$$\mathbf{F}^{n+1/2}_{i+1/2,j} = \mathcal{R}(\mathbf{W}^{n+1/2}_{i+1/2,j}) \tag{218}$$

$$\mathbf{G}^{n+1/2}_{i,j+1/2} = \mathcal{R}(\mathbf{W}^{n+1/2}_{i,j+1/2}) \tag{219}$$

where $\mathbf{W}$ is the primitive state vector defined by the conservative state vector $\mathbf{Q}$. In order to estimate the the numerical fluxes at the half time-step, a Taylor series expansion in space through $\Delta x/2$ and in time through $\Delta t/2$ is used.

$$\mathbf{W}^{n+1/2}_{i+1/2,j} = \mathbf{W}^{n}_{i,j} + \frac{\Delta x}{2}\frac{\partial \mathbf{W}}{\partial x}\bigg|_{i,j} + \frac{\Delta t}{2}\frac{\partial \mathbf{W}}{\partial t}\bigg|_{i,j} + \dots \tag{220}$$

$$= \mathbf{W}^{n}_{i,j} + \frac{\Delta x}{2}\frac{\partial \mathbf{W}}{\partial x}\bigg|_{i,j} - \frac{\Delta t}{2}\left(\mathbf{A}\frac{\partial \mathbf{W}}{\partial x}\right)_{i,j} \tag{221}$$

$$= \mathbf{W}^{n}_{i,j} + \frac{1}{2}\left[1 - \frac{\Delta t}{\Delta x}\mathbf{A}_{i,j}\right]\Delta W_{i,j} \tag{222}$$

This expression can be simplified by using the left and right eigenvectors, $\mathbf{l}$ and $\mathbf{r}$, respectively,

$$\mathbf{W}^{n+1/2}_{i+1/2,j,L} = \mathbf{W}^{n}_{i,j} + \frac{1}{2}\sum_{s;\lambda^{(s)}\geq 0}\left[1 - \frac{\Delta t}{\Delta x}\lambda^{(s)}_{i,j}\right]\left(\bar{\mathbf{l}}^{(s)}_{i,j}\cdot\overline{\Delta W_{i,j}}\right)\bar{\mathbf{r}}^{(s)} \tag{223}$$

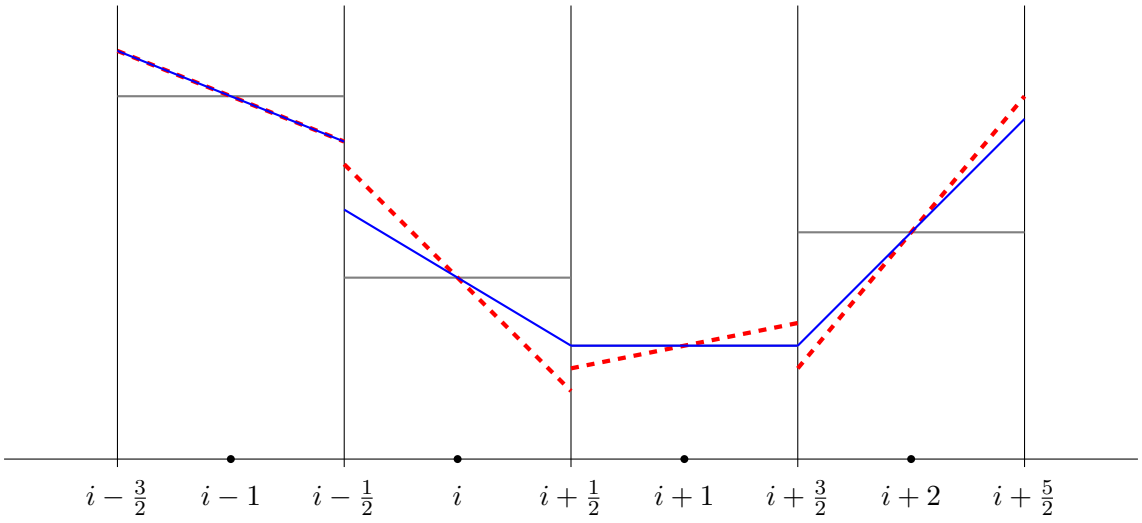

Figure 12: Piecewise linear reconstruction (PLM) of the cell-centered primitive variables. The dotted red lines show the unlimited reconstructed slopes, and the solid blue lines show the limited slopes.

$$\mathbf{W}^{n+1/2}_{i+1/2,j,R} = \mathbf{W}^{n}_{i+1,j} - \frac{1}{2}\sum_{s;\lambda^{(s)}\le 0}\left[1-\frac{\Delta t}{\Delta x}\lambda^{(s)}_{i,j}\right]\left(\bar{\mathbf{l}}^{(s)}_{i,j}\cdot\overline{\Delta W_{i,j}}\right)\bar{\mathbf{r}}^{(s)} \tag{224}$$

where the lowercase **l** and **r** eigenvectors are used to distinguish them from the eigenvectors **L** and **R**, which are based on the conservative rather than primitive variables.

Only those jumps moving toward the interface contribute to the interface state. referred to as characteristic tracing, which involves decomposition in terms of the eigenvectors and eigenvalues. The reconstruction is either linear as illustrated in Fig. 12 or parabolic as illustrated in Fig. 13. The details of the reconstruction are not given here since this method is commonly used in many MHD codes.

The most important feature of this scheme is that it use a corner-transport update (CTU) scheme so that the time integration is multi-dimensional. This involves an additional step of updating the reconstructed primitives using the transverse fluxes. The details of the scheme are given elsewhere [67, 68], but it can be summarized in the following steps. First, the primitive x- and y-interface states are reconstructed using the PPM algorithm. For MHD, this requires the addition of multi-dimensional source terms in order for the method to be consistent. A Riemann solver is then used

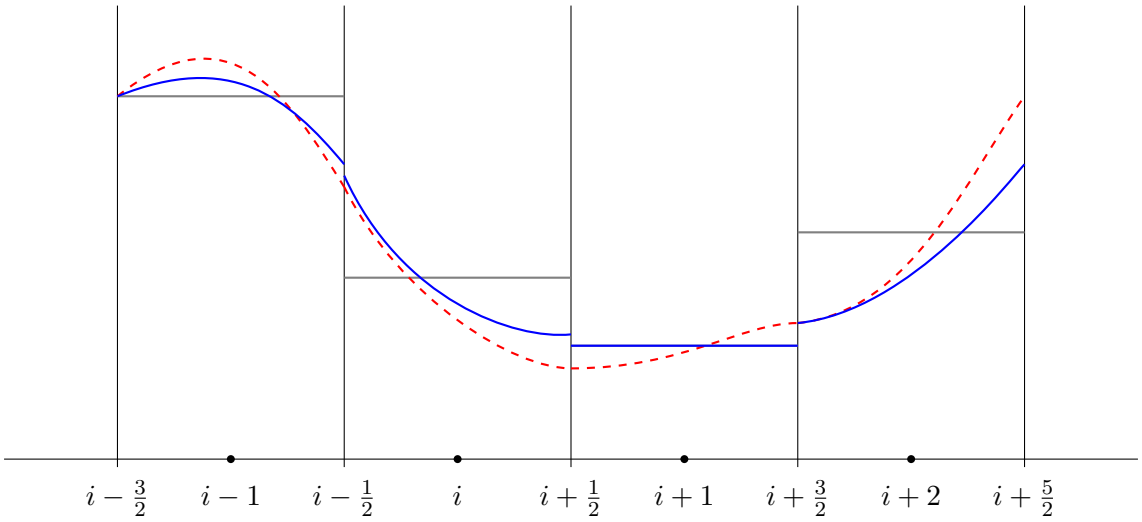

Figure 13: Piecewise parabolic reconstruction (PPM) of the cell-centered primitive variables. The dotted red lines show the unlimited parabolas, and the solid blue lines show the limited parabolas.

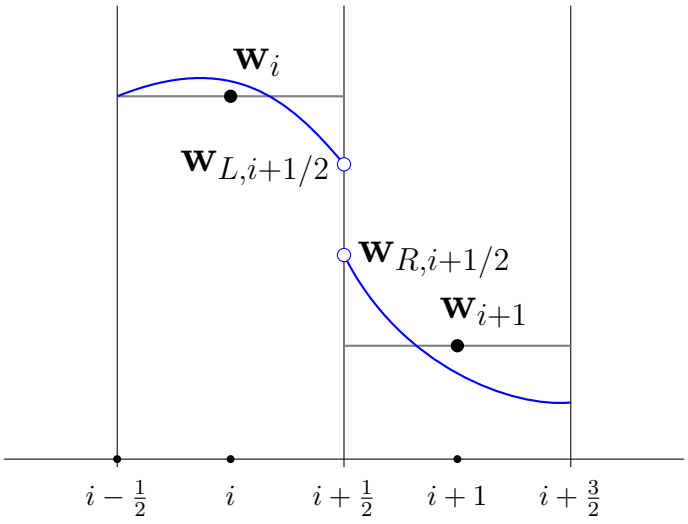

Figure 14: One-dimensional schematic of the reconstruction process for primitive variables using the piecewise parabolic method to compute the left and right states defining the Riemann problem at the cell interface.

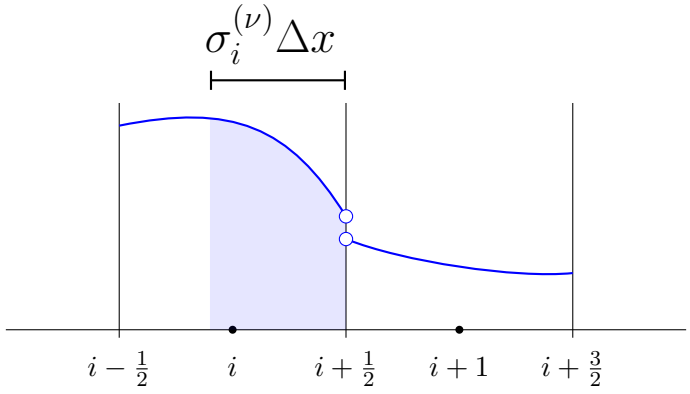

Figure 15: One-dimensional schematic of the area of integration under the parabolic profile that is swept out by each of the characteristic waves, where $\sigma\Delta x = \lambda\Delta t$. The shaded region indicates the portion of the characteristics that contribute to the left state at $i + 1/2$.

to compute the fluxes, and the CT method is used to compute the electric field fluxes at the corner. Using the transverse fluxes in each direction the primitive x- and y-interface states computed in the first step are updated so that they are integrated to the corner of the cell. Since the reconstruction step involves a characteristic tracing step, these corner fluxes are evaluated at the half time step. The CT algorithm is once again used to compute the electric field fluxes at the half time step. Once this is done, all the conservative variables are time updated. Note that this procedure is for a two-dimensional integration only. The CTU process is more complex in three-dimension [68]. In the next section, the details of the Riemann solver are discussed.

3.4.1 MHD Riemann Solvers

A family of approximate Riemann solvers called HLL, named for the developers Harten, Lax, and van Leer [83], can be easily adapted to MHD flows because of its generality. In the HLL formulation, n characteristic waves are assumed to subdivide each cell interface into n+1 constant-property regions. Expressions for each of the n+1 states and their corresponding fluxes can be derived by applying the

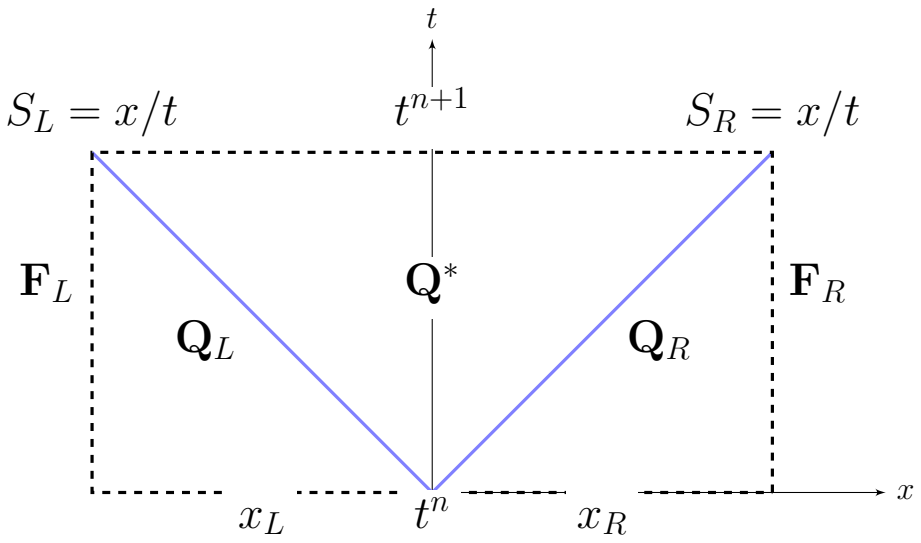

Figure 16: Schematic of the Riemann fan with a single intermediate state. The fastest left- and right-going wave speeds are given by S_L and S_R, respectively.

Rankine-Hugoniot jump relations across each wave and calculating (or approximating) each of n characteristic wave-speeds. Harten et al. [83] carried out a full derivation for a two-wave problem, but did not specify an procedure for the evaluation of the the characteristic wave-speed. Since then, many variants of the HLL-type Riemann solver have been developed, including the HLLD Riemann solver derived by Miyoshi for MHD flows [142]. Since a three-wave HLL Riemann solver, HLLC, has previously been implemented for hydrodynamic flows, the HLLD was natural choice for extending the capability to MHD flows. The HLLD Riemann solver has also been demonstrated to preform relatively well compared to other Riemann solvers [142].

For simplicity, consider a simple two wave HLL method. Figure 16 shows a typical (x, t) diagram of an approximate Riemann problem evolution with two characteristic waves. As mentioned in the previous paragraph, the HLLD Riemann solver is a generalization of the HLL method. For the general hyperbolic conservation law in a single dimension,

$$\frac{\partial \mathbf{Q}}{\partial t} + \frac{\partial \mathbf{F}}{\partial x} = 0 \tag{225}$$

where the vectors $\mathbf{Q}$ and $\mathbf{F}$ are as previously defined, an integral form of the conservation law can be stated as

$$\oint \left[\mathbf{Q}\mathrm{d}x - \mathbf{F}(\mathbf{Q})\mathrm{d}t\right] = 0. \tag{226}$$

Applying this to the Riemann fan, which is defined by the rectangular region $(x_L, x_R)\times(t^n, t^{n+1})$ results in

$$\begin{aligned}\int_0^{-x_L} \mathbf{Q}(x,0)\mathrm{d}x - \int_0^{\Delta t} \mathbf{F}(\mathbf{Q}(x_L,t))\mathrm{d}t + \int_{-x_L}^{x_R} \mathbf{Q}(x,\Delta t)\mathrm{d}x \\ - \int_{\Delta t}^{0} \mathbf{F}(\mathbf{Q}(x_R,t))\mathrm{d}t + \int_{x_R}^{0} \mathbf{Q}(x,0)\mathrm{d}x = 0\end{aligned} \tag{227}$$

After some re-arrangement, the average state is defined as

$$\mathbf{Q}^* = \frac{\mathbf{F}_L - S_L\mathbf{Q}_L - (\mathbf{F}_R - S_R\mathbf{Q}_R)}{S_R - S_L} \tag{228}$$

As a result, once the left and right interface values, $\mathbf{Q}_L$ and $\mathbf{Q}_R$, are known from the reconstruction procedure and the wave speeds S_L and S_R are estimated, the states across the Riemann fan are known. The fluxes can be calculated using the Rankine-Hugoniot relations across the wave. For MHD, this procedure is merely complicated by the existence of more characteristic waves. The mechanics, however, are the same. Figure 17 shows the (x,t) diagram of the MHD Riemann problem. In this case, the average state value can be defined

$$S_M = \frac{(S_R - u_R)\rho_R u_R - (S_L - u_L)\rho_L u_L - p_{T_R} + p_{T_L}}{(S_R - u_R)\rho_R - (S_L - u_L)\rho_L} \tag{229}$$

The normal velocity is assumed to be constance over the Riemann fan, which implies

$$u_L^* = u_L^{**} = u_R^{**} = u_R^* = S_M, \tag{230}$$

and

$$p_{T_L}^* = p_{T_L}^{**} = p_{T_R}^{**} = p_{T_R}^* = p_T^*. \tag{231}$$

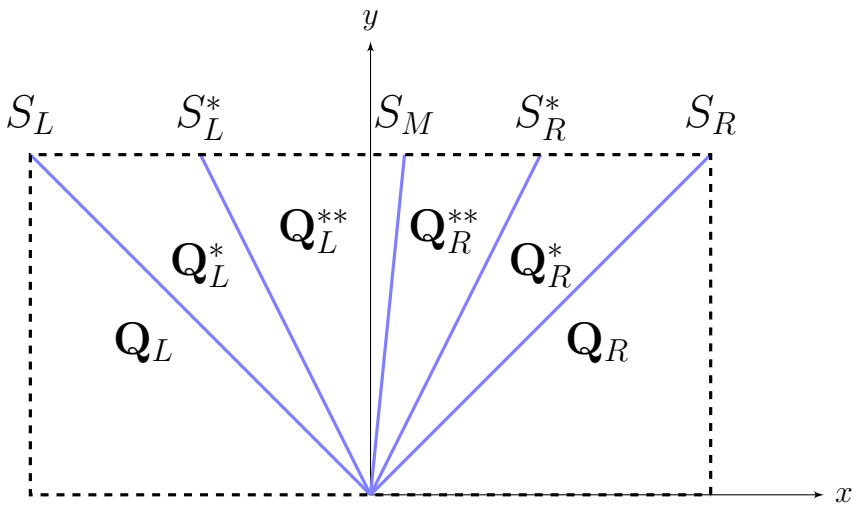

Figure 17: Schematic of the Riemann fan with a four intermediate states. The fastest left- and right-going wave speeds, given by S_L and S_R, respectively, form the outsides of the Riemann fan which is divided by the contact wave of speed S_M and two Alfvén waves with speeds approximated by S_L^* and S_R^* .

Even with this assumption contact, tangential, and rotational discontinuities can be formed. The average total pressure is computed using the jump conditions for each wave. The result is

$$p_T^* = \frac{(S_R - u_R)\rho_R p_{T_L} - (S_L - u_L)\rho_L p_{T_R} + \rho_L \rho_R (S_R - u_R)(S_L - u_L)(u_R - u_L)}{(S_R - u_R)\rho_R - (S_L - u_L)\rho_L} \tag{232}$$

Once S_M and p_T^* are known the $\mathbf{Q}_\alpha^*$ states can be obtained using the jump conditions

across S_α, where $\alpha = (L, R)$. These are given by

$$S_\alpha \begin{pmatrix} \rho^*_\alpha \\ \rho^*_\alpha S_M \\ \rho^*_\alpha v^*_\alpha \\ \rho^*_\alpha w^*_\alpha \\ B^*_{y,\alpha} \\ B^*_{z,\alpha} \\ e^*_\alpha \end{pmatrix} - \begin{pmatrix} \rho^*_\alpha S_M \\ \rho^*_\alpha S_M^2 + p^*_T - B_x^2 \\ \rho^*_\alpha v^*_\alpha S_M - B_x B^*_{y,\alpha} \\ \rho^*_\alpha w^*_\alpha S_M - B_x B^*_{z,\alpha} \\ B^*_{y,\alpha} S_M - B_x v^*_\alpha \\ B^*_{z,\alpha} S_M - B_x w^*_\alpha \\ (e^*_\alpha + p^*_T) S_M - B_x (\mathbf{v}^*_\alpha \cdot \mathbf{B}^*_\alpha) \end{pmatrix} = S_\alpha \begin{pmatrix} \rho_\alpha \\ \rho_\alpha u_\alpha \\ \rho^*_\alpha v_\alpha \\ \rho^*_\alpha w_\alpha \\ B_{y,\alpha} \\ B_{z,\alpha} \\ e_\alpha \end{pmatrix}$$

$$- \begin{pmatrix} \rho_\alpha u_\alpha \\ \rho^*_\alpha u_\alpha^2 + p_{T_\alpha} - B_x^2 \\ \rho^*_\alpha v_\alpha u_\alpha - B_x B_{y,\alpha} \\ \rho^*_\alpha w_\alpha u_\alpha - B_x B_{z,\alpha} \\ B^*_{y,\alpha} u_\alpha - B_x v_\alpha \\ B^*_{z,\alpha} u_\alpha - B_x w_\alpha \\ (e_\alpha + p_{T_\alpha}) u_\alpha - B_x (\mathbf{v}_\alpha \cdot \mathbf{B}_\alpha) \end{pmatrix}, \tag{233}$$

The first equation gives

$$\rho^*_\alpha = \rho_\alpha \frac{S_\alpha - u_\alpha}{S_\alpha - S_M} \tag{234}$$

Solving the third and fifth equations simultaneously, results in expressions for

$$v^*_\alpha = v_\alpha - B_x B_{y,\alpha} \frac{S_M - u_\alpha}{\rho_\alpha (S_\alpha - u_\alpha)(S_\alpha - S_M) - B_x^2}, \tag{235}$$

$$w^*_\alpha = w_\alpha - B_x B_{z,\alpha} \frac{S_M - u_\alpha}{\rho_\alpha (S_\alpha - u_\alpha)(S_\alpha - S_M) - B_x^2}, \tag{236}$$

Likewise, solving the fourth and sixth equations simultaneously, result in

$$B^*_{y,\alpha} = B_{y,\alpha} \frac{\rho_\alpha (S_\alpha - u_\alpha)^2 - B_x^2}{\rho_\alpha (S_\alpha - u_\alpha)(S_\alpha - S_M) - B_x^2}, \tag{237}$$

$$B^*_{z,\alpha} = B_{z,\alpha} \frac{\rho_\alpha (S_\alpha - u_\alpha)^2 - B_x^2}{\rho_\alpha (S_\alpha - u_\alpha)(S_\alpha - S_M) - B_x^2}, \tag{238}$$

$$\tag{239}$$

Note that some care is necessary in the implementation of these expressions since the denominators can go to zero if $S_M = u_\alpha$, $S_\alpha = u_\alpha \pm c_{f,\alpha}$, $B_{y,\alpha} = B_{z,\alpha} = 0$ and $B_x^2 \geq \gamma p_\alpha$. Lastly, the averaged energy state is

$$e_\alpha^* = \frac{(S_\alpha - u_\alpha)e_\alpha - p_{T_\alpha} u_\alpha + p_T^* S_M + B_x(\mathbf{v}_\alpha \cdot \mathbf{B}_\alpha - \mathbf{v}_\alpha^* \cdot \mathbf{B}_\alpha^*)}{S_\alpha - S_M} \tag{240}$$

In a similar manner, the inner intermediate states $\mathbf{Q}_\alpha^{**}$ can be determined from the jump conditions across the Alfven waves. The speed of these waves are computed as

$$S_L^* = S_M - \frac{|B_x|}{\sqrt{\rho_L^*}}, \qquad S_R^* = S_M + \frac{|B_x|}{\sqrt{\rho_R^*}} \tag{241}$$

Considering the jump conditions for the tangential components of the velocity and magnetic fields gives

$$S_\alpha^* \begin{pmatrix} \rho_\alpha^* v_\alpha^{**} \\ \rho_\alpha^* w_\alpha^{**} \\ B_{y,\alpha}^{**} \\ B_{z,\alpha}^{**} \end{pmatrix} - \begin{pmatrix} \rho_\alpha^* v_\alpha^{**} S_M - B_x B_{y,\alpha}^{**} \\ \rho_\alpha^* w_\alpha^{**} S_M - B_x B_{z,\alpha}^{**} \\ B_{y,\alpha}^{**} S_M - B_x v_\alpha^{**} \\ B_{z,\alpha}^{**} S_M - B_x w_\alpha^{**} \end{pmatrix} = S_\alpha^* \begin{pmatrix} \rho_\alpha^* v_\alpha^* \\ \rho_\alpha^* w_\alpha^* \\ B_{y,\alpha}^* \\ B_{z,\alpha}^* \end{pmatrix} - \begin{pmatrix} \rho_\alpha^* v_\alpha^* S_M - B_x B_{y,\alpha}^* \\ \rho_\alpha^* w_\alpha^* S_M - B_x B_{z,\alpha}^* \\ B_{y,\alpha}^* S_M - B_x v_\alpha^* \\ B_{z,\alpha}^* S_M - B_x w_\alpha^* \end{pmatrix} \tag{242}$$

After some algebra, the intermediate states can be evaluated as

$$v^{**} = \frac{\sqrt{\rho_L^*} v_L^* + \sqrt{\rho_R^*} v_R^* + (B_{y,R}^* - B_{y,L}^*)\text{sign}(B_x)}{\sqrt{\rho_L^*} + \sqrt{\rho_R^*}} \tag{243}$$

$$w^{**} = \frac{\sqrt{\rho_L^*} w_L^* + \sqrt{\rho_R^*} w_R^* + (B_{z,R}^* - B_{z,L}^*)\text{sign}(B_x)}{\sqrt{\rho_L^*} + \sqrt{\rho_R^*}} \tag{244}$$

$$B_y^{**} = \frac{\sqrt{\rho_L^*} B_{y,L}^* + \sqrt{\rho_R^*} B_{y,R}^* + \sqrt{\rho_L^* \rho_R^*}(v_R^* - v_L^*)\text{sign}(B_x)}{\sqrt{\rho_L^*} + \sqrt{\rho_R^*}} \tag{245}$$

$$B_z^{**} = \frac{\sqrt{\rho_L^*} B_{z,L}^* + \sqrt{\rho_R^*} B_{z,R}^* + \sqrt{\rho_L^* \rho_R^*}(w_R^* - w_L^*)\text{sign}(B_x)}{\sqrt{\rho_L^*} + \sqrt{\rho_R^*}} \tag{246}$$

where sign(B_x) is 1 for $B_x > 0$ and -1 for $B_x < 0$. From the jump condition of the energy density, the intermediate energy state is

$$e_\alpha^{**} = e_\alpha^* \mp \sqrt{\rho_\alpha^*}(\mathbf{v}_\alpha^* \cdot \mathbf{B}_\alpha^* - \mathbf{v}_\alpha^{**} \cdot \mathbf{B}_\alpha^{**})\text{sign}(B_x) \tag{247}$$

Once all the intermediate states, $\mathbf{Q}_L^*$, $\mathbf{Q}_L^{**}$, $\mathbf{Q}_R^*$, and $\mathbf{Q}_R^{**}$ are computed, the corresponding fluxes can be computed by integrating the conservation laws over the left and right halves of the Riemann fan. For $S_L \leq 0 \leq S_L^*$,

$$\mathbf{F} = \mathbf{F}_L + S_L \mathbf{U}_L^* - S_L \mathbf{U}_L = \mathbf{F}_L^* \tag{248}$$

and for $S_L^* \leq 0 \leq S_M$,

$$\mathbf{F} = \mathbf{F}_L + S_L^* \mathbf{U}_L^* * -(S_L^* - S_L)\mathbf{U}_L - S_L \mathbf{U}_L = \mathbf{F}_L^{**} \tag{249}$$

Lastly, the fluxes are given by

$$\mathbf{F}_{\text{HLLD}} = \begin{cases} \mathbf{F}_L & \text{if} S_L > 0, \\ \mathbf{F}_L^* & \text{if} S_L \leq 0 \leq S_L^*, \\ \mathbf{F}_L^{**} & \text{if} S_L \leq 0 \leq S_M, \\ \mathbf{F}_R^{**} & \text{if} S_M \leq 0 \leq S_R^*, \\ \mathbf{F}_R^* & \text{if} S_R^* \leq 0 \leq S_R, \\ \mathbf{F}_R & \text{if} S_R < 0, \end{cases} \tag{250}$$

In the case of $B_x = 0$, the HLLD Riemann solver reduces to the two-state HLL Riemann solver. Lastly, to complete the formulation of the HLL approximate Riemann solver, the wave speeds must be computed. There are a variety of methods to approximate these wave speeds. Each method has a varying degree of robustness and dissipation. In this thesis, the wave speeds are estimated in the following manner,

$$S_L = \min\left(u_L - c_L, \widetilde{u} - \widetilde{c}\right) \tag{251}$$

and

$$S_R = \min\left(u_R + c_R, \widetilde{u} + \widetilde{c}\right) \tag{252}$$

where $\widetilde{u}$ and $\widetilde{c}$ are the Roe-averaged velocity and speed of sound. The Roe-averaged

quantities are computed as

$$\widetilde{\mathbf{Q}} = \frac{1}{\sqrt{\rho_L} + \sqrt{\rho_R}} \left(\sqrt{\rho_L} \begin{bmatrix} \sqrt{\rho_L}\sqrt{\rho_R} \\ u_L \\ v_L \\ w_L \\ B_{y,L} \\ B_{z,L} \\ e_L \end{bmatrix} + \sqrt{\rho_R} \begin{bmatrix} \sqrt{\rho_L}\sqrt{\rho_R} \\ u_R \\ v_R \\ w_R \\ B_{y,R} \\ B_{z,R} \\ e_R \end{bmatrix} \right), \tag{253}$$

where the Roe-averaged speed of sound is computed from the Roe-average variables. This solver has been shown to be robust and accurate for many MHD applications.

The two-wave HLL approximate Riemann solver is non-contact-preserving since like the HLLD Riemann solver does not explicitly include the intermediate state. Non-contact-preserving Riemann solvers are much more dissipative, however, this dissipation is stabilizing. The HLLD Riemann solver, as well as the HLLC Riemann solver, the hydrodynamic analogous to the HLLD Riemann (it is a contact preserving three-wave Riemann solver), suffer from instabilities near shock regions. The odd-even decoupling and the carbuncle phenomena can result in post-shock oscillations and deformation of shock fronts.

Previous studies have found that these instabilities arise when using the contact preserving solvers in the directions transverse to the shock front. In order to limit the onset of the instabilities the two-wave HLL Riemann solver is coupled with the HLLD Riemann solver to add extra dissipation when necessary. In order to switch between the HLL and HLLD Riemann solvers, a shock detection procedure is necessary.

Shock detection is also used in the reconstruction process. In addition to switching between the HLL and HLLD Riemann solvers in the computation of the fluxes in the directions to the propagating shock, the order of the reconstruction is reduced to avoid instabilities related to the self-steepening property of shocks. The flattening

method described here is implemented in the current formulation to evaluate when to add additional dissipation to the FDS scheme. Shock wave detection is achieved by testing following two conditions,

$$\delta p_i = \frac{|p_{i+1} - p_{i-1}|}{\min(p_{i+1}, p_{i-1})} - \frac{1}{3} > 0, \tag{254}$$

$$\delta u_i = u_{i+1} - u_{i-1} < 0 \tag{255}$$

??The shock thickness is measured by comparing the pressure difference across two cells to the difference across four cells,

$$\Delta p_i = \frac{p_{i+1} - p_{i-1}}{p_{i+2} - p_{i-2}}. \tag{256}$$

Using this ratio, the shock sensing variable is computed as

$$\widetilde{\Phi} = \max\left[0, \min\left(1, 10(\Delta p_i - 0.75)\right)\right], \tag{257}$$

where finally, the variable Φ_i is used to determine the computational cell is neighboring a shock. It is computed as

$$\Phi_i = \begin{cases} \max\left(\widetilde{\Phi}_i, \widetilde{\Phi}_{i+1}\right), & \text{if } \; p_{i+1} - p_{i-1} < 0, \\ \max\left(\widetilde{\Phi}_i, \widetilde{\Phi}_{i-1}\right), & \text{otherwise} \end{cases} \tag{258}$$

3.5 Hybrid Schemes for MHD

The objective of a hybrid methodology is to optimally design a numerical scheme with the ability to resolve any physical discontinuities arising the flow while still retaining the benefits of using a low numerical dissipation in smooth regions of the flow. WENO schemes do this to some extent by changing the order of the differencing stencil when necessary. However, these schemes are still more numerically dissipative when compared to high order compact schemes, since WENO schemes naturally introduce dissipation through the flux vector splitting procedure. In the hybrid framework proposed in this thesis, a smoothness function is used to determine

whether the numerical flux should be computed using a shock capturing scheme or a low dissipation central differencing scheme. In the current hybrid methodology, the switch variable s is given as a Heaviside step function, thus the computed fluxes are not blended, the method either uses one or the other. The benefit of this approach is that the computational cost associated with any shock capturing scheme can be avoided if possible. Additionally, it is not immediately obvious that a blending procedure would be conservative. Explicitly, the numerical flux is computed in the following manner

$$\mathbf{F}_{i+1/2,j,k} = s_{i+1/2,j,k}\mathbf{F}^{c}_{i+1/2,j,k} + (1 - s_{i+1/2,j,k})\mathbf{F}^{u}_{i+1/2,j,k} \tag{259}$$

where a similar procedure is used for the y- and z-directional fluxes. Here, $\mathbf{F}^{c}_{i+1/2,j,k}$ is used to represent the numerical flux computed from a low dissipation central scheme, and $\mathbf{F}^{u}_{i+1/2,j,k}$ is used to represent the numerical flux computed from a shock capturing scheme.

Several smoothness indicating functions can be found in the literature. Such functions are also used self-adjusting artificial diffusion schemes where an explicit diffusive term is integrated into the governing equations in order to control numerical oscillations. These functions are dynamically computed using the physical variables of the flow. For example, the first use of a self-adjusting parameter, computed it in the following manner,

$$s_{i+i/1} = n\left[\frac{|\phi_{i+1} - \phi_i|}{\max_{j\in\mathcal{D}}|\phi_{j+1} - \phi_j|}\right]^m, \tag{260}$$

where n and m are user defined constants, and ϕ is a some physical variable, such as pressure. The denominator captures the largest jump in the flow. More recent methods adopt the Jameson artificial dissipation scheme, which was design to stabilize central schemes near shocks. The smoothness indicator in this approach is based on the the curvature of the pressure field, i.e.,

$$s_i = \frac{p_{i+1} - 2p_i + p_{i-1}}{p_{i+1} + 2p_i + p_{i-1}} \tag{261}$$

The concept of switching between two numerical schemes with dispersive and dissipative characteristics is more recent. The design of these adopt some of the similar ideas used for artificial dissipation methods, however, the smoothness functions are more varied. Adams and Shariff [2] and Pirozzoli [155] use smoothness indicating function based on the gradient in the fluxes. Hill and Pullin [91] suggest a switch based on WENO smoothness factors. Ducros et al. [58] develop a sensor based on the ratio of bulk dilatation to the total vorticity magnitude since large values of bulk dilatation is associated with shock waves.

In this thesis, a previously developed hybrid methodology is applied to MHD [69]. In this approach, three types of discontinuities are detected by monitoring the change in the flow gradients. Let the variable ϕ represent either the pressure or density field. The sensor function based on ϕ is computed as

$$s_{\phi,i} = \begin{cases} \frac{|\phi_{i+1}-2\phi_i+\phi_{i+1}|}{|\phi_{i+1}-\phi_i|+|\phi_i-\phi_{i-1}|} - s^0_\phi, & \text{if } \ |\phi_{i+1} - 2\phi_i + \phi_{i+1}| > \epsilon_\phi \phi_i \\ -s^0_\phi, & \text{otherwise} \end{cases} \tag{262}$$

where the coefficients s^0_p, s^0_ρ, ϵ_p, and ϵ_ρ are user determined constants, which must be determined from numerical experimentation on a per case basis. These sensors identify the regions where the pressure and/or density fields show rapid variations and where these variables show significant gradients, which are combined to give the parameter $s_{i+1/2}$ as

$$s_{i+1/2} = \begin{cases} 1, & \text{if } \ \max\left(s_{p,i}, s_{\rho,i}, s_{p,i+1}, s_{\rho,i+1}\right) \leq 0 \\ 0, & \text{otherwise} \end{cases} \tag{263}$$

3.6 Verification of Numerical Methods for MHD

In the following sections, the conservative finite difference and finite volume MHD schemes are evaluated using several one dimensional and two dimensional test problems. No three dimensional verification tests are conducted, but all tests produce

the same results regardless the orientation of the Cartesian plane. Three dimensional simulations are used to conduct the validation tests, which are discussed in the next chapter. In all of the following tests, the ratio of specific heats is assumed to be constant ($\gamma = 5/3$).

The proposed method in this thesis is a finite difference, hybrid numerical method either using a CT method or the projection method. The upwind scheme uses a fifth -order WENO-Z reconstruction method coupled with a high order compact scheme using the hybrid methodology. Time integration is done using a low storage, strong stability preserving, five stage, fourth order Runge-Kutta scheme. This numerical method is compared to the a finite volume CTU scheme using the PPM. This method is commonly used in astrophysics for MHD simulations, and thus, it serves as a baseline for comparison of the newly proposed finite difference hybrid scheme for MHD.

Table 2 compares the two methods. The finite difference method is referred to as the FD-Hybrid scheme while the baseline finite volume scheme is referred to as the FV-CT scheme, which is a temporally and spatially un-split constrained transport method for two-dimensional MHD simulations. This method is second order both in time and space. As a FDS scheme, a Riemann solver is necessary to compute the inviscid fluxes. For all tests, a hybrid HLLD / HLL approximate Riemann solver is used, and the approximated wave speeds are computed using the Roe-type averaging. Furthermore, to avoid numerical oscillations near very strong shocks, it is often necessary to reduce the order of reconstruction step. A second-order flow sensor is used to detect large gradients in the pressure or density.

Table 2: Summary of the two different numerical methods. The finite difference scheme is herein referred to as the FD-Hybrid scheme. The finite volume scheme is referred to as FV-CT and is implemented as a reference case since this method is most commonly used in the astrophysical community [67].

	FD-Hybrid	**FV-CT**
Discretization	Finite Difference	Finite Volume
Dimensions	1-D, 2-D, or 3-D	1-D or 2-D
Hybrid Methodology	Yes	No
Spatial Integration	5^{th}-order WENO-Z / Compact	2^{nd}-order PPM
Time Integration	5-stage, 4^{th}-order Runge-Kutta	Forward Euler
Directional Splitting	Direct Split	$\perp$ reconstruction
$\nabla \cdot \mathbf{B}$ method	Projection, 2^{nd}-order CT	3^{rd}-order CT
Resistive MHD	Yes	No

3.6.1 One-Dimensional Tests

To test the ability of the numerical schemes to accurately obtain solutions to flows with both continuous and discontinuous features, the one-dimensional MHD equations, Eq. 204, are solved in a shock tube configuration with initial conditions defined by two MHD Riemann problems. The first test problem, originally used by Dai and Woodward [47] (herein referred to as the DW94 Riemann problem), is designed to test the accuracy of the numerical scheme when all seven characteristic waves are present; fast shocks, slow shocks, and rotational discontinuities all propagate on either side of a contact discontinuity. The second test problem, originally discussed by Brio and Wu [28] and later modified by Ryu and Jones [173] to use a constant adiabatic index of $\gamma = 5/3$ (herein referred to as the RJ95 Riemann problem), is designed to demonstrate the existence compound wave solutions to the MHD hyperbolic equations. It is worth noting that the hydrodynamic data in this test are the same as for Sod's Riemann problem.

- The DW94 Riemann problem

The one-dimensional computational domain is defined in the interval $-0.5 < x < 0.5$ using N grid points. The numerical results are compared to the exact solution at a time of $t_{max} = 0.2$. The solution contains two fast shocks, two rotational discontinuities, two slow shocks, and a contact discontinuity [47, 173]. The Riemann problem is initially defined by the primitive left and right state vectors given by $\mathbf{u}_L$ for $x < 0$ and $\mathbf{u}_R$ for $x > 0$, where

$$\mathbf{u}_L = \begin{bmatrix} \rho_L \\ v_{x,L} \\ v_{y,L} \\ v_{z,L} \\ B_{x,L} \\ B_{y,L} \\ B_{z,L} \\ p_L \end{bmatrix} = \begin{bmatrix} 1.08 \\ 1.2 \\ 0.01 \\ 0.5 \\ 2/\sqrt{4\pi} \\ 3.6/\sqrt{4\pi} \\ 2.0/\sqrt{4\pi} \\ 0.95 \end{bmatrix}, \quad \mathbf{u}_R = \begin{bmatrix} \rho_R \\ v_{x,R} \\ v_{y,R} \\ v_{z,R} \\ B_{x,R} \\ B_{y,R} \\ B_{z,R} \\ p_R \end{bmatrix} = \begin{bmatrix} 1.0 \\ 0.0 \\ 0.0 \\ 0.0 \\ 2/\sqrt{4\pi} \\ 4.0/\sqrt{4\pi} \\ 2.0/\sqrt{4\pi} \\ 1.0 \end{bmatrix}. \tag{264}$$

Figure 18 shows the discontinuous density, pressure, velocity and magnetic fields at a time of$t = 0.2$ for two resolutions, $N = 800$ and $N = 200$. Besides very small oscillations near the flow discontinuities, the results for $N = 800$ compare extremely well to the exact solution. Both the FD-Hybrid and the FV-CT schemes are able to sufficiently resolve discontinuous within 1-2 grid points without generating large spurious oscillations. The L1 errors for both schemes are shown in Fig. 19. Since the solution contains discontinuities, the numerical results are only expected to demonstrate first order convergence. More importantly, both schemes have similar error magnitudes.

- The RJ95 Riemann problem

Similar to the DW94 Riemann problem, RJ95 Riemann problem is numerically simulated in a one-dimensional computational shock tube configuration with a domain

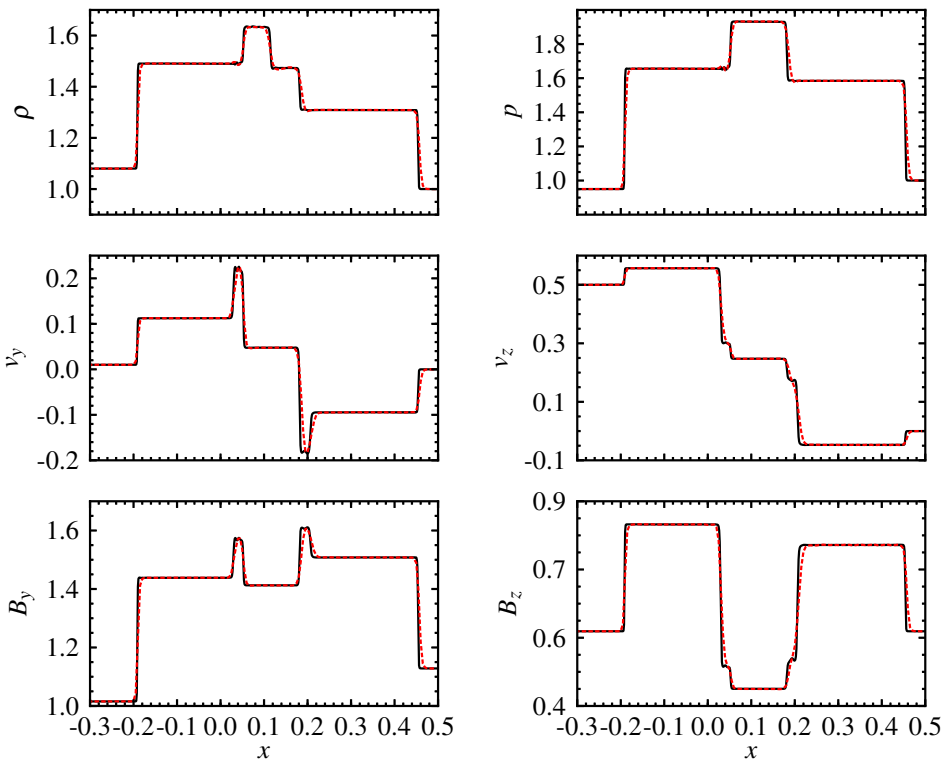

Figure 18: Results of the DW94 shock tube test for the variables ρ, p, v_y, v_z, B_y, B_z at two grid resolutions, $N = 800$ (black) and $N = 200$(red).

defined in the interval $-0.5 < x < 0.5$ using N grid points. The numerical results are compared to the exact solution at a time of $t_{max} = 0.1$. The solution not only contains ordinary waves (two fast rarefaction waves, a slow shock, and a contact discontinuity), but also compound waves resulting from the non-convexity of the MHD hyperbolic system. For this problem, the compound wave is formed by an intermediate shock followed by a slow rarefaction wave [28, 173]. The Riemann problem is initially defined by the primitive left and right state vectors, which are given by $\mathbf{u}_L$ for $x < 0$ and $\mathbf{u}_R$

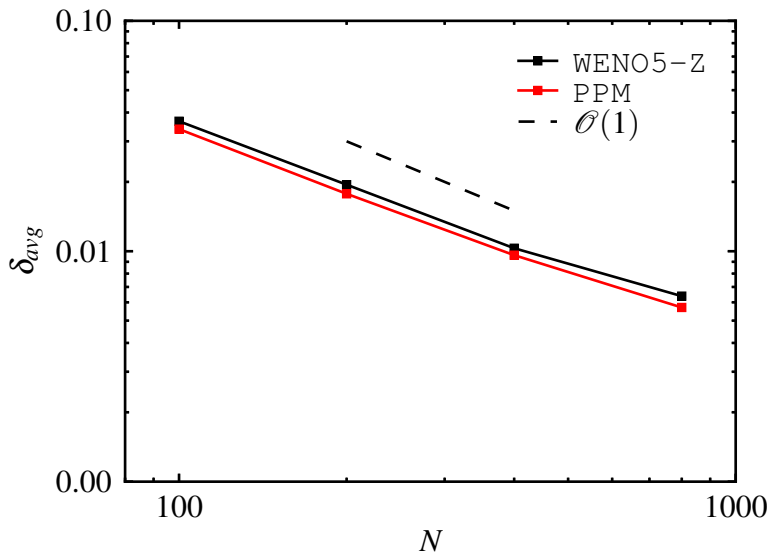

Figure 19: Sum of the numerical errors for the finite-difference and finite-volume schemes. The convergence is first-order because of the presence of discontinuities in the computational domain.

for $x > 0$, where

$$\mathbf{u}_L = \begin{bmatrix} \rho_L \\ v_{x,L} \\ v_{y,L} \\ v_{z,L} \\ B_{x,L} \\ B_{y,L} \\ B_{z,L} \\ p_L \end{bmatrix} = \begin{bmatrix} 1.0 \\ 0.0 \\ 0.0 \\ 0.0 \\ 0.75 \\ 1.0 \\ 0.0 \\ 1.0 \end{bmatrix}, \quad \mathbf{u}_R = \begin{bmatrix} \rho_R \\ v_{x,R} \\ v_{y,R} \\ v_{z,R} \\ B_{x,R} \\ B_{y,R} \\ B_{z,R} \\ p_R \end{bmatrix} = \begin{bmatrix} 0.125 \\ 0.0 \\ 0.0 \\ 0.0 \\ 0.75 \\ -1.0 \\ 0.0 \\ 0.1 \end{bmatrix} \tag{265}$$

Figure 20 shows the discontinuous density, pressure, velocity and magnetic fields at a time of$t = 0.1$ for two resolutions, $N = 800$ and $N = 200$. Besides very small oscillations near the flow discontinuities, the results for both the $N = 800$ and $N = 200$ resolutions compare extremely well to the exact solution. Both the FD-Hybrid and the FV-CT schemes are able to sufficiently resolve discontinuous within

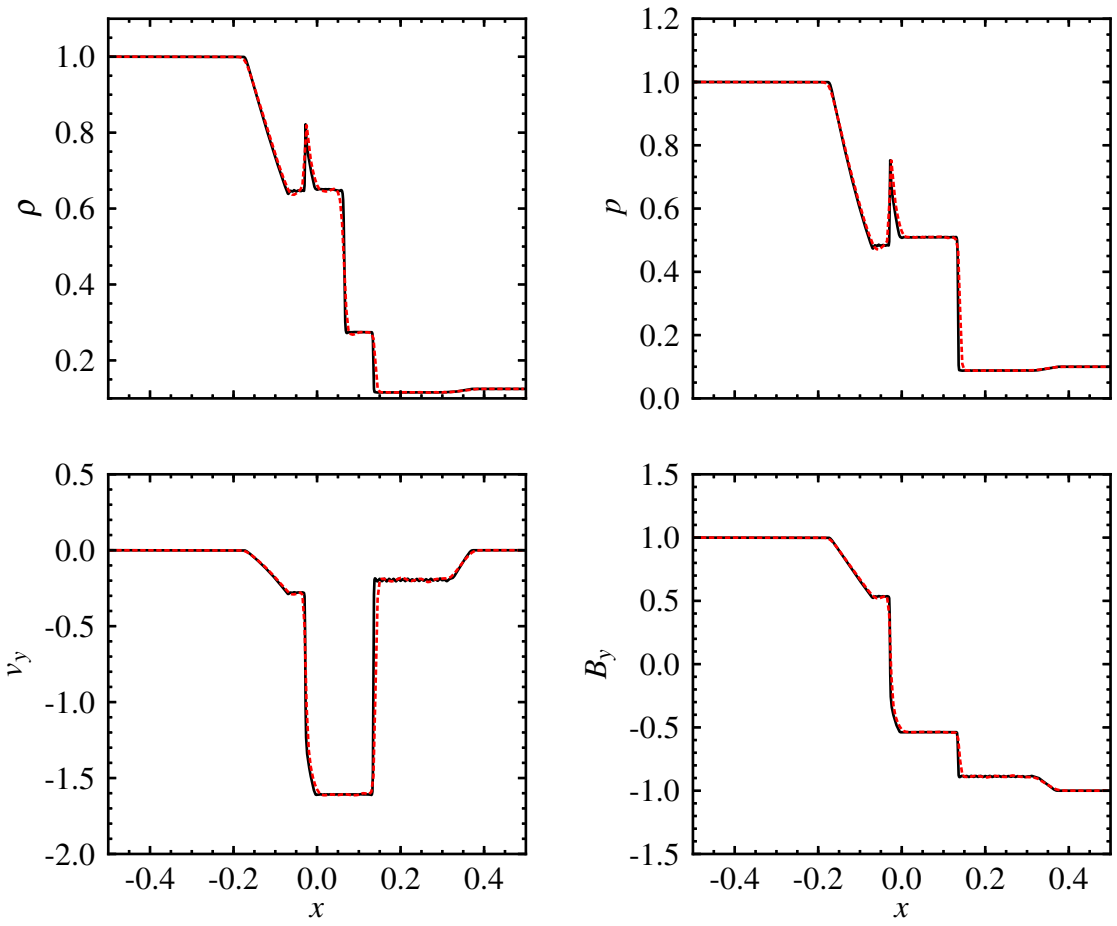

Figure 20: Results of the RJ95 shock tube test for the variables ρ, p, v_y, v_z, B_y, B_z at two grid resolutions, $N = 800$ (black) and $N = 200$(red).

1-2 grid points without generating large spurious oscillations.

3.6.2 Circularly-Polarized Alfvén Wave

This test problem involves the simulation of a propagating circularly polarized (CP) Alfv'en wave on a (x,y) Cartesian plane at angle α relative to the x-axis. The test is particularly useful since the initial condition is a non-linear solution of the multi-dimensional MHD system. For periodic boundary conditions, the computational domain is defined by $0 < x < 1/\cos\alpha$ and $0 < y < 1/\sin\alpha$. Letting $\xi = x\cos\alpha + y\cos\alpha$ be the coordinate in the direction of wave propagation, and $\eta = y\cos\alpha - x\sin\alpha$ be

the coordinate in direction transverse to the wave propagation, the exact solution to the propagating CP Alfv'en wave is given as

$$\mathbf{v} = \begin{bmatrix} v_\xi \\ v_\eta \\ v_z \end{bmatrix} = \begin{bmatrix} 0 \\ A_0 \sin(2\pi\xi) \\ A_0 \cos(2\pi\xi) \end{bmatrix}, \quad \mathbf{B} = \begin{bmatrix} B_\xi \\ B_\eta \\ B_z \end{bmatrix} = \begin{bmatrix} 1 \\ A_0 \sin(2\pi\xi) \\ A_0 \cos(2\pi\xi) \end{bmatrix}. \tag{266}$$

where A_0 is the wave amplitude. The density and pressure are constant, $\rho = 1$ and $p = 0.1$, respectively. For these values, the Alfvén wave has a period of $T = 1$ and a propagation speed of $v_A = 1$. The sound speed is $c_s = \sqrt{\gamma p/\rho} \approx 0.4$.

As has been observed by a few others, the numerical solution of this problem is subject to a parametric decay instability due to the non-linear wave-wave interactions of the compressive modes [128]. Once this happens, it is no longer possible to compare the exact solution. If the wave amplitude is set to some small value, $A_0 = 0.1$, and the simulation only run for a few cycles, the instability can be avoided.

Figure 21 shows the error magnitudes after one cycle of the CP Alfvén wave for various numerical methods. The finite-difference, fifth-order WENO-Z scheme with the constrained transport method and the projection method is compared to the finite-volume PPM method. Since the both FD-Hybrid and FV-CT use a the same second-order constrained transport algorithm, both schemes converge to second order. This is one of the significant drawbacks of using this type of constrained transport method, which involves averaging the magnetic field fluxes, with high-order finite-difference schemes. While such methods exactly preserve $\nabla \cdot \mathbf{B} = 0$ to the discretization error of the computational grid, to achieve high-order accurate solutions other methods are required. For instance, in Fig. 21, the fifth-order WENO-Z scheme coupled with a projection method FD-Hybrid is able to achieve an approximately fourth-order accurate solution. The reduction in accuracy at higher resolution is a limitation of the projection scheme. The implemented Poisson solver is only second order accurate. Since this is a smooth flow, it is important to note that it is possible

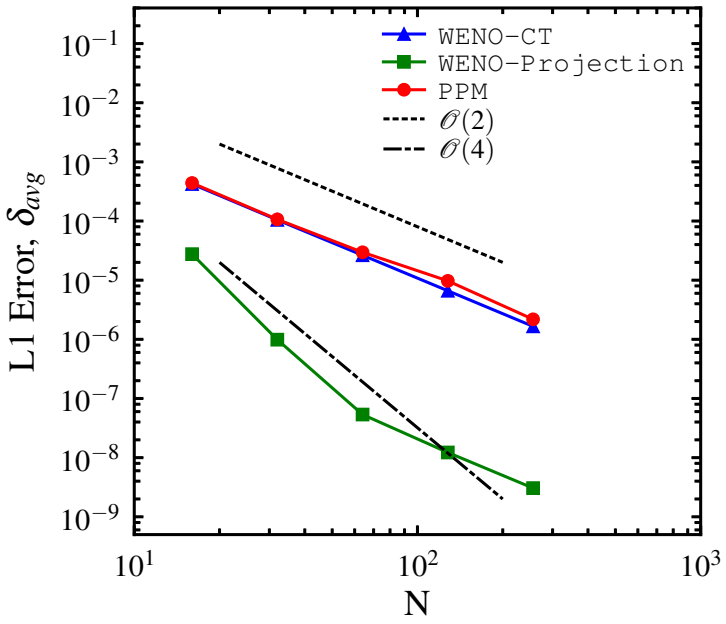

Figure 21: Average error for the finite-volume, piecewise parabolic method FV-CT, the fifth-order WENO-Z method with constrained transport and a projection scheme.

to achieve a similarly accurate solution using the finite-difference methods without any magnetic divergence method. This is because the the accuracy of the numerical scheme is high enough to keep the errors in $\nabla \cdot \mathbf{B}$ small. This is not the case for the finite volume scheme.

3.6.3 Magnetic Field Loop Advection

For this test problem, the advection and diffusion of weak magnetic field loop is simulated. Since the field is weak, the magnetic field essentially propagates as a passive scalar. The test is particularly challenging for all numerical MHD schemes. If the magnetic field divergence errors are not properly controlled, the initial geometry of the magnetic field loop quickly disintegrates. For the advection problem, the most stringent test is when the magnetic field loop moves at angle α relative to the x-axis in the (x, y) Cartesian plane. The computational domain extends from $-1 < x < 1$, and $-0.5 < y < 0.5$ with $2N \times N$ grid points and period boundary conditions on

both the $x-$ and $y-$boundaries.

The pressure and density are initially uniform, $p = 1.0$ and $\rho = 1$, respectively. The velocity vector is defined by

$$\mathbf{v} = \begin{bmatrix} v_\xi \\ v_\eta \\ v_z \end{bmatrix} = \begin{bmatrix} v_0 \cos(\alpha) \\ v_0 \sin(\alpha) \\ 0 \end{bmatrix}. \tag{267}$$

where $\cos\theta = 2/\sqrt{5}$ and $\sin\theta = 1/\sqrt{5}$. In the diffusion tests, $v_0 = 0$, and in the advection tests, $v_0 = \sqrt{5}$. The velocity is set such at that $t = 2$ the magnetic field loop will have advection one complete cycle along the grid diagonal. The magnetic field components are initialized from the magnetic vector potential where

$$A_z = \begin{cases} A_0(R - r) & : \text{for} \quad r \leq R \\ 0 & : \text{for} \quad r > R \end{cases} \tag{268}$$

where $A_0 = 10^{-3}$, $R = 0.3$, and $r = \sqrt{x^2 + y^2}$. Inside the magnetic field loop, the ratio of the thermodynamic and magnetic pressure is $\beta = 2p/B^2 = 2 \times 10^6$.

Figure 22 shows the magnetic pressure $(B_x^2 + B_y^2)$ at $t = 0$ and $t = 2$ for the finite-difference method with constrained transport.

3.6.4 Orszag-Tang Vortex

Originally used to study the transition to supersonic MHD turbulence, the Orszag-Tang vortex is now a standard test problem for multi-dimensional MHD codes. The test is a useful qualitative indicator of whether the MHD scheme is correctly maintaining the constraint of a divergent-free magnetic field. While the problem is sensitive to errors in the magnetic field divergence, and over time if such errors are not maintained to small values, negative pressures will develop late into the simulation, but the results seem to be more dependent on the spatial order of the numerical scheme. As such, this test is treated only as a weak indicator of code verification.

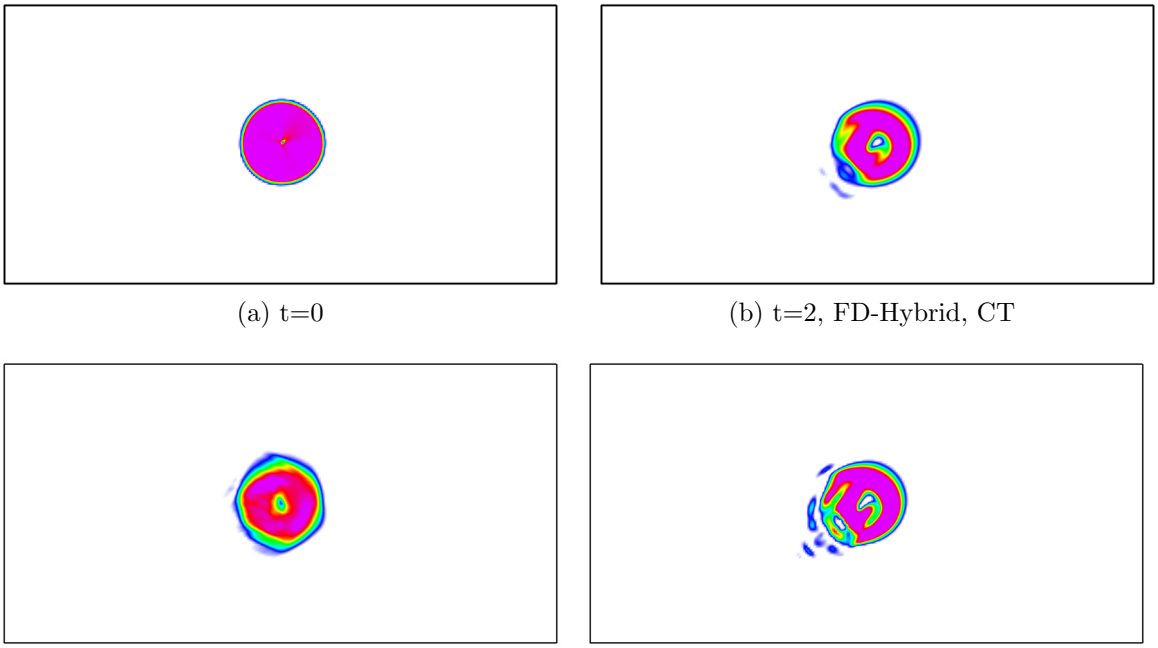

(a) t=0 (b) t=2, FD-Hybrid, CT

(c) t=2, FD-Hybrid, Projection (d) t=2, FV-CT

Figure 22: Magnetic pressure at $t = 2$ for the fifth-order WENO-Z method with constrained transport.

The Orszag-Tang vortex problem exhibits the unsteady formation of several MHD shock waves and the development of current sheets, and as such it is relevant to many of the problems of interest since instabilities arising from the formation of these current sheets results in a transition to turbulence. The initial conditions of the problem are given by:

$$\mathbf{v} = \begin{bmatrix} v_x \\ v_y \\ v_z \end{bmatrix} = \begin{bmatrix} -\sin(y) \\ \sin(x) \\ 0 \end{bmatrix}, \quad \mathbf{B} = \begin{bmatrix} B_x \\ B_y \\ B_z \end{bmatrix} = \begin{bmatrix} -\sin(y) \\ \sin(2x) \\ 0 \end{bmatrix}. \tag{269}$$

For these conditions, the initial Mach number is 1. The computational domain is a square $0 < x, y < 2\pi$, $N \times N$ box with periodic boundary conditions in both directions. The final time is $t_{max} = \pi$. For comparisons to other results, the magnetic field here has been normalized by $1/\sqrt{4\pi}$.

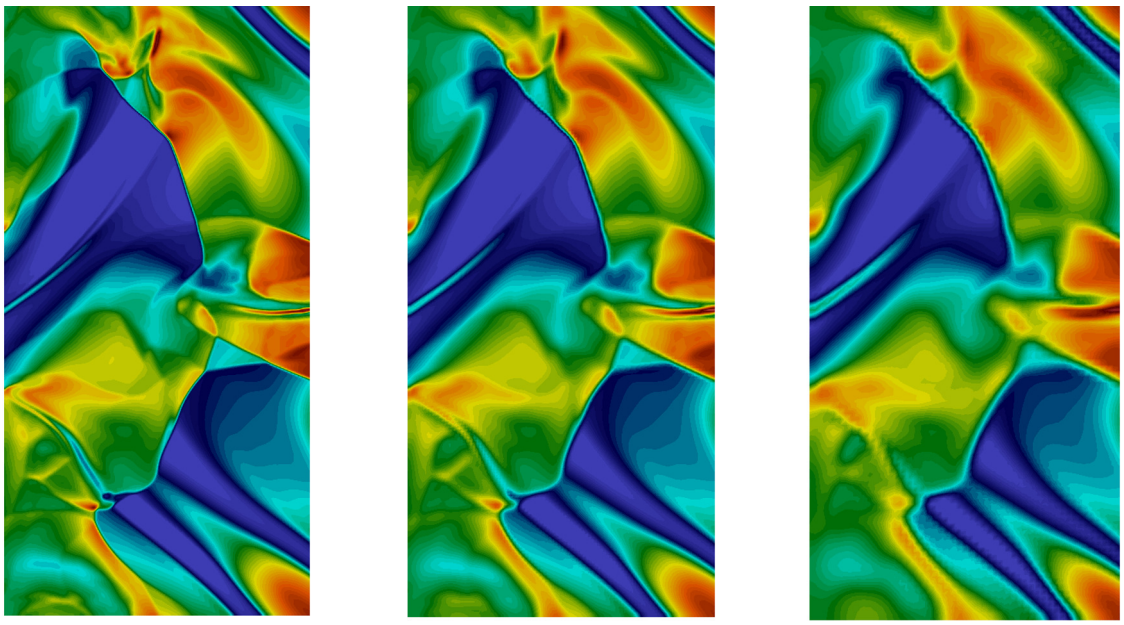

(a) $N = 400$, FD-Hybrid, CT (b) N=200, FD-Hybrid, CT (c) N=100, FD-Hybrid, CT

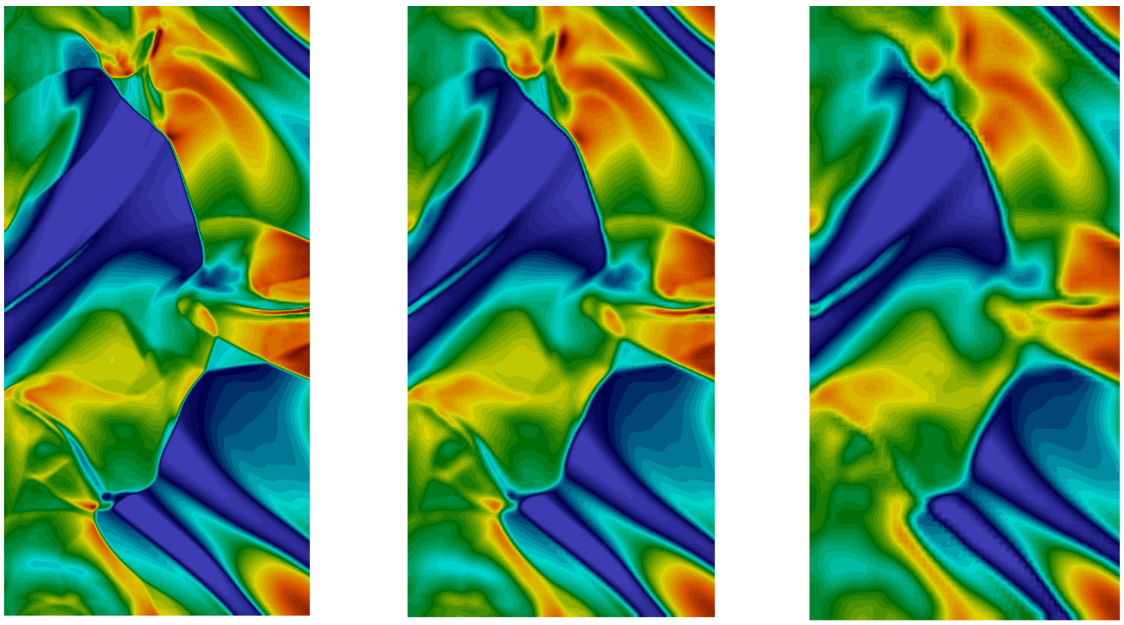

(d) $N = 400$, FV-CT (e) N=200, FV-CT (f) N=100, FV-CT

Figure 23: The temperature at at $t = \pi$ for the fifth-order WENO-Z method with constrained transport and the finite-volume PPM scheme at difference grid resolutions.

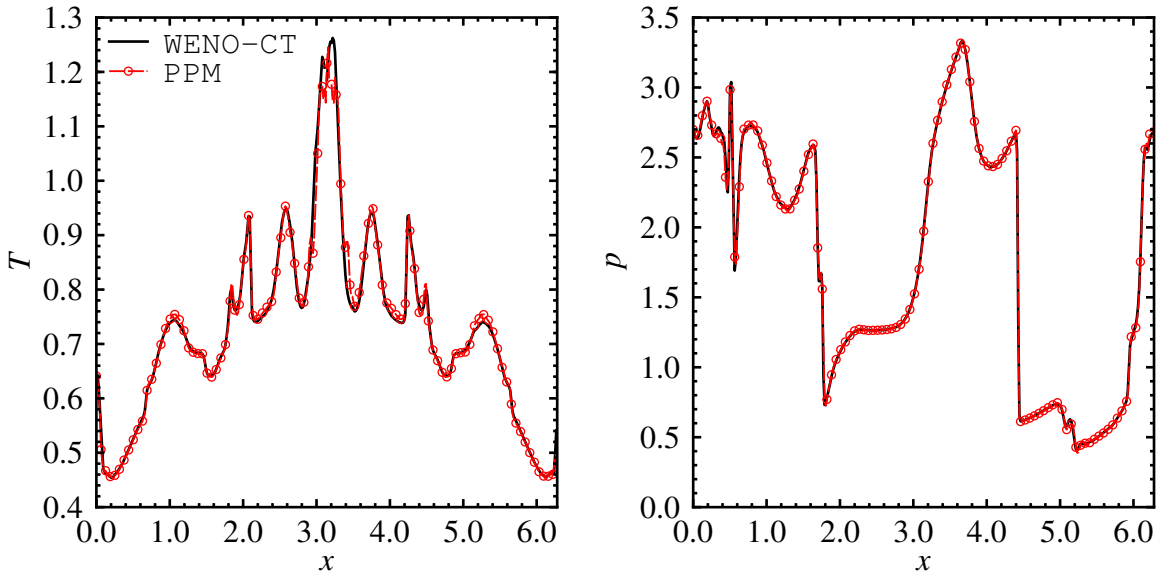

(a) Temperature at $y = \pi$ (b) Pressure at $y = 0.625\pi$

Figure 24: (a) Line plot of the temperature at $y = \pi$, and (b) line plot of the pressure at $y = 0.625\pi$.

3.6.5 The fast MHD rotor

This test problem was first suggested by Brackbill [26] and was used by Balsara [10] to evaluate the ability of a numerical scheme to simulate a propagating strong torsional Alfvén waves. These waves are a mechanism for the loss of angular momentum during star formation, and for this reason, the test has some physical importance besides testing the robustness of the numerical scheme. The problem is defined by a disk of dense fluid, $\rho_1 = 10$, with a radius $R = 0.1$ rotating at a high angular velocity, $\omega = 20$, relative to a static, magnetized background fluid of lower density, $\rho_2 = 1$. The ambient pressure and magnetic field are uniform, $p = 1$, $B_x = 5\sqrt{4\pi}$, respectively. The adiabatic index is constant and set to $\gamma = 1.4$ in this simulation.

The computational domain defined by $0 < x < 1$ and $0 < y < 1$ resolved by $N \times N$ grid points or cells. A taper function is used to smooth the numerical transition between the dense and light species avoiding initial transients. The function is defined as $f = (R_1 - r)/(R_1 - R_0)$ where $R_0 = R = 0.1$ and $R_1 = 0.115$. The velocity is then

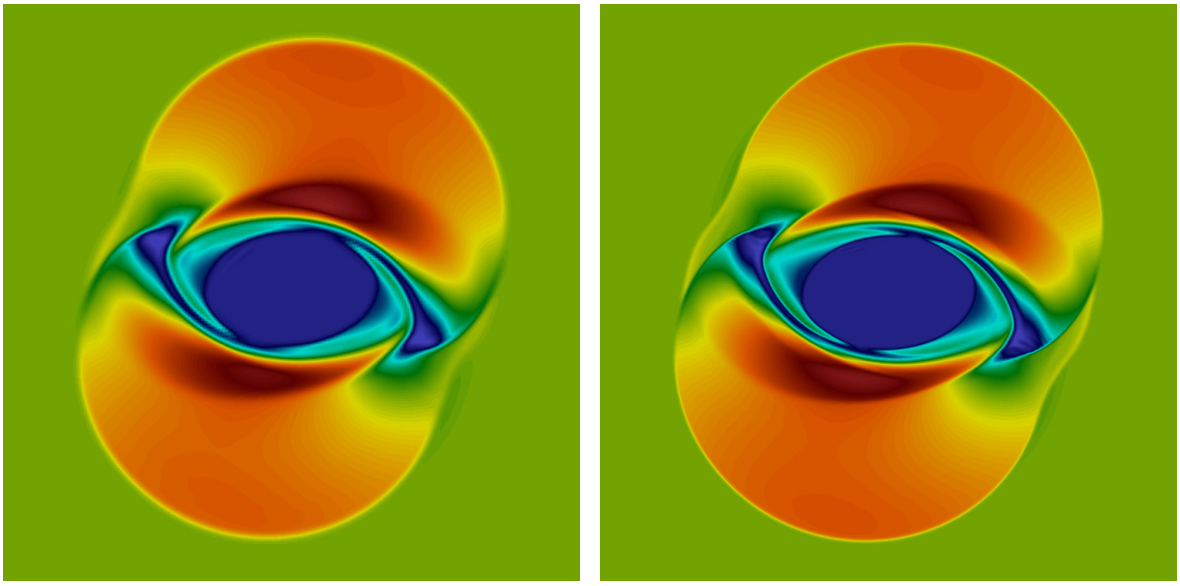

(a) FD-Hybrid, CT (b) FD-Hybrid, Projection

Figure 25: Contours of the magnetic pressure $p_m = (B_x^2 + B_y^2)/2$ at $t = 0.15$ for the FVS method with fifth-order WENO-Z reconstruction using the (a) constrained transport method, and (b) the projection scheme. For both simulations, $N = 200$.

specified by

$$\mathbf{v}^T = \begin{cases} \left(\frac{-v_0(y-0.5)}{r_0}, \frac{v_0(x-0.5)}{r_0}, 0\right) & : \text{for} \quad r \leq R_0 \\ \left(\frac{-fv_0(y-0.5)}{r_0}, \frac{fv_0(x-0.5)}{r_0}, 0\right) & : \text{for} \quad R_0 < r < R_1 \\ (0,0,0) & : \text{for} \quad r \geq R_1 \end{cases} \tag{270}$$

and similarly $\rho = 1 + 9f$. As the magnetic field "winds up", the rotating dense fluid is confined eventually taking the oblong shape shown in Fig. 25. Numerical schemes that do not maintain magnetic divergence errors well show significant oscillations inside the disk. For both the schemes here, at $N = 200$, the numerical schemes perform well. From the contour plots, shown in Fig. 25, the projection scheme is less diffuse since it avoids the use of constrained transport second-order averaging. The projection scheme is used once every 10 iterations. The frequency of the cleaning depends on the problem, but ideally, the projection step should be used at a minimum to maintain high-order accuracy.

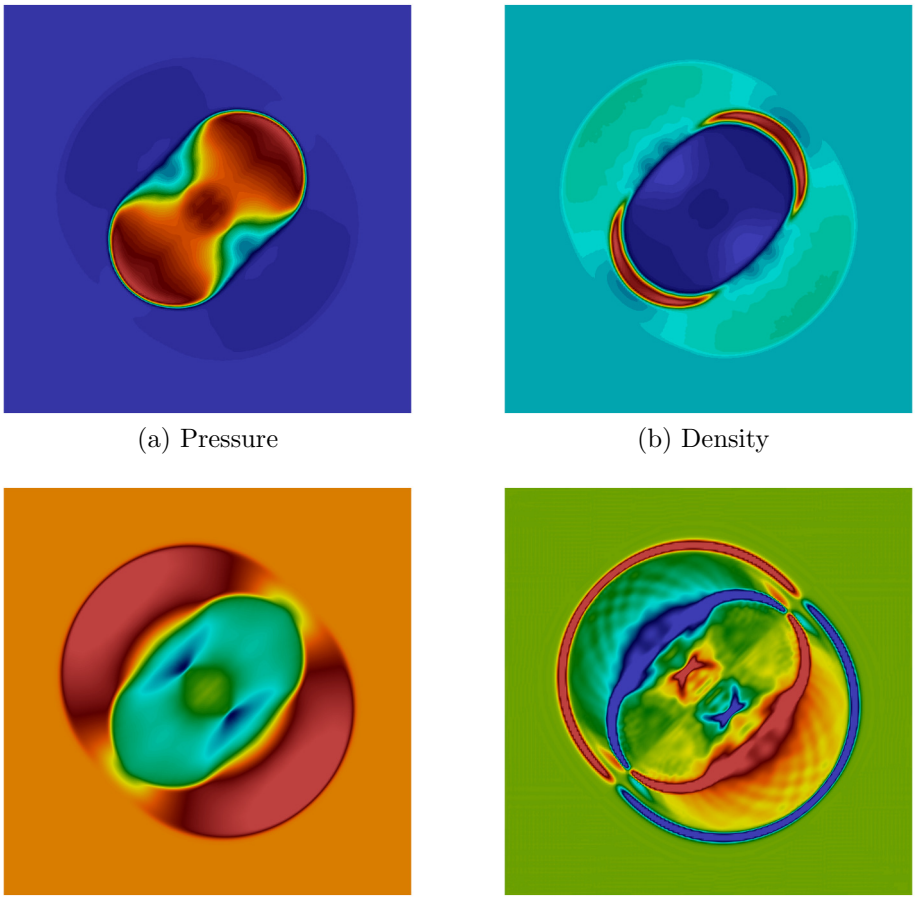

(a) Pressure (b) Density

(c) Magnetic Pressure (d) Current Density

Figure 26: Contours of the magnetic pressure (a) thermodynamic pressure (b) density (c) magnetic pressure $p_m = (B_x^2 + B_y^2)/2$(d) current density at $t = 0.2$ with a resolution of $N = 200$.

3.6.6 MHD Blast Wave

As a final test problem, one which has some importance to the focus of this work, the explosion of a dense central region of pressured gas into a static, magnetized surrounding region is simulated. This test has been adopted by many others and is used to test the numerical scheme's ability to model the formation and propagation of strong discontinuities. As with the rotor problem, any numerical schemes with large magnetic field divergence errors will fail to preserve a positive thermodynamic pressure.

The computational domain is defined by the unit square, $-0.5 < x < 0.5$ and $-0.5 < x < 0.5$ discretized by $N \times N$ grid points or cells. In the surrounding gas, the density $\rho = 1$, the pressure $P = 1$, the velocity, $\mathbf{v} = 0$, and the magnetic field components $B_x = B_y = 10/\sqrt{2}$, and $B_z = 0$ are all uniform. In the center of the domain, a high pressure region with a radius of $R = 0.125$ and pressure $P = 100$ is defined. This high pressure region drives the explosion. For the plasma, in the high pressure zone, $\beta = 2P/B^2 = 2$, and in the ambient surroundings, $\beta = 2 \times 10^{-2}$.

Figure 26 shows the contours of pressure, density, magnetic pressure, and current density at a time $t = 0.2$ using $N = 200$ grid points. Two denser regions of gas are noticeable in the contours of density. These two regions are bounded by a slow magneto-acoustic secondary shock wave on the outside and the contact discontinuity on the inside separating the explosively driven gases (surrounding) from the exploding gases (products). The motion of the fluid is aligned in the direction of the magnetic field, which is aligned along the domain diagonal. Figure 27 shows the same simulation but with different values of the initial magnetic field. As the strength of the magnetic field is reduced, the small-scale features associated with the fluid instabilities are visible in the density contours.

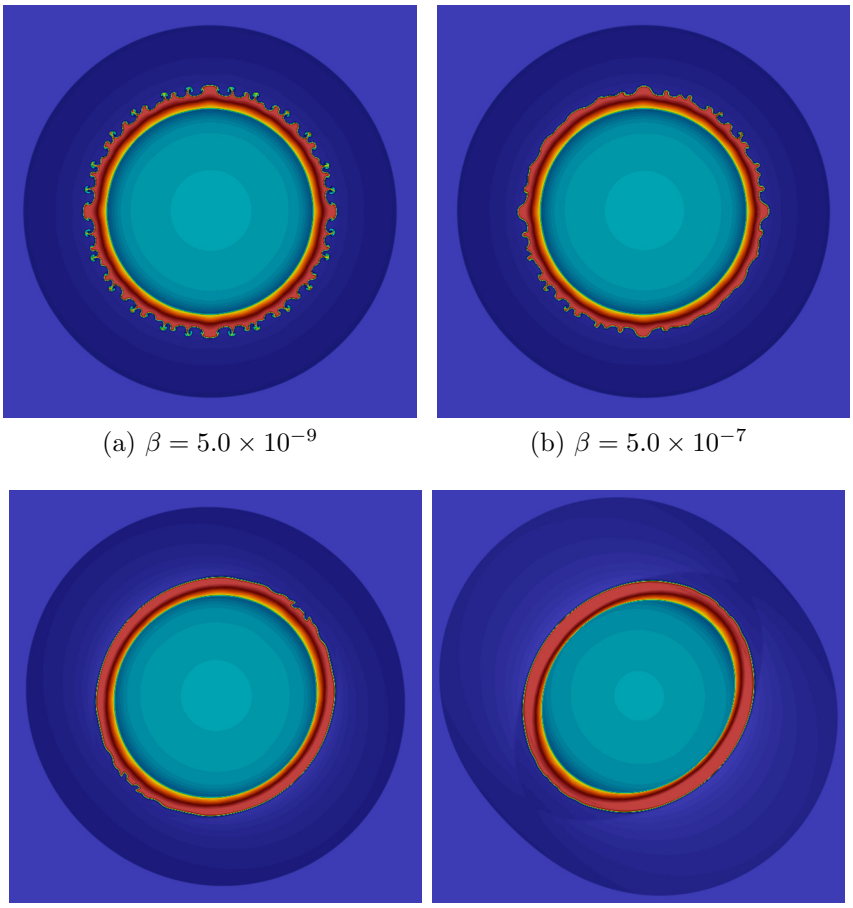

(a) $\beta = 5.0 \times 10^{-9}$ (b) $\beta = 5.0 \times 10^{-7}$

(c) $\beta = 1.25 \times 10^{-5}$ (d) $\beta = 5.0 \times 10^{-3}$

Figure 27: Contours of the density at $t = 0.2$ for three different values of the magnetic field (a) $\beta = 0.001$ (b) $\beta = 0.01$ (c) $\beta = 0.05$, (d) $\beta = 1.0$

CHAPTER IV

NUMERICAL STUDIES FOR MHD

In the previous section, several simple tests were used to verify the implementation of two MHD numerical schemes, a flux-vector splitting, finite-difference method using fifth-order WENO-Z reconstruction, and a flux-difference splitting, finite-volume method using the PPM for MHD, which in some regards is a standard approach in the astrophysical community.

In the following subsections, a few simple, but physically important problems are discussed, which have a direct significance to the objectives of this work. The purpose is two-fold. To address some of the numerical issues and to demonstrate, if only qualitatively, that the MHD schemes have been implemented correctly and are producing physically meaningful results.

4.1 Decaying Isotropic Turbulence in an External Magnetic Field

In this problem, a decaying isotropic turbulence problem is considered on a uniformly discretized by N grid points or cells in each direction of a Cartesian computational domain defined by $x \in [0, L]$, $y \in [0, L]$, and $z \in [0, L]$ where the length scale L left as a free parameter in defined the Reynolds number of the numerical simulation. The simulations are considered to be DNS and are conducted for a low magnetic Reynolds number. Previous work has investigated high magnetic Reynolds number isotropic turbulence using both DNS and LES methods [139, 140]. The initial turbulent modes of random phase and amplitude are defined by a Kraichnan energy spectrum [180],

$$E(k) = Ak^4 \exp\left(-\frac{2k^2}{k_0^2}\right) = 16\sqrt{2\pi}u_{\text{rms}}\left(\frac{k^4}{k_0^5}\right)\exp\left(-\frac{2k^2}{k_0^2}\right) \tag{271}$$

Table 3: Summary of the initial conditions and parameters for the numerical simulations of the decaying isotropic compressible turbulence.

Case	Resolution	Re_λ	M_t	$k_{max}\eta$	u_{rms} (m/s)	λ (m)	σ (S/m)	N
H1	256^3	175	0.488	2.3514	98.1	0.799	0.0	0
H2	256^3	243	0.712	1.8974	145	0.768	0.0	0
M2	256^3	243	0.712	1.8974	145	0.768	10	1
M3	256^3	243	0.712	1.8974	145	0.768	10	5
M4	256^3	243	0.712	1.8974	145	0.768	10	20

where the orientation of the modes $\mathbf{k}$ are chosen based on a set of random orthogonal basis vectors ($\mathbf{e_k} := \mathbf{k}/k, \mathbf{e}_1, \mathbf{e}_2 := \mathbf{e_k} \times \mathbf{e}_1$) such that the linear combination of vector field is initially divergent free [169]. The coefficient A sets the initial value of the turbulent kinetic energy.

Decaying isotropic compressible turbulence is limited by the startup-process since the turbulent state often rapidly decays before the initial turbulent field can become correlated. There are multiple approaches to address this problem [180]. For this qualitative demonstration, the simplest option is the best. The initial zero divergence random vector field ($\mathbf{u}$ or $\mathbf{B}$) is used with constant pressure, density, and temperature fields. The properties of the initial turbulent state are defined by case H1 in Table 3. For this initial state, a large-eddy turnover time $\tau = 3.46$ ms. Fig. 28 shows the decay of Re_λ and the skewness of the velocity field. Once a homogenous, isotropic turbulent state is achieved, the velocities are scaled up in case H2 to be used with the magnetohydrodynamic simulations, cases M1-4. For these cases, only the low magnetic Reynolds number limit is considered. The non-dimensional number describing the dynamics of such flows is the Stuart number N, which was defined in the previous chapter as the ratio of the magnetic force to the inertial force. The electrical conductivity $\sigma = 10$ is assumed to be constant. The value is typical of plasmas produced by high-energy explosives. Figure 29 shows the decay of Re_λ and

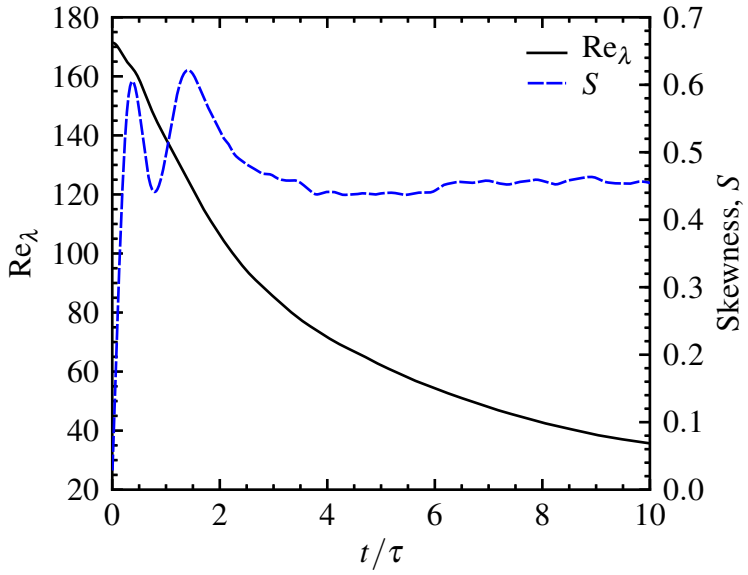

(a)

Figure 28: Time history of the Re_λ and skewness for a decaying isotropic turbulence simulation.

the velocity derivative skewness S_3^i for $N = 1$, 5, and 20, where

$$S_3^i = \frac{\langle (\partial u_i/\partial x_i)^3 \rangle}{\langle (\partial u_i/\partial x_i)^2 \rangle^{3/2}}. \tag{272}$$

4.2 The Richtmyer-Meshkov Instability

4.2.1 Computational Domain and Description

Numerical simulations of the RMI are conducted in a horizontal shock-tube configuration analogous to many experimental and numerical studies [210, 7]. While some experiments are conducted in vertical or inclined shock-tubes, there is no benefit to do so in numerical simulations. Experimentally, however, such configurations allow for the use of gravity to stabilize and control the immiscible interface between the two fluids [100] and the shock-tube inclination to control the impulsive force of the shock normal to the fluid interface. Unlike the Rayleigh-Taylor instability, the affect of gravitational acceleration on the fluid is typically much less the flow acceleration from the shock impulse in the RMI. Thus, for the horizontal configuration used in

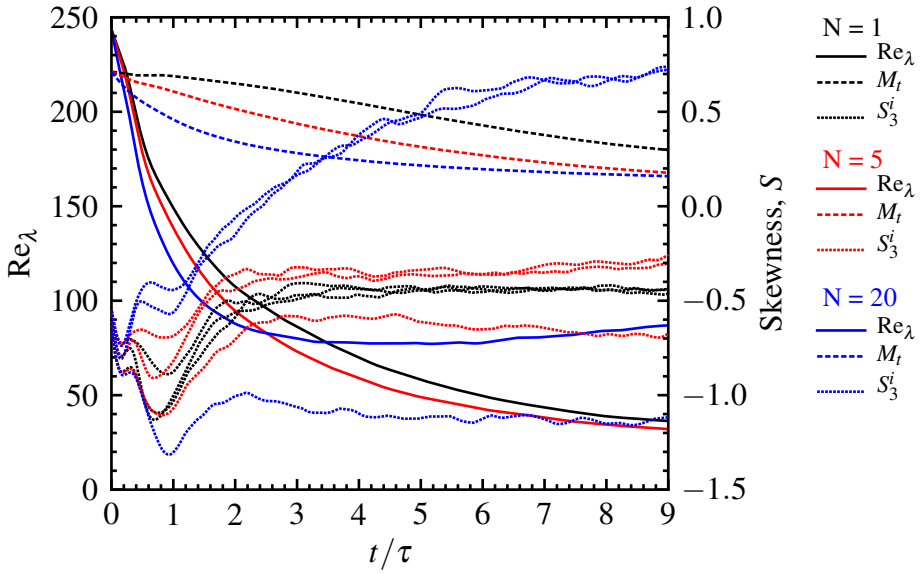

(a)

Figure 29: Time history of the Re_λ and skewness for a decaying isotropic turbulence simulation for three difference values of the Stuart number. At large N, the skewness shows the preferential decay of the velocity fluctuations perpendicular to the magnetic field.

this study, gravity is neglected. Figure 31 is a two-dimensional representation of the computational domain. For all the studies in this work, periodic boundary conditions are used in the directions transverse to the motion of the shock wave. This is mathematically consistent when comparing numerical simulations to theoretical models of the single-mode RMI, but some work is necessary to prove they can be used in the numerical simulation of more realistic configurations, such as multi-mode RMI or re-shock RMI. These issues are discussed in more detail in the later sections, but in summary, the periodic boundary condition is adequate with some qualification [199].

As apparent in Fig. 31, two configurations are considered depending on the type of boundary condition used at the right end of the computational domain. These configurations correspond to a "single-shocked" RMI simulation where the right boundary is treated as an open boundary and a re-shocked RMI simulation where the right boundary is treated as closed. Since the initial shock wave undergoes refraction as it

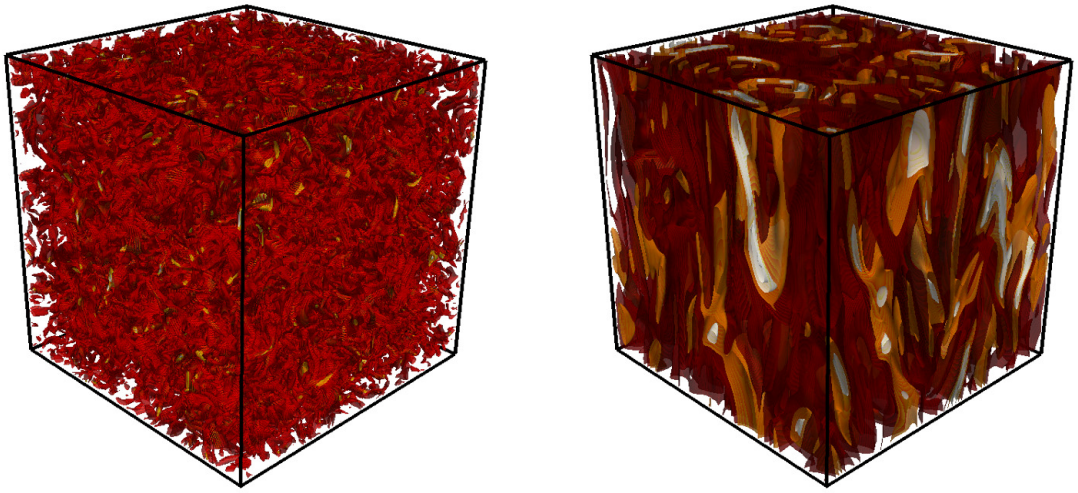

(a) $N = 0$ (b) $N = 20$

Figure 30: Vorticity contours for a decaying isotropic turbulence simulations at $t/\tau = 6$ for (a) $N = 0$ (b) $N = 2-$

propagates through the material interface, a reflected and transmitted wave are produced. The reflected wave travels back towards the inflow plane, and the transmitted wave continues propagating through the mixture. The type of boundary conditions determines the behavior of these waves when exiting the computational domain at the left and right.

For single-shocked RMI simulations, the flow is supersonic at the inflow and outflow plane, thus simple extrapolated boundary conditions are used. In this condition, however, the inflow boundary is at least partially reflective. As a result, the reflected wave, produced during the initial shock refraction and traveling in the direction opposite of the mean flow, is partially reflected when it passes through the inflow plane. While a more complex non-reflective boundary condition could be used here, the simplest solution is to stop the simulation before this interaction can corrupt the solution. The validation and verification studies below show that this is indeed sufficient.

For re-shock RMI simulations, the right boundary is defined as a slip-wall. Once

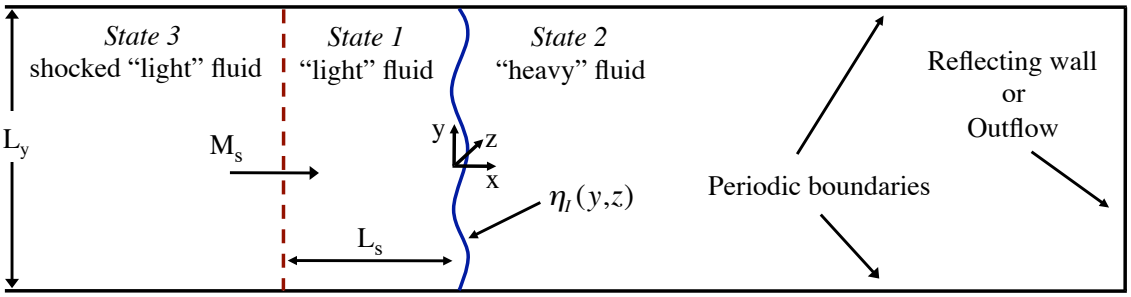

Figure 31: Schematic of the simulation domain where M_s is the Mach number of the shock, L_x is the distance from the end wall to the contact, and L_s is the distance from the contact to the initial shock position.

the transmitted shock reaches the wall, it is reflected and travels back through the shock-accelerated mixing layer. As this wall-reflected shock refracts through the mixing layer, the RMI is once again excited. The re-shock event is typically marked by a rapid increase in the mixing-rate and a subsequent quick transition to fully-developed turbulence [90]. The time at which this occurs is controlled by the strength of the shock and the initial distance from the contact discontinuity and the end wall.

The geometry of the configuration can be succinctly summarized as follows. The computational domain is Cartesian and has a square cross-section in the transverse directions defined by the $y-$ and $z-$axis with the $x-$coordinate defining the longitudinal direction. The origin of the domain is located at the contact discontinuity, such that the horizontal coordinate position is defined by $-L_{x_L} \leq x \leq L_{x_R}$ and the transverse coordinates defined by $-L/2 \leq y \leq L/2$ and $-L/2 \leq z \leq L/2$. The total length of the shock-tube $L_x = L_{x_L} + L_{x_R}$, and the shock wave is initially defined at $x = -L_s$. The computational domain is uniformly discretized by N_x points in the x-direction, N_y points in the y-direction, and N_z points in the $z-$direction. For two-dimensional simulations, the computational domain is a subset of the three-dimensional domain taken as the xy-plane at $z = 0$.

4.2.2 Initial Conditions

In the current numerical simulations, only a single material interface is considered. Recent experimental work has drawn attention to the benefits of studying the gas-curtain RMI, since in such a configuration experiments are highly repeatable and do not require a membrane to separate the two materials. While the gas-curtain RMI configuration is interesting, this work focuses on RMI simulations with only a single material interface, which physically corresponds to an interfacial boundary between two fluids of different molecular weights, but at the same temperature and pressure. This results in contact discontinuity defined by a jump in density. Numerically, it is possible to create a contact discontinuity in a single fluid with a corresponding jump in temperature as well as density. All previous studies of the RMI in a magnetized plasma have adopted this approach. In the current work, however, since the focus is on mixing, the contact discontinuity is defined as a interface between two different fluids.

Mathematically, the contact discontinuity can be defined by specifying the mass fraction of the heavy fluid, $\mathrm{Y_h}$, with an initial hyperbolic tangent profile [125] centered at $x = 0.0$ m and a characteristic thickness of L_δ given by

$$Y_\mathrm{h}(x, y, z; 0) = \frac{1}{2} - \frac{1}{2} \tanh\left(\frac{x - \eta_I(y, z)}{L_\delta}\right), \tag{273}$$

where $\eta_I(y, z)$ defines the interface perturbation. Since the flow is composed of only two fluids, a light and heavy, the mass fraction of the light fluid is by definition $Y_l = 1 - Y_h$. For the single-mode RMI, $\eta_I(y, z)$ is defined by a cosine or sine function with a single wavenumber $k_0 = 2\pi/L$ where L is the width of the channel. For the multi-mode RMI, $\eta_I(y, z)$ is a more complicated expression, but qualitatively, it is defined as the superposition of several cosine or sine functions of different wavenumber, typically centered about some dominant wavenumber, k_0. More exact definitions of $\eta_I(y, z)$ are given later.

Once the mass fractions of the light and heavy gases are defined, the density can be determined from the ambient pressure and temperature, p_0 and T_0, respectively. From the ideal gas law, the light and heavy gas densities can be defined as

$$\rho_l = \rho Y_l = \left(\frac{p_0}{RT_0}\right) Y_l = \frac{W_l}{\mathcal{R}} \frac{p_0}{T_0} \tag{274}$$

$$\rho_h = \rho Y_h = \left(\frac{p_0}{RT_0}\right) Y_h \frac{W_h}{\mathcal{R}} \frac{p_0}{T_0} \tag{275}$$

where W_l is the molecular weight of the light gas, and W_h is the molecular weight of the heavy gas. The Atwood number is often used as a non-dimensional representation of the density jump across the contact discontinuity. It is defined as

$$A = \frac{\rho_h - \rho_l}{\rho_h + \rho_l}, \tag{276}$$

With p_0, T_0 and the Mach number, M_s, of the initial shock wave defined, the Rankine-Hugionot jump conditions are used to compute the jump conditions in the light fluid that are required for existence of a M_s shock wave. In the current simulations, the flow is assumed to be a calorically perfect gas, thus the adiabatic index, γ, is constant, and the post-shock pressure, p_1, and temperature, ρ_1 in the light fluid are computed from

$$\frac{p_1}{p_0} = 1 + 2\frac{\gamma}{\gamma+1}(M_s^2 - 1) \tag{277}$$

$$\frac{\rho_1}{\rho_0} = \frac{(\gamma+1)M_s^2}{2 + (\gamma-1)M_s^2} \tag{278}$$

$$M_1 = \left[\frac{(1 + \frac{1}{2}(\gamma+1)M_s^2}{\gamma M_s^2 - \frac{1}{2}(\gamma-1)}\right]^{1/2} \tag{279}$$

If $u_s = M_s c_0$, where c_0 is the speed of sound at the ambient conditions, then $u_1 = M_1\sqrt{\gamma p_1/\rho_1}$. The post-shock velocity is defined $u = u_1 - u_s$. With this definition, the fluid to the right of the initial shock location, including the contact discontinuity, has zero initial velocity.

For simulations of the RMI in a magnetized plasma, a uniform magnetic field is initialized in the $x-$direction where the magnitude of the magnetic field is set by the

$\beta = B^2/2\mu_0 p$ of the plasma. Note that for this simple initial magnetic vector field, the condition $\nabla \cdot \mathbf{B} = 0$ is trivially met. Conveniently, the shock jump conditions are not modified in MHD for a magnetic field normal to the shock propagation. Thus, the dynamics of the magnetic field are initially "turned off" and only triggered once the fluid develops motions perpendicular to the magnetic field lines.

In summary, along with the geometrical definitions of L, L_x, and L_s, by specifying the perturbation $\eta_I(y, z)$, the reference pressure (p_0) and temperature (T_0), the Mach number, M_s, and the Atwood number, A, the RMI problem is completely defined. The minimum grid resolution, which is uniform is all directions, is defined as Δ_0. Additionally, for single-mode simulations, the amplitude and wavelength of the perturbation of the contact discontinuity, η_0 and λ respectively, are used to non-dimensional the simulation parameters. For instance, the groupings $k_0\eta_0$, L_x/λ, and L_y/λ are used. For multi-mode simulations, such non-dimensionalized parameters are not as characteristic of the simulation.

4.2.3 Contact Discontinuity for Single-mode and Multi-mode RMI

The RMI can be categorized based on the modal content of material interface perturbations. For single-mode perturbations of wavenumber $k_0 = 2\pi/\lambda_0 = 2\pi/L$, the RMI behaviors as a single "bubble" of lighter fluid raising into the heavier fluid and a "spike" of heavier fluid falling in the lighter fluid. The bubble and spike velocities are well-defined and can be predicted using analytical models. For a multi-mode perturbation, the material interface consists of a superposition of wavenumbers $\sum k$ over a range of length scales $\lambda_{min} < \lambda < \lambda_{max}$ limited physically only by the Kolmorogov and inertial length scale of the flow. Thus, it is useful to define the multi-mode interface in wavenumber space with a power spectrum $E_\eta(k)$ associated with the mean r.m.s of the interface fluctuations. As a result of the wider range of scales associated with the initial contact discontinuity, the multi-mode RMI is highly sensitive to the

initial structure of the interface. In various contexts, this sensitivity has been studied parametrically [182] and more recently using statistical sampling methods[203].

Recalling that the contact discontinuity can be defined by specifying the mass fraction of the heavy fluid, $\mathrm{Y_h}$, with an initial hyperbolic tangent profile centered at $x = 0.0$ m and with a characteristic thickness of L_δ given by

$$\mathrm{Y_h}(x, y, z; 0) = \frac{1}{2} - \frac{1}{2} \tanh\left(\frac{x - \eta_I(y, z)}{L_\delta}\right), \tag{280}$$

a definition of the contact discontinuity $\eta_I(y, z)$ defines the initial density field. Completing this definition then, one can define $\eta_I(y, z)$ as one of the following:

1. Single-mode

For the single-mode RMI in two- and three-dimensional simulations, the initial perturbation of the contact discontinuity is defined by

$$\eta_I(y) = \eta_0 \sin(k_0 y), \tag{281}$$

$$\eta_I(y, z) = \frac{a_0}{2}\Big(\sin(k_0 y) + \sin(k_0 z)\Big). \tag{282}$$

where η_0 and k_0 are the amplitude and wavenumber of the initial perturbation. Table 7 summarizes the initial conditions for the single-mode RMI simulations conducted in this study. As discussed previously, the non-dimensional parameters, $k_0\eta_0$, M_s, and A effectively define the mixing characteristics of the single-mode RMI.

2. Multi-mode Type 1

For the multi-mode RMI simulations, there are several ways to define the interface perturbations. In the current study, $\eta_I(y, z)$ is computed from an annular Gaussian energy spectrum with the spectral energy

$$E_\eta(k) = \frac{1}{\sqrt{2\pi^3} k_0 \sigma} \exp\left(-\frac{(k - k_0)^2}{2\sigma^2}\right). \tag{283}$$

where k is the radial wavenumber in spectral space and is computed as $k = \sqrt{k_y^2 + k_z^2}$ with $k_y = 2\pi/L_y$ and $k_z = 2\pi/L_z$. The power spectrum $E_\eta(k)$ peaks at k_0, and the value of σ is equal to $k_0/5.0$. The perturbation function $\eta_I(y, z)$ is computed by taking the inverse Fourier transform, and the magnitude of the spectral energy is normalized such that the resulting contact perturbation has with a perturbation amplitude with a standard deviation of η_0. Here, however, λ_{min} and λ_{max} are important.

3. Multi-mode Type 2

For RMI simulations corresponding the experiments using a cellulose membrane to initially separate the light and heavy fluids, the multi-mode interface has a very specific definition. This type of initialization is required if the growth-rate data from simulations is to match the experimental date. Following previous numerical simulations [40, 90, 182], an "egg-carton" sinusoidal perturbation for $\eta_I(y, z)$ is used to model the wire-meshed membrane separating gases in the experiments and is described by the expression

$$\eta_I(y, z) = a_0 |\sin(k_0 y)\sin(k_0 z)| + a_1 \cos(k_1 y)\cos(k_1 z) + a_2 \Psi(y, z), \tag{284}$$

where the first term represents the small-scale perturbations resulting from the wire-mesh, and the second term represents the scales associated with the transverse dimensions of the shock tube. The last term includes random perturbations, which are used to account for small-scale irregularities and to break the symmetry of the initial conditions and accelerate the transition of the RMI to non-linear growth. An von Karman power spectrum is used to compute $\Psi(y, z)$ [182],

$$E_\Psi(k) = k^{-2} \left[\frac{kL}{\sqrt{(kL)^2 + B}} \right]^4, \tag{285}$$

where $L = 0.95$ cm, $B = 5\sqrt{2}$ and $k = \sqrt{k_y^2 + k_z^2}$ where $k_y = 2\pi/L_y$ and $k_z = 2\pi/L_z$. The random fluctuations, $\Psi(y, z)$, are again normalized such that the r.m.s. amplitude

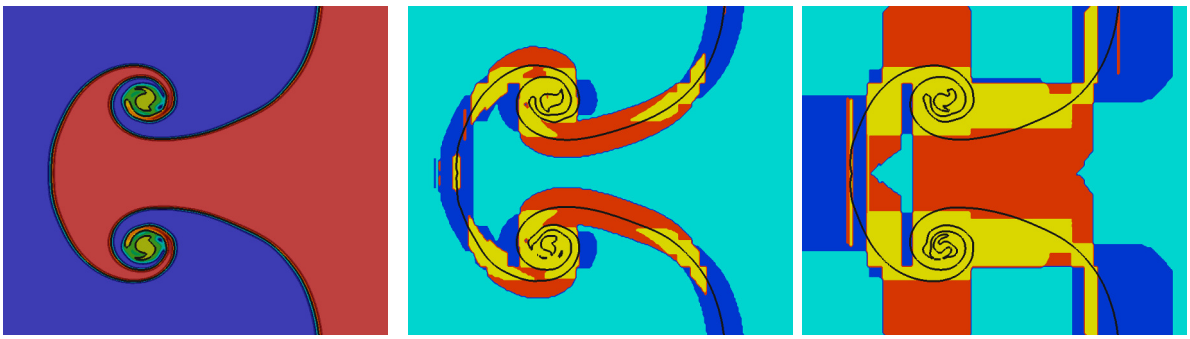

(a) FD-FVS (b) Hybrid, $s = 10$ (c) Hybrid, $s = 50$

Figure 32: Location within computational domain where the numerical scheme switches between a central finite-difference method and an upwind flux-vector splitting (FVS) method using 5th order WENO-Z reconstruction for the fluxes. (a) Density contours for the pure 5th order WENO-Z finite-difference FVS scheme, (b) hybrid switch for a buffer width s=10 points, (c) hybrid switch for a buffer width s=50 points. The color legend is as follows, central scheme (Teal), FVS in $i-$direction (blue), FVS in $j-$direction (red), FVS in both $i-$ and $j-$directions (yellow).

is set by a_2. These initial conditions are used for the multi-mode RMI simulations corresponding to the Vetter and Strutevant experiments [210]. For more details about the verification and validation of this case see Schulz et al. [185].

However simplistic the RMI may seem, the problem poses a difficult set of criteria that the numerical method must meet in order for the scheme to obtain accurate solutions. Not only must the scheme be required to correctly capture shocks and large gradients in the scalar terms such as density and the species mass fraction, but it also must resolve a large enough range of length scales in the flow without introducing too much dissipation if the simulation is to be classified as a direct numerical simulation and not rely on some sort of turbulent closure modeling. There is a large compendium of discussion in the research literature on this topic. To met these requirements, the hybrid central/upwind finite-difference methods discussed previously are an attractive candidate for simulating the RMI. For the current set of simulations, a hybrid finite-difference flux reconstruction method using a 6th order accurate compact central finite-difference scheme and 5th order flux-vector splitting scheme using WENO-Z

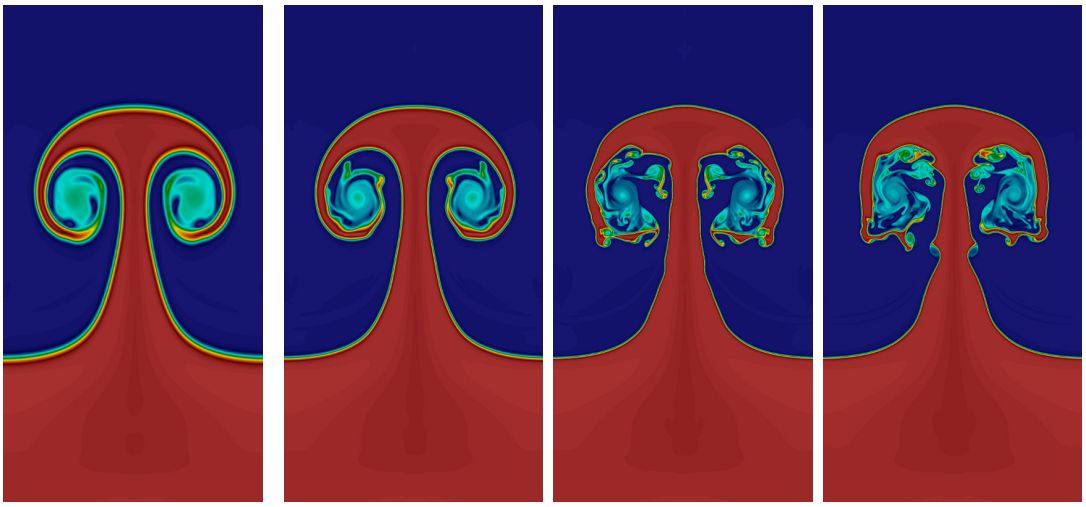

(a) $\lambda/\Delta_x = 64$ (b) $\lambda/\Delta_x = 128$ (c) $\lambda/\Delta_x = 256$ (d) $\lambda/\Delta_x = 256$

Figure 33: Contours of the normalized density for the single-mode RMI corresponding to the initial conditions $k_0\eta_0 = 0.1$, $M_s = 1.5$, and $A = 0.5$ for three different resolutions (a) $\lambda/\Delta_x = 64$, (b)$\lambda/\Delta_x = 128$, and (c) $\lambda/\Delta_x = 256$ using the inviscid Euler equations and (d) $\lambda/\Delta_x = 256$ using the Navier-Stokes equations. The color contours are scaled from 1.5 (blue) to 6.0 (red).

reconstruction method is used for the initial studies. Time integration is achieved using a low storage 5th order, 4-stage Runge-Kutta time integration method.

Unfortunately, while it is ideal to use the central finite-difference scheme in smooth regions of the flow and a flux-vector splitting method only in regions where discontinuities exist, how the actual blending between two fluxes computed from the different schemes occurs in the computational domain is not straightforward. Experience indicates that some central schemes couple better to a corresponding upwind scheme. For instance in the RMI, using a hybrid finite-volume scheme based on central predictor-corrector MacCormack scheme and a flux-difference splitting upwind scheme, numerical fluctuations are easily introduced to the contact discontinuity as a result of the switching between the central to upwind schemes. In practice, the hybrid finite-difference scheme used here performs better, but upon close investigation the numerical oscillations are still visible. This is best controlled by properly selecting the

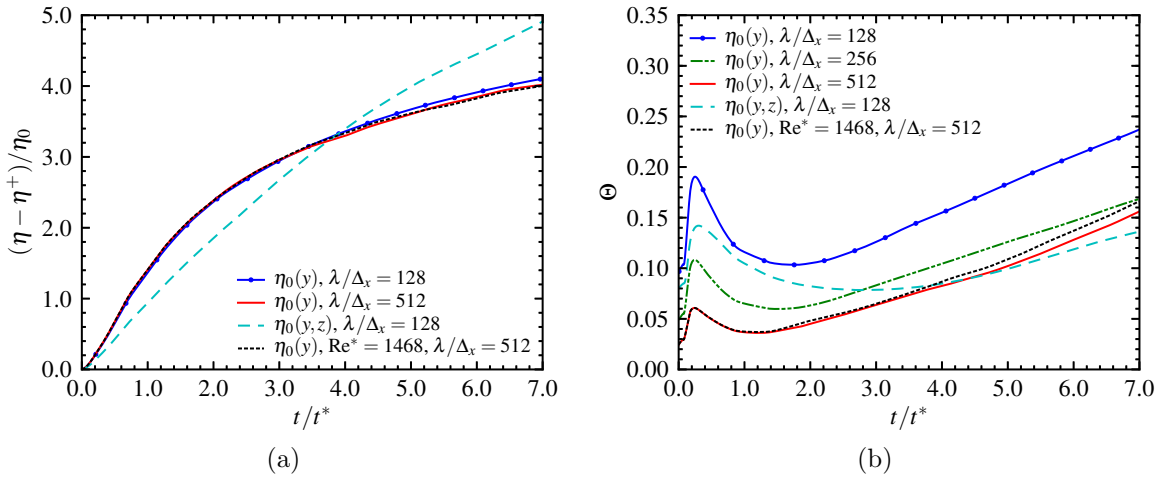

Figure 34: Time history of (a) the normalized mixing length and (b) the mixing fraction in single-mode RMI at the different grid resolutions (Δx_1, Δx_2) and for inviscid and viscous simulations.

switch parameters, which are dependent on the problem and the initial conditions, such that the switching of the individual schemes are used in large contiguous regions if possible. Figure 32 shows the regions where the hybrid switch is selecting either the upwind or central scheme. Since the fluxes are computed on a directional basis, the colors indicate the number of directions upon which the upwind scheme was used.

It is notoriously difficult to prove that numerical simulations of the RMI are convergent with increasing grid resolution. This is a result of scale generation process occurring during the growth of the RMI, which is often described as fractal-like. Thus, with an ever increasing grid resolution, ever smaller scales or vortical structures are produced. In particular, this occurs in numerical simulations where the Reynolds number is ill-defined either because the simulation is inviscid, in which the scale generation is only limited by the numerical dissipation of the scheme, or because the flow is transitioning from a laminar to a partially turbulent state where the physical dissipation is not yet limiting the scale generation process. Yet, scale generation at some point must be limited at the smallest levels by the molecular diffusion processes, but given the range of Reynolds numbers, which are often large for shock-accelerated,

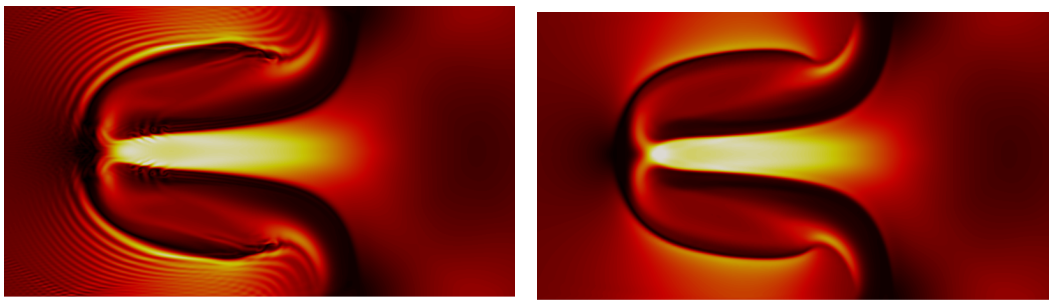

(a) $v_x = \Delta V$ (b) $v_x = 0$

Figure 35: Contours of the normalized magnetic field B^2/B_0 for the RMI in a $\beta = 1000$ plasma for simulations using two different frames of references. (a) The RMI at $t/t* = 7$ with a background velocity $v_x = \Delta V$. (b) The RMI at $t/t* = 7$ with a background velocity $v_x = 0$.

it may be computationally impossible to sufficiently numerically resolve the simulation at these scales. Figure 33 shows contours of the RMI for three different grid resolutions at the same physical time for case SM1.

In all of the single-mode and multi-mode RMI simulations, the constrained transport method is used to control the magnetic divergence errors produced during the shock refraction process. While using the projection scheme allows one to achieve high order of accuracy in both the magnetic and velocity fields since the second-order averaging of the magnetic filed is not required as it is in the constrained transport method, it is computationally very expensive since in practice it is necessary to clean the magnetic field frequently to avoid a numerical instability. A compromise is possible, however, since for low-β plasmas dominated by the magnetic field, the generation of small-scale structures is limited by the magnetic field. Thus, grid-converged solutions are easily obtained making second-order accuracy tolerable. In high-β plasmas, the velocity field dominates the dynamics of the RMI and thus it could be argued that some sacrifice in the numerical accuracy of the magnetic field is beneficial if the computational efficiency is greatly increased. Though this discussion centers around the formal order of accuracy of the scheme, the finite-difference hybrid method used

Table 4: A list of coefficients for semi-empirical models of the single-mode RMI following the Sadot [175]

Model	Dim.	$D_{b/s}$	$E_{b/s}$
Sadot et al. [175]	2D	$1 \pm A$	$3(1 \pm A)/2(1 \pm A)$
Neiderhaus and Jacobs [144]	2D	$1 \pm A$	$1 \pm A$
Goncharov et al. [76]	2D	$1 \pm A$	$3(1 \pm A)/(3 \pm A)$
Sohn et al. [226]	2D	$1 \pm A$	$(2 \pm A)/2$
Chapman and Jacobs [34]	3D	$1 \pm (0.01221A^3 + 0.69844A)$	$(1 \pm A)/2$

here provides solutions with significantly less error magnitude compared to similar finite-volume methods.

As seen in the magnetic field loop test case summarized in Fig. 22, the constrained transport method suffers a limitation in a high-β plasma propagating in a grid-aligned direction. While the oscillations in the magnetic field loop test are controlled, they are still present. There have been several proposed methods to reduce these oscillations by altering the constrained transport method, however, none seem to work well for the RMI problem. One viable solution is to use the projection scheme, but a simpler solution exists for the single-mode and multi-mode RMI simulations with open boundaries. The velocity of the heavy fluid can be set such that once shock refraction occurs, the impulse in the $x-$direction halts the movement of the contact discontinuity. Thus, the RMI develops in a quasi-steady fluid with $v_x \approx 0$. Figure 35 shows the magnetic field lines for the RMI in a moving frame of reference and steady frame of reference. Note that this translation in the frame of reference does not affect the growth-rate of the RMI nor the mixing processes.

4.2.4 Comparisons to Theory

For the single-mode RMI, the growth-rate of interface perturbation is predicted to be linear. By analogy to the Rayleigh-Taylor instability, Richtmyer provided an impulsive model to predict the linear growth-rate of the RMI [165] states $\dot{\eta} = v_0 =$

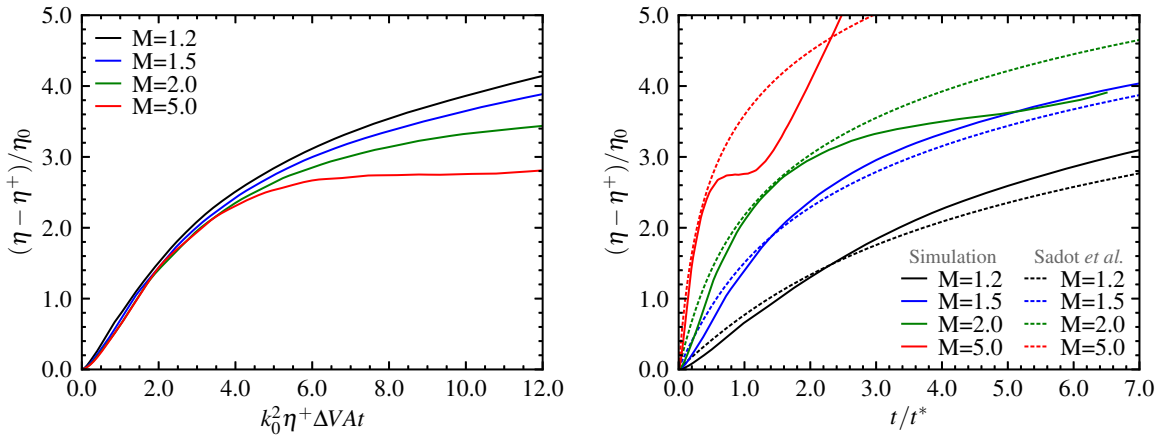

Figure 36: Time history of the normalized mixing length in single-mode RMI at the same grid resolutions (Δx_1, Δx_2) with a comparison to the non-linear theory of Sadot et al. [175].

$k_0\eta_0^+ A^+\Delta V$, where η_0^+ is the post-shock perturbation amplitude, A^+ is Atwood number computed using the post-shock densities, and ΔV is the change in velocity supplied to the contact discontinuity once the shock has refracted through the material interface. Meshkov later estimated the post-shock amplitude to be

$$\eta_0^+ = \eta_0 \left(1 - \frac{\Delta V}{M_s c_0}\right) \tag{286}$$

where c_0 is the speed of sound in the light fluid and M_s is the Mach number of the incident shock. The sign of the initial growth-rate is dependent on the Atwood number, which is positive when the shock wave moves from a light gas toward a heavy gas, and negative when shock wave propagates from a heavy gas into a light gas. In the later case, a phase inversion occurs at the interface, and the initial growth-rate is negative. This model, referred to as the impulsive model, is only valid for in the linear regime, corresponding to approximately $\eta/\lambda << 0.1$, after which the RMI transitions to non-linear growth-rate and then saturates as it reaches asymptotic growth.

More detailed theoretical models are required to capture this behavior for which there are a large number of reliable theoretical and empirical models. Two popular

models are discussed. The semi-analytical model of Sadot et al. [175] is able to predict the RMI growth-rate as it transitions to non-linear growth and was correlated with the experiments of Jones et al. [100]. Many researchers have followed this model and made various improvements. In the general form, the bubble and spike velocities are computed using the following relationship

$$\dot{\eta}_{b/s}(t) = v_{b/s}(t) = v_0 \frac{1 + v_0 kt}{1 + D_{b/s} v_0 kt + E_{b/s}(v_0 kt)^2} \tag{287}$$

where the constants are $D_{b/s}$ and $E_{b/s}$ are given in Table 4. Since the Sadot et al. model is an empirical fit to the initial linear growth-rate and the asymptotic growth, the model is expected to only correctly represent the early and late growth of the RMI. The model is also limited to $A \leq 0.9$ and is based on experimental date for $M_s \leq 2$.

A time-dependent, analytic expression for the evolution of the two-dimensional RMI in both the linear and non-linear regimes was developed by Mikaelian [138] It is a simple model based on the work of Layzer [136], and is one of the few models that do not require solving an ordinary or partial differential equation to arrive at an explicit expression for $\eta(t)$. Mikaelian proposes a piece-wise function for the amplitude of the perturbation in time. In the linear regime, Richtmyer's impulsive model states $\eta(t) = \eta_0^+ (1 + \Delta V k A^+ t)$ and in the nonlinear regime, the amplitude of the perturbation is given as

$$\eta(t) = \eta_0^+ + \frac{3 + A^+}{3(1 + A^+)k} \ln\left(1 + 3\dot{\eta}_0 kt \frac{1 + A^+}{3 + A^+}\right), \tag{288}$$

where $\dot{\eta}_0$ is the initial growth rate. The threshold for changing between the linear and non-linear growth equations occurs when $\eta(t) = 1/3k$

Figure 36 shows a comparison of the two models with the results from the numerical simulations. Obviously, the model of Sadot et al. [175] is not expected to correctly capture the growth-rate of SM4 since $M_s = 5$ in the late stages.

CHAPTER V

IONIZING DETONATION WAVES

5.1 Introduction

In some scenarios, it is possible for a detonation wave to increase the temperature of the product gases high enough so that ionization occurs in the post-detonation flow. Experiments show that condensed-phase explosions are capable of producing a ionized gas of a relatively large electrical conductivity, 100-2000 S/m. The kinetic mechanisms for such pathways to ionization, however, are not well understand. Thus, the focus of this study is on the interaction of a freely-propagating, potassium carbonate seeded, H_2-air gaseous detonation with a magnetic field. While the ionized gas produced in gaseous detonation waves have a much lower electrical conductivity as compared to a high-energy explosion, owing to the smaller about of chemical energy released, detailed kinetic mechanisms for the ionization and combustion of the gaseous species are more easily determined and thus more reliably used to study the interaction between a magnetic field and a propagating detonation wave. Furthermore, this study attempts to avoid any arbitrary assumptions, such as assuming a constant electrical conductivity in the post-detonation flow. If the results can be shown to be scale invariant, then it is possible they are applicable to the study of condensed-phase explosions.

This study is divided into three parts. The first part addresses the numerical aspects of modeling gaseous detonations using finite-rate, detailed kinetic mechanisms. The sensitivity to the numerical scheme, grid resolution, and boundary conditions is discussed as well as the steps involved in the initialization of multi-dimensional detonations. The second part discusses a numerical investigation into the parameters

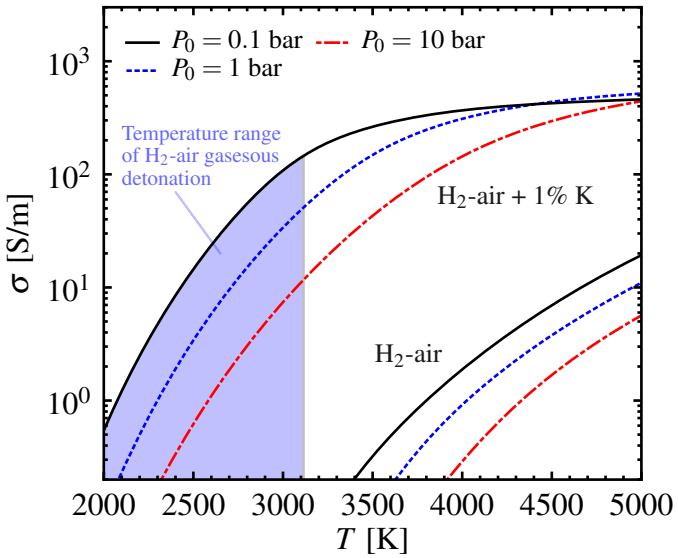

Figure 37: The equilibrium electrical conductivity is shown as a function of pressure and temperature for a stoichiometric H_2-air mixture. Seeding by potassium drastically increases the electrical conductivity.

affecting ionization in gaseous H_2-air detonations with and without seeding [184]. Calculations of the electrical conductivity are compared to experimental measurements, and particular emphasis is made on the impact that adding seeding particles has on the stability of the detonation wave. The third part details the effects a magnetic field has on the propagation of a gaseous detonation. Since the magnetic Reynolds number is always much less than one for such detonations, the quasi-static MHD equations are used in this study. While the magnetic field and the velocity field may be explicitly decoupled, the dynamics of the flow are still coupled through the current density and the electrical conductivity.

5.2 Ionizing Gaseous Detonations

5.2.1 One-dimensional detonation waves

A freely-propagating detonation wave forms when a strong shock-wave dynamically couples to a reaction-wave in such a way that a balance occurs between the release of chemical energy and the energy expended by expansion. Once formed, such a

Table 5: Summary of parameter set for the numerical simulations used to study the ionization of gaseous detonation waves. The baseline simulations are used in the next section to study the effect of a magnetic field on the detonation propagation. P_a is the ambient pressure, and the percent (%) concentration given in the table for N_2 and K is in per weight.

Case	Dimension	P_a (bar)	N_2 (%)	K (%)
Baseline Simulations				
1	1d, 2d	0.2	74.52	0.0
2	1d, 2d	0.2	74.52	0.05
3	1d, 2d	0.2	74.52	0.10
4	1d, 2d	0.2	74.52	0.25
Pressure/Stoichiometic Sensitivity Studies				
5	1d	0.1	0.667	0.0
6	1d	0.2	0.667	0.0
7	1d	0.4	0.667	0.0
8	1d	0.2	10.00	0.0
9	1d	0.2	30.00	0.0
10	1d	0.2	50.00	0.0
Potassium Seeding Sensitivity Studies				
11	1d	0.2	74.52	0.01
12	1d	0.2	74.52	0.03
13	1d	0.2	30	0.05
14	1d	0.2	50	0.05
15	1d, 2d	0.2	74.52	0.05
16	1d, 2d	0.2	74.52	0.10
17	2d	0.2	74.52	0.75
18	2d	0.2	74.52	1.00
19	2d	0.2	74.52	1.25
20	2d	0.2	74.52	2.00

detonation wave propagates at a velocity fluctuating around the Chapman-Jouget (CJ) velocity, D_j. This scenario, however, is dependent on the boundary conditions. If the density at the (rear) boundary, ρ_b, is greater than the CJ density, ρ_j, which is defined by the point of tangency between the Rayleigh and Hugoniot curves, then instead of a rarefaction wave decreasing ρ_j to ρ_b in the post-detonation flow, a constant shocked state exists, and the detonation is said to be supported. This means that

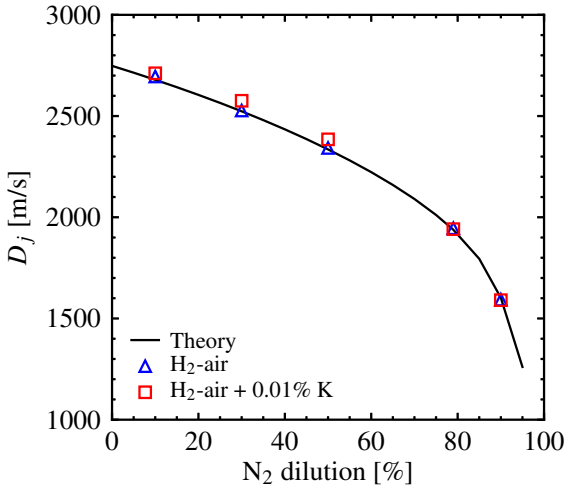

Figure 38: The detonation velocity is computed for detonation in a H_2-O_2/N_2 mixture with an ambient pressure and temperature of 0.2 bar and 298 K, respectively. The values are compared to the theoretical detonation velocity (D_{CJ}) obtained from NASA's CEA code.

the rear boundary condition determines how the detonation propagates through the mixture, not the intrinsic properties of the gas mixture. The propagation velocity of a supported or overdriven detonation is defined by the overdrive factor, $f = {}^{D}/_{D_j}$, where D is the measured detonation velocity. In the absence of a continually supported pressure from the read boundary, f reduces to unity. Thus, the strong detonation solution is not a focus of this study. Only the CJ or weak detonation solution is of interest.

As a result, in numerical simulations using detailed kinetic mechanisms, specific attention must be given to obtaining detonation waves that are not overdriven or dependent on the boundary conditions. For simplified, one-step chemistry, an direct solution can be obtained directly using ZND theory. Lacking this, the shock-to-detonation transition in a stoichiometric mixture of H_2 and air seeded with potassium carbonate particles is simulated in a one-dimensional domain with the rear boundary defined by a stationary purely-reflecting wall. The choice of ρ_b and the back pressure, P_b, determine the distance required for transition and set detonation velocity, or f,

once the shock transitions to a detonation wave. In a one-dimensional domain, it is not possible to simulate a freely-propagating steady detonation. The solution lacks transverse waves, and as a result a one-dimensional detonation wave decays slowly; D decreases below D_j until the detonation is no longer supported by the shock-induced release of chemical energy. This does not necessarily preclude the use of one-dimensional simulations in studying detonation behavior. As discussed below, one-dimensional simulations are used to study the stability of a detonation wave propagating in a gas mixture seeded by potassium carbonate. The time scales of interest in this study are much shorter than the time scales for the numerical decay of the detonation solution.

Figure 39 shows profiles of temperature and mass fractions of a few species just downstream of the detonation front. The initial sharp rise in the temperature is a result of the propagating shock wave ($M_s = 4.76$). The temperature ratio across the shock is 5.17 and compares reasonably well to the theoretical value of 5.32. The difference is attributed to the instability of the detonation, which is illustrated in Fig. 40. The average peak pressure is only slightly over-predicted. Following the shock wave, radicals are formed in the induction zone as the reactants, H_2 and O_2, begin to break-down. The sharp increase in the radicals H_2O_2 and HO_2 marks the beginning of heat release. As the temperature increases downstream (with N_2/O_2 and ionization chemistry), N_2 begins to break down, and the presence of N atoms prompts the Zel'dovich reactions and the beginning of NO formation.

Since NO has a low ionization potential, the electrical conductivity is directly dependent on the formation of NO ions [59]. Since the ionized mixture is assumed to be quasi-neutral, the electron number density, n_e, must be equal to the positive ion number density. Here n_e=3.052×10^{17} m^{-3} and n_{NO^+}=2.956×10^{17} m^{-3}. From Eq. 152, the electrical conductivity is seen to be directly proportional to n_e. Thus the formation of NO ions is critical to increasing the electrical conductivity of the

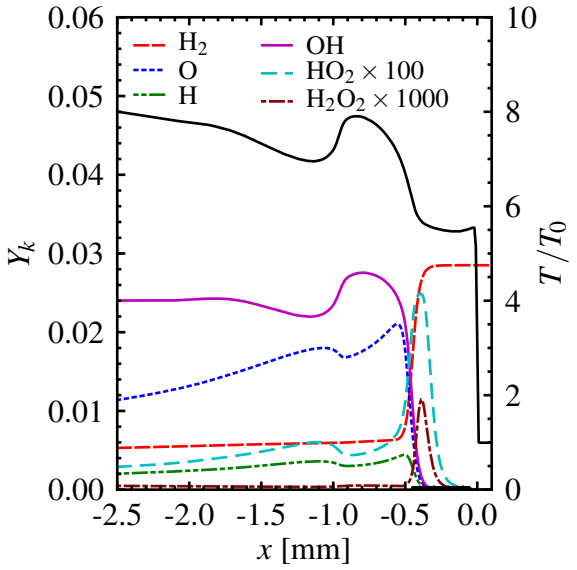

Figure 39: (a) One-dimensional profiles of temperature and species mass fraction directly behind the detonation-sustained shock wave. The results are shown for a stoichiometric H_2-air detonation in an ambient pressure and temperature of 0.2 bar and 298 K, respectively.

mixture. Even though both OH and NO are easily ionizable, the production of NO ions dominates. This is because the concentration of OH is depleted downstream due to formation of H_2O resulting in a negligible contribution to the n_e by OH ion production ($n_{OH^+} = 21.33$ m^{-3}). Non-stoichiometric H_2/O_2 detonations could possibly reveal OH ionization to be of more significance.

As the ambient pressure increases, the formation of NO occurs earlier and its equilibrium value increases slightly. This in turn increases the electrical conductivity. The trend is easily observable in the profiles of the electrical conductivity shown in Fig. 41a. Similarly, as the dilution of the N_2 is reduced, the electrical conductivity also increases as shown in Fig. 41b. Both affects are largely a result of the change in the post-detonation temperature. As the ambient pressure is increased from 0.1 bar to 0.4 bar, the detonation velocity increases roughly 2.75 percent with a corresponding 6.7 percent rise in temperature. This increases the reaction rates in the post-detonation mixture and thus increases NO formation. Also as the temperature is increased, N_2

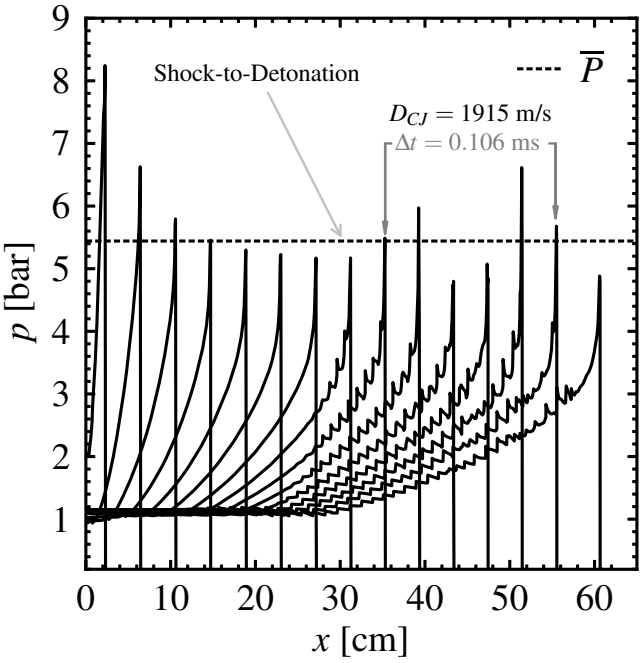

Figure 40: One-dimensional profiles of pressure shown at two instances in time as the detonation propagates through the domain. The peak pressures oscillate indicating the detonation is in the oscillatory regime. Both results are shown for a stoichiometric H_2-air detonation in an ambient pressure and temperature of 0.2 bar and 298 K, respectively.

is more easily dissociated. Similar logic applies to why the electrical conductivity increases at lower N_2 concentrations. The reduction of N_2 reduces the heat capacity of the mixture and thus increases the detonation velocity and post-detonation temperature. However, as observed in Fig. 41b, the trend reverses at low concentrations regardless of the higher post-detonation temperatures since the reduction of N_2 limits NO production because of the lack of available nitrogen.

As mentioned previously, detonations in H_2-air mixtures produce ionized mixtures with low electrical conductivities of order 10^{-3} S·m^{-1}. In order to increase these values potassium can be used to seed the gas with easily ionizable particles. In experiments, potassium is typically injected into the flow as atomized salt particles such as potassium carbonate. These particles quickly decompose and undergo phase change [190]. However to simplify the current study the phase change process is not

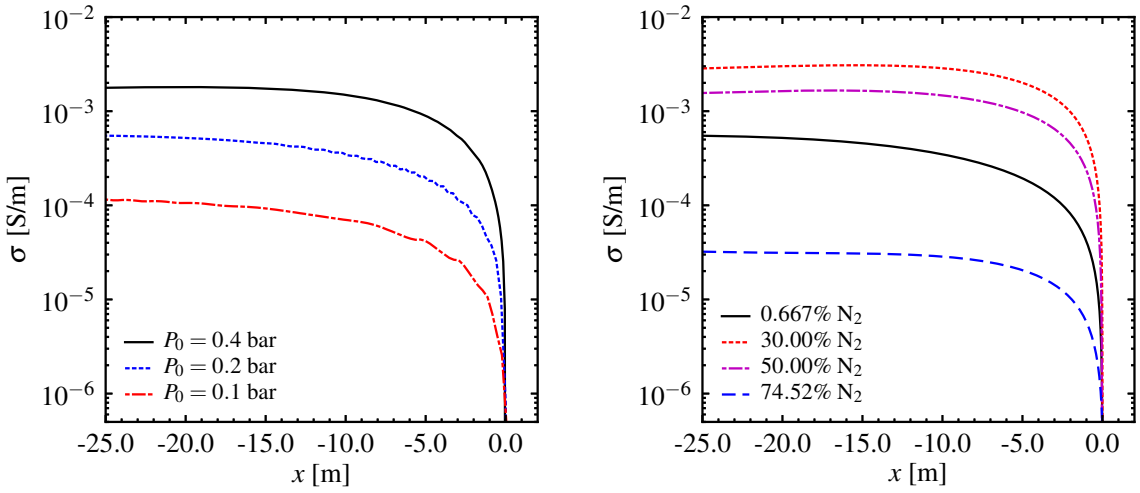

(a) 5μm (b) 10μm

Figure 41: (a) One-dimensional profiles of the electrical conductivity computed for a stoichiometric H_2/O_2 mixture with 0.667% N_2 dilution at three different ambient pressures. (b) A comparison of the electrical conductivity at different N_2 dilutions. The peak post-detonation temperature for 0.667%, 30%, 50%, and 79% N_2 dilution is 3408, 3265, 3180, 2751 K respectively.

modeled and gaseous KOH is injected uniformly at the inflow plane instead. The injected KOH then convects until it reacts at the detonation front due to the elevated temperatures and pressures as well as the presence of H and OH radicals. Gaseous potassium quickly forms which ionizes and increases the electron number density of the mixture. Figure 42a shows the electrical conductivity for potassium seedings of 0.01, 0.03 and 0.05 percent by weight. The electrical conductivity not only increases at a faster rate but is 4 orders of magnitude larger than the electrical conductivity of the unseeded detonation.

In the one-dimensional studies conducted, a potassium seeding of larger than 0.06% was observed to kill the detonation as demonstrated in Fig. 42b. This is a result of the potassium chemistry competing for the O and H radicals necessary for combustion. This disruption increases the induction time for combustion which subsequently causes the heat release zone to decouple from the shock wave triggering

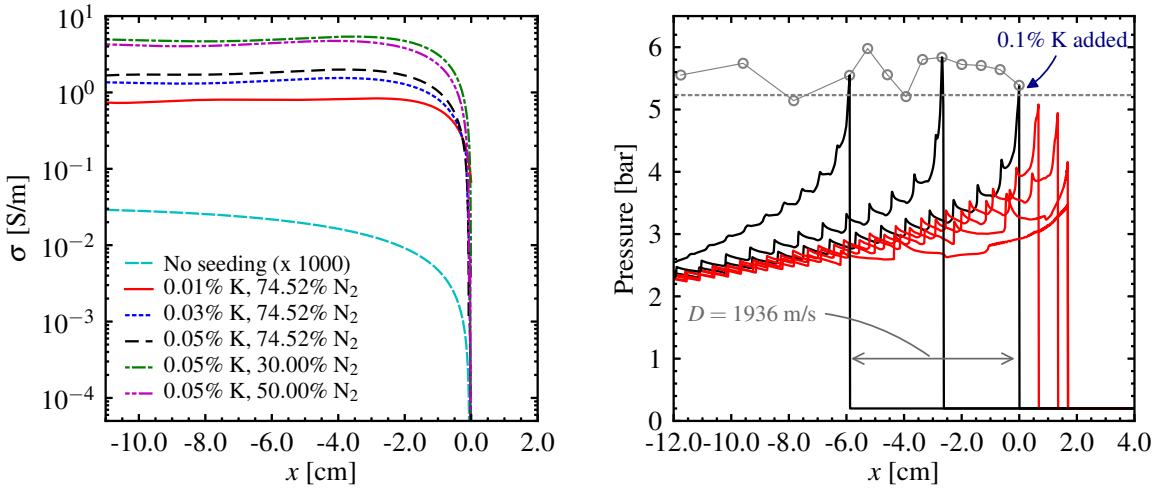

(a) 5μm (b) 10μm

Figure 42: (a) A comparison of the electrical conductivity at different potassium seeding percentages. The reference case for detonation of a stoichiometric H_2-air mixture at ambient pressure and temperature of 0.2 bar and 298 K is shown for comparison. (b) At seeding percentages higher than 0.06%K the detonation wave decays into a propagating shock wave.

a reduction in the the heat release such that the propagating shock can no longer be sustained. This process is observable in the pressure profiles shown in Fig. 42b. The detonation profiles following the addition of the seed are shown approximately every 20 μs. The peak pressures as well as the CJ peak pressure are shown prior to the seeding as reference.

This result is in some contradiction to experiments which use higher seeding percentages [14, 129]. Yet this is expected since in one-dimension the detonation lacks the structure necessary for self-propagation and therefore is more sensitive to the disruptions caused by seeding. This does not, however, invalidate the conclusions drawn from these simulations. While in two and three dimensions the detonation may be more impervious to potassium seeding, a critical point most likely exists where too much seeding results in a failure of the detonation. This is investigated in the next section.

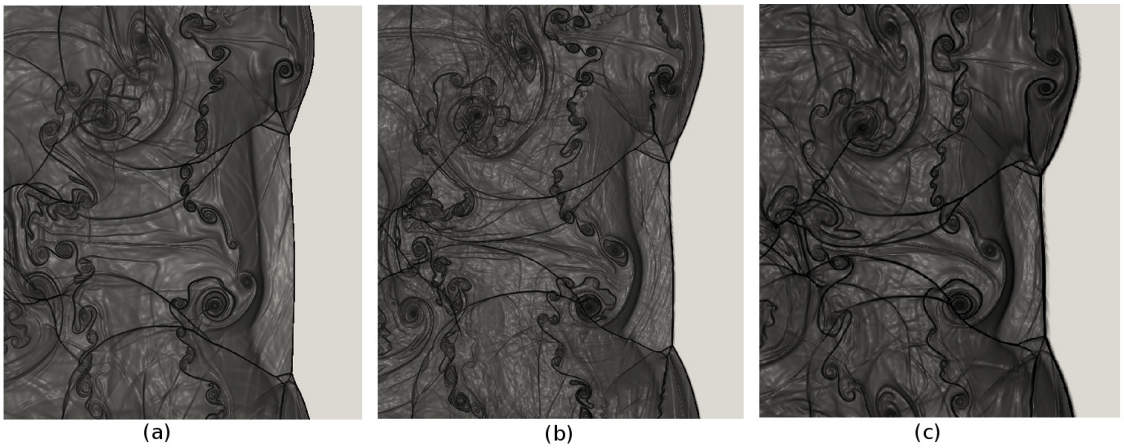

Figure 43: Contours of the $\ln(|\bigtriangledown \rho| + 1)$ for different schemes and resolutions (a) 5μm FV, (b) 5μm FD and (c) 10μm FD.

5.2.2 Two-dimensional detonation waves

A two-dimensional stoichiometric hydrogen-air detonation is simulated by initializing the domain with a one-dimensional solution. As in the one-dimensional simulations, the detonation is simulated in the frame of reference moving with the detonation wave. The boundaries in the y-direction are taken as periodic, and a simulation domain of 18 mm $\times$ 3 mm is used. From a grid-resolution study, a 10 μm resolution is determined to be sufficient to resolve the Mach stem, incident shock and transverse wave interactions at the detonation front. This interaction, shown in Fig. 43 for three different grid resolutions, is critical in sustaining the detonation as it creates local zones of high pressure and temperature causing the detonation front to pulsate in the direction of propagation. This introduces fluid mixing time-scales which impact the electrical conductivity in the post-detonation mixture.

A grid-resolution study is performed to determine the required resolution, which is determined by the ability to resolve the interaction between the Mach stem, incident shock and transverse waves. The interaction is critical in sustaining the detonation as it creates a zone of high pressure and temperature that causes the gas to expand as chemical energy is released. Figure 43 shows the shock structures formed behind

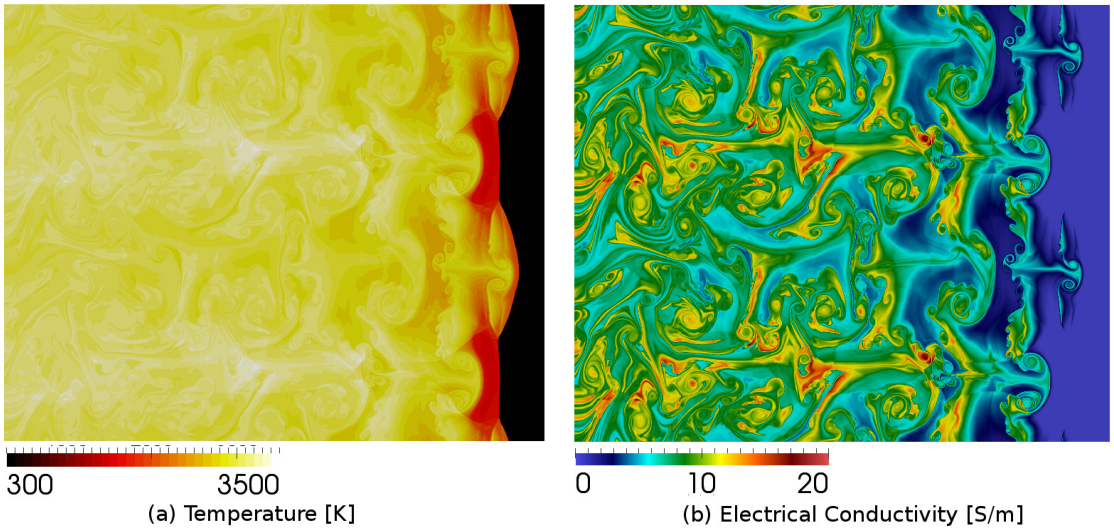

Figure 44: Stoichiometric H_2-air detonation at an ambient temperature and pressure of 298 K and 0.2 atm seeded with 0.25 % K by weight. (a) Contours of temperature, and (b) the electrical conductivity.

the detonation front for half of the channel at two different resolutions: 5, 10 μm. At the highest resolution, the incident shock, Mach stem and the transverse shock are clearly defined as well as are the slip-lines. A uniform resolution of 10 μm is used in the remainder of the studies.

Since the location of the transverse wave, incident shock and Mach stem interaction oscillates perpendicularly to the detonation front a series of vortical structures separated by slip lines are propagated downstream creating a non-uniform distribution of temperature and species mass fraction as illustrated in Fig. 44. Only in the regions of high temperature does significant dissociation of N_2 and NO formation occur. As the vortices interact and merge, the high temperature regions become less distinct and the ion density becomes more uniform. As a result, the distance between the weakly-ionized plasma and the detonation front is both a result of the mixing rate of the vortices and the chemical non-equilibrium of the explosion products. This creates a non-uniform distribution of the electrical conductivity with peak values of order 10^{-3} S$\cdot$m^{-1}, which are similar to those observed in the one-dimensional simulations.

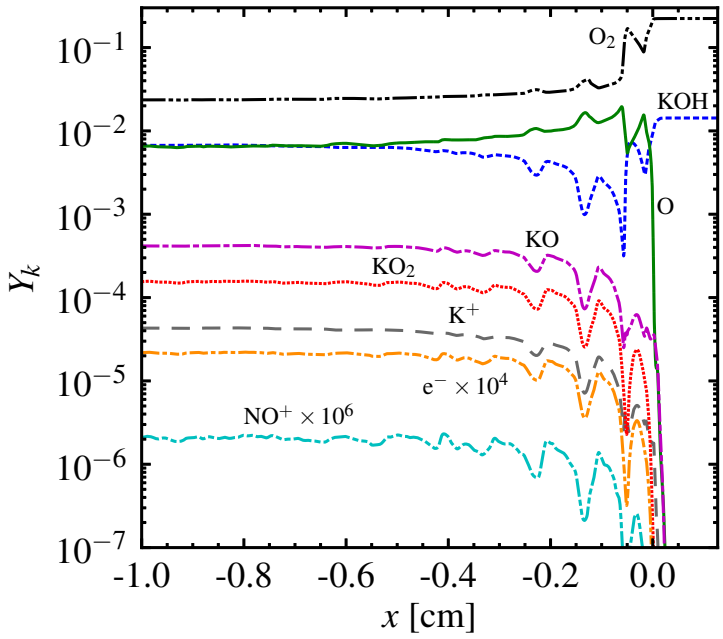

Figure 45: Planar averaged mass fractions of the species involved in potassium ionization behind the detonation front with 1% K seeding.

When KOH is injected into the inflow, the ionization mechanism becomes dominated by the potassium chemistry. The ionization is now prompt, occurring at the detonation front, and is no longer rate-limited by the slow formation of NO. This could have important consequences in applications where an external magnetic field is present since a combination of a high electrical conductivity at the detonation front and a strong magnetic field could alter the way the transverse waves interact at the detonation front.

The main difference from the one-dimensional and two-dimensional simulations is that the strong interaction between the Mach stem, incident shock and transverse waves at the detonation front creates local regions of high temperature and pressure. These regions of heat release allow for the two-dimensional detonation to sustain higher mass fractions of potassium seeding. Yet above a seeding of 1.25 percent by weight of K, the detonation becomes unstable and decays into a propagating shock wave. This indicates that the ionization fraction of the gas mixture that can be

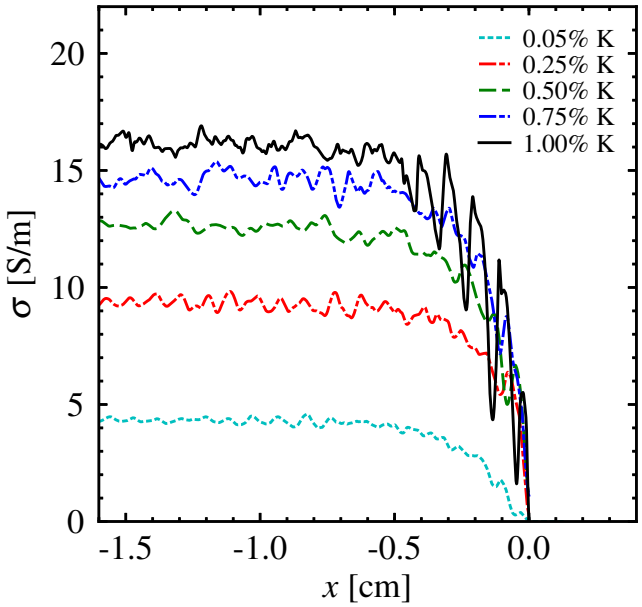

Figure 46: Planar averaged profiles of the electrical conductivity for various potassium seeding percentages.

achieved through detonation is limited. This constraint is imposed along with the additional problems of uniform mixing and burning of the seed particles. Future work will investigate these issues in more detail.

5.3 Effects of Applied Magnetic Fields

A distinctive feature of MHD flows is the generation of induced currents resulting from the relative motion of a conductive fluid in an external magnetic field not aligned with the flow velocity. These currents introduce an additional mechanism for the dissipation of energy within the flow, which is characterized by the magnetic diffusivity, $\eta = 1/\mu\sigma$, where μ is the permeability of free space, and σ is the electrical conductivity. Most importantly, however, is the ratio of the time scale of magnetic diffusion ($\tau_\eta = \eta^2/L$) to the flow time scale ($\tau_u = u/L$), where u and L are the characteristic velocity and length scales. This ratio is defined as the magnetic Reynolds number, $Re_m = \tau_\eta/\tau_u = u/L = \mu\sigma uL$. For a typical ionizing hydrogen-air detonation, Re_m is estimated to be of the order of 10^{-3}. For MHD flows, when $Re_m << 1$, the induced

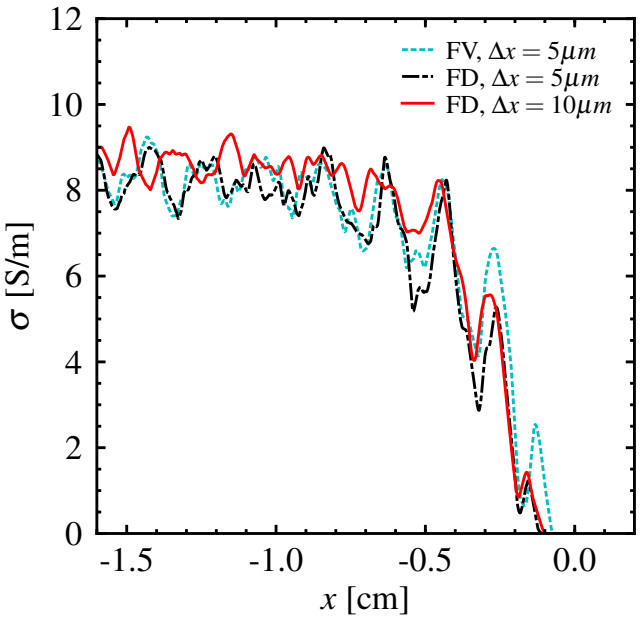

Figure 47: Planar averaged profiles of the electrical conductivity for 0.25% potassium seeding by weight for finite difference and finite volume schemes at two grid resolutions.

magnetic fields diffuse quickly and can be neglected relative to the imposed magnetic field, B_0. The induced currents, however, play a dominant role in the conversion of the Lorentz force into heat via the process of ohmic dissipation, which occurs at a time-scale of τ_η. This process is highly anisotropic. Fluids motions misaligned with the magnetic field are preferentially dissipated at a rate which is proportional to $\cos\theta^2$ where θ is the angle between B_0 and the wavenumber vector k. As a result, an elongation of vortical structures along the direction of B_0 is observed. These effects are counteracted, however, by the natural development of the non-linear flow. The magnetic interaction parameter or Stuart number, N, is a measure of the balance of the inertial and Lorentz forces and is given by $N = \sigma B_0^2 L/\rho u$, where ρ is the density of the gas. For example, in the simplistic scenario of a decaying isotropic turbulent flow, vortex flux tubes, aligned in direction of the magnetic field, begin to form with the complete transition to a two-dimensional turbulent state independent of B_0 at very large N [139]. For detonations, the dynamics of the flow are complicated

Table 6: A summary of parameter set for the simulations used in this study. To compute the non-dimensional parameters the following reference values were used: L=6 mm, u = 1900 m/s, ρ_0=0.17 kg/m^3 where L is the transverse channel dimension, $u \approx D$, and ρ is the ambient density.

Case	P_a (bar)	N_2 (%)	K (%)	σ (S/m)	B_x, B_y (T)	Re_m	N
1	0.2	74.52	0.0	0.0	0.0	0.0	0.0
2-a	0.2	74.52	0.05	0.0	1000.0	0.0	0.0
2-b	0.2	74.52	0.05	0.0	2000.0	0.0	0.0
2-c	0.2	74.52	0.05	0.0	3000.0	0.0	0.0
2-d	0.2	74.52	0.05	0.0	6000.0	0.0	0.0
3-a	0.2	74.52	0.10	0.0	1000.0	0.0	0.0
3-b	0.2	74.52	0.10	0.0	2000.0	0.0	0.0
3-c	0.2	74.52	0.10	0.0	3000.0	0.0	0.0
4-a	0.2	74.52	0.25	0.0	1000.0	0.0	0.0
4-b	0.2	74.52	0.25	0.0	2000.0	0.0	0.0

by the persistent energy release and generation of large-scale fluid structures at the detonation front. The effect of the magnetic field on these structures is investigated here.

To investigate the effect of a magnetic field on the propagation of a detonation, numerical simulations are conducted for various magnetic Reynolds numbers and interaction parameters under the assumption of $Re_m << 1$. The external field is applied in either perpendicular or parallel to the direction of the propagation to a gaseous detonation seeded with potassium of 0.05, 0.1, and 0.25 percent. The numerical setup and configuration of these simulations were discussed in the last section and are the same here expect for the inclusion of the magnetic terms in the momentum and energy equations, and the fact that the $y-$direction dimension was doubled so that two detonation cells are captured in the domain. This makes the visualization of the magnetic field affects more apparent. Flow parameters, along with the reaction zone widths, are analyzed to quantify the effect of the applied field

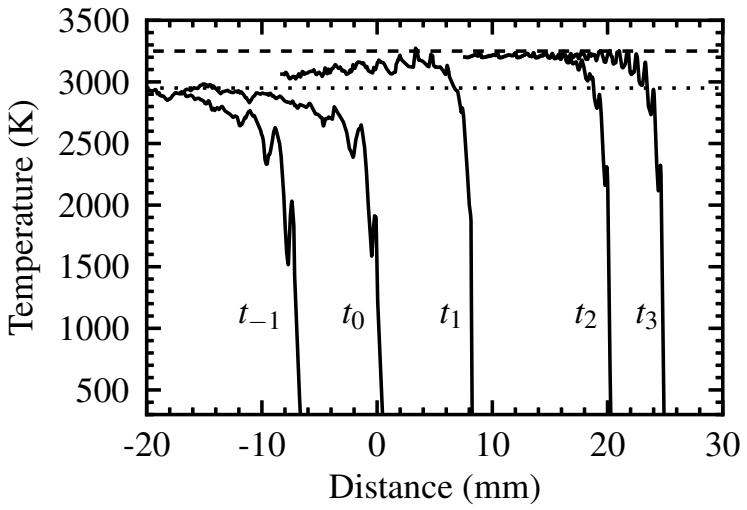

Figure 48: The averaged temperature profiles for case with a B_y field at different times: $t_{-1} = 0.104$ ms, $t_0 = 0.113$ ms, $t_1 = 0.127$ ms, $t_2 = 0.149$ ms and $t_3 = 0.157$ ms.

on the detonation.

Numerical simulations are conducted for different Re_m, N, and magnetic field orientations i.e., parallel ($B_{0,x}$) and transverse ($B_{0,y}$) to the detonation propagation. Table 6 summarizes the parameters studied in this work. Since $Re_m << 1$, the non-dimensional parameter Re_m, however, is of less importance, and N and the magnetic field orientation govern the dynamics of the detonation. The value of Re_m is recorded to ensure the validity of the quasi-static assumption. The detonation is first simulation without a magnetic field for each case. At a physical time of $t_0 = 0.113$ ms, the magnetic field is switched on. The magnitude of the field is slowly increased numerically throughout the simulation in order to limit the any unphysical changes a rapid increase may introduce. In practice, however, there are no observed differences in the results if this is done or not. The magnetic field is always taken as positive, since in two dimensions, the components of the Lorentz force do not change (only the orientation of the current density changes), and thus the detonation dynamics are unchanged.

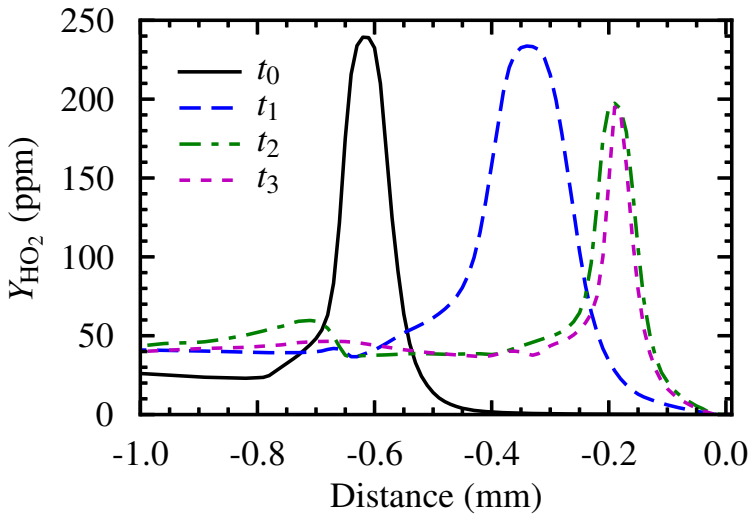

Figure 49: The profiles of mass fraction of HO_2 taken at the transverse location corresponding to the center of Mach stem for a B_y field at different times: $t_0 = 0.113$ ms, $t_1 = 0.127$ ms, $t_2 = 0.149$ ms and $t_3 = 0.157$ ms.

5.3.1 Effect of $B_{y,0}$

When the magnetic field is applied, the electromagnetic energy generated by action of the Lorentz force in the post-detonation flow is quickly converted into heat via Joule dissipation. In particular, since the induced currents are largest at the detonation front, a significant amount of electromagnetic energy is deposited directly in the induction zone of the detonation. For case Y4, the post-detonation temperature increases by nearly 450 K after the magnetic field is turned on. Moreover, the Joule dissipation does not decrease in time as in decaying problems due to the continual formation of new scales from combustion at the detonation front. As the temperature gradually increases, see Fig. 48, the reaction zone length reduces, and the distance to the peak HO_2 mass fraction reduces to 0.2 mm from 0.7 mm as in the case without a magnetic field (see Fig. 49). A characteristic of propagating detonations is the formation of cellular structures whose cell widths in transverse direction are dependent on $L_{1/2}$ [186]. These structures create characteristic large-scale structures in the post-detonation flow. In case with a $y-$direction magnetic field, smaller cellular structures

are formed in comparison to simulations without a magnetic field. Interestingly, the cell width is reduced to nearly 3 mm at $t = 0.15$ ms. At lower N, this does not occur. Although Joule dissipation continues to occur, the detonation front adjusts to a steady value as the kinetics become rate-limited by radical production. Thus, at $t = 0.16$ ms the cell width remains at approximately 3 mm. Since the magnetic field modifies the observed detonation cell-width, and this change is related through N, estimation of the electrical conductivity of the gaseous mixture is possible from observations of the cellular structure in a give magnetic field.

The heat addition by the magnetic field also affects the detonation velocity. Since the Joule dissipation is proportional to B_0^2, and thus N, the effect of heating on detonation is more profound in cases with higher N. Thus, the deviation in the detonation velocity (see Fig. 50) increases with N. Even in case Y1, the detonation velocity is marginally augmented in comparison to case without afield. Note that the Lorentz force is in the direction opposite of the detonation propagation. The momentum deficit, however, is negligible in comparison to the subsequent expansion occurring from heat addition. This is due to the application of the field in the direction perpendicular to the direction of the dominant velocity component (in x-direction).

5.3.2 Effect of $B_{x,0}$

When the magnetic field is applied in the x-direction, the detonation velocity increases slightly, but this increase is independent of N as shown in Fig. 50. The current density, and likewise the electromotive force, is proportional to the component of the velocity perpendicular to the magnetic field, in this case, the transverse velocity. Similar to cases with a B_y field, Joule dissipation results in reduction of $L_{1/2}$ at lower N as shown in Fig. 51. For simulations with an applied $B_{x,0}$, however, the Lorentz force counters the movement of transverse waves in the post-detonation flow since their motion is perpendicular to $B_{x,0}$. This introduces new dynamics. At higher

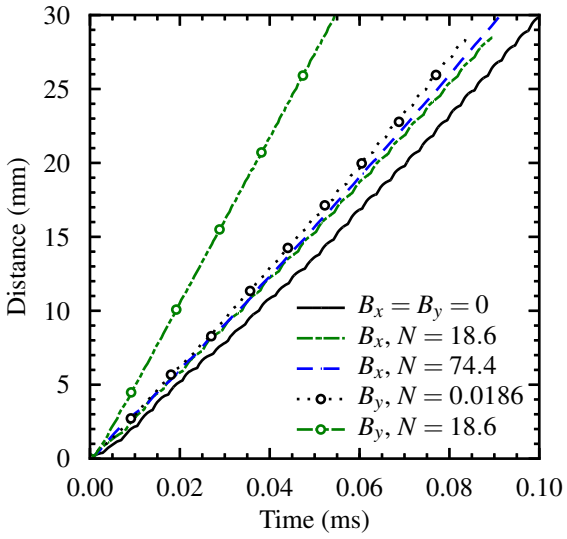

Figure 50: The average location of the detonation front as a function of time for the cases given in Table 6

values of N, the transverse waves are actively suppressed. This suppression reduces the strength of the transverse wave interaction with the Mach stem and incident shock at the detonation front, and over time the front becomes relatively flat. The formation of the characteristic cellular structures are thus eliminated. This results in a reduction in the $L_{1/2}$. The combined effect of heat addition via Joule dissipation and transverse wave suppression, which disables the high temperature triple point formation [77], results in only a marginal increase in the detonation velocity for any given N. For the times simulated here, and for the values of N investigated, the reaction front does not decouple from the shock wave. This was determined by switching off the magnetic field after some time. For any given N, the typical cellular structures are regenerated by turning off the applied field.

To summarize, the magnetic field applied in the direction of detonation propagation affects the detonation through a combined effect of Joule heating and Lorentz force. While the Lorentz force acts to eliminate transverse waves and cellular structure, the heating effect resulted in temperature increase and sustained coupling of

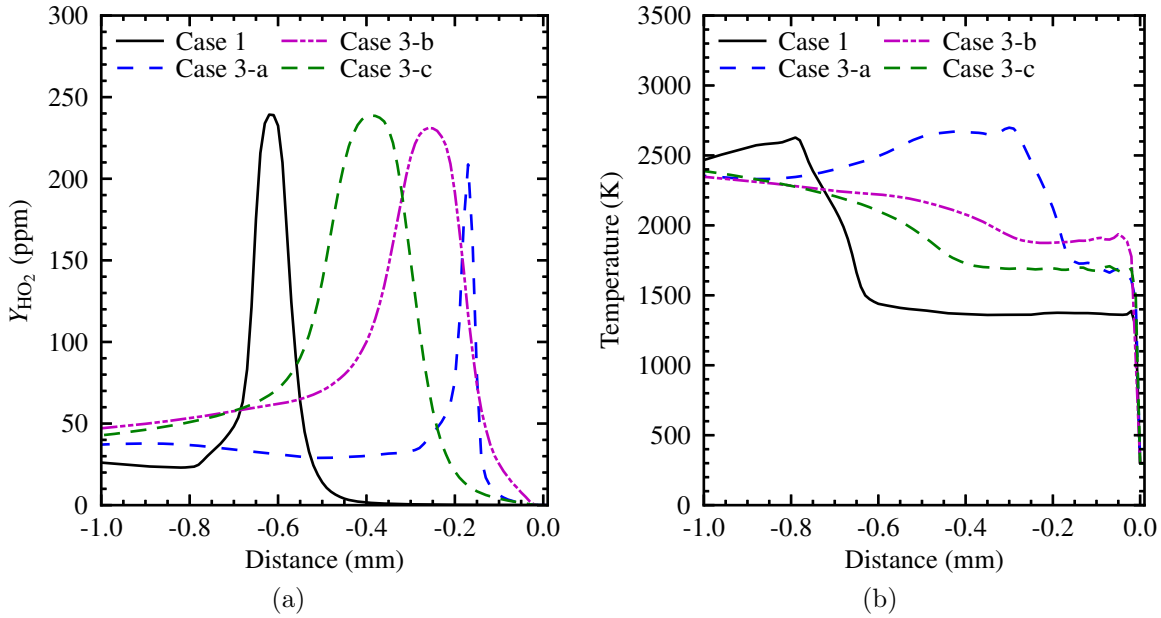

Figure 51: Profiles of the HO_2 mass fraction and temperature for with an increasing magnetic field corresponding to the center of the Mach stem for each detonation front at approximately 0.175 ms.

reaction zone with the shock propagation. Thus, for any given N, the change in detonation velocity is marginal. Due to the difference in the magnitude of velocity components in x- and y -directions, $B_{0,x}$ affected the detonation both by momentum and energy coupling where as the dominant effect of $B_{0,y}$ is Joule dissipation.

5.4 Conclusions

The electrical conductivity of a plasma produced by a hydrogen-air detonation is computed. The proposed detailed chemistry is able to model both hydrogen-oxygen combustion and ionization in hydrogen-air mixtures. Basic detonation properties, such as D_{CJ}, are reproducible at various pressures and N_2 dilutions indicating that the numerical approach is both robust and accurate. For unseeded detonations, ionization is slower as a result of the relatively slow formation of NO. At higher ambient pressures, the post-detonation temperature is increased resulting in an increase in the electrical conductivity. Reducing the N_2 dilution also increases the post-detonation

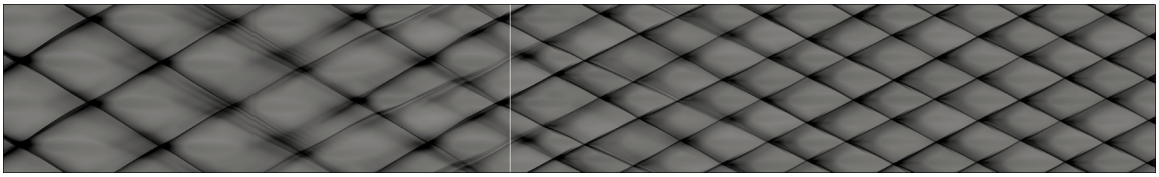

Figure 52: A numerical sootfoil for a gaseous detonation seeded with 0.25 percent by mass of potassium. The maximum magnetic field is $B_x = 2000$ T . The cellular structures clearly indicate an altercation in the detonation dynamics.

temperature and the electrical conductivity until the reduction of nitrogen in the mixture begins to limit NO production. Since the observed electrical conductivities in unseeded detonations are too low for MHD devices to be efficient, seeding the mixture with low ionization potential alkali salts is necessary. While seeding does increase the electrical conductivity, simulations in both one and two dimensions show that the detonation is sensitive to the amount of seeding material injected into the flow. Too high of a seeding percentage can adversely affect the detonation propagation, however, even at lower seeding percentages (less than 1.25%) a four to five order of magnitude increase in the electrical conductivity is observed.

CHAPTER VI

RICHTMYER-MESHKOV INSTABILITY

6.1 Introduction

In the following chapter, the Richtmyer-Meshkov instability (RMI) is numerically investigated in a magnetized plasma. In Sec. 4.2.1, the parameters, initial conditions, and boundary conditions required for the numerical simulation of the RMI are defined. The same conditions are used here with the exception of magnetic field in the direction normal to shock propagation. In a magnetized plasma, fluid instabilities are much more complex since the presence of Alfvèn wave can cause a coupling between the velocity and magnetic fields to alter the dynamics of the fluid. As a result of the influence of the magnetic field, a different classification is added defined based on the ratio of the magnetic to thermodynamic pressure or $\beta = B^2/2p$ and grouped into low-β or high-β plasmas. In the following, some definitions are first introduced and the RMI is discussed for low and high β plasma.

6.2 Definitions and Simulation Parameters

Given the definitions of the computational configuration and the initial flow conditions introduced in the last two sections, it is useful to next define some important variables governing the evolution of the RMI and used to analyze the shock-accelerated mixing layer. As discussed in the Introduction, as the shock refracts through the material interface, a misalignment in the density and pressure gradients occurs. This results in a deposition of vorticity through the production of baroclinic torque along the contact discontinuity causing the perturbations to grow in amplitude. This process can be investigated using the compressible vorticity transport equation, given by Eq. 289,

which is derived by taking the curl of the momentum conservation equation. Ignoring the viscous and resistive terms, the tensor form of this equation is given as

$$\begin{aligned}\frac{D\omega_i}{Dt} &= \omega_j \frac{\partial u_i}{\partial x_j} - \omega_i \frac{\partial u_j}{\partial x_j} + \frac{1}{\rho^2}\epsilon_{ijk}\frac{\partial \rho}{\partial x_j}\frac{\partial p}{\partial x_k} + \epsilon_{ijk}\frac{\partial}{\partial x_j}\left(\frac{\epsilon_{klm}J_l B_m}{\rho}\right) \\ &= \Omega_i^s + \Omega_i^d + \beta_i^v + \Pi_i.\end{aligned} \tag{289}$$

The first two terms in this equation, Ω_i^s and Ω_i^d, represent the transport of vorticity through vortex stretching and dilatation. The third term, β_i^v, represents the production/destruction of vorticity by baroclinic torque. In addition to these terms, an additional vorticity production occurs in magnetized plasmas, which is represented by the term, Π_i. The viscous contribution to vorticity dissipation is ignored here. At the contact discontinuity, β_i^v is orders of magnitude larger than the viscous term [185].

Once the circulation is deposited on the material interface, the amplitude of the perturbations grow linearly for a short period of time. As the two fluids become entrained and start to mix, the rate at which the mixing layer grows begins to saturate and the RMI becomes non-linear. In practice, there are many ways to define the width of the mixing layer in order to deduce the growth-rate of the instability. In this study, an integral definition is adopted where the mixing length is given by

$$\eta(t) = 4\int_{-0.2}^{L_x} \langle Y_h \rangle \left(1.0 - \langle Y_h \rangle\right) \mathrm{d}x. \tag{290}$$

The quantity $\langle \cdot \rangle$ represents a volumetric average in the transverse directions over the distances L_y and L_z, and is a function of only the time, t, and x, the longitudinal direction. Other methods, such as defining the boundary of the mixing layer as the maximum and minimum values of Y_h and taking the difference between these two points are less precise and somewhat arbitrary.

The mixing length η is representative of the entrainment mixing processes and does not lend any information on how well mixed the two fluids are on a molecular

level. For this, other quantities are needed. The molecular mixing fraction, Θ, is defined as

$$\Theta(t) = \frac{\int \langle Y_h Y_l \rangle \mathrm{d}x}{\int \langle Y_h \rangle \langle Y_l \rangle \mathrm{d}x}. \tag{291}$$

It is a more useful description of how well-mixed the two species are in the mixing zone since the span-wise averaged mass fraction carries no distinction between regions that are completely mixed and those regions that are unmixed, but contain equal portions of species. Thus, Θ quantifies the relative amount of molecularly mixed fluid within the mixing layer, a $\Theta = 1.0$ would mean that the entrained fluids were completely mixed within each transverse plane. In experiments, η is the easiest to measure. More recent experiments using simultaneous PIV an PLIF imaging are able to deduce more detailed information about the mixing processes in the RMI. This is a boon for numerical simulations, since the averaged quantities like η and Θ are to some extent still measurements of the large-scale mixing process and do not provide information about the turbulent mixing processes that may exist in the mixing layer at very late times or after re-shock.

In a magnetized plasma, the dynamics of the RMI is altered significantly. As a result of the electromotive force, the stretching and compression of magnetic field lines by the velocity field results in a small-scale dynamo process that amplifies the magnetic field. The dynamics of this process are determined by three parameters, the helicity, the cross helicity, and the electrical conductivity. Thinking of the RMI as a departure from equilibrium, it is useful to define these parameters by equating them to the possible equilibrium states of a plasma in MHD. There are two equilibrium states, the force-free state and the Alfvenic state.

Depending on the initial β of the plasma, a emf resulting from the mixing layer amplifies the magnetic field until the induction process is saturated and the magnetic field becomes "frozen" into the fluid. Depending on the strength of this saturated magnetic field, the mixing process could be drastically altered since fluid mixing by

Table 7: Summary of the initial conditions and parameters for the numerical simulations of the single-mode RMI where $u^* = \sqrt{p_0/\rho^*}$ is the reference velocity, $t^* = \lambda/u^*$ is the reference time, and $\rho^* = \rho_l^+$ is the reference density.

Case	$k_0\eta$	M_s	ρ_h/ρ_l	A	A^+	$\Delta V/u^*$	τ_f/t^*	λ/Δ_0	L_x/λ
SM1	0.1	1.2	3.0	0.5	0.499	0.313	1.019	512	20
SM2	0.1	1.5	3.0	0.5	0.516	0.849	0.375	512	20
SM3	0.1	2.0	3.0	0.5	0.546	1.726	0.184	512	20
SM4	0.1	5.0	3.0	0.5	0.517	6.642	0.048	512	20

either small-scale or large-scale vortical motions could be completely inhibited. In order to analyze this, the following scalar equation for the time-rate of growth of the magnitude of the magnetic field can be derived

$$\frac{1}{2}\frac{\partial B_k^2}{\partial t} = -B_i v_i \frac{\partial B_j}{\partial x_i} B_i + B_i B_i \frac{\partial v_j}{\partial x_i} - B_k^2 \frac{\partial u_i}{\partial x_i} \tag{292}$$

where the last two terms represent stretching and compression.

In summary, given a defined initial condition, the growth-rate of the RMI is first analyzed through the large-scale measurements of $\eta(t)$ and $\Theta(t)$. In some sense, these are categorical measurements, A more detailed analysis relies on computing the terms in the vorticity transport equation and the scalar equation for the amplification of the magnetic field. Lastly, the mixing processes occurring by the small-scale turbulent motions (occurring only once transition from a laminar flow has occurred) can be analyzed through the kinetic and magnetic energy spectrum in wavenumber space. The analysis is carried out for single-mode RMI. The multi-mode RMI and the re-shocked, multi-mode RMI will be investigated in the future.

6.3 Suppression of the RMI

In the previous sections, the RMI has been discussed in the context of hydrodynamics for non-magnetized mediums. The single-mode RMI is now analyzed for the scenario when an incident shock impulsively accelerates a contact discontinuity under the

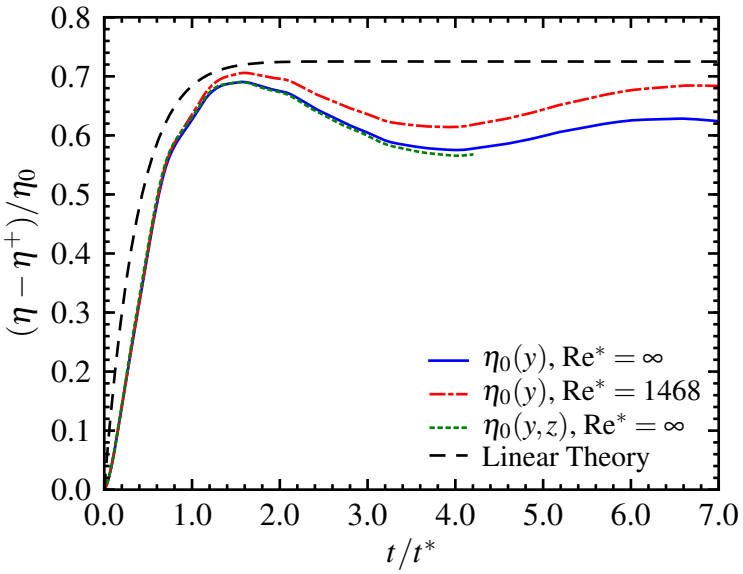

Figure 53: Time evolution of the mixing layer width for the single-mode RMI in a magnetized plasma with $\beta = 10$ and initial conditions of $M_s = 1.5$, $k_0\eta_0 = 0.1$, $A = 0.5$. The results for two- and three-dimensional numerical simulations using both the ideal ($Re^* = \infty$)and resistive MHD equations are compared to the linear theory, where $Re^* = Re_m^*$ are both computed from the reference parameters.

assumption that both the light and the heavy fluids are magnetized and have the same electrically conductivity. In MHD, the dynamics of the incident shock as it refracts through the medium is significantly different since the jump conditions for the shock and contact discontinuities are different. For example, and most critical to this applications, contact discontinuities do not support a jump in the transverse velocity. Instead, Alfven waves carry this jump condition. As a result, the vorticity generated by the baroclinic torque term in the vorticity transport equation is swept away by the Alfvén waves, which propagate to the left and right of the contact discontinuity. Depending on the speed of the vorticity propagation along the magnetic field lines via the Alfvén waves, the interface can be potentially stabilized.

A similar incompressible linear analysis used to study the growth-rate of the RMI in non-magnetized flow can be done for MHD. Instead of the result being a single

ordinary differential equation for the interface displacement, however, there is additional differential equation for the magnetic field fluctuation. This coupled set of equations can still be solved analytically. Wheatley et al. [215, 216] have derived the full analytical expressions for the growth-rate of the RMI in the presence of a normal magnetic field. Interestingly, the initial growth rate of the interface is not affected by the presence of the RMI, specifically Richtmyer's impulsive model is recovered $\dot{\eta}(t = 0^+) = \eta_0 k \Delta V A$. The time evolution of the mixing layer width is [215, 216],

$$\eta(t) = \eta_\infty - (\eta_\infty - \eta_0) e^{\sigma t} \cos(\tau t) \tag{293}$$

where α and τ are parameters defined as

$$\sigma = -\frac{Bk\left(\sqrt{\rho_l} + \sqrt{\rho_h}\right)}{\rho_l + \rho_h}, \tag{294}$$

$$\tau = \frac{\left(B^2 k^2 \left(\rho_l + \rho_h - 2\sqrt{\rho_l \rho_h}\right)\right)^{1/2}}{\rho_l + \rho_h}, \tag{295}$$

and η_∞ is the asymptotic mixing layer width,

$$\eta_\infty = \eta_0 \left[1 + \Delta V \left(\frac{1}{v_{a,h}} - \frac{1}{v_{a,l}}\right)\right], \tag{296}$$

where $v_{a,h} = B/\sqrt{\rho_h}$ is the Alfvén velocity in the heavy fluid and $v_{a,l} = B/\sqrt{\rho_l}$ is the Alfvén velocity in the light fluid. Figure 53 shows a comparison of two- and three-dimensional numerical simulations of the single-mode RMI to the linear theory for a $\beta = 10$ plasma. The under prediction of η_∞ and the low frequency oscillations are consistent with the non-linear simulations presented by Wheatley et al. [215, 216] when assessing the validity of the model. Additionally, the results show here that the predictions are consistent in the generalization to three-dimensions. With the inclusion of the viscous diffusion, species mass diffusion, heat conduction, and magnetic resistivity terms, there is a noticeable increase in η_∞ for a $Re^* = Re_m^* = 1470$. To explain this, some explanation of the ideal MHD case is necessary.

The linearized model of Wheatley et al. [215, 216], however, always predicts that the RMI is stabilized no matter the initial β of the plasma. This is not precisely

(a) $t/t^* = 1.1$

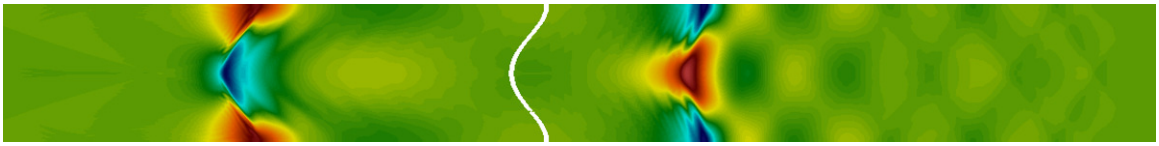

(b) $t/t^* = 3.5$

(c) $t/t* = 5.2$

Figure 54: Contours of the normalize magnitude of the magnetic field B^2/B_0 at three different times for the single-mode RMI in a $\beta = 10$ plasma. The white contour line represents the material interface defined by $Y_h = Y_l = 0.5$.

correct. The stability of the contact discontinuity is dependent on the transport of the vorticity by the Alfvén waves supported by the B_x magnetic field lines. Thus, stability requires that the speed of the Alfvén wave to be larger than the *linear* growth-rate of the RMI resulting in the criteria [181]

$$v_a^* \geq \dot{\eta} \approx k_0 \eta_0^+ A^+ \Delta V. \tag{297}$$

where the initial linear growth-rate of the Richtmyer's impulsive model is used to approximate the initial growth velocity of the RMI. Since $v_a^* = B/\sqrt{\rho^*}$, it is possible to define a critical β for which stability of the RMI is guaranteed. This criteria has been parametrically studied by Sano et al. [181], who show that the stability of the RMI is not only dependent on β, but also on M_s and A. The numerical simulations in this study of the low-β plasma verify that relations holds for both the single-mode and multi-mode RMI in two- and three-dimensions.

The reason is that in all cases the initial linear growth rate of the RMI is adequately described by Richtmyer's impulsive model [165] and once the vorticity is transported

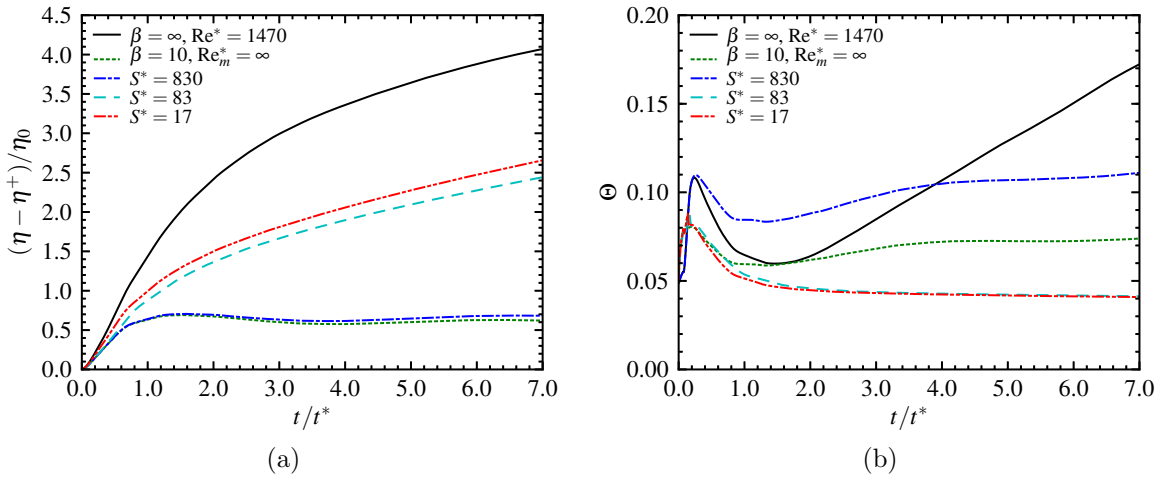

Figure 55: Time evolution of the mixing length $\eta(t)$ and the mixing fraction $\Theta(t)$ for the single-mode RMI in a resistive plasma of $\beta = 10$ and a non-magnetized gas of $\beta = \infty$ is shown for reference.

away from the contact discontinuity, any acceleration of the growth through can not occur. Stability, in the case of low-β plasma, depends only on the transport process of vorticity by the Alfvén waves away from the contact discontinuity. Increasing the magnetic resistivity of the plasma alters the transport of vorticity by the Alfvén waves. Figure 55 shows the mixing length $\eta(t)$ and the mixing fraction $\Theta(t)$ for the single-mode RMI in a resistive plasma. The more appropriate non-dimensional number is the Lundquist number S, which is like a Reynolds number, but with the Alfvén velocity, v_a^* used as the velocity scale instead. This value represents the rate of diffusion of perturbations along the magnetic field lines to the propagation velocity of the Alfvén wave. For smaller values of S^*, the RMI is no longer stabilized by the magnetic field.

Figure 54 shows contours of the normalized magnetic field with a contour line marking the species interface, $Y_h = Y_l = 0.5$. The perturbations in the magnetic field mirror the vorticity generated initially at the material interface. This is more clearly demonstrated by Fig. 56, which shows the spanwise averaged normalized vorticity $\langle\omega\rangle/ku^*$ for three cases, $\beta = 10$, $\beta = 1000$, and $\beta = \infty$. At the higher values of β,

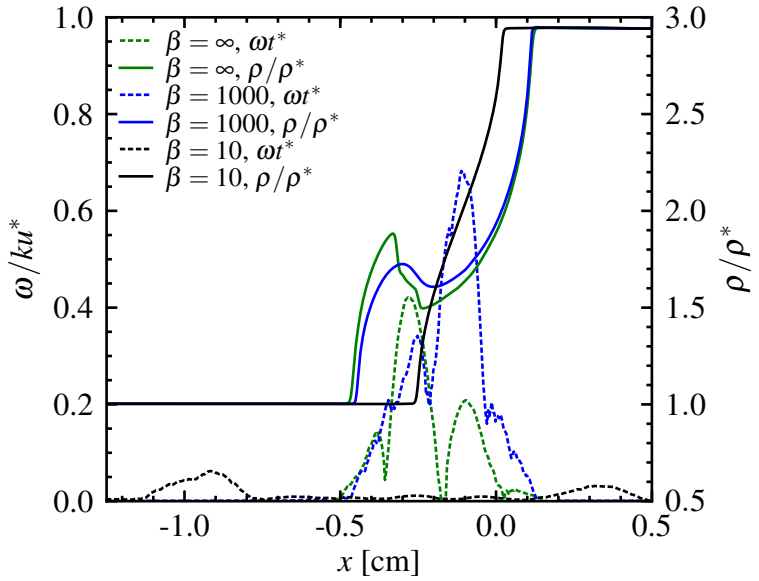

Figure 56: Spanwise averages of the normalized density and normalized vorticity profiles for different values of β demonstrating the stabilization of the RMI at high β values.

smaller initial values of B_x, the magnetic field no longer stabilizes the RMI. In Fig. 56, the spanwise averaged normalized density ρ/ρ^* illustrates this.

6.4 Magnetic Field Amplification by the RMI

Low-β plasmas are more characteristic of the confined laboratory plasmas in terrestrial applications such as fusion, however, even in such cases, the pressure of the gas is often large enough to require very strong magnetic fields for the RMI to be suppressed. Thus, in many magnetized plasmas, such as those common in astrophysics, the values of β are very large. Moreover, as M_s increases, the value of β_c increases as well. As a result, suppression of the RMI is a less common scenario. If $\beta > \beta_c$, then to a varying degree the growth-rate of the RMI is non-zero.

Figure 57 shows the time evolution of the mixing length in a magnetized plasma with $\beta = 10^3$ and $\beta = 10^4$ for the single-mode RMI with $M_s = 1.5$. In all cases, the growth-rate of the RMI is not suppressed. The mixing fraction, Θ, however, shows that for these two cases, the flow is not as well mixed as it is in non-magnetized

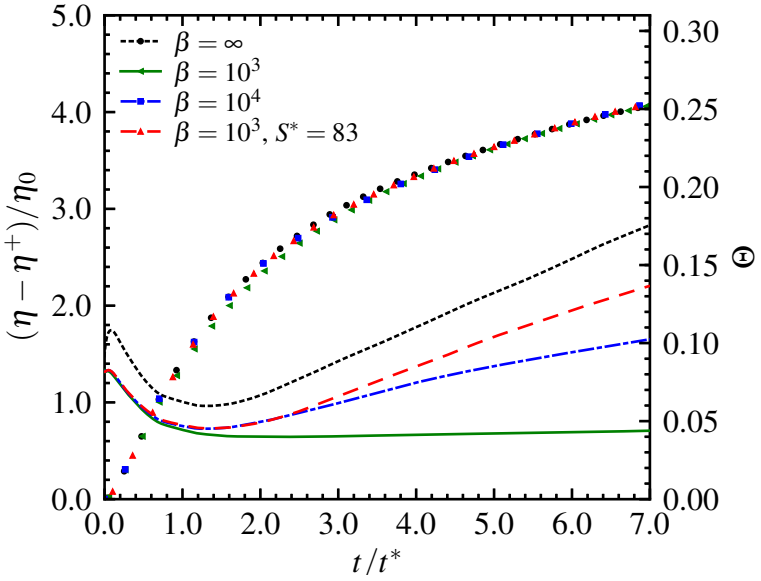

Figure 57: Time evolution of the mixing length $\eta(t)$ and the mixing fraction $\Theta(t)$ for the single-mode RMI in a magnetized plasma of $\beta = 10^3$ and $\beta = 10^4$ as well as for a non-magnetized mixture ($\beta = \infty$).

plasma. This is because the secondary instabilities have been almost completely suppressed in the $\beta = 10^3$ and partially suppressed in the $\beta = 10^4$ cases. Figure 58b shows a contour line of the material interface defined by $Y_h = 0.5$. The Kelvin-Helmholtz instability typically results in the generation of a pair of vortices on either side of the spike. These vortices further the mixing process increasing the surface area over which molecular diffusion can occur. In the case of $\beta = 10^4$, the generation of these vortices is slightly suppressed, which is observed by the noticeable decrease in Θ compared to a non-magnetized single-mode RMI of the same initial conditions.

As the initial growth of the RMI generates vorticity causing the heavy and light fluids begin to mix, this also results in the entrainment of the the magnetic field lines by the vortical motions. By compressing and stretching the magnetic field lines, the magnetic field is greatly amplified in magnitude over its background initial value. Figure 59a shows the time evolution of the peak magnetic field. The magnetic field increases initially as a result of compression, but as the RMI develops the magnetic

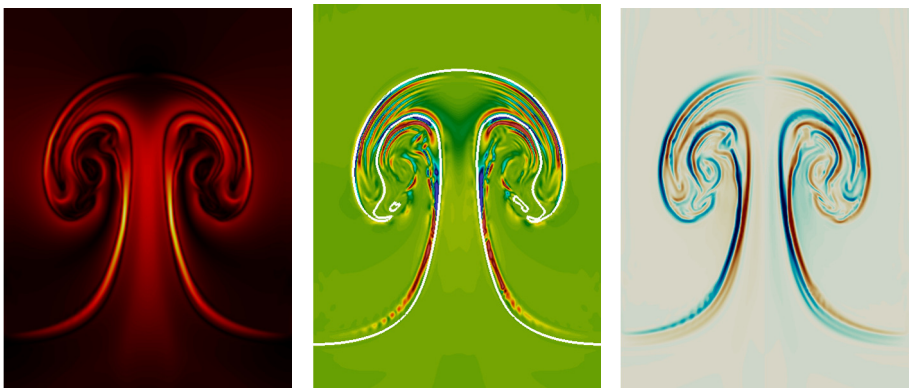

(a) B^2/B_0 (b) $\langle \mathbf{B}(\mathbf{B}\cdot\nabla)\mathbf{v}\rangle/(B_0 k u^*)$ (c) j/kB_0

Figure 58: Contours of (a) the normalized magnetic field magnitude, (b) the magnetic field stretching term, and (c) the current density for the single-mode RMI in a $\beta = 10^4$ plasma at $t/t^* = 7$.

field lines begin to be stretched by the fluid. This results in a significant increase in the amplification of the magnetic field. Figure 59b shows the spanwise averaged values of the term $\langle \mathbf{B}(\mathbf{B}\cdot\nabla)\mathbf{v}\rangle$, which is responsible for the time-rate of increase in the magnetic field due to stretching. There is an obvious increase in the magnitude of this term for $t/t^* > 2$.

As the the magnitude of the magnetic field increases, sheets of current density become entangled in the region of mixing. As the magnitude of the current density increases, the sheets become thinner and more prone to magnetic reconnection, which results a tearing instability and a conversion of magnetic energy into kinetic and thermal energy. For the numerical simulations shown here, however, magnetic reconnection does not seem to occur. This is likely because the tearing instability is stabilized by shearing motion. The current density contours at t/t^* are shown in Figure 58c.

6.5 Conclusion

During an explosion, a primary blast wave propagates into the surrounding medium followed by a secondary shock and a contact discontinuity separating the burnt gas

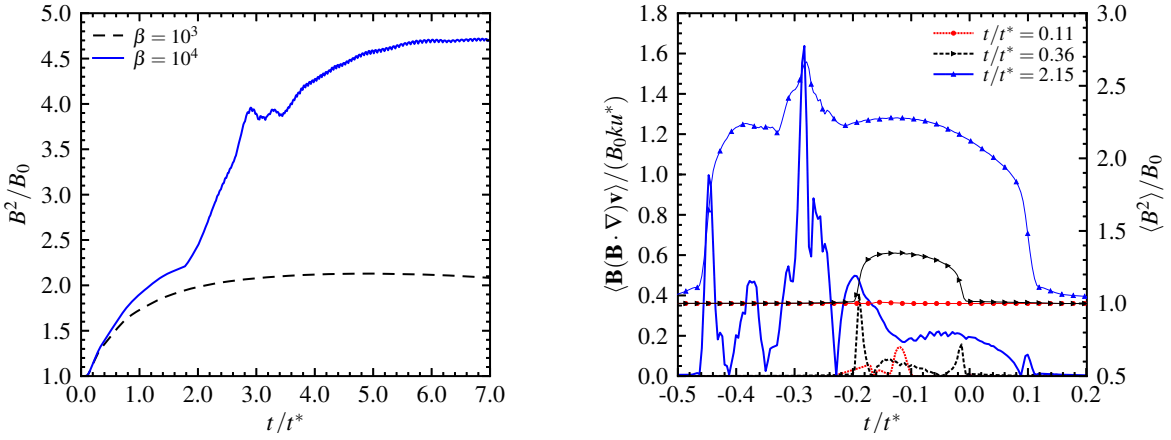

Figure 59: (a) Time evolution of the peak magnetic field magnitude in the domain normalized by initial magnetic field B_0, and (b) the spatial variation of the spanwise averaged magnetic field stretching,$\langle \mathbf{B}(\mathbf{B}\cdot\nabla)\mathbf{u}\rangle/(B_0 k u^*)$ and magnetic field at three times $t/t^* = 0.11$, $t/t^* = 0.36$, and $t/t^* = 2.15$. The marked lines refer to the magnetic field values which normalized have a value of 1 in the regions of the domain other than shown here.

products from the shocked gases. Since the contact discontinuity is Rayleigh-Taylor unstable, mixing slowly occurs during the primary phase. In a spherical explosion, a reflected shock resulting from implosion re-shocks the mixing layer between the burnt gases and the surrounding medium triggering the RMI and accelerating the mixing process. The RMI quickly results in the development of a turbulent inertial range that drives the mixing layer to a state of fully developed turbulence. The accelerated mixing between the burnt and unburnt products with the surroundings results in an afterburn phase that continuously provides the a release of energy to support the expansion of the gas products.

The RMI also occurs when the initial blast wave or the secondary shock impacts a gas mixture of variable density or temperature. In an astrophysical setting this occurs when the supernovae remnants interact with the interstellar medium, which is composed of warm molecular clouds and denser, colder regions of gas. The acceleration of these gases in the interstellar medium initiates the RMI. Interestingly, in both

scenarios the gases are plasmas, which are also slightly magnetized by an ambient magnetic field in interstellar space. Moreover, during supernovae of the core-collapse type, the presence of a magnetic field is the likely reason for the asymmetric nature of the explosion. As a result, the dynamics of the magnetic field become important during the mixing processes, which are in part initiated as a result of the RMI.

Shock-accelerated mixing of plasmas does not only just have implications to astrophysical flows. For instance in Chapter 4, the seeded gaseous detonations and particularly the condensed-phase explosions generate plasmas of sufficient electrically conductivity. Such explosions occurring in a confined space, could easily result in the product gases becoming magnetized by the presence of an external magnetic field. Another example is during the inertial confinement fusion process. In this scenario, it is ideal to avoid the onset of instabilities since they increase mixing and thus reduce the burn temperature. It is possible that a strong magnetic field could aid in the stability of these devices. In all such cases, further understanding how mixing is altered in a magnetized medium if only in a fundamental configuration could offer important insights into the dynamics of these aforementioned problems.

Several numerical simulations of the RMI were discussed in this chapter and used to illustrate shock-accelerated mixing in both magnetized plasma and non-magnetized flows. Three different configurations were introduced, single-mode RMI, multi-mode RMI, and re-shock RMI. A hybrid, high-order finite difference scheme is used in all simulations. The shock-capturing scheme employs a the flux vector splitting scheme using 5th order WENO-Z flux reconstruction. This is coupled with a central scheme using a compact 4th order stencil order. For MHD simulations, the constrained transport method is used for the single-mode and multi-mode RMI. For re-shock simulations, the projection scheme is used. This is because standard constrained transport schemes develop oscillations when a weak magnetic field propagates in a computational domain. The easiest solution is modify the frame of reference of the

RMI.

The numerical results are compared to the linear theory of plasmas for which $\beta < \beta_c$. For such plasmas, numerical simulations demonstrate that both the single-mode and the multi-mode RMI are unequivocally suppressed in two- and three-dimensions if the magnetic resistivity is small. Increasing the magnetic resistivity or decreasing the Lundquist number results in destabilizing the RMI. For $\beta > \beta_c$ plasmas, the vorticity generated by the baroclinic torque term during shock refraction results in the initiation of a small-scale dynamo. The magnetic field lines are compressed and stretched by the fluid and become entangled resulting in an increase in the magnitude of the magnetic field and a thinning or compression of current sheets. In a fully-turbulent state, magnetic reconnection events would likely to further drive the mixing processes.

CHAPTER VII

CONCLUSIONS AND RECOMMENDATIONS

7.1 Conclusions

Explosions are a common phenomena in the Universe. Beginning with the Big Bang, one could say the history of the Universe is narrated by a series of explosions. This is nowhere more apparent than in the life cycle of a star. The large clouds of gases expelled from a supernova propagate through the Universe populating it with the heavy matter necessary for the creation of new stars and galaxies. Explosions, however, come in a wide variety of types and can be classified in a broad manner by the type of energy injected into the system, e.g., magnetic, nuclear, chemical, etc. For the system to exhibit explosive behavior, the rate of injection of energy must occur at rates faster than which the system can equilibrate to the change. Since all types of explosions occur in a series of interactions incorporating many different physical processes beginning with their initiation to their dynamical interaction with the environment, a piecemeal approach is adopted in this thesis for study the explosion phenomena occurring in a magnetized medium or in the presence of background magnetic field. Two disparate ranges of time scales occurring during explosion are identified in order to simplify the analysis of the problem into two parts. The first involves the study of a freely propagating detonation wave in a background magnetic field. Detonation waves are typical in condensed-phase, high-energy chemical explosives, but the problem in this thesis has been further simplified to only consider detonation in a single gaseous phase. The second problem involves the mixing processes of the explosive products gases with the surrounding environment. This occurs at time scales many orders of magnitude larger than the time scales at which the initiation processes of

the explosion take place. Thus, this problem addresses a much broader question of how mixing occurs in a shock-accelerated, magnetized flow. To address this question, numerical simulations of the Richtmyer-Meshkov instability are used.

An additional benefit of using such canonical simulations is that they can also be used to assess and understand how different numerical methods alter the solution. A primary objective of this thesis has been to develop a general methodology within the framework of a multi-physics code that can be used to simulate a wide variety of MHD flows. In the narrower scope of this thesis, three criteria are delineated as being important to the successful implementation of numerical methods for high-speed, MHD turbulent flows. The first requirement is that the numerical methods necessary to resolve shocks and large gradients in a flow are diametrically inconsistent with the criteria for the numerical simulation of turbulence. High-order central difference methods are generally preferred in such cases since they contain a minimum amount of numerical dissipation, but suffer instability near discontinuities. Upwind, shock-capturing methods resolve discontinuities extremely well, but do so only by introducing numerical dissipation. A solution is to adopt a hybrid methodology that attempts to blend the benefits of both schemes. These schemes have been used in the past for the study of shock-turbulence interaction in hydrodynamic flows with much success. Extending this numerical modeling capability to MHD allows for the study of wide variety of compressible plasma flows. Hindering a direct extension of these numerical methods used for the Euler or Navier-Stokes equations in hydrodynamics to the governing equations of MHD is the requirement that the magnetic field remains divergence free throughout the simulation. As a result of this involution requirement, several algorithms have been proposed in the literature to maintain the divergence of the magnetic field to values near the order of the grid resolution. The difficulty is that these methods are not necessary consistent or easy to extend to a hybrid methodology, which may be needed in flows relevant to detonation and explosion. In

Chapters 3 and 4, this issue is discussed in detail. The unfortunate conclusion is that there is not straight-forward answer. The application of these methods are inherently problem dependent. For simulations of the RMI, the hybrid approach can be used, but based on the switching criteria used in this thesis, the shock-capturing scheme is needed in the regions where mixing occurs as a result of the high gradients in density and temperature. While the hybrid approach did not affect the solution, the benefits of the low-dissipation central scheme in the mixing region are lost. It is possible that this approach is better utilized in other applications, such as shock-turbulence interaction.

Two classes of numerical models are implemented and validated for a large number of test conditions. The classical unsplit, finite-volume, Piece-Wise Parabolic Method is compared to a hybrid, high-order finite-difference method employing a compact central difference scheme and a flux vector splitting scheme based on flux reconstruction using a fifth order WENO-Z method. The later is used to study the gaseous detonation of hydrogen and air mixtures seeded by potassium carbonate and the single-mode, multi-mode, and re-shock Richtmyer-Meshkov instability in a magnetized plasma. Each has their drawbacks and advantages. A constrained transport method is used for the majority numerical simulations conducted in this thesis since numerically is the most consistent, however, the use of such methods does limit the formal order of accuracy of the numerical method since these methods involves translating variables from the cell-centers to the face-centers.

Numerical simulations of the ionizing detonation are validated against experimental measurements and then used to study the stability of the propagating detonation wave in particle seeded flows. Since gaseous detonations do not produce plasma of a large electrical conductivity, this seeding is necessary, but it is limited since adding a significant amount of seeding reduces the amount of energy available to maintain

the expansion of the products. The propagation of stable, ionizing detonation occurring in the presence of a magnetic field is altered. For such conditions, the electrical conductivity is small enough for the governing equations to be approximated in the low magnetic Reynolds number limit or in other words by the quasi-static form of the MHD equations. Thus, the Stuart number, or magnetic interaction parameter, governs the dynamics of the flow. For magnetic fields orientated in the direction of propagation, the transverse waves are altered. This causes the interaction of the shock wav, transverse wave, and Mach stem occurring at the detonation front to become altered. Ultimately, this transitions the propagating detonation wave to a higher mode as indicated by the numerical soot foils.

Next, the variable density mixing in the magnetized plasma is discussed. Such flows are are known to be unstable to impulsive acceleration. This instability, referred to as the Richtmyer-Meshkov instability or RMI, is the primary mechanism for triggering a rapid increase in the mixing of the explosively generated gases. In a magnetized medium, the vortical motions driving mixing also induce a emf resulting in the amplification of a background magnetic field. Numerical simulations of the RMI in a magnetized medium are used to study this process and investigate how it affects scalar mixing. Using these simulations, a background magnetic field is observed to be amplified up to a 100 times its original magnitude, a result that corroborates the observed measurements of synchrotron radiation in supernovae remnants.

7.2 Recommendations for Future Work

Given that the numerical methods developed in this work are applicable to any compressible, reacting MHD flow, many types of problems can be considered in the future without any necessity to add further physics-based models. First and foremost, let us consider the problem of magnetic field amplification by explosive events such as supernovae remnant propagating through the interstellar medium. There are two processes

that result in an amplification of the magnetic field, the first is the Richtmyer-Meshkov instability, which was studied here, and the second is the interaction of a shock wave with a turbulent magnetized medium. In the shock-turbulence problem, the induced magnetic field is initiated by the anisotropies generated as the shock amplifies the velocity and magnetic vector field fluctuations. Direct numerical simulations can first be used to study this problem following the well-established methodology of hydrodynamic shock-turbulence interaction. The numerical methods implemented in this thesis are extremely suited for this problem.

In a related problem to the variable-density mixing studied in this thesis using the Richtmyer-Meshkov instability is to more clearly identify how the turbulent scalar mixing processes are altered in either an incompressible or compressible environment. The scalar mixing problem in hydrodynamic turbulence is rich with many unanswered questions, but is much more well understand in comparison to magnetohydrodynamic turbulence. This knowledge could easily be extended using the numerical methods discussed in this thesis using simulations of forced isotropic turbulence containing a passive scalar. The knowledge is directly applicable to the multi-species mixtures in astrophysical plasmas.

In all of the problems discussed in this thesis, direct numerical simulations were used. This is a severe limitation since once these simulations are extended to more realistic systems, the computational requirements become prohibitively expensive. As a result, it becomes required to use a turbulence closure modeling approach to provide a physical mechanism for the dissipation. In previous work, a large-eddy simulation (LES) turbulence model has been developed for MHD. Both shock-turbulence interaction and scalar mixing problem could also be investigated using the MHD-LES approach. Once again analogs to the study of these topics in hydrodynamics exist. The simulations conducted in this thesis, hint that the implemented numerical methods can easily be applied to these problems. With LES, a large-scale, realistic

simulation of spherical explosion could be studied. Such studies would provide be able to leverage the results discussed in the context of very simplified problems by offering a more direct analogy between the problems.

Lastly, while the hybrid finite-difference numerical method implemented in this thesis is capable of being applied to a large range of problems, some significant improvements could be made. First, the question of the best way to extend the numerical method consistently to a high order should be addressed. Constrained transport methods using a staggered grid approach become extremely complex and impractical in their extension between third-order. A promising method is the Hamilton-Jacobi method. Some initial efforts have been made to implement this method, but they were ultimately unsuccessful. Since this class of numerical scheme for MHD integrates the magnetic vector potential directly these schemes naturally preserve the divergence free condition on the magnetic field and can be extended to higher-orders using the same finite differencing methods used developed in this thesis.

APPENDIX A

CHEMICAL KINETIC MODELS

The combined model for both hydrogen-air detonation and the subsequent ionization consists of 26 species and 65 reactions and is described by Tables 8 and 9. From experimental analysis [59], the ionization of NO is the primary pathway for ionization in hydrogen-air mixtures. Thus, modeling of the N_2/O_2 chemistry is most important in non-seeded mixtures, however, for completeness ionization reactions involving all of the hydrogenous species are included whenever reliable data could be found. The N_2/O_2 chemistry relies heavily on the reaction mechanism developed by Park [151, 152], which is widely used with slight modifications in a variety of applications. The electron impact dissociation and ionization reactions are taken from the data collected by Teulet *et al.* [198] and Riahi *et al.* [164]. All reactions are taken as reversible.

This kinetic model is verified by comparison to theoretical values of the detonation velocity and to equilibrium values of the electrical conductivity. The theoretical value of the detonation velocity, D_{CJ}, is computed using NASA's Chemical Equilibrium with Applications (CEA) code [132]. The percent of N_2 in the H_2/O_2 mixture is varied and for each mixture the detonation velocity is calculated using the proposed kinetic mechanisms. The addition of ionization chemistry should not change the overall detonation parameters. For one, N_2/O_2 and ionization chemistry occurs mostly downstream so it doesn't affect the chemical thermicity at the detonation front, and two, the inclusion of the N_2/O_2 and ionization chemistry is actually more accurate with the 18-step and 21-reaction H_2/O_2 model being merely a subset. Regardless, the values from the one-dimensional simulations are within 3-5% of the theoretical values for the range of N_2 dilution considered. As shown in Fig. 38, both mechanisms are

Table 8: Summary of the hydrogen-air combustion mechanism used in the present detonation simulations. For the three-body reactions, M includes H_2, O_2, H, O, OH, HO_2, H_2O_2, H_2O and N_2 where the collision efficiency is unity with the exceptions: M_a does not include O_2, H_2O, or N_2, and the collision efficiencies for H_2 and H_2O in M_b are 2.4 and 6.0, in M_c are 1.7 and 7.0, in M_d are 2.4 and 15.4, and in M_e are 0.73 and 3.65, respectively. For reactions $r11$ and $r14$, $k = k_a + k_b$, and for reaction $r12$, $k = k_{\text{inf}}[P_r/(1+P_r)]F$ with $P_r = k_0[\text{M}]/k_{\text{inf}}$ and F as defined in [154].

Number	Reaction	Rate Coefficients			
		A	n	E	
1	$O + H_2 \rightarrow H + OH$	5.0×10^4	2.70	6290	
2	$H + O_2 \rightarrow O + OH$	8.3×10^{13}	0.00	14413	
3	$H + O_2 + M_a \rightarrow HO_2 + M_a$	2.8×10^{18}	−0.90	0	
4	$H + O_2 + O_2 \rightarrow HO_2 + O_2$	3.0×10^{20}	−1.70	0	
5	$H + O_2 + H_2O \rightarrow HO_2 + H_2O$	9.38×10^{18}	−0.80	0	
6	$H + O_2 + N_2 \rightarrow HO_2 + N_2$	2.60×10^{19}	−1.20	0	
7	$H + HO_2 \rightarrow OH + OH$	1.34×10^{14}	0.00	635	
8	$OH + H_2 \rightarrow H_2O + H$	2.16×10^8	1.50	3430	
9	$H + H_2O_2 \rightarrow HO_2 + H_2$	1.21×10^7	2.00	5200	
10	$H + HO_2 \rightarrow O_2 + H_2$	2.80×10^{13}	0.00	1068	
11	$HO_2 + HO_2 \rightarrow O_2 + H_2O_2$	1.30×10^{11}	0.00	−1630	k_a
		4.20×10^{14}	0.00	12000	k_b
12	$OH + OH + M_b \rightarrow H_2O_2 + M_b$	7.40×10^{13}	−0.40	0	k_{inf}
		2.30×10^{18}	−0.90	−1700	k_0
13	$OH + HO_2 \rightarrow O_2 + H_2O$	2.90×10^{13}	0.00	−500	
14	$OH + H_2O_2 \rightarrow HO_2 + H_2O$	1.75×10^{12}	0.00	320	k_a
		5.80×10^{14}	0.00	9560	k_b
15	$H + H + M_c \rightarrow H_2 + M_c$	1.00×10^{18}	−1.00	0	
16	$O + O + M_d \rightarrow O_2 + M_d$	1.20×10^{17}	−1.00	0	
17	$H + OH + M_e \rightarrow H_2O + M_e$	2.20×10^{22}	−2.00	0	
18	$O + H + M_b \rightarrow OH + M_b$	5.00×10^{17}	−1.00	0	

good at predicting the proper detonation parameters.

The electrical conductivity of a stoichiometric mixture of hydrogen and air is computed for various temperatures and pressures using Eq. 152. The species mass fractions at equilibrium are determined by integrating in time the conservation of mass, species and energy equations under the assumption of constant pressure. Once the equilibrium species mass fractions are determined, the electrical conductivity is computed. A similar calculation is done with the addition of 1% potassium by weight. The results are shown in Fig. 37. The values are similar to those reported elsewhere in the literature [129].

Table 9: Arrhenius rate coefficients for the dissociation reactions. All collision efficiencies are unity. M_f includes N_2, O_2, H_2, NO, OH, H_2O_2, HO_2, H_2O and all ions, and M_g includes N, O, H. In order not to repeat reactions included in the combustion chemistry, M_h only includes NO and all ions, and M_i includes NO, N and all ions.

Number	Reaction	Rate Coefficients			Ref.
		A	n	E	
Dissociation					
19	$N_2 + M_f \rightarrow N + N + M_g$	7.0×10^{21}	-1.60	113200	[152]
20	$N_2 + M_g \rightarrow N + N + M_g$	3.0×10^{22}	-1.60	113200	[152]
21	$O_2 + M_h \rightarrow O + O + M_h$	2.0×10^{21}	-1.50	59360	[152]
22	$O_2 + N \rightarrow O + O + N$	1.0×10^{22}	-1.50	59360	[152]
23	$H_2 + M_i \rightarrow H + H + M_i$	2.2×10^{14}	0.00	48300	[152]
24	$NO + M_f \rightarrow N + O + M_f$	5.0×10^{15}	0.00	75500	[151]
25	$NO + M_g \rightarrow N + O + M_g$	1.1×10^{17}	0.00	75500	[151]
Electron Impact Dissociation					
26	$N_2 + e \rightarrow N + N + e$	2.48×10^{-9}	6.16	113263	[198]
27	$O_2 + e \rightarrow O + O + e$	3.47×10^{2}	3.52	59370	[198]
28	$H_2 + e \rightarrow H + H + e$	2.69×10^{20}	-0.80	126565	[164]
29	$H_2O + e \rightarrow H + OH + e$	3.20×10^{15}	0.50	92832	[108]
30	$NO + e \rightarrow N + O + e$	1.05×10^{-2}	4.52	75390	[198]
31	$OH + e \rightarrow O + H + e$	1.54×10^{20}	-0.76	80107	[164]
Electron Impact Ionization					
32	$N_2 + e \rightarrow N_2^+ + e + e$	5.17×10^{12}	0.72	184300	[198]
33	$O_2 + e \rightarrow O_2^+ + e + e$	2.20×10^{10}	1.16	130102	[198]
34	$H_2 + e \rightarrow H_2^+ + e + e$	1.78×10^{9}	1.61	207369	[164]
35	$H_2O + e \rightarrow H_2O^+ + e + e$	8.40×10^{15}	0.50	174060	[108]
36	$H_2O + e \rightarrow H + OH^+ + e + e$	2.80×10^{15}	0.50	209376	[108]
37	$NO + e \rightarrow NO^+ + e + e$	2.70×10^{10}	1.13	95092	[198]
38	$OH + e \rightarrow OH^+ + e + e$	6.99×10^{6}	1.78	160267	[164]
39	$N + e \rightarrow N^+ + e + e$	2.50×10^{34}	-3.82	168600	[151]
40	$O + e \rightarrow O^+ + e + e$	3.90×10^{33}	-3.78	158500	[151]
41	$H + e \rightarrow H^+ + e + e$	2.20×10^{30}	-2.80	157800	[152]
Zel'dovich Reactions					
42	$O_2 + N \rightarrow NO + O$	2.49×10^{9}	1.18	4006	[24]
43	$N_2 + O \rightarrow NO + N$	5.69×10^{12}	0.42	42938	[23]
Dissociative Recombination					
44	$N + N \rightarrow N_2^+ + e$	4.40×10^{7}	1.50	67500	[151]
45	$O + O \rightarrow O_2^+ + e$	7.10×10^{2}	2.70	80600	[151]
46	$N + O \rightarrow NO^+ + e$	8.80×10^{8}	1.00	31900	[151]
47	$OH^+ + e \rightarrow O + H$	3.91×10^{17}	-0.50	0	[141]
48	$H_2O^+ + e \rightarrow OH + H$	3.29×10^{18}	-0.50	0	[141]
Charge Exchange					
49	$O + NO^+ \rightarrow O_2 + N^+$	1.00×10^{12}	0.50	77200	[151]
50	$N_2 + N^+ \rightarrow N + N_2^+$	1.00×10^{12}	0.50	12200	[151]
51	$N + O_2^+ \rightarrow O_2 + N^+$	8.70×10^{13}	0.14	28600	[151]
52	$NO + O^+ \rightarrow O_2 + N^+$	1.40×10^{5}	1.90	15300	[151]
53	$N_2 + O_2^+ \rightarrow O_2 + N_2^+$	9.90×10^{12}	0.00	40700	[151]
54	$O + O_2^+ \rightarrow O_2 + O^+$	4.00×10^{12}	-0.09	18000	[151]
55	$N + NO^+ \rightarrow N_2 + O^+$	3.40×10^{13}	-1.08	12800	[151]
56	$O_2 + NO^+ \rightarrow NO + O_2^+$	2.40×10^{13}	0.41	32600	[151]
57	$O + NO^+ \rightarrow N + O_2^+$	7.20×10^{12}	0.29	48600	[151]
58	$N_2 + O^+ \rightarrow O + N_2^+$	9.10×10^{11}	0.36	22800	[151]
59	$N + NO^+ \rightarrow O + N_2^+$	7.20×10^{13}	0.00	35500	[151]
Potassium Reactions					
60	$K + O_2 + M \rightarrow KO_2 + M$	1.138×10^{2}	-2.68	596	[190]
61	$K + OH + M \rightarrow KOH + M$	1.144×10^{-1}	-2.00	0	[190]
62	$KOH + H \rightarrow K + H_2O$	2.21×10^{12}	0.50	0	[190]
63	$KO_2 + H \rightarrow KO + OH$	2.21×10^{12}	0.50	0	[190]
64	$KO + H_2O \rightarrow KOH + OH$	5.95×10^{11}	0.50	0	[190]
65	$K + M \rightarrow K^+ + e + M$	5.962×10^{15}	0.50	101055	[5]

APPENDIX B

COLLISION INTEGRALS

Collision integrals are often used to accurately compute the coefficients of viscosity, thermal conductivity, diffusivity, and electrical conductivity in high-temperature non-equilibrium flows. The collision integral $\Omega^{(l,s)}$ is defined by averaging the appropriate collision cross-section over the relative energy ϵ of the impacting species. The integers l and s specify the collision integral type, i.e. diffusion or viscosity type.

$$\Omega^{(l,s)}(T) = \frac{4(l+1)}{\pi(s+1)!\left[2l+1-(-1)^l\right]} \frac{1}{2kT} \int_0^\infty \left(\frac{\epsilon}{kT}\right)^{s+1} Q^{(l)}(\epsilon) e^{(-\epsilon/kT)}\, d\epsilon \tag{298}$$

If the cross section $Q^{(l)}$ is not known experimentally, calculating $\Omega^{(l,s)}$ can be done analytically if the interaction potential $\Phi(r)$ is known. Determination of $\Phi(r)$ is often difficult or impossible because of a lack of information, however, for electron-electron, ion-ion, or electron-ion collisions, theoretical computations of the collision integrals are quite accurate. Regardless, the theoretical approach serves first order estimate for the collision integral in situations where no experimental data exists. With $\Phi(r)$ being the unknown, $Q^{(l)}$ is computed as:

$$Q^{(l)}(\epsilon) = 2\pi \left[1 - \frac{1+(-1)^l}{2(l+1)}\right]^{-l} \int_0^\infty b\left[1 - cos^l\Theta(b,\epsilon)\right]\, db \tag{299}$$

where $\Theta(b,\epsilon)$ is defined as the classical deflection angle $\Theta(b,\epsilon)$ where b is the impact parameter and ϵ is the relative collision energy. If r_c is the distance of closest approach (the outermost root of $F(r,b,\epsilon)$), then the deflection angle can be written as

$$\Theta(b,\epsilon) = \pi - \int_{r_c}^\infty \frac{2br^2}{\left[F(r,b,\epsilon)\right]^{1/2}}\, dr = \pi - \int_{r_c}^\infty \frac{2br^2}{\left[1 - b^2/r^2 - \Phi(r)/\epsilon\right]^{1/2}}\, dr \tag{300}$$

From Chapman-Enskog theory, the transport properties of a gas mixture can be determined by solving the Boltzmann equation. Using a Sonine polynomial expansion and only retaining the first term, approximations for the coefficients of viscosity, thermal conductivity and mass diffusion can be computed in terms of three interaction parameters. These collision integrals are identified as the diffusion collision integral $\Omega^{(1,1)}$, the viscosity collision integral $\Omega^{(2,2)}$ and the collision integral ratio $B = (5\Omega^{(1,2)} - 4\Omega^{(1,3)})/\Omega^{(1,1)}$. These parameters can be computed as previously discussed. For many gas mixtures, however, data or curve-fits for these collision integrals can be found directly. In the following sections, the sources and procedures for determining $\Omega^{(1,1)}$, $\Omega^{(2,2)}$ and B are given. Interactions between charged particles (electron-electron, ion-ion, electron-ion) are computed as curve-fits.

REFERENCES

[1] "Essentially non-oscillatory and weighted essentially non-oscillatory schemes for hyperbolic conservation laws," in *Advanced Numerical Approximation of Nonlinear Hyperbolic Equations* (Quarteroni, A., ed.), vol. 1697 of *Lecture Notes in Mathematics*, Springer Berlin Heidelberg, 1988.

[2] Adams, N. A. and Shariff, K., "A high-resolution hybrid compact-ENO scheme for shock-turbulence interaction problems," *Journal Computational Physics*, vol. 127, pp. 27–51, 1996.

[3] Albousséire, T., "Fundamentals of MHD," in *Dynamos* (Cardin, P. and Cugliandolo, L., eds.), Elsevier, 2007.

[4] Arnett, D., "The role of mixing in astrophysics," *Astrophysical Journal Supplement Series*, vol. 127, pp. 213–217, 2000.

[5] Ashton, A. and Hayhurst, A., "Kinetics of collisional ionization of alkali metal atoms and recombination of electrons with alkali metal ions in flames," *Combustion and Flame*, vol. 21, no. 1, pp. 69–75, 1973.

[6] Balakrishnan, K. and Menon, S., "On turbulent chemical explosions into dilute aluminum particle clouds," *Combustion Theory and Modeling*, vol. 14, no. 4, pp. 583–617, 2010.

[7] Balakumar, B., Orlicz, G., Ristorcelli, J., Balasubramanian, S., Prestridge, K., and Tomkins, C., "Turbulent mixing in a Richtmyer-Meshkov fluid layer after reshock: velocity and density statistics," *Journal of Fluid Mechanics*, vol. 696, pp. 67–93, 2012.

[8] Balescu, R., *Transport Processes in Plasmas; Vol 1: Classical Transport Theory, Vol. 2: Neoclassical Transport*. Amsterdam: North Holland, 1988.

[9] Balsara, D., Benjamin, R., and Cox, D., "The evolution of adiabatic supernova remnants in a turbulent, magnetized medium," *The Astrophysical Journal*, vol. 563, pp. 800–805, 2001.

[10] Balsara, D., "Total variation diminishing scheme for adiabatic and isothermal magnetohydrodynamics," *The Astrophysical Journal Supplement Series*, vol. 116, pp. 339–349, 1998.

[11] Balsara, D. and Kim, J., "A comparison between divergence-cleaning and staggered-mesh formulations for numerical magnetohydrodynamics," *The Astrophysical Journal*, vol. 602, pp. 1079–1090, 2004.

[12] Balsara, D., Kim, J., Mac Low, M., and Mathews, G., "Amplification of interstellar magnetic fields by supernova-driven turbulence," *The Astrophysical Journal*, vol. 617, pp. 339–349, 2004.

[13] Balsara, D. and Spicer, D., "A staggered mesh algorithm using higher order godunov fluxes to ensure solenoidal magnetic fields in mhd simulations," *Journal Computational Physics*, vol. 149, pp. 270–292, 1999.

[14] Basu, S., "Ionization in seeded detonation waves," *Physics of Fluids*, vol. 3, no. 3, pp. 456–463, 1960.

[15] Basu, S. and Fay, J., "Ionization in detonation waves," in *Proceedings of the 7th (International) Symposium on Combustion*, p. 277, 1959.

[16] Bauer, A., Cook, M., and Keyes, R., "Detonation-generated plasmas," *Proc. Roy. Soc. A Math. Phys. Eng. Sci.*, vol. 259, no. 1299, pp. 508–517, 1961.

[17] Bethe, H., "Energy production in stars," *Physical Review*, vol. 55, no. 5, pp. 434–456, 1939.

[18] Biskamp, D., *Magnetohydrodynamics Turbulence*. Cambridge University Press, 2001.

[19] Biskamp, D. and Müller, W.-C., "Scaling properties of three-dimensional isotropic magnetohydrodynamic turbulence," *Physics of Plasmas*, vol. 7, no. 12, pp. 4889–4891, 2000.

[20] Bittencourt, J., *Fundamentals of Plasma Phsysics*. New York: Pergamon Press, 1995.

[21] Bletzinger, P., Ganguly, B., Van Wie, D., and Garscadden, A., "Plasma in high speed aerodynamics," *Journal of Physics D: Applied Physics*, vol. 38, no. 4, 2004.

[22] Boldyrev, S., Nordlund, A., and Padoan, P., "Scaling relations of supersonic turbulence in star-forming molecular clouds," *Astrophysical Journal*, vol. 573, no. 2, pp. 678–684, 2002.

[23] Bose, D. and Candler, G., "Thermal rate constants of the $N_2 + O \rightarrow NO + N$ reaction using *ab initio* $^3A''$ and $^3A'$ potential energy surfaces," *Journal of Chemical Physics*, vol. 104, no. 8, pp. 2825–2833, 1996.

[24] Bose, D. and Candler, G., "Thermal rate constants of the $O_2 + N \rightarrow NO + O$ reaction using *ab initio* $^2A'$ and $^4A'$ potential-energy surfaces," *Journal of Chemical Physics*, vol. 107, no. 16, pp. 6163–6145, 1997.

[25] Boyd, T. and Sanderson, J., *The Physics of Plasmas*. Cambridge: Cambridge University Press, 2003.

[26] Brackbill, J. and Barnes, D., "The effect of nonzero $\bigtriangledown \cdot B = 0$ on the numerical solution of the magnetohydrodynamic equations," *Journal of Computational Physics*, vol. 35, pp. 426–430, 1980.

[27] Braginskii, S., "Transport processes in a plasma," in *Reviews of Plasma Physics, Vol. 1* (Leontovich, M., ed.), pp. 205–311, Consultants Bureau, 1965.

[28] Brio, M. and Wu, C., "An upwind differencing scheme for the equations of ideal magnetohydrodynamics," *Journal of Computational Physics*, vol. 75, no. 2, pp. 400–422, 1988.

[29] Brouillette, M., "The Richtmyer-Meshkov instability," *Annual Review of Fluid Mechanics*, vol. 34, pp. 445–468, 2002.

[30] Brouillette, M. and Strutevant, B., "Experiments on the Richtmyer-Meshkov instability: small-scale perturbations on a continuous interface," *Journal of Fluid Mechanics*, vol. 263, pp. 271–292, 1994.

[31] Cao, J., Wu, W., Ren, H., and Li, D., "Richtmyer-Meshkov instability of a stratified fluid in transverse magnetic field," *Physics of Plasmas*, vol. 16, no. 062103, 2009.

[32] Cavenor, M., Munday, G., and Ubbelohde, G., "Chemi-ionization in detonation chemistry," *Combustion and Flame*, vol. 18, pp. 99–101, 1972.

[33] Chandrasekhar, S., *Hydrodynamic and Hydromagnetic Stability.* Dover, 1961.

[34] Chapman, P. R. and Jacobs, J. W., "Experiments on the three-dimensional incompressible Richtmyer-Meshkov instability," *Physics of Fluids*, vol. 18, p. 074101, 2006.

[35] Charakhch'yan, A., "Reshocking at the non-linear stage of the Richtmyer-Meshkov instability," *Plasma Physics and Controlled Fusion*, vol. 43, pp. 1169–1179, 2001.

[36] Chen, F., *Introduction to Plasma Physics.* Plenum Press, second ed., 1974.

[37] Christlieb, A., Rossmanith, J., and Tang, Q., "Finite difference weighted essentially non-oscillatory schemes with constrained transport for ideal magnetohydrodynamics," *Journal of Computational Physics*, vol. 268, pp. 302–325, 2014.

[38] Ciaraldi-Schoolmann, F., Seitenzahl, I., and R opke, F., "A subgrid-scale model for deflagration-to-detonation transitions in type Ia supernova explosion simulations," *Astronomy and Astrophysics*, vol. 559, p. A117, 2013.

[39] Clark, D. and Stephenson, F., *The Historical Supernovae*. Headington Hill Hall, Oxford: Pergamon Press Ltd., 1977.

[40] Cohen, R., Dannevik, W., Dimits, A., Eliason, D., Mirin, A., Zhou, Y., Porter, D., and Woodward, P., "Three-dimensional simulation of a Richtmyer-Meshkov instability with a two-scale initial perturbation," *Physics of Fluids*, vol. 14, pp. 3692–3709, 2002.

[41] Colella, P. and Woodward, P., "The Piecewise-Parabolic Method for hydrodynamics," *Journal Computational Physics*, vol. 54, pp. 174–201, 1984.

[42] Cook, M., *The Science of High Explosives*. New York: Reinhold Publishing Corporation, 1958.

[43] Cook, M., Keyes, R., and Udy, L., "Propagation characteristics of detonation-generated plasmas," *Journal of Applied Physics*, vol. 30, no. 12, pp. 1882–1892, 1959.

[44] Cook, M. and McEwan, W., "Cohesion in plasma," *Journal of Applied Physics*, vol. 29, pp. 1612–1613, Apr 1958.

[45] Crockett, K., Colella, P., Fisher, R., Klein, R., and Mckee, C., "An unsplit, cell-centered Godunov method for ideal MHD," *Journal of Computational Physics*, vol. 203, 2005.

[46] Dafermos, C., *Hyperbolic conservation laws in continuum physics*. Berlin: Springer-Verlag, 2010.

[47] Dai, W. and Woodward, P., "Extension of the Piecewise Parabolic Method to multidimensional ideal magnetohdrodynamics," *Journal of Computational Physics*, vol. 115, no. 2, pp. 485–514, 1994.

[48] Dai, W. and Woodward, P., "A high-order iterative implicit-explicit hybrid scheme for magnetohydrodynamics," *SIAM Journal of Scientific Computing*, vol. 19, no. 6, pp. 1827–1846, 1998.

[49] Davidson, P., *An Introduction to Magnetohydrodynamics*. Dover Publications, 2001.

[50] Davis, W. and Campbell, W., "Ultra-high-speed photographs refuting "Cohesion in Plasma"," *Journal of Applied Physics*, vol. 31, no. 7, pp. 1225–1227, 1960.

[51] Dedner, A., Kemm, F., Kröner, D., Munz, C., Schnitzer, T., and Wesenberg, M., "Hyperbolic Divergence Cleaning for the MHD Equations," *Journal of Computational Physics*, vol. 175, no. 2, pp. 645–673, 2002.

[52] Del Zanna, L., Bucciantini, N., and Londrillo, P., "An efficient shock-capturing central-type scheme for multidimensional relativistic flows," *Astronomy and Astrophysics*, vol. 400, pp. 397–413, 2003.

[53] Dimonte, G., Frerking, C., and Schneider, M., "Richtmyer-Meshkov instability in the turbulent regime," *Physical Review Letters*, vol. 74, pp. 4855–4858, 1995.

[54] Dimonte, G. and Schneider, M., "Turbulent Rayleigh-Taylor instability experiments with strong radiatively drive shocks," *Physics of Plasmas*, vol. 4, pp. 4347–4357, 1997.

[55] Dimonte, G. and Schneider, M., "Density ratio dependence of Rayleigh-Taylor mixing for sustained and impulsive acceleration histories," *Physics of Fluids*, vol. 12, pp. 304–321, 2000.

[56] Dionne, J.-P., Ng, H., and Lee, J., "Transient development of friction-induced low-velocity detonations," *Proceedings of the Combustion Institute*, vol. 28, no. 1, pp. 645–651, 2000.

[57] Döring, W., "On detonation processes in gases," *Annuals of Physics*, vol. 43, pp. 421–436, 1943.

[58] Ducros, F., Ferrand, V., Nicoud, F., Weber, C., Darracq, D., Gacherieu, C., and Poinsot, T., "Large-eddy simulation of the shock/turbulence interaction," *Journal Computational Physics*, vol. 152, no. 1, pp. 517–549, 1999.

[59] Edwards, D., Hooper, G., and Collyer, A., "Ionization measurement in reactive shock and detonation waves using microwave techniques," *Journal of Physics D: Applied Physics*, vol. 4, pp. 854–870, 1971.

[60] Evans, C. and Hawley, J., "Simulation of magnetohydrodynamic flows: A constrained transport method," *Astrophysical Journal*, vol. 332, pp. 659–677, 1988.

[61] Falgout, R., Jones, J., and Yang, U., "The design and implementation of hypre, a library of parallel high performance preconditioners," in *Numerical Solution of Partial Differential Equations on Parallel Computers* (Bruaset, A. M. and Tveito, A., eds.), vol. 51, pp. 267–294, Springer-Verlag, 2006.

[62] Fey, M. and Torrilhon, M., "A constrained transport upwind scheme for divergence-free advection," in *Hyperbolic Problems: Theory, Numerics, and Applications* (Hou, T. and Tadmor, E., eds.), no. 529–538, Springer, 2003.

[63] Fickett, W. and Davis, W., *Detonation*. Berkeley, California: University of California Press, 1979.

[64] Freidberg, J., *Ideal Magnetohydrodynamics*. Springer, 1987.

[65] Friedrichs, K. and Kranzer, H., "Notes on Magnetodynamics: Non-linear wave motion," Tech. Rep. NYO-6486, New York University, 1959.

[66] Fryxell, B. and Menon, S., "Hybrid simulations of richtmyer-meshkov instability," *AIAA-2005-0314, 43rd AIAA Aerospace Sciences Meeting, Reno, NV. January*, 2005.

[67] Gardiner, T. A. and Stone, J. M., "An unsplit Godunov method for ideal MHD via constrained transport," *Journal of Computational Physics*, vol. 205, no. 2, pp. 509–539, 2005.

[68] Gardiner, T. A. and Stone, J. M., "An unsplit Godunov method for ideal MHD via constrained transport in three dimensions," *Journal of Computational Physics*, vol. 227, no. 8, pp. 4123–4141, 2008.

[69] Génin, F. and Menon, S., "Dynamics of sonic jet injection into supersonic crossflow," *Journal of Turbulence*, vol. 11, no. 4, pp. 1–30, 2010.

[70] Giacalone, J. and Jokipii, J., "Magnetic field amplification by shocks in turbulent fluids," *The Astrophysical Journal*, vol. 663, pp. L41–L44, 2007.

[71] Gilev, S. and Trubachev, A., "Detonation properties and electrical conductivity of explosive-metal additive mixtures," *Combustion, Explosion, and Shock Waves*, vol. 38, no. 2, pp. 219–234, 2002.

[72] Godlewski, E. and Raviart, P.-A., *Numerical approximation of hyperbolic systems of conservation laws*. New York, New York: Springer Verlag, 1996.

[73] Godunov, S., "A finite difference method for the computation of discontinuous solutions of the equations of fluid dynamics," *Mat. Sbornik*, vol. 47, pp. 357–393, 1959.

[74] Goedbloed, H. and Poedts, S., *Principles of Magnetohydrodynamics: With Applications to Laboratory and Astrophysical Plasmas*. Cambridge University Press, 2004.

[75] Goldstein, B., "Evidence for a supernova of A.D. 1006," *The Astronomical Journal*, vol. 70, no. 1, pp. 105–114, 1965.

[76] Goncharov, V., "Analytical model of nonlinear, single-mode, classical rayleigh-taylor instability at arbitrary atwood number," *Physical Review Letters*, vol. 88, p. 134502, 2002.

[77] Gottiparthi, K., Schulz, J., and Menon, S., "On the neutralization of bacterial spores in post-detonation flows," *Shock Waves*, 2014.

[78] Gottlieb, S. and Shu, C.-W., "Total variation diminishing Runge-Kutta schemes," *Mathematics of Computation*, vol. 67, no. 221, pp. 73–85, 1998.

[79] Gowardhan, A. and Grinstein, F., "Numerical simulation of Richtmyer-Meshkov instabilities in shock gas curtains," *Journal of Turbulence*, vol. 12, no. 43, pp. 1–24, 2011.

[80] Guo, F., Li, S., Li, H., Giacalone, J., Jokipii, J., and Li, D., "On the amplification of magnetic field by a supernova blast shock wave in a turbulent medium," *The Astrophysical Journal*, vol. 747, pp. 98–107, 2012.

[81] Gupta, R., Yos, J., and Thompson, R., "A review of reaction rates and thermodynamic and transport properties for the 11-species air model for chemical and thermal non-equilibrium calculations to 30000 K," Tech. Rep. RP 1232, NASA, 1990.

[82] Harten, A., "High resolution schemes for hyperbolic conservation laws," *Journal Computational Physics*, vol. 49, pp. 357–393, 1983.

[83] Harten, A., Lax, P., and van Leer, B., "On upstream differencing and Godunov-type schemes for hyperbolic conservation laws," *SIAM Review*, vol. 25, pp. 35–61, 1983.

[84] Harten, A. and Osher, S., "Uniformly high-order accurate nonoscillatory schemes," *SIAM Journal of Numerical Analysis*, vol. 24, no. 2, pp. 279–309, 1987.

[85] Hecht, H., Alon, U., and Shvarts, D., "Potential flow models of Rayleigh-Taylor and Richtmyer-Meshkov bubble fronts," *Physics of Fluids*, vol. 6, pp. 4019–4030, 1994.

[86] Helliwell, J., "Gas-ionizing shock and combustion waves in magnetogasdynamics," *Journal of Fluid Mechanics*, vol. 14, no. 3, pp. 405–420, 1962.

[87] Helliwell, J., "Magnetogasdynamic deflagaration and detonation waves with ionization," *Journal of Fluid Mechanics*, vol. 16, no. 2, pp. 243–261, 1963.

[88] Helzel, C., Rossmanith, J., and Taetz, B., "A high-order unstaggered constrained-transport method for the three-dimensional ideal magnetohydrodynamic equations based on the method of lines," *SIAM Journal of Scientific Computing*, vol. 35, no. 2, pp. 623–651, 2013.

[89] Herant, M., Benz, W., and Hix, W., "Inside the supernova: a power convection engine," *Astrophysical Journal*, vol. 435, no. 339–348, 1994.

[90] Hill, D., Pantano, C., and Pullin, D., "Large-eddy simulation and multiscale modelling of a Richtmyer-Meshkov," *Journal of Fluid Mechanics*, vol. 557, pp. 29–61, 2006.

[91] Hill, D. and Pullin, D., "Hybrid tuned center-dfiference-WENO method for large-eddy simulations in the presence of strong shocks," *Journal Computational Physics*, vol. 194, pp. 435–450, 2004.

[92] Hirsch, C., *Numerical computation of internal and external flows*. Chichester, England: John Wiley & Sons, 1988.

[93] Holmes, R., Dimonte, G., Fryxell, B., Gittings, M., and Grove, J., "Richtmyer-Meshkov instability growth: experiment, simulation and theory," *Journal of Fluid Mechanics*, vol. 389, pp. 55–79, 1999.

[94] Houas, L. and Chemouni, I., "Experimental investigation of the Richtmyer-Meshkov instability in shock tube," *Physics of Fluids*, vol. 8, pp. 614–627, 1996.

[95] Hundhausen, A., "The solar wind," in *Introduction to Space Physics* (Kivelson, M. and Russell, C., eds.), New York: Cambridge University Press, 1995.

[96] Iroshnikov, P., "Turbulence of a conducting fluid in a strong magnetic field," *Soviet Astronomy*, vol. 7, no. 4, pp. 566–571, 1964. translated from Astronomicheskii Zhurnal, Vol. 40, No. 4, pp.742-750, 1963.

[97] Jahn, R., *Physics of Electric Propulsion*. Dover Publications, 1968.

[98] Jiang, G. and Shu, C.-W., "Efficient implementation of weighted ENO schemes," *Journal Computational Physics*, vol. 126, no. 202–228, 1996.

[99] Jiang, G.-S. and Wu, C.-C., "A high-order WENO finite difference scheme for the equations of ideal MHD," *Journal of Computational Physics*, vol. 150, pp. 561–594, 1999.

[100] Jones, M. and Jacobs, J., "A membraneless experiment for the study of Richtmyer-Meshkov instability of a shock-accelerated gas interface," *Physics of Fluids*, vol. 9, pp. 3078–3085, 1997.

[101] Jun, B.-I., Norman, M., and Stone, J., "A numerical study of Rayliegh-Taylor instability in magnetic fluids," *Astrophysical Journal*, vol. 453, pp. 332–349, 1995.

[102] Kailasanth, K., "Recent developments in the research on pulse detonation engines," *AIAA Journal*, vol. 41, no. 2, pp. 145–159, 2003.

[103] Kawai, S., "Divergence-free-preserving high-order schemes for magnetohydrodynamics: An artificial magnetic resistivity method," *Journal of Computational Physics*, vol. 251, pp. 292–318, 2013.

[104] Kelly, J. and Toong, T., "Detonation wave in electromagnetic field," *Symposium (Internation) on Combustion*, vol. 11, no. 1, pp. 657–664, 1967.

[105] Khan, M., Mandal, L., Banerjee, R., Roy, S., and Gupta, M. R., "Development of Richtmyer-Meshkov and Rayleigh-Taylor instability in the presence of a magnetic field," *Nucluear Instruments and Methods A*, vol. 653, pp. 2–6, 2011.

[106] Kifonidis, K., Plewa, T., Janka, H.-T., and M uller, E., "Non-spherical core collapse supernovae: I. neutrino-driven convection, Rayleigh-Taylor instabilities, and the formation and propagation of metal clumps," *Astronomy and Astrophysics*, vol. 408, no. 2, pp. 621–649, 2003.

[107] Knaepen, B. and Moreau, R., "Magnetohydrodynamic turbulence at low magnetic Reynolds number," *Annual Review of Fluid Mechanics*, vol. 40, pp. 25–45, 2008.

[108] Konstantinovskii, R., Shibkov, V., and Shibkova, L., "Effect of a gas discharge on the ignition in the hydrogen-oxygen system," *Kinetics and Catalysis*, vol. 46, no. 6, pp. 775–788, 2005.

[109] Kraichnan, R., "Inertial-range spectrum of hydromagnetic turbulence," *Physics of Fluids*, vol. 8, pp. 1385–1387, 1965.

[110] Krause, F. and Radler, K., *Mean-field Magnetohydrodynamics and Dynamo Theory*. Elsevier, 1980.

[111] Lamers, H. and Cassinelli, J., *Introduction to Stellar Winds*. Cambridge: Cambridge University Press, 1999.

[112] Larsson, J., Fransson, C., Ostlin, G., Gr oningsson, P., Jerkstrand, A., Kozma, C., Sollerman, J., Challis, P., Kirshner, R., Chevalier, R., Heng, K., McCray, R., Suntzeff, N., Bouchet, P., Crotts, A., Danziger, J., Dwek, E., France, K., Garnavich, P., Lawrence, S., Leibundgut, B., Lundqvist, P., Panagia, N., Pun, C., Smith, N., Sonneborn, G., Wang, L., and Wheeler, J., "X-ray illumination of the ejecta of supernova 1987a," *Nature*, vol. 474, pp. 484–486, 1987.

[113] Larsson, J. and Lele, S., "Direct numerical simulation of canonical shock/turbulence interaction," *Physics of Fluids*, vol. 21, p. 126101, 2009.

[114] Lax, P., "Hyperbolic systems of conservation laws and the mathematical theory of shock waves," *SIAM Regional Conference Series in Applied Mathematics*, vol. 11, 1972.

[115] Lee, D. and Deane, A. E., "An unsplit staggered mesh scheme for multidimensional magnetohydrodynamics," *Journal of Computational Physics*, vol. 228, no. 4, pp. 952–975, 2009.

[116] Lee, J., *The Detonation Phenomenon*. Cambridge University Press, 2008.

[117] Lee, S., Lele, S., and Moin, P., "Interaction of isotropic turbulence with shock waves: Effect of shock strength," *Journal of Fluid Mechanics*, vol. 340, pp. 225–247, 1997.

[118] Leinov, E., Malamud, G., Elbaz, Y., Levin, L., Ben-Dor, G., Shvarts, D., and Sadot, O., "Experimental and numerical investigation of the Richtmyer-Meshkov instability under re-shock conditions," *Journal of Fluid Mechanics*, vol. 626, pp. 449–480, 2009.

[119] Lele, S., "Compact finite difference schemes with spectral-like resolution," *Journal Computational Physics*, vol. 103, pp. 16–42, 1992.

[120] LeVeque, R., "High-resolution conservative algorithms for advection in incompressible flow," *SIAM Journal of Numerical Analysis*, vol. 33, pp. 627–665, 1996.

[121] LeVeque, R., *Finite difference methods for ordinary and partial differential equations: steady state and time dependent problems*. Philadelpha: SIAM, 2007.

[122] Levy, Y., Jaouen, S., and Canaud, B., "Numerical investigation of magnetic Richtmyer-Meshkov instability," *Lasers and Particle Beams*, vol. 30, pp. 415–419, 2012.

[123] Lin, S., Resler, E., and Kantrowitz, A., "Electrical conductivity of highly ionized argon produced by shock waves," *Journal of Applied Physics*, vol. 26, pp. 95–109, 1955.

[124] Liu, X.-D., Osher, S., and Chan, T., "Weighted essentially non-oscillatory schemes," *Journal Computational Physics*, vol. 115, pp. 200–212, 1994.

[125] Lombardini, M., Hill, D., Pullin, D., and Meiron, D., "Atwood ratio dependence of Richtmyer-Meshkov flows under reshock conditions using large-eddy simulations," *Journal of Fluid Mechanics*, vol. 670, pp. 439–480, 2011.

[126] Lombardini, M., Pullin, D., and Meiron, D., "Transition to turbulence in shock-driven mixing: a Mach number study," *Journal of Fluid Mechanics*, vol. 690, pp. 203–226, 2012.

[127] Londrillo, P. and Del Zanna, L., "High-order upwind schemes for multidimensional magnetohydrodynamics," *The Astrophysical Journal*, vol. 530, pp. 508–524, 2000.

[128] Londrillo, P. and Del Zanna, L., "On the divergence-free condition in Godunov-type schemes for ideal magnetohydrodynamics: the upwind constrained transport method," *Journal of Computational Physics*, vol. 195, no. 1, pp. 17–48, 2004.

[129] Lu, F., Liu, H.-C., and Wilson, D., "Electrical conductivity channel for a shock tube," *Measurements in Science and Technology*, vol. 16, pp. 1730–1740, 2005.

[130] Mac Low, M., "Control of star formation by supersonic turbulence," *Reviews of Modern Physics*, vol. 76, no. 1, pp. 125–194, 2004.

[131] MacCormack, R. and Paullay, A., "Computational efficiency achieved by time splitting of finite difference operators," *AIAA Paper 72-154, AIAA Aerospace Sciences Meeting, January 17-19*, 1972.

[132] McBride, B. J. and Gordon, S., "Computer program for calculating and fitting thermodynamic functions," Tech. Rep. RP-1271, NASA, 1992.

[133] McDonald, P. W., "The computation of transonic flow through two-dimensional gas turbine cascades," *ASME*, 1971.

[134] Meier, D., Koide, S., and Uchida, Y., "Magnetohydrodynamic production of relativistic jets," *Science*, vol. 291, no. 84–92, 2001.

[135] Meshkov, E., "Instability of the interface of two gases acclerated by a shock wave," *Soviet Fluid Dynamics*, vol. 4, pp. 101–108, 1969.

[136] Mikaelian, K., "Richtmyer-Meshkov instabilities in stratified fluids," *Physical Review A*, vol. 31, pp. 410–419, 1985.

[137] Mikaelian, K., "Turbulent mixing generated by Rayleigh-Taylor and Richtmyer-Meshkov instabilities," *Physica D*, vol. 36, pp. 356–368, 1989.

[138] Mikaelian, K., "Analytic approach to nonlinear Rayleigh-Taylor and Richtmyer-Meshkov instabilities," *Physical Review Letters*, vol. 80, pp. 508–511, 1998.

[139] Miki, K. and Menon, S., "Localized dynamic subgrid closure for simulation of MHD turbulence," *Physics of Plasmas*, vol. 15, no. 072306, 2008.

[140] Miki, K., Schulz, J., and Menon, S., "Large eddy simulation of equilibrium plasma-assisted combustion in supersonic flow," *Proceedings of the Combustion Institute*, vol. 32, pp. 2413–2420, 2008.

[141] Mitchell, J., "The dissociation recombination of molecules," *Physical Report*, vol. 186, pp. 216–248, 1990.

[142] Miyoshi, T. and Kusano, K., "A multi-state HLL approximate Riemann solver for ideal magnetohydrodynamics," *Journal of Computational Physics*, vol. 208, pp. 315–344, 2005.

[143] Monchaux, R., Berhanu, M., Aumaître, S., Chiffaudel, A., Daviaud, F., Dubrulle, B., Ravelet, F., Fauve, S., Mordant, N., Pétrélis, F., Bourgoin, M., Odier, P., Pinton, J.-F., Plihon, B., and Volk, R., "The von Kármán sodium experiment: turbulent dynamical dynamos," *Physics of Fluids*, vol. 21, no. 035108, 2009.

[144] Niederaus, C. and Jacobs, J. *Journal of Fluid Mechanics*, vol. 485, pp. 243–277, 2003.

[145] Oran, E. and Williams, F., "The physics, chemistry and dynamics of explosions," *Philosophical Transactions of the Royal Society A*, vol. 370, pp. 534–543, 2012.

[146] Orlicz, G., Balakumar, S., Tomkins, C., and Prestridge, K., "A Mach number study of the Richtmyer-Meshkov instability in a varicose, heavy-gas curtain," *Physics of Fluids*, vol. 21, no. 064102, 2009.

[147] Oron, D., Arazl, L., Kartoon, D., Rikanati, A., Alon, U., and Shvarts, D., "Dimensionality dependence of the Rayleigh-Taylor and Richtmyer-Meshkov instability late-time scaling laws," *Physics of Plasmas*, vol. 8, no. 6, pp. 2883–2889, 2001.

[148] Palmer, G. and Wright, M., "A comparison of methods to compute high temperature gas thermal conductivity," *AIAA-2003-3913, 36th AIAA Thermophysics Conference*, Orlando, FL, 23-26 June 2003.

[149] Palmer, G. and Wright, M., "Comparison of methods to compute high-temperature gas viscosity," *Journal of Thermodynamics and Heat Transfer*, vol. 17, pp. 232–239, 2003.

[150] Panagia, N., "Distance to SN1987A and the LMC," in *New Views of the Magellanic Clouds, IAU Symposium* (Chu, Y.-H., Suntzeff, N., Hesser, J., and Bohlender, D., eds.), vol. 190, 1999.

[151] Park, C., "Review of chemical-kinetic problems of future nasa missions, i: Earth entries," *Journal of Thermodynamics and Heat Transfer*, vol. 7, pp. 385–398, 1993.

[152] Park, C., "Chemical-kinetic parameters of hyperbolic earth entry," in *38th Aerospace Sciences Meeting*, no. AIAA-2000-0210, (Reno, NV), 10-13 January 2000.

[153] Perkins, L., Betti, R., LaFortune, K., and Williams, W., "Shock ignition: A new approach to high gain inertial confinement fusion on the National Ignition Facility," *Physical Review Letters*, vol. 103, no. 045004, 2009.

[154] Petersen, E. and Hanson, R., "Reduced kinetic mechanisms for ram accelerator combustion," *Journal of Propulsion and Power*, vol. 15, no. 4, pp. 591–600, 1999.

[155] Pirozzoli, S., "Conservative hybrid compact-weno schemes for shock-turbulence interaction," *Journal Computational Physics*, vol. 178, pp. 81–117, 2002.

[156] Plett, E., "Interaction of electromagnetically produced shocks with detonation waves," *AIAA Journal*, vol. 7, no. 6, pp. 1180–1182, 1969.

[157] Powell, K., "An approximate Riemann solver for magnetohydrodynamics (that works in more than one dimnesion)," tech. rep., ICASE, 1994.

[158] Prasad, J., Rasheed, A., Kumar, S., and Sturtevant, B., "The late-time development of the Richtmyer-Meshkov instability," *Physics of Fluids*, vol. 12, pp. 2108–2015, 2000.

[159] Qiu, Z., Wu, Z., Cao, J., and Li, D., "Effects of transverse magnetic field and viscosity on the Richtmyer-Meshkov instability," *Physics of Plasmas*, vol. 15, p. 042305, 2008.

[160] Quirk, J., "A contribution to the great Riemann solver debate," *International Journal of Numerical Methods*, vol. 18, pp. 555–574, 1994.

[161] Radulescu, M. and Lee, J., "The failure mechanism of gaseous detonations: experiments in porous wall tubes," *Combustion and Flame*, vol. 131, no. 1–2, pp. 29–46, 2002.

[162] Ramshaw, J., "Simple model for linear and nonlinear mixing at unstable fluid interfaces with variable acceleration," *Physical Review E*, vol. 58, pp. 5834–5840, 1998.

[163] Ren, Y., Liu, M., and Zhang, H., "A characteristic-wise hybrid compact-WENO scheme for solving hyperbolic conservation laws," *Journal of Computational Physics*, vol. 192, pp. 365–386, 2003.

[164] Riahi, R., Teulet, P., Lakhdar, Z., and Gleizes, A., "Cross-section and rate coefficient calculate for electron impact excitation, ionisation and dissociation of H_2 and OH molecules," *European Physical Journal D*, vol. 2006, pp. 223–230, 40.

[165] Richtmyer, R., "Taylor instability in shock acceleration of compressible fluids," *Communications of Pure Applied Mathematics*, vol. 8, pp. 297–319, 1960.

[166] Rizzetta, D., Visbal, M., and Gaitonde, D., "Large-eddy simulation of supersonic compression-ramp flow by a high-order method," *AIAA Journal*, vol. 12, pp. 2283–2292, 2001.

[167] Roe, P., "Approximate Riemann solver, parameters vectors and difference schemes," *Journal of Computational Physics*, vol. 43, pp. 357–371, 1981.

[168] Roe, P., "Characteristic-based schemes for the euler equations," *Annual Review of Fluid Mechanics*, vol. 18, pp. 337–365, 1986.

[169] Rogallo, R. S. and Moin, P., "Numerical simulation of turbulent flows," *Annual Review of Fluid Mechanics*, vol. 66, pp. 99–137, 1984.

[170] Rosenbluth, M., MacDonald, W., and Judd, D., "Fokker-Planck equation for an inverse-square law," *Physical Review*, vol. 107, pp. 1–6, 1957.

[171] Rossmanith, J., "An unstaggered, high-resolution constrained transport method for magnetohydrodynamics," *SIAM Journal of Scientific Computing*, vol. 28, pp. 1766–1797, 2006.

[172] Ruuth, S., "Global optimization of explicit strong-stability-preserving Runge-Kutta methods," *Mathematics of Computation*, vol. 75, no. 253, pp. 183–207, 2005.

[173] Ryu, D. and Jones, T. W., "Numerical magnetohydrodynamics in astrophysics: Algorithm and tests for one-dimensional flow," *Astrophysical Journal*, vol. 442, pp. 228–258, 1995.

[174] Ryu, D., Miniati, F., Jones, T. W., and Frank, A., "A divergence-free upwind code for multidimensional magnetohydrodynamics flows," *Astrophysical Journal*, vol. 509, pp. 244–255, 1998.

[175] Sadot, O., Erez, L., Alon, U., Oron, D., and Levin, L., "Study of nonlinear evolution of single-mode and two-bubble interaction under Richtmyer-Meshkov instability," *Physical Review Letters*, vol. 80, pp. 1654–1657, 1998.

[176] Sadot, O., Erez, L., Oron, D., Erez, G., and Ben-Dor, G., "Studies on the nonlinear evolution of the Richtmyer-Meshkov instability," *Astrophysical Journal Supplemental Seris*, vol. 127, pp. 469–473, 2000.

[177] Saffman, P. and Meiron, D., "Kinetic energy generated by the incompressible Richtmyer-Meshkov instability in a continuous stratified fluid," *Physics of Fluids A*, vol. 1, pp. 1767–1771, 1989.

[178] Saito, K., "Measurements of the high electron density zone in c_2h_2–o_2 detonation wave by microwave reflection," *Combustion and Flame*, vol. 21, pp. 241–251, 1973.

[179] Samtaney, R., "Suppression of the Ritchmyer-Meshkov instability in the presence of a magnetic field," *Physics of Fluids*, vol. 15, no. 8, pp. L53–56, 2003.

[180] Samtaney, R., "Suppression of the Ritchmyer-Meshkov instability in the presence of a magnetic field," *Physics of Fluids*, vol. 15, no. 8, pp. L53–56, 2003.

[181] Sano, T., Nishihara, K., Matsuoka, C., and Inoue, T., "Magnetic field amplification associated with the Richtmyer-Meskhov instability," *Astrophysical Journal*, vol. 758, pp. 126–139, 2012.

[182] Schilling, O. and Latini, M., "High-order WENO simulations of three-dimensional reshocked Richtmyer-Meshkov instability to late times: dynamics, dependence of initial conditions, and comparisons to experimental data," *Acta Mathematica Science*, vol. 30B, no. 2, pp. 595–620, 2010.

[183] Schrijver, C. and Zwaan, C., *Solar and Stellar Magnetic Activity*. Cambridge: Cambridge University Press, 2000.

[184] Schulz, J., Gottiparthi, K., and Menon, S., "Ionization in gaseous detonation waves," *Shock Waves*, vol. 22, no. 6, pp. 579–590, 2012.

[185] Schulz, J., Gottiparthi, K., and Menon, S., "Richtmyer-meshkov instability in dilute gas-particle mixtures with re-shock," *Physics of Fluids*, vol. 25, p. 114105, 2013.

[186] Shepherd, J., "Detonation in gases," *Proceedings of the Combustion Institute*, vol. 32, no. 1, pp. 83–98, 2009.

[187] Shu, C.-W., "High order weighted essentially non-oscillatory schemes for convection dominated problems," *SIAM Review*, vol. 51, pp. 82–126, 2009.

[188] Shu, C.-W.and Osher, S., "Efficient implementation of essentially non-oscillatory shock-capturing schemes," *Journal of Computational Physics*, vol. 77, pp. 439–471, 1988.

[189] Shukla, P., "A survey of dusty plasma physics," *Physics of Plasmas*, vol. 8, no. 5, pp. 1791–1804, 2001.

[190] Slack, M., Cox, J., Grillo, A., and Ryan, R., "Potassium kinetics in heavily seeded atmospheric pressure laminar methane flames," *Combustion and Flame*, vol. 77, pp. 311–320, 1989.

[191] Stallcop, J., Partridge, H., and Levin, E., "Collision integrals for the interaction of the ions of nitrogen and oxygen in a plasma at high temperatures and pressures," *Physics of Fluids B*, vol. 4, pp. 386–391, 1992.

[192] Stix, M., *The Sun, An Introduction*. Berlin: Springer-Verlag, 2nd ed., 2002.

[193] Stone, J. M., Gardiner, T. A., Teuben, P., Hawley, J., and Simon, J. B., "ATHENA: A New Code for Astrophysical MHD," *The Astrophysical Journal*, vol. 178, pp. 137–177, 2008.

[194] Sur, S., Pan, L., and Scannapieco, E., "Mixing in magnetized turbulent media," *The Astrophysical Journal*, vol. 784, pp. 94–107, 1014.

[195] Sutton, G., *Engineering Magnetohydrodynamics*. McGraw-Hill, 1965.

[196] Tasker, D., "The properties of condensed explosives for electromagnetic energy coupling," Tech. Rep. 85-360, NSWC, Sliver Spring, Maryland, 1985.

[197] Tasker, D., Whitley, V., Mace, J., Pemberton, S., Sandoval, T., and Lee, R., "Electromagnetic effects on explosive reaction and plasma," in *Proceedings of the 14^{th} International Detonation Symposium*, 2009.

[198] Teulet, P., Sarrette, J., and Gomes, A., "Calculation of electron impact inelastic cross sections and rate coefficients for diatomic molecules. applications to air molecules," *Journal of Quantitative Spectroscopy and Radiative Transfer*, vol. 62, pp. 549–569, 1999.

[199] Thornber, B., Drikakis, D., Youngs, D., and Williams, R., "The influence of initial conditions on turbulent mixing due to Richtmyer-Meshkov instability," *Journal of Fluid Mechanics*, vol. 654, pp. 99–139, 2010.

[200] Thornber, B., Drikakis, D., Youngs, D., and Williams, R., "Growth of a Richtmyer-Meshkov turbulent layer after reshock," *Physics of Fluids*, vol. 23, no. 095107, pp. 1–14, 2011.

[201] Toro, E., *Riemann solvers and numerical methods for fluid dynamics*. Berlin, Heidelberg: Springer Verlag, 2nd edition ed., 1999.

[202] Toth, G., "The $\bigtriangledown \cdot B = 0$ constraint in shock-capturing magnetohydrodynamic code," *Journal of Computational Physics*, vol. 161, pp. 605–652, 2000.

[203] Tritschler, V. K., Avdonin, A., Hickel, S., Hu, X. Y., and Adams, N. A., "Quantification of initial-data uncertainty on a shock-accelerated gas cylinder," *Physics of Fluids*, vol. 26, no. 2, p. 026101, 2014.

[204] Trubinkov, B., "Particle interactions in a fully ionized plasma," in *Reviews of Plasma Phsyics, Vol 1.* (Leontovich, M., ed.), 105–204: Consultants Bureau, 1965.

[205] Uchiyama, Y., Aharonian, F., Tanaka, T., Takahashi, T., and Maeda, Y., "Extremely fast acceleration of cosmic rays in a supernova remnant," *Nature*, vol. 449, pp. 576–578, 2007.

[206] Ukai, S., Balakrishnan, K., and Menon, S., "Growth rate predictions of single- and multi-mode Richtmyer-Meshkov instability with reshock," *Shock Waves*, vol. 21, no. 6, pp. 533–546, 2011.

[207] van Leer, B., "Towards the ultimate conservative difference scheme i: the quest for monotonicy," *Lecture Notes in Physics*, vol. 18, pp. 163–168, 1973.

[208] van Leer, B., "Towards the ultimate conservative difference scheme ii: monotonicy and conservation combined in a second-order scheme," *Journal of Computational Physics*, vol. 14, pp. 361–370, 1974.

[209] van Leer, B., "Towards the ultimate conservative difference scheme v: A second-order sequel to Godunov's methods," *Journal of Computational Physics*, vol. 32, pp. 101–136, 1979.

[210] Vetter, M. and Sturtevant, B., "Experiments on the Richtmyer-Meshkov instability of an air/SF_6 interface," *Shock Waves*, vol. 4, pp. 247–252, 1995.

[211] von Neumann, J., "Theory of detonation waves," in *John von Neumann, Collected Works* (Taub, A., ed.), New York: MacMillan, 1942.

[212] Vorobev, A. and Zikanov, O., "Instability and transition to turbulence in a free shear layer affected by a parallel magnetic field," *Journal of Fluid Mechanics*, vol. 574, pp. 131–154, 2007.

[213] Wang, X., Ye, D., and Gu, F., "Research on the thermal ionization model of detonation products by quantum mechanics methods," *Combustion, Explosion, and Shock Waves*, vol. 44, no. 1, pp. 101–109, 2008.

[214] Wheatley, V., Pullin, D., and Samtaney, R., "Regular shock refraction at an oblique planar density interface in magnetohydrodynamics," *Journal of Fluid Mechanics*, vol. 522, pp. 179–214, 2005.

[215] Wheatley, V., Pullin, D., and Samtaney, R., "Stability of an impulsively accelerated density interface in magnetohydrodynamics," *Physical Review Letters*, vol. 95, no. 125002, pp. 1–4, 2005.

[216] Wheatley, V., Samtaney, R., and Pullin, D., "The Richtmyer-Meshkov instability in magnetohydrodynamics," *Physics of Fluids*, vol. 21, no. 082102, pp. 1–13, 2009.

[217] Wheeler, J., *Cosmic Castrophes: Supernovae, Gamma-Ray Bursts, and Adventures in Hyperspace*. Cambridge, United Kingdom: Cambridge University Press, 2000.

[218] Wilke, C., "A viscosity equation for gas mixtures," *Journal of Chemical Physics*, vol. 18, no. 4, pp. 517–519, 1950.

[219] Winkler, P. and Gupta, G., "The sn1006 remnant: Optical proper motions, deep imaging, distance, and brightness at maximum," *The Astrophysical Journal*, vol. 585, pp. 324–335, 2003.

[220] Wright, M., Bose, D., Palmer, G., and Levin, E., "Recommended collision integrals for transport property computations, part 1: Air species," *AIAA Journal*, vol. 43, no. 12, pp. 2558–2564, 2005.

[221] Yousfi, M. and Benabdessadok, M., "Boltzmann equation analysis of electron-molecule collision cross sections in water vapor and ammonia," *Journal of Applied Physics*, vol. 80, no. 12, pp. 6619–6630, 1996.

[222] Zabusky, N., "Vortex paradigm for accelerated inhomogeneous flows: visiometrics for the rayleigh-taylor and richtmyer-meshkov environments," *Annual Review of Fluid Mechanics*, vol. 31, no. 495–536, 1999.

[223] Zachary, A., Malagoli, A., and Colella, P., "A higher-order godunov method for multidimensional ideal magnetohydrodynamics," *SIAM Journal of Scientific Computing*, vol. 15, pp. 263–284, 1994.

[224] Zel'dovich, I., "On the theory of the propagation of detonation in gaseous systems," *Zh. Eksp. Teor. Fiz.*, vol. 10, pp. 542–568, 1940.

[225] Zel'dovich, I. and Raizer, Y., *Physics of Shock Waves and High-Temperature Hydrodynamic Phenomena*. Mineola, New York: Dover Publications, 2002.

[226] Zhang, Q. and Sohn, S.-I., "An analytical nonlinear theory of Richtmyer-Meshkov instability," *Physics Letters A*, vol. 212, pp. 149–155, 1996.

[227] Zhang, Q. and Sohn, S.-I., "Nonlinear theory of unstable fluid mixing drive by shock wave," *Physics of Fluids*, vol. 9, pp. 1106–1124, 1997.